AMIDOPHOSPHINE COMPLEXES OF EARLY AND LATE TRANSITION ELEMENTS

by

Alyssa Mae Yeo

B.Sc., Brandon University, 2010

A THESIS SUBMITTED IN PARTIAL FULFILLMENT OF

THE REQUIREMENTS FOR THE DEGREE OF

DOCTOR OF PHILOSOPHY

in

THE FACULTY OF GRADUATE AND POSTDOCTORAL STUDIES

(Chemistry)

THE UNIVERSITY OF BRITISH COLUMBIA

(Vancouver)

April 2020

© Alyssa Mae Yeo, 2020

The following individuals certify that they have read, and recommend to the Faculty of Graduate and Postdoctoral Studies for acceptance, the dissertation entitled:

AMIDOPHOSPHINE COMPLEXES OF EARLY AND LATE TRANSITION ELEMENTS

submitted by Alyssa Mae Yeo in partial fulfillment of the requirements for

the degree of Doctor of Philosophy

in Chemistry

Examining Committee:

Michael Fryzuk, Chemistry

Supervisor

Laurel Schafer, Chemistry

Supervisory Committee Member

Chris Orvig, Chemistry

University Examiner

Katherine Ryan, Chemistry

University Examiner

D. Michael Heinekey, Chemistry

External Examiner

Additional Supervisory Committee Members:

Michael Wolf, Chemistry

Supervisory Committee Member

Abstract

Expanding on the work of previously reported amidophosphine ligand frameworks, novel coordination chemistry and dinitrogen functionalization of transition metal complexes was pursued, utilizing both early and late transition-metals. A variety of group 5 (V, Nb, Ta) and group 9 (Co, Rh) amidophosphine complexes are described and characterized using NMR spectroscopy and X-ray crystallography.

A tantalum dinitrogen complex containing a modified amidophosphine ligand was used to examine further functionalization of the dinitrogen unit. Hydrosilylation of the modified tantalum dinitrogen complex generated a novel dinitrogen-functionalized tantalum species.

Dinitrogen functionalization of amidophosphine complexes of niobium and vanadium was explored via treatment with various electrophiles and oxidants. The formation of numerous paramagnetic niobium and vanadium complexes are described, although the desired outcome of producing oxidized dinitrogen species or cleavage and functionalization of the dinitrogen moiety was often challenged by loss of the dinitrogen unit entirely. Reactivity of a paramagnetic niobium dinitrogen complex with an oxygen-containing radical reagent resulted in generation of a novel diamagnetic niobium dinitrogen complex, incorporating a bridging oxo ligand and altered binding of the dinitrogen unit.

Paramagnetic amidophosphine cobalt complexes were examined for reactivity, in relation to previously reported work with paramagnetic cobalt species, leading to formation of an oxidized-phosphine species and a cobalt iodide complex. Synthesis of cobalt alkyl complexes was accomplished via treatment of a cobalt iodide complex with alkyllithium and Grignard

reagents. Attempts to generate a cobalt hydride complex yielded regeneration of the antecedent amidophosphine cobalt complex.

The synthesis of diamagnetic amidophosphine complexes of rhodium was investigated and the reactivity of these novel rhodium complexes with alkyl halides and H_2 was explored, in order to observe their ability to undergo oxidative addition. Several rhodium iodide and rhodium hydride species are described. Synthesis of rhodium carbonyl complexes was accomplished via ligand exchange using CO gas.

Lay Summary

Researchers are continually developing and refining processes that are designed to further benefit society. Some processes involve the use of remarkable chemicals that not only improve the efficiency, but also moderate the amount of energy and resources expended in these practices. Metal complexes (chemicals that contain a scaffold of atoms that are anchored to a central metal atom) are a notable category of chemicals that can be used for such purposes. Similar to how astronomers observe matter in outer space to gain knowledge outside the understanding of our regular environment, scientists explore chemical space to better understand how chemical systems behave. Continuing to build on this information allows for the prospect of formulating enhanced chemicals and improved processes.

The research presented in this thesis describes the creation and study of a variety of metal complexes and the surrounding foray deeper into chemical space.

Preface

I designed and performed all experiments described in this thesis, in consultation with my research supervisor, Dr. Michael Fryzuk. The synthesis and NMR spectroscopic characterization of all new compounds in Chapters 2–6 was completed by myself, with the exception of 2D NMR spectroscopy experiments for complexes **2.7**, **5.5** and **5.6** that were conducted with the aid of Dr. Maria Ezhova. For compounds that were previously prepared and reported with incomplete characterization, I repeated the synthesis, NMR spectroscopy and X-ray crystallography experiments as needed to complete characterization. All X-ray crystallographic data was collected and refined by myself, with the exception of the X-ray diffraction data for complex **3.6** that was collected by Dr. Vincent T. Annibale and structural refinements that were made by Dr. Brian Patrick. Aside from portions of this thesis that were adapted from previously published manuscripts (*vide infra*) the contents of this thesis were written by myself, with input and revisions from Dr. Richard Burford and Dr. Michael Fryzuk.

Chapter 1 is adapted from the publication: Burford, R. J.; [Yeo, A.]; Fryzuk, M. D., *Coord. Chem. Rev.* **2017,** *334*, 84-99. The above manuscript was originally drafted by Dr. Richard Burford and myself, in collaboration with Dr. Michael Fryzuk. Sections of Chapter 1 that were not adapted from the above publication were written by myself.

Chapter 2 is adapted from the publication: [Yeo, A.]; Shaver, M. P.; Fryzuk, M. D., *Z. Anorg. Allg. Chem.* **2015,** *641*, 123-127. Dr. Michael Fryzuk wrote the above manuscript and I adapted it for use in Chapter 2, with contributions that were not featured in the aforementioned publication written by myself. Complex **2.4** was originally synthesized and characterized by Dr. Michael P. Shaver.

Table of Contents

Abstract ..... **iii**

Lay Summary ..... **v**

Preface ..... **vi**

Table of Contents ..... **vii**

List of Tables ..... **xii**

List of Figures ..... **xiii**

List of Schemes ..... **xix**

List of Equations ..... **xxii**

List of Charts ..... **xxiii**

List of Symbols ..... **xxiv**

List of Abbreviations ..... **xxv**

Acknowledgements ..... **xxviii**

Chapter 1: Ligand design and dinitrogen activation: Transition-metal complexes supported by phosphine-amido containing ligands **1**

1.1 Dinitrogen activation and functionalization 1

1.2 The [PNP] ligand system: $M[N(SiMe_2CH_2P^iPr_2)_2]$ 3

1.2.1 Zirconium [PNP] complexes 3

1.2.2 Titanium [PNP] complexes 5

1.3 The $[P_2N_2]$ ligand system: $M[PhP(CH_2SiMe_2NSiMe_2CH_2)_2PPh]$ 6

1.3.1 Zirconium $[P_2N_2]$ complexes 7

1.3.2 Titanium $[P_2N_2]$ complexes 10

1.3.3 Zirconium and titanium [As_2N_2] complexes 10

1.3.4 Tantalum [P_2N_2] complexes 11

1.3.5 Niobium [P_2N_2] complexes 12

1.4 The [NPN^{Si}] ligand system: M[$PhP(CH_2SiMe_2NPh)_2$] 14

1.4.1 Zirconium and titanium [NPN^{Si}] complexes 15

1.4.2 Tantalum [NPN^{Si}] complexes 16

1.4.3 Niobium [NPN^{Si}] complexes 20

1.5 The [^{Mes}NPN*] ligand system: M[[(2,4,6-$Me_3C_6H_2$)N-2-(5-MeC_6H_3)]$_2$PPh] 21

1.5.1 Zirconium [^{Mes}NPN*] complexes 23

1.5.2 Titanium [^{tol}NPN*] complexes 25

1.5.3 Tantalum [^{Mes}NPN*] complexes 26

1.6 The [NPN^{S}] and [NPN^{cp}] ligand systems: M[[(2,4,6-$Me_3C_6H_2$)N-2-(C_4H_2S)]$_2$PPh] and M[[(2,6-$Me_2C_6H_3$)N-2-(C_5H_6)]$_2$PPh] and coordination to zirconium(IV) 27

1.7 Cobalt and rhodium coordination chemistry 29

1.7.1 Cobalt and rhodium [^{Ph}PNP] complexes 30

1.7.2 Rhodium [$^{xyl}NPN^{cp}$] complexes 32

1.7.3 Cobalt complexes with alternative ligand scaffolds 33

1.8 Scope of thesis 35

Chapter 2: Hydrosilylation of side-on end-on coordinated dinitrogen 37

2.1 Introduction 37

2.2 Synthesis and molecular structure of (^{Cy}[NPN^{Si}]Ta)$_2$(μ-η^2:η^1-N_2)(μ-H)$_2$ 41

2.3 Hydrosilylation of (^{Cy}[NPN^{Si}]Ta)$_2$(μ-η^2:η^1-N_2)(μ-H)$_2$ with $BuSiH_3$ 43

2.3.1 Monitoring hydrosilylation by $^{31}P\{^1H\}$ and ^1H NMR spectroscopy 43

2.3.2 Molecular structure of $^{Cy}[NPN^{Si}]TaH(BuSiN\text{-}\mu\text{-}Si(H)Bu\text{-}\mu\text{-}N)(\mu\text{-}H)_2Ta[NPN^{Si}]^{Cy}$ 49

2.3.3 Characterization of $^{Cy}[NPN^{Si}]TaH(BuSiN\text{-}\mu\text{-}Si(H)Bu\text{-}\mu\text{-}N)(\mu\text{-}H)_2Ta[NPN^{Si}]^{Cy}$ 51

2.3.4 Synthesis of $(^{Cy}[NPN]Ta)_2(\mu\text{-}\eta^2:\eta^1\text{-}N_2)(\mu\text{-}D)_2$ and ^2H NMR spectroscopic studies. 53

2.4 Hydrosilylation of $(^{Cy}[NPN]Ta)_2(\mu\text{-}\eta^2:\eta^1\text{-}N_2)(\mu\text{-}H)_2$ with $PhSiH_3$ 55

2.5 Conclusions 57

Chapter 3: Reactivity of paramagnetic niobium and vanadium dinitrogen complexes.....58

3.1 Introduction 58

3.2 Reactivity of $([P_2N_2]Nb)_2(\mu\text{-}N_2)$ with Lewis acids 61

3.3 Reactivity of $([P_2N_2]Nb)_2(\mu\text{-}N_2)$ with electrophiles and oxidants 67

3.3.1 Treatment of $([P_2N_2]Nb)_2(\mu\text{-}N_2)$ with iodine-containing reagents 68

3.3.2 Treatment of $([P_2N_2]Nb)_2(\mu\text{-}N_2)$ with silver salts and ferrocenium salts..... 70

3.3.3 Treatment of $([P_2N_2]Nb)_2(\mu\text{-}N_2)$ with oxygen-containing reagents..... 75

3.4 Synthesis of $([P_2N_2]V)_2(\mu\text{-}N_2)$ 78

3.5 Reactivity of $([P_2N_2]V)_2(\mu\text{-}N_2)$ with electrophiles and oxidants 81

3.5.1 Treatment of $([P_2N_2]V)_2(\mu\text{-}N_2)$ with 1,2-diiodoethane 81

3.5.2 Treatment of $([P_2N_2]V)_2(\mu\text{-}N_2)$ with silver tetraphenylborate 83

3.5.3 Treatment of $([P_2N_2]V)_2(\mu\text{-}N_2)$ with other oxidants 84

3.6 Synthesis of $[P_2N_2]VMe$ 86

3.7 Conclusions 88

Chapter 4: Synthesis and reactivity of paramagnetic $[P_2N_2]$ cobalt complexes.....90

4.1 Introduction 90

4.2 Synthesis and reactivity of *syn*-$[P_2N_2]Co$ 94

4.3 Reactivity of *syn*-$[P_2N_2]CoI$..... 99

4.3.1 Synthesis of *syn*-$[P_2N_2]$Co alkyl complexes 100

4.4 Conclusions 108

Chapter 5: Synthesis and reactivity of $[P_2N_2]$ rhodium complexes 110

5.1 Introduction 110

5.2 Synthesis and reactivity of $[P_2N_2][Rh(COD)]_2$ 112

5.2.1 Reactivity of $[P_2N_2][Rh(COD)]_2$ with alkyl halides 116

5.2.2 Reactivity of $[P_2N_2][Rh(COD)]_2$ with H_2 and CO 118

5.3 Synthesis and reactivity of $([Rh(COE)][P_2N_2]Li)_2$(dioxane) 121

5.3.1 Reactivity of $([Rh(COE)][P_2N_2]Li)_2$(dioxane) with alkyl halides 124

5.3.2 Reactivity of $([Rh(COE)][P_2N_2]Li)_2$(dioxane) with H_2 and CO 125

5.4 Conclusions 132

Chapter 6: Thesis overview, diversions and future outlook 134

6.1 Overview 134

6.2 Diversions 135

6.3 Future outlook 137

Chapter 7: Experimental 140

7.1 General procedures 140

7.2 Starting materials and reagents 141

7.3 Synthesis of compounds and experimental procedures 142

7.3.1 Compounds pertaining to Chapter 2 142

7.3.2 Experiments pertaining to Chapter 2 144

7.3.3 Compounds pertaining to Chapter 3 145

7.3.4 Compounds pertaining to Chapter 4 150

7.3.5 Compounds pertaining to Chapter 5 153

7.3.6 Compounds pertaining to Chapter 6 158

References 159

Appendices 167

Appendix A – Selected NMR spectra 167

A.1 Selected NMR spectra pertaining to Chapter 2 167

A.2 Selected NMR spectra pertaining to Chapter 3 170

A.3 Selected NMR spectra pertaining to Chapter 4 171

A.4 Selected NMR spectra pertaining to Chapter 5 172

Appendix B – IR spectra 177

Appendix C – Crystallographic data 178

List of Tables

Table 2.1 Selected bond distances (Å) of **2.4**..... 42

Table 2.2 Selected $^{31}P\{^{1}H\}$ and ^{1}H NMR spectroscopy chemical shifts for **2.4**, **2.5**, **2.6** and **2.7**. 48

Table 2.3 Selected bond distances (Å) and angles (°) of **2.7**. 50

Table 4.1 Selected bond lengths (Å) and angles (°) of **4.4-$_{MeCN}$** and **4.4-$_{dioxane}$**..... 103

Table 5.1 Selected bond lengths (Å) and angles (°) of **5.1** 115

Table C.1 Crystal structure and refinement data for **2.4** and **2.7** 178

Table C.2 Crystal structure and refinement data for **3.1** and **3.2** 179

Table C.3 Crystal structure and refinement data for **3.4** and **3.5** 180

Table C.4 Crystal structure and refinement data for **3.6** and **3.7** 181

Table C.5 Crystal structure and refinement data for **3.8**..... 182

Table C.6 Crystal structure and refinement data for $[P_2N_2]VCl$ and $([P_2N_2]V)_2(\mu\text{-}N_2)$ 183

Table C.7 Crystal structure and refinement data for **3.9** and **3.10** 184

Table C.8 Crystal structure and refinement data for **3.11**..... 185

Table C.9 Crystal structure and refinement data for **4.1** and **4.2** 186

Table C.10 Crystal structure and refinement data for **4.3** and **4.4-$_{MeCN}$** 187

Table C.11 Crystal structure and refinement data for **4.4-$_{dioxane}$** and **4.5**..... 188

Table C.12 Crystal structure and refinement data for **5.1** and **5.2** 189

Table C.13 Crystal structure and refinement data for **5.3** and **5.4** 190

Table C.14 Crystal structure and refinement data for **5.5** and **5.6** 191

Table C.15 Crystal structure and refinement data for **6.1**..... 192

List of Figures

Figure 2.1 ORTEP depiction (ellipsoids at 50 % probability) of (^{Cy}[NPN^{Si}]Ta)$_2$(μ-η^2:η^1-N$_2$)(μ-H)$_2$ (**2.4**)..... 42

Figure 2.2 ^{31}P{^{1}H} NMR spectra (121.4 MHz, C_6D_6) recorded after treatment of **2.4** with excess $BuSiH_3$. 44

Figure 2.3 Stack plot of ^{1}H{^{31}P} NMR spectra (300 MHz, C_6D_6) in the Ta hydride region, during the reaction of **2.4** with excess $BuSiH_3$ in C_6D_6 over the course of 72 h. 45

Figure 2.4 Stack plot of ^{31}P{^{1}H} NMR spectra (161.9 MHz, C_6D_6) during reaction of **2.4** with four equivalents of $BuSiH_3$ in C_6D_6 over the course of 46 h. 47

Figure 2.5 ORTEP depiction (ellipsoids at 50 % probability) of **2.7**..... 49

Figure 2.6 Analysis of the ^{1}H – ^{31}P HMBC spectrum (400 MHz, ^{1}H and 161.9 MHz, ^{31}P external projections) of **2.7** (in C_6D_6). 52

Figure 2.7 ^{1}H–^{29}Si HSQC spectrum (400 MHz, ^{1}H and 79.5 MHz, ^{29}Si external projections) of **2.7** in C_6D_6. 53

Figure 3.1 ORTEP depiction (ellipsoids at 50 % probability) of ([P$_2$N$_2$]NbN)$_2$(AlMe$_2$)$_2$ (**3.2**).. 62

Figure 3.2 Comparison of the paramagnetic ^{1}H NMR (400 MHz, C_6D_6) spectra of **3.2** (bottom) versus **3.3** (top)..... 63

Figure 3.3 Comparison of the paramagnetic ^{1}H NMR (400 MHz, C_6D_6) spectrum of **3.1** (bottom) to that of the material isolated from the thermolysis of ([P$_2$N$_2$]Nb)$_2$(μ-N$_2$) in the presence of BEt_3 (top). 64

Figure 3.4 ORTEP depiction (ellipsoids at 50 % probability) of [([P$_2$N$_2$]Nb)$_2$(μ-N$_2$)] [H$_2$B(C$_6$F$_5$)$_2$] (**3.4**)..... 66

Figure 3.5 Comparison of the paramagnetic ^{1}H NMR (400 MHz, C_6D_6) spectrum of ([P_2N_2]Nb)$_2$(μ-N_2) (bottom) to that of the material isolated from the reaction of ([P_2N_2]Nb)$_2$(μ-N_2) with [Ph_2I][OTf] (top). 68

Figure 3.6 ORTEP depiction (ellipsoids at 50 % probability) of ([P_2N_2]NbI)$_2$(μ-N_2) (**3.5**)..... 70

Figure 3.7 Paramagnetic ^{1}H NMR (400 MHz, THF-d_8) spectrum of red needle crystals isolated from the reaction between $AgBPh_4$ and ([P_2N_2]Nb)$_2$(μ-N_2). 71

Figure 3.8 ORTEP depiction (ellipsoids at 50 % probability) of **3.6**..... 72

Figure 3.9 Comparison of the paramagnetic ^{1}H NMR (400 MHz) spectrum of **3.6** (top, C_6D_6) to that of the dark red-brown material isolated from the reaction of AgOTf and ([P_2N_2]Nb)$_2$(μ-N_2) in the absence of aromatic solvent (bottom, THF-d_8)..... 73

Figure 3.10 ORTEP depiction (ellipsoids at 50 % probability) of [([P_2N_2]Nb)$_2$(μ-F)$_3$][BF_4] (**3.7**). 75

Figure 3.11 ORTEP depiction (ellipsoids at 50 % probability) of ([P_2N_2]Nb)$_2$(μ-η^2:η^2-N_2)(μ-O) (**3.8**)..... 77

Figure 3.12 ORTEP depiction (ellipsoids at 50 % probability) of [P_2N_2]VCl. 79

Figure 3.13 ORTEP depiction (ellipsoids at 50 % probability) of ([P_2N_2]V)$_2$(μ-N_2)..... 80

Figure 3.14 ORTEP depiction (ellipsoids at 50 % probability) of [P_2N_2]VI (**3.9**). 82

Figure 3.15 ORTEP depiction (ellipsoids at 50 % probability) of [([P_2N_2]V)(THF)$_2$][BPh_4] (**3.10**)..... 84

Figure 3.16 Comparison of the paramagnetic ^{1}H NMR (400 MHz, C_6D_6) spectrum of the material isolated from the reaction of ([P_2N_2]V)$_2$(μ-N_2) with [$FeCp_2$][BF_4] (top) to that of the starting ([P_2N_2]V)$_2$(μ-N_2) (bottom)..... 85

Figure 3.17 Comparison of the paramagnetic ^{1}H NMR (400 MHz, C_6D_6) spectrum of the dark purple material isolated from the treatment of $([P_2N_2]V)_2(\mu\text{-}N_2)$ with pyridine N-oxide (top) to that of the starting $([P_2N_2]V)_2(\mu\text{-}N_2)$ (bottom)..... 86

Figure 3.18 ORTEP depiction (ellipsoids at 50 % probability) of $[P_2N_2]$VMe (**3.11**). 88

Figure 4.1 ORTEP depiction (ellipsoids at 50 % probability) of *syn*-$[P_2N_2]$Co (**4.1**). 95

Figure 4.2 ORTEP depiction (ellipsoids at 50 % probability) of *syn*-$[(P{=}O)_2N_2]$Co (**4.2**). 97

Figure 4.3 ORTEP depiction (ellipsoids at 50 % probability) of *syn*-$[P_2N_2]$CoI (**4.3**)..... 99

Figure 4.4 ^{1}H NMR (400 MHz, C_6D_6) spectrum of the material isolated from the reaction of *syn*-$[P_2N_2]$CoI with one equivalent of MeLi, showing a mixture of diamagnetic and paramagnetic species. 101

Figure 4.5 Comparison of the paramagnetic ^{1}H NMR (400 MHz, C_6D_6) spectra of the material isolated from the reaction of two equivalents of MeLi with *syn*-$[P_2N_2]$CoI (top) and the crystal mixture isolated after the addition of acetonitrile (middle) to the aforementioned material. 102

Figure 4.6 ORTEP depiction (ellipsoids at 50 % probability) of **4.4-$_{\mathbf{MeCN}}$** and **4.4-$_{\mathbf{dioxane}}$**..... 103

Figure 4.7 ^{31}P{^{1}H} NMR (161.9 MHz) spectrum (inset) and ^{1}H NMR (400 MHz) spectrum of **4.4-$_{\mathbf{dioxane}}$** (in C_6D_6). 104

Figure 4.8 Comparison of the paramagnetic ^{1}H NMR (400 MHz, C_6D_6) spectra of the material generated from the treatment of *syn*-$[P_2N_2]$CoI with ethylmagnesium chloride (top spectrum), and the preceding *syn*-$[P_2N_2]$CoI species (middle spectrum) and *syn*-$[P_2N_2]$Co complex (bottom spectrum)..... 105

Figure 4.9 ORTEP depiction (ellipsoids at 50 % probability) of *syn*-$[P_2N_2]CoCH_2SiMe_3$ (**4.5**). 107

Figure 5.1 $^{31}P\{^{1}H\}$ NMR (161.9 Hz) spectrum (inset) and $^{1}H\{^{31}P\}$ NMR (400 MHz) spectrum of **5.1** (in C_6D_6). 113

Figure 5.2 ORTEP depiction (ellipsoids at 50 % probability) of $[P_2N_2][Rh(COD)]_2$ (**5.1**)..... 114

Figure 5.3 $^{31}P\{^{1}H\}$ NMR (161.9 MHz) spectrum (inset) and $^{1}H\{^{31}P\}$ NMR (400 MHz) spectrum of **5.2** (in THF-d_8). 116

Figure 5.4 ORTEP depiction (ellipsoids at 50 % probability) of $[P_2N_2]Rh(\mu\text{-}I)_2Rh(COD)$ (**5.2**). 118

Figure 5.5 $^{31}P\{^{1}H\}$ NMR (161.9 MHz) spectrum (inset) and ^{1}H NMR (400 MHz) spectrum of **5.3** (in C_6D_6)..... 120

Figure 5.6 ORTEP depiction (ellipsoids at 50 % probability) of $[P_2N_2]Rh(CO)[Rh(CO)_2]$ (**5.3**). 121

Figure 5.7 $^{31}P\{^{1}H\}$ NMR (161.9 MHz) spectrum (inset) and $^{1}H\{^{31}P\}$ NMR (400 MHz) spectrum of **5.4** (in C_6D_6). 122

Figure 5.8 ORTEP depiction (ellipsoids at 50 % probability) of $([Rh(COE)][P_2N_2]Li)_2$(dioxane) (**5.4**). 123

Figure 5.9 $^{31}P\{^{1}H\}$ NMR (161.9 MHz) spectrum (inset) and ^{1}H NMR (400 MHz) spectrum of complex **5.5** (in C_6D_6)..... 126

Figure 5.10 Comparison of the ^{1}H NMR spectra (400 MHz, C_6D_6) of the material generated from treatment of **5.4** with H_2 (top spectrum) and complex **5.5** isolated from the aforementioned reaction (bottom), focused on the alkyl and hydride regions of the spectra. 126

Figure 5.11 ORTEP depiction (ellipsoids at 50 % probability) of $[P_2N_2H]Rh(H)_2$ (**5.5**). 128

Figure 5.12 $^{31}P\{^{1}H\}$ NMR (161.9 MHz) spectrum (inset) and ^{1}H NMR (400 MHz) spectrum of **5.6** (in C_6D_6)..... 129

Figure 5.13 $^{31}P\{^{1}H\}$ NMR (161.9 MHz) spectra (left) and the alkyl region of the $^{1}H\{^{31}P\}$ NMR (400 MHz) spectra (right), all in C_6D_6, comparing the material generated from the reaction of CO with an Et_2O solution of **5.4** (top) and the material generated from the reaction of CO with a THF solution of **5.4** (middle) to complex **5.6** (bottom)..... 131

Figure 5.14 ORTEP depiction (ellipsoids at 50 % probability) of $[P_2N_2H]Rh(CO)$ (**5.6**)..... 132

Figure 6.1 ORTEP depiction (ellipsoids at 50 % probability) of $[P_2N_2]V(OTf)_2NH_3$ (**6.1**)..... 138

Figure A.1.1 $^{31}P\{^{1}H\}$ NMR spectrum (121.4 MHz, C_6D_6) of $(^{Cy}[NPN^{Si}]Ta)_2(\mu\text{-}\eta^2\text{:}\eta^1\text{-}N_2)(\mu\text{-}H)_2$ (**2.4**)..... 167

Figure A.1.2 $^{1}H\{^{31}P\}$ NMR spectrum (300 MHz, C_6D_6) of **2.4**..... 167

Figure A.1.3 $^{31}P\{^{1}H\}$ NMR spectrum (161.9 MHz) of $^{Cy}[NPN^{Si}]TaH(BuSiN\text{-}\mu\text{-}Si(H)Bu\text{-}\mu\text{-}N)(\mu\text{-}H)_2Ta[NPN^{Si}]^{Cy}$ (**2.7**) in C_6D_6..... 168

Figure A.1.4 ^{1}H NMR spectrum (400 MHz, C_6D_6) of **2.7**..... 168

Figure A.1.5 $^{31}P\{^{1}H\}$ NMR spectra (161.9 MHz, C_6D_6) recorded after treatment of **2.4** with excess $PhSiH_3$, showing resonances corresponding to **2.8**, **2.9** and **2.10**. 169

Figure A.1.6 $^{1}H\{^{31}P\}$ NMR spectrum (400 MHz, C_6D_6) recorded after treatment of **2.4** with excess $PhSiH_3$, focused on the hydride region..... 169

Figure A.2.1 $^{31}P\{^{1}H\}$ NMR (161.9 MHz) spectrum (inset) and $^{1}H\{^{31}P\}$ NMR spectrum (400 MHz) of $([P_2N_2]Nb)_2(\mu\text{-}\eta^2\text{:}\eta^2\text{-}N_2)(\mu\text{-}O)$ (**3.8**) in THF-d_8..... 170

Figure A.2.2 ^{13}C APT NMR spectrum (100.6 MHz, THF-d_8) of **3.8** 170

Figure A.3.1 $^{13}C\{^{1}H\}$ NMR spectrum (100.6 MHz, C_6D_6) of **4.4-$_{dioxane}$** (bottom) and ^{13}C APT NMR spectrum (top) 171

Figure A.3.2 ^{7}Li NMR (155.5 MHz, C_6D_6) spectrum of **4.4-$_{dioxane}$**. 171

Figure A.4.1 $^{31}P\{^{1}H\}$ NMR spectrum (161.9 MHz, C_6D_6) of the material isolated from heating a THF solution of *syn*-$[P_2N_2]Li_2$ with half an equivalent of $[Rh(COD)Cl]_2$ at 60 °C for 12 h 172

Figure A.4.2 Comparison of the $^{31}P\{^{1}H\}$ NMR spectra (161.9 MHz, C_6D_6) of the material isolated after the treatment of complex **5.1** with H_2 gas, before heating (top) and after heating at 80 °C for 12 h (bottom)..... 173

Figure A.4.3 $^{1}H\{^{31}P\}$ NMR spectrum (400 MHz, C_6D_6) of the material isolated after the treatment of complex **5.1** with H_2 gas, after heating at 80 °C for 12 h..... 173

Figure A.4.4 $^{31}P\{^{1}H\}$ NMR spectrum (161.9 MHz, C_6D_6) of the material isolated after treatment of $([Rh(COE)][P_2N_2]Li)_2$(dioxane) (**5.4**) with excess MeI. 174

Figure A.4.5 $^{31}P\{^{1}H\}$ NMR spectrum (161.9 MHz, C_6D_6) of the material isolated after treatment of $([Rh(COE)][P_2N_2]Li)_2$(dioxane) (**5.4**) with I-CH_2CH_2-I. 174

Figure A.4.6 ^{1}H–^{13}C HMBC NMR spectrum (400 MHz, ^{1}H and 100.6 MHz, ^{13}C external projections, C_6D_6) of **5.5** displaying a multiple-bond correlation between the N–H proton and silyl methyl carbons. 175

Figure A.4.7 ^{13}C APT NMR spectrum (100.6 MHz, C_6D_6) of **5.5** 175

Figure A.4.8 ^{1}H–^{13}C HMBC NMR spectrum (400 MHz, ^{1}H and 100.6 MHz, ^{13}C external projections, C_6D_6) of **5.6** displaying a multiple-bond correlation between the N–H proton and silyl methyl carbons. 176

Figure A.4.9 ^{13}C APT NMR spectrum (100.6 MHz, C_6D_6) of **5.6** 176

Figure B.1 IR spectrum of complex **5.3** (ν_{CO} = 1938, 1988 and 2020 cm^{-1}). 177

Figure B.2 IR spectrum of complex **5.6** (ν_{CO} = 1929 cm^{-1})..... 177

List of Schemes

Scheme 1.1 4

Scheme 1.2 6

Scheme 1.3 7

Scheme 1.4 9

Scheme 1.5 10

Scheme 1.6 11

Scheme 1.7 12

Scheme 1.8 13

Scheme 1.9 14

Scheme 1.10 15

Scheme 1.11 17

Scheme 1.12 18

Scheme 1.13 19

Scheme 1.14 22

Scheme 1.15 24

Scheme 1.16 25

Scheme 1.17 26

Scheme 1.18 27

Scheme 1.19 28

Scheme 1.20 29

Scheme 1.21 30

Scheme 1.22 31

Scheme 1.23 32

Scheme 1.24 33

Scheme 1.25 34

Scheme 1.26 35

Scheme 2.1 38

Scheme 2.2 39

Scheme 2.3 40

Scheme 2.4 46

Scheme 2.5 56

Scheme 3.1 59

Scheme 3.2 60

Scheme 3.3 61

Scheme 3.4 67

Scheme 3.5 80

Scheme 3.6 82

Scheme 3.7 87

Scheme 4.1 93

Scheme 4.2 108

Scheme 4.3 109

Scheme 5.1 110

Scheme 5.2 111

Scheme 5.3 127

Scheme 5.4 131

Scheme 5.5 133

Scheme 6.1 136

Scheme 6.2 137

Scheme 6.3 137

List of Equations

Equation 1.1 3

Equation 1.2 21

Equation 2.1 41

Equation 3.1 83

Equation 4.1 94

Equation 4.2 95

Equation 4.3 96

Equation 4.4 97

Equation 4.5 100

Equation 4.6 105

Equation 5.1 113

Equation 5.2 117

Equation 5.3 119

Equation 5.4 122

List of Charts

Chart 1.1 Five ligand manifolds explored in Fryzuk Group dinitrogen chemistry. 2

Chart 4.1 PDI cobalt precatalysts employed in asymmetric hydrogenation of alkenes. 90

Chart 4.2 Diphosphinoamine cobalt alkyl and hydride complexes utilised as precatalysts. 91

Chart 4.3 Cobalt dichloride precatalysts applied in hydrogenation and alkylation reactions. 91

Chart 4.4 Structure of *syn*-[P_2N_2]Co compared to *anti*-[P_2N_2]Co 93

List of Symbols

Å	–	Ångström (10^{-10} meters)
β	–	Refers to 1,3- substitution or the second carbon atom from an atom, functional group or moiety of interest
C_1	–	A point group that contains only the identity symmetry operation
°C	–	Degrees Celsius
°	–	Degrees
Δ	–	Heat
δ	–	Chemical shift in NMR spectroscopy measured in parts per million
J	–	Coupling constant in NMR spectroscopy
κ^n	–	Indicates single ligating atom attachments of a polyatomic ligand to a metal centre, where n denotes the number of such attachments
η^n	–	Hapticity, where n denotes the number of contiguous atoms in a ligand coordinated to a metal centre
μ	–	Denotes that a ligand is bridging between two metal centres
μ_B	–	Bohr magneton
μ_{eff}	–	Effective magnetic moment
ν	–	Frequency in IR spectroscopy measured in wavenumber(s)

List of Abbreviations

Anal.	–	Combustion elemental analysis
APT	–	Attached proton test
Ar	–	Aryl
atm	–	Atmosphere(s)
br	–	Broad
^{n}Bu, Bu	–	*n*-butyl, normal (primary) butyl
^{t}Bu	–	*tert*-butyl (tertiary butyl)
C_6D_6	–	Benzene-d_6
Calcd	–	Calculated
cm^{-1}	–	Wavenumber(s)
COD	–	Cyclooctadiene
COE	–	*cis*-cyclooctene
COSY	–	Correlation spectroscopy
Cp	–	Cyclopentadienyl
Cy	–	Cyclohexyl
d	–	Doublet in spectroscopy
DFT	–	Density functional theory
DIPP	–	2,6-diisopropylphenyl
DME	–	1,2-dimethoxyethane
DMSO	–	Dimethyl sulfoxide

EA	–	Elemental Analyses
EPR	–	Electron paramagnetic resonance
Eq	–	Equation
equiv	–	Equivalent(s)
Et	–	Ethyl
Et_2O	–	Diethyl ether
g	–	Gram(s)
h	–	Hour(s)
HMBC	–	Heteronuclear multiple bond coherence
HMDSO	–	Hexamethyldisiloxane
HSQC	–	Heteronuclear single quantum coherence
Hz	–	Hertz ($seconds^{-1}$)
^{i}Pr	–	Isopropyl
KC_8	–	Potassium graphite
LDA	–	Lithium diisopropylamide
M	–	Metal
m	–	Multiplet in spectroscopy
Me	–	Methyl
Mes	–	Mesityl (2,4,6-trimethylphenyl)
mg	–	milligram(s)
MHz	–	Megahertz, one million hertz
mL	–	millilitre(s)

mmol	–	millimole(s)
NMR	–	Nuclear magnetic resonance
ORTEP	–	Oak Ridge Thermal-Ellipsoid Plot Program
Ph	–	Phenyl
ppm	–	Part(s) per million
RT	–	Room temperature
s	–	Singlet in spectroscopy
t	–	Triplet in spectroscopy
t	–	Time
TEMPO	–	2,2,6,6-tetramethylpiperidin-1-oxyl
THF	–	Tetrahydrofuran
THT	–	Tetrahydrothiophene
TMS	–	Trimethylsilyl
VT	–	Variable-temperature

Acknowledgements

My experiences during graduate school at UBC were undoubtedly enriched by my connections with diverse personalities, cultures and ideas; it is difficult to fully express the gratitude I feel for everyone that contributed to my perseverance.

I would like to thank Dr. Michael Fryzuk for the opportunities and support provided in his research laboratory. Thanks to Dr. (Sam) Yan for pointing me in this direction and Dr. Mark Berry and Dr. Patrick Jackson for also believing I should pursue graduate education. Many thanks to Dr. Joachim Ballmann for his patience and kindness in teaching me air-sensitive chemistry techniques; without the solid foundation he provided I would not have felt capable of pursuing graduate research. To Dr. Richard Burford, thank you for improving my scientific writing skills, and for your willingness to engage in endless conversations about chemistry and life. I have no idea how this thesis would have been written were it not for your commitment to offering me advice and support. To all my past Fryzuk group labmates, it was a pleasure to have spent time with you all, sharing in conversation and laughter that helped us make it through each day. Special thanks to those who I worked most closely with: Achim, Rui, Bryan, JM, Nathan, Truman, Lee, Fraser, Nick, Amanda, Eye, Thomas, Tiko, Rich, Corey and Pedro, your presence in my corner was appreciated along the way. For my labmates from another mother: Joe, Scott, Andy, Ying, Erin, Peter and Nirmal, I thank you for your friendship and solidarity during this journey.

The support staff in the Chemistry Department deserves considerable recognition for their time and expertise, without which I would not have been able to complete my research. Thank you to Dr. Maria Ezhova of the NMR spectroscopy facilities and Dr. Brian Patrick and

Anita Lam of the X-ray crystallography facilities for all of their assistance and teachings. Thanks to the electronics shop and mech shop for their dedication to fixing and maintaining all our equipment, with special thanks to Milan Coschizza and Ken Love for always making sure our gloveboxes and pumps were running smoothly. Additional gratitude is merited for Ken Love, for your kind presence and kind words; I thank you for your continued support. Most of all I would like to thank Brian Ditchburn of the glassblowing shop, who always has time for me, whether it's for broken glass or a broken heart; thank you for your unwavering support and true friendship.

Lastly, I would like to thank my sweetest friends, Stephanie, Diana, Andrea and Matt, your genuine love and support always makes me feel like I can and will persist. Thank you to all the friends who were there for me through this wild ride, through the long days and nights, through joy and sorrow, I appreciate you for all the light you have given me to make it through the dark.

This work was completed with generous financial support from NSERC (CGS-M and CGS-D) as well as UBC (Chemistry Graduate Fellowship, Faculty of Science Graduate Award, Gladys Estella Laird Research Fellowship and 4YF).

Chapter 1: Ligand design and dinitrogen activation: Transition-metal complexes supported by phosphine-amido containing ligands

1.1 Dinitrogen activation and functionalization

Efficient catalytic reduction-functionalization of molecular nitrogen (N_2) represents an as yet unsolved synthetic challenge inspired by nature.[1-4] Nitrogen is an essential element for all living systems. While abundant in the atmosphere, the intrinsic inertness of N_2 limits its entry into the biosphere to just two processes. Biologically, the nitrogenase enzyme carries out the difficult catalytic transformation of N_2 into ammonia (NH_3) by the use of the iron-molybdenum-sulfur protein known as the FeMo-cofactor,[5-6] although the operative mechanism of nitrogen fixation is still a matter of conjecture.[7-10] Industrially, the extremely energy-intensive[11] Haber-Bosch process produces ammonia from N_2 and H_2.[12-13] Despite being perfected over a hundred years ago, this is still the only known industrial process that uses molecular nitrogen as a feedstock.

The discovery of the first dinitrogen complex, $[Ru(NH_3)_5N_2]^{2+}$,[14] was an inspiration for numerous research groups to study the coordination chemistry of molecular nitrogen[15-20] with the ultimate goal to discover systems that can functionalize the N_2 unit.[21-22] However, even with more than 50 years of research invested, a new, efficient catalytic transformation of this unreactive small molecule remains elusive.[23-25] Dinitrogen complexes of many metals across the periodic table have been reported,[26-28] and with each advancement, the importance of the ligands that surround the metal centre becomes increasingly apparent.[29] What has also become evident is that small changes in ligand designs can effect large changes in the outcome of the reactions of metal complexes, particularly in dinitrogen activation.[30] While this has made predictability of

matching new ligand designs with anticipated outcomes difficult, it has not slowed creative attempts to discover new combinations of ligands and metals that can activate and functionalize one of the most inert small molecules, dinitrogen.

This thesis has two main foci: dinitrogen coordination chemistry by group 5 elements, and the coordination chemistry of group 9 elements Co and Rh using a macrocyclic ligand. Although dinitrogen activation and functionalization is a key theme, ligand design is also an important strategy that has evolved in the Fryzuk group.[31] The design of ancillary ligands incorporating phosphine and amido donors and their subsequent coordination chemistry with the early transition elements, titanium, zirconium, niobium and tantalum will be discussed. While a number of successes have been achieved, several ligand systems have failed to generate desired outcomes, illustrating the unpredictability of ligand changes on the reactivity of the resultant metal complexes. As an aside from dinitrogen activation, alternative coordination chemistry to the late transition metals cobalt and rhodium is also presented. Chart 1.1 illustrates the generic ancillary ligand-metal complexes focused on with respect to Fryzuk group dinitrogen chemistry.

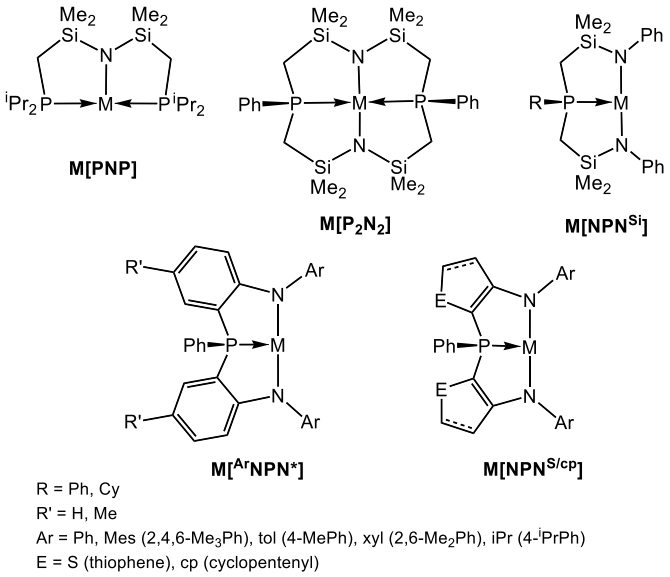

Chart 1.1 Five ligand manifolds explored in Fryzuk Group dinitrogen chemistry.

1.2 The [PNP] ligand system: $M[N(SiMe_2CH_2P^iPr_2)_2]$

The design of tridentate meridional, monoanionic ancillary ligands with bulky flanking phosphines (so called pincer ligands) comprises a large field of study in organometallic chemistry.[32] While the extent of pincer-complex catalysis is beyond the scope of this work, the regularity with which pincer-ligated transition metal systems mediate difficult bond transformations is well known.[33-36] The synthesis of [PNP] and subsequent coordination chemistry with late metals was first reported in the early 1980's.[37-38] While there was interest in the coordination chemistry of this ligand with early metals, as described elsewhere,[39] its use in dinitrogen activation was serendipitous.[37] The synthesis of the lithium salt of the [PNP] ligand, shown in Equation 1.1, is straightforward and utilizes commercially available starting materials.[38]

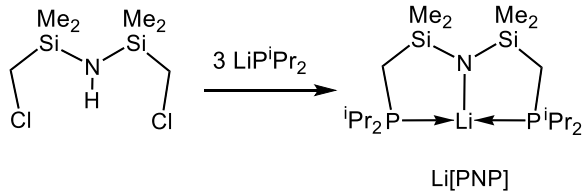

[1.1]

1.2.1 Zirconium [PNP] complexes

After the success of the [PNP] system in late transition-metal chemistry,[40] a lack of early transition metal coordination chemistry involving phosphine donors as ancillary ligands was noticed.[41-42] Consequently, investigation of zirconium PNP complexes, starting with the preparation of $[PNP]ZrCl_3$ (**1.1**) and subsequent reduction chemistry under N_2 was pursued. As shown in Scheme 1.1, reaction of **1.1** with sodium-amalgam under dinitrogen generated the side-on dizirconium dinitrogen complex $([PNP]ZrCl)_2(\mu\text{-}\eta^2\text{:}\eta^2\text{-}N_2)$ (**1.2**), with an activated N_2 unit as evidenced by the very long N–N bond length of 1.548(7) Å.[43]

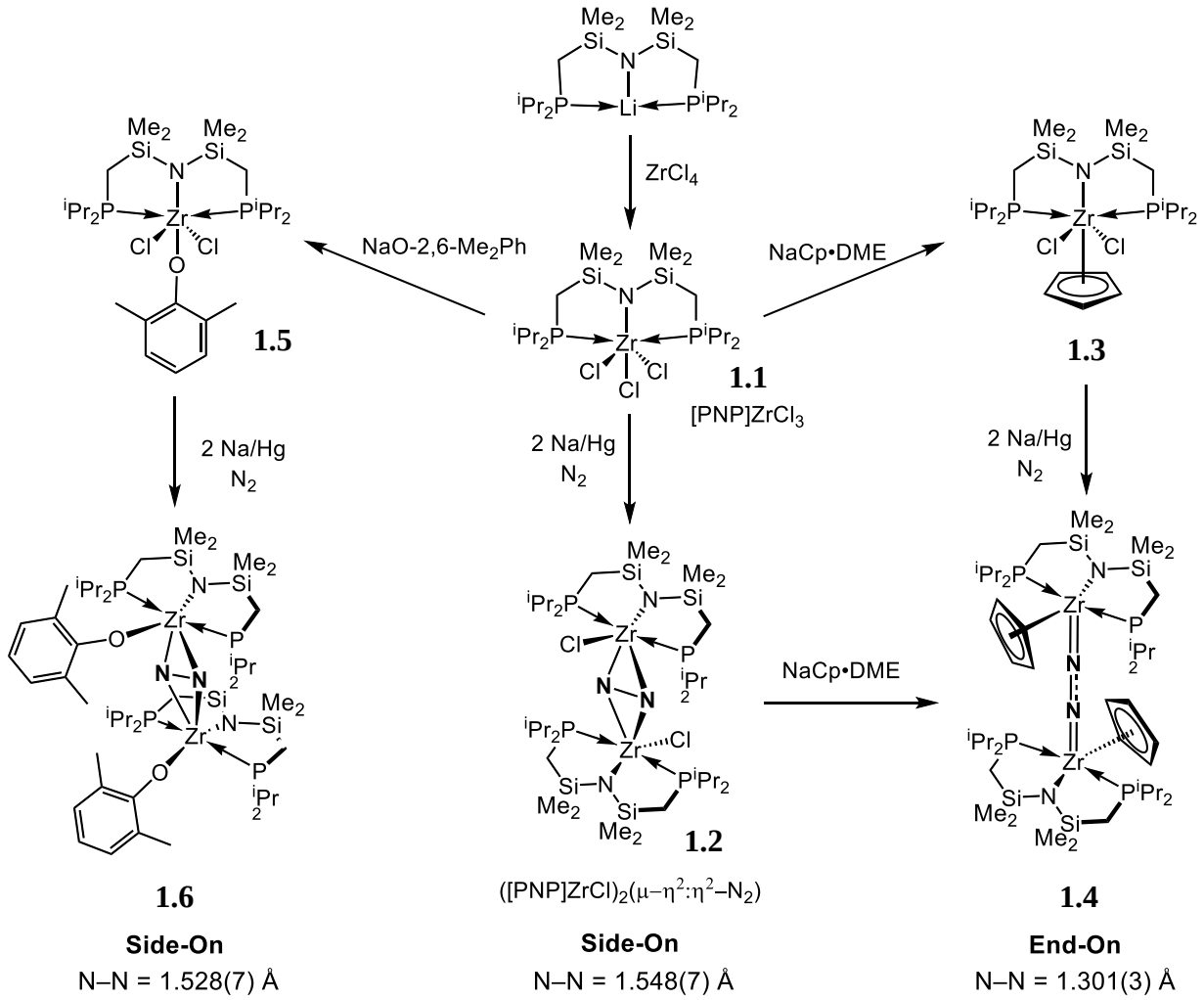

Scheme 1.1

Prior to this discovery, the few reports of characterized zirconium N_2 complexes showed end-on bonding.[14] The measured N–N bond distance of 1.548(7) Å was the longest reported at that time, and is typical of an N–N single bond similar to hydrazine (H_2NNH_2). Subsequent reports have shown that the N–N bond can vary in length from unactivated N_2 (1.088(12) Å)[44] to significantly activated (1.635(5) Å), as reported for a dihafnium dinitrogen complex.[45]

The very activated, side-on bridging bonding mode observed in **1.2** prompted further computational[46] and spectroscopic (Resonance Raman)[47] studies to provide baseline data on this,

at the time, rare interaction. Replacement of one of the chlorides with a cyclopentadienyl unit (**1.3**) and subsequent reduction resulted in formation of the dinuclear end-on bridging dinitrogen complex $([PNP]ZrCp)_2(\mu\text{-}N_2)$ (**1.4**) (Scheme 1.1); the observed N–N bond distance of 1.301(3) Å is long when compared with other end-on bridging N_2 units.[46] Computational and orbital analysis suggested that the presence of pi-donor ligands would promote the side-on mode of bonding, confirmed by the synthesis of the aryloxy derivative $[PNP]Zr(OAr)Cl_2$ (OAr = 2,6-dimethylphenoxy) (**1.5**). Upon reduction, the side-on dinitrogen complex $([PNP]ZrOAr)_2(\mu\text{-}\eta^2{:}\eta^2\text{-}N_2)$ (**1.6**) is generated (Scheme 1.1) that displays a very long N–N bond distance of 1.528(7) Å.

1.2.2 Titanium [PNP] complexes

Expansion of [PNP] chemistry to the lighter group 4 metal titanium was investigated. Synthesis of an analogous precursor complex using Li[PNP] and $TiCl_4$ resulted in isolation of $[PNP]TiCl_3$ (**1.7**) in very good yield. Upon reduction with excess elemental magnesium under N_2, the dititanium dinitrogen complex $([PNP]TiCl)_2(\mu\text{-}N_2)$ (**1.8**) was obtained as shown in Scheme 1.2.[48] In this complex, the N_2 unit is end-on bound to the two titanium centres with an N–N bond distance of 1.275(7) Å, consistent with a significantly less activated N_2 molecule, as compared to the analogous side-on dizirconium congener **1.2**. Nevertheless, this end-on bridging dinitrogen is considered to be formally N_2^{4-}, even though the N–N bond lengths of **1.8** and **1.2** are quite different. Treatment of **1.8** with hydrochloric acid resulted in hydrazine production, albeit in low yield.[48] End-on bound dinitrogen complexes have proven to engage in considerably less reaction chemistry than related side-on coordinated complexes; for example, there was no reaction with H_2 or silanes. As such, the titanium [PNP] chemistry was not pursued further.

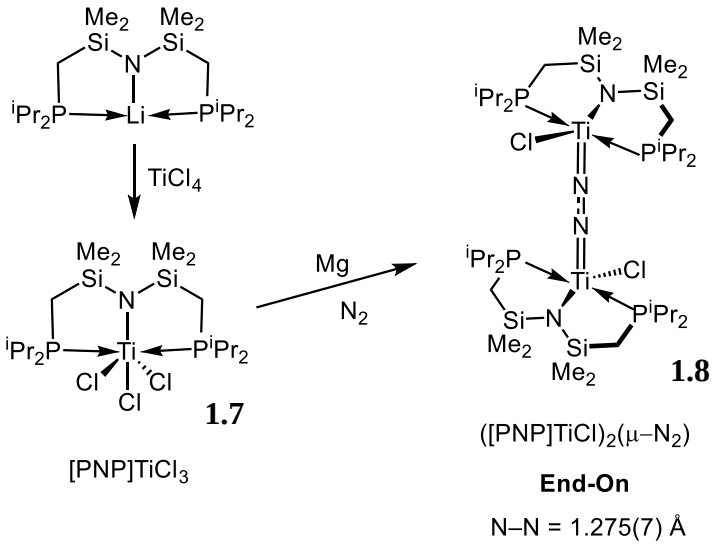

Scheme 1.2

The efforts invested in the coordination chemistry of the [PNP] ligand on zirconium led to fruitful results in terms of dinitrogen chemistry. Furthermore, ligand modification by replacement of the flanking phosphines with dimethylamine donors resulted in formation of $HN(SiMe_2CH_2NMe_2)_2$, which was subsequently investigated in complexes of group 4 metals (Ti, Zr, Hf). Unfortunately, reduction under N_2 did not lead to tractable materials.[49]

1.3 The $[P_2N_2]$ ligand system: $M[PhP(CH_2SiMe_2NSiMe_2CH_2)_2PPh]$

The discovery of side-on N_2 binding to zirconium with [PNP] as the ancillary ligand was the starting point for a longstanding interest in dinitrogen activation and functionalization. While **1.2** was very reactive to added reagents such as H_2, silanes, and other small molecules, pure materials eluded isolation. It's probable that the phosphine arms of the [PNP] system readily dissociate from Zr(IV) causing undesired side reactions to ensue. In an effort to mitigate

phosphine dissociation, pursuing the synthesis of a macrocyclic system should, by virtue of the macrocyclic effect,[50-51] reduce the tendency for phosphine dissociation.

The synthesis of $[P_2N_2]Li_2$ (Scheme 1.3) utilizes the same chloromethylene silyl amine starting material used in the preparation of Li[PNP] (Equation 1.1). Issues normally associated with macrocycle syntheses, such as high dilution and formation of different ring sizes, were not encountered, likely due to the templating effect of the lithium ions present.[52] The formation of two diastereomers of the dilithium salt, *syn*- and *anti*-$[P_2N_2]Li_2$, occurs when the reaction is carried out in THF; the syn form can be favoured by the choice of solvent and lower temperatures.[52]

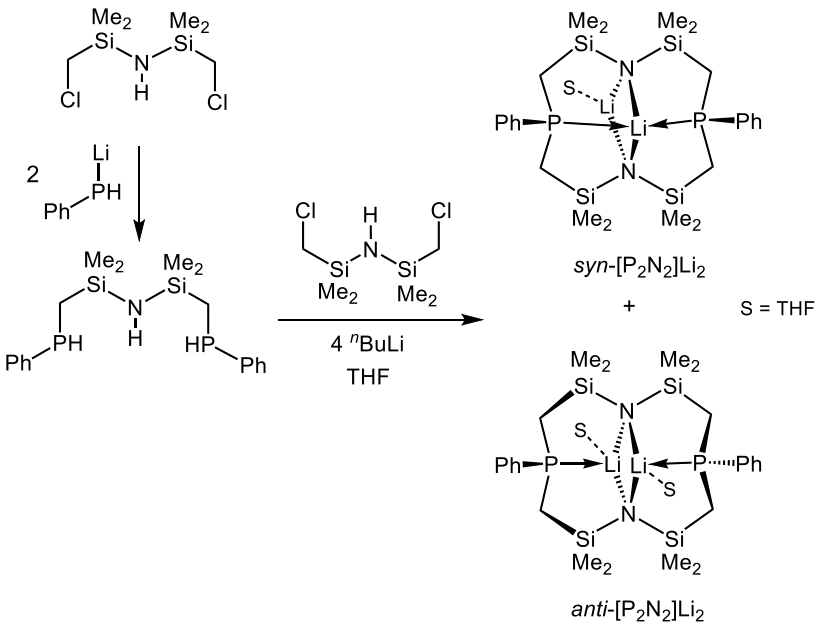

Scheme 1.3

1.3.1 Zirconium $[P_2N_2]$ complexes

Initial investigations of the macrocyclic $[P_2N_2]$ ligand involved complexation with zirconium. Reaction of *syn*-$[P_2N_2]Li_2$ with $ZrCl_4(THT)_2$ (THT = tetrahydrothiophene) resulted in

quantitative formation of $[P_2N_2]ZrCl_2$ (**1.9**). Analogous to that described above for **1.1**, reduction of **1.9** with KC_8 under N_2 resulted in the formation of the corresponding bimetallic side-on bound N_2 complex $([P_2N_2]Zr)_2(\mu\text{-}\eta^2\text{:}\eta^2\text{-}N_2)$ (**1.10**).[53-54] While this dinitrogen complex bears a slightly shorter N–N bond length of 1.465(19) Å as compared to the [PNP] supported zirconium **1.2** (1.548(7) Å), the electronic and steric environment offered by the macrocyclic $[P_2N_2]$ ligand results in the formation of the same side-on bound N_2^{4-} ligand. More importantly, the added stability of the macrocycle enabled further reactivity of the coordinated dinitrogen unit, as described below.

Hydrogenation of the side-on N_2 unit was accomplished by addition of H_2 to **1.10**,[53] (Scheme 1.4), which resulted in the formation of $([P_2N_2]Zr)_2(\mu\text{-}\eta^2\text{-}N_2H)(\mu\text{-}H)$ (**1.11**). Observation of the N–H functionality marked the first report of such a transformation by addition of H_2 to a dinitrogen complex.[53] Further stoichiometric functionalization of coordinated dinitrogen led to a variety of transformations involving heterolytic bond cleavage, as illustrated in Scheme 1.4. For example, addition of *n*-butylsilane resulted in the formation of an N–Si bond, as found in $([P_2N_2]Zr)_2(N_2Si^nBuH_2)(H)$ (**1.12**).[53] This complex was characterized by X-ray crystallography and bears a long N–N bond distance of 1.530(4) Å (Scheme 1.4). The formation of an N–C bond was discovered by treatment of **1.10** with alkynes. Crystalline materials were isolated from the reaction of terminal aryl acetylenes with **1.10**. The resulting crystal structure showed $([P_2N_2]Zr)_2(N_2(H)C{=}CArH)(CCAr)$ (**1.13)** (Scheme 1.4) in which the N–N bond is 1.457(4) Å (for Ar = 4-methylphenyl) and bears an *E*-alkene at one nitrogen atom. A bridging acetylide is also present and provides evidence for a [2+2] mechanism that involves cycloaddition of the alkyne unit to a Zr–N bond, followed by protonation of the newly formed Zr–C unit by the second alkyne.[55]

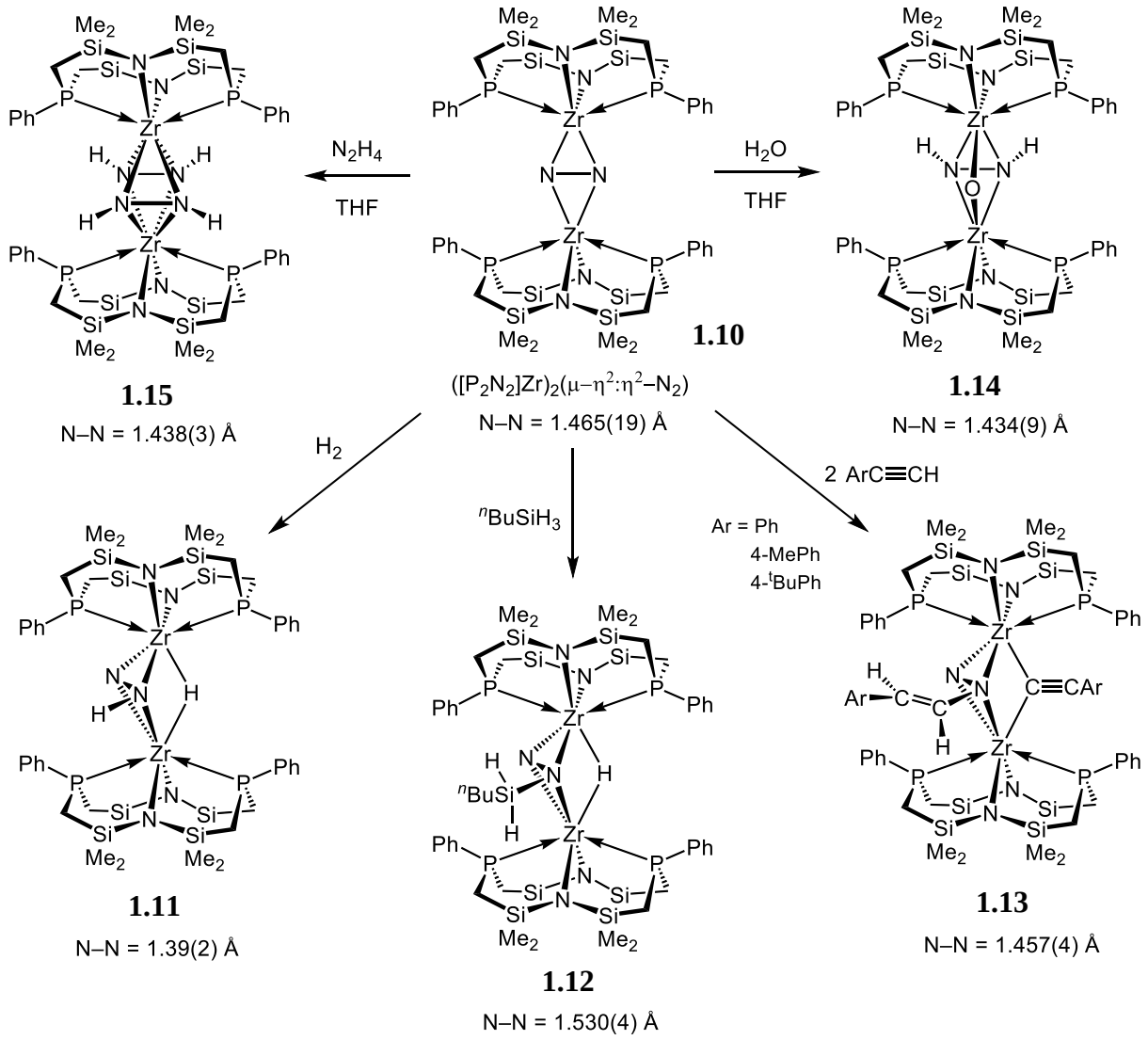

Scheme 1.4

The side-on dinitrogen unit in **1.10** is quite basic, as evidenced by reactions with water and hydrazine: deprotonation of H_2O generates the μ-oxo derivative $([P_2N_2]Zr)_2(N_2H_2)(O)$ (**1.14**), while deprotonation of N_2H_4 results in the formation of $([P_2N_2]Zr)_2(N_2H_2)_2$ **1.15**, containing two $N_2H_2^{2-}$ units (unpublished results).[54]

1.3.2 Titanium [P_2N_2] complexes

Since the dinitrogen functionalization chemistry with the zirconium [P_2N_2] system was so rich, the analogous chemistry with the lighter group 4 congener titanium was explored. Salt metathesis of *syn*-[P_2N_2]Li_2 with $TiCl_4$ afforded [P_2N_2]$TiCl_2$ (**1.16**) in excellent yield. Reduction of **1.16** with 2 equivalents of KC_8 under an N_2 atmosphere resulted in formation of ([P_2N_2]Ti)$_2$(μ-N_2) **1.17** (Scheme 1.5). X-ray diffraction analysis showed end-on coordination with an N–N bond length of 1.255 (7) Å,[56] typical of moderately activated coordinated N_2 in the end-on bridging mode. Similar to the [PNP] analogue, the dinitrogen moiety in **1.17** is formally assigned as an N_2^{4-} unit. The lack of reactivity of this dinitrogen complex with H_2, silanes or alkynes is further evidence that the end-on bridging mode of N_2 is less reactive than the side-on bridging mode.

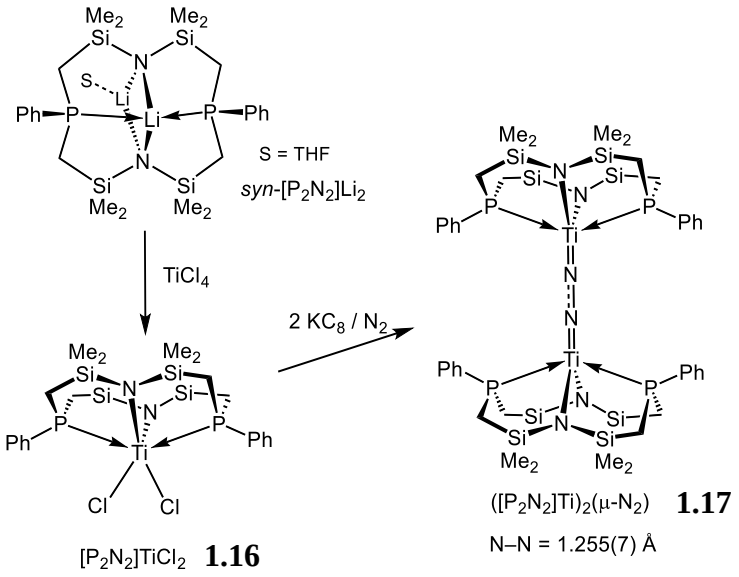

Scheme 1.5

1.3.3 Zirconium and titanium [As_2N_2] complexes

The macrocyclic arsine analogue [As_2N_2] was also examined as a ligand framework. Scheme 1.6 shows the synthesis of [As_2N_2], utilizing PhAsHLi in place of PhPHLi, however, in

the case of arsenic, only the syn isomeric form of the dilithium species could be detected.[57] Reaction of *syn*-$[As_2N_2]Li_2$ with Ti(IV) and Zr(IV) chloride complexes resulted in the formation of the desired precursors for reduction. Unfortunately, all attempts to reduce $[As_2N_2]MCl_2$ (M = Ti, Zr) under dinitrogen yielded intractable materials.[57]

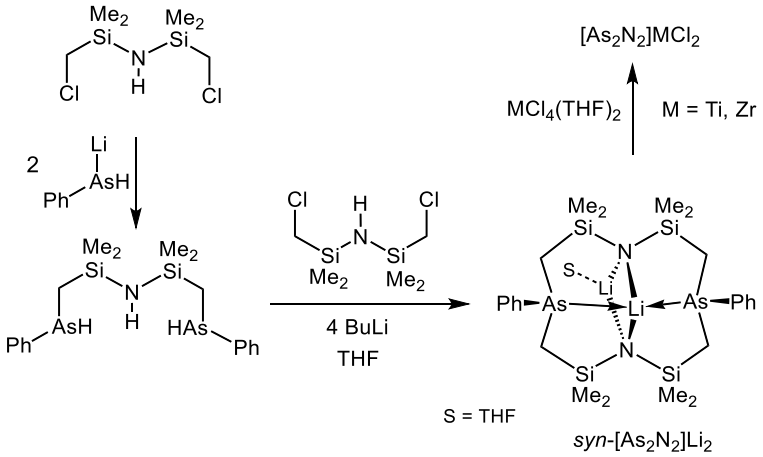

Scheme 1.6

1.3.4 Tantalum $[P_2N_2]$ complexes

Expansion of the coordination chemistry of $[P_2N_2]$ to tantalum uncovered new challenges. Attempts to prepare a $[P_2N_2]$ bound Ta(V) trihalide complex by reaction of $[P_2N_2]Li_2$ with $TaCl_5$ resulted in complex mixtures of products that resisted purification.[58] However, reaction of $[P_2N_2]Li_2$ with Me_3TaCl_2 generated $[P_2N_2]TaMe_3$ (**1.18**), which was subsequently hydrogenated to generate the ditantalum tetrahydride species $([P_2N_2]Ta)_2(\mu\text{-}H)_4$ (**1.19**) as shown in Scheme 1.7. Attempts to replace the bridging hydrides with halides by reaction with alkyl halides failed; with methyl iodide, oxidation of the formally Ta(IV)-Ta(IV) tetrahydride led to the cationic mixed oxidation state Ta(V)-Ta(IV) tetrahydride **1.20**, as shown in Scheme 1.7.[59]

Although **1.19** was not disposed to small molecule activation, it did serve as impetus to design less sterically and electronically saturated ligand systems (see Section 1.4.2).

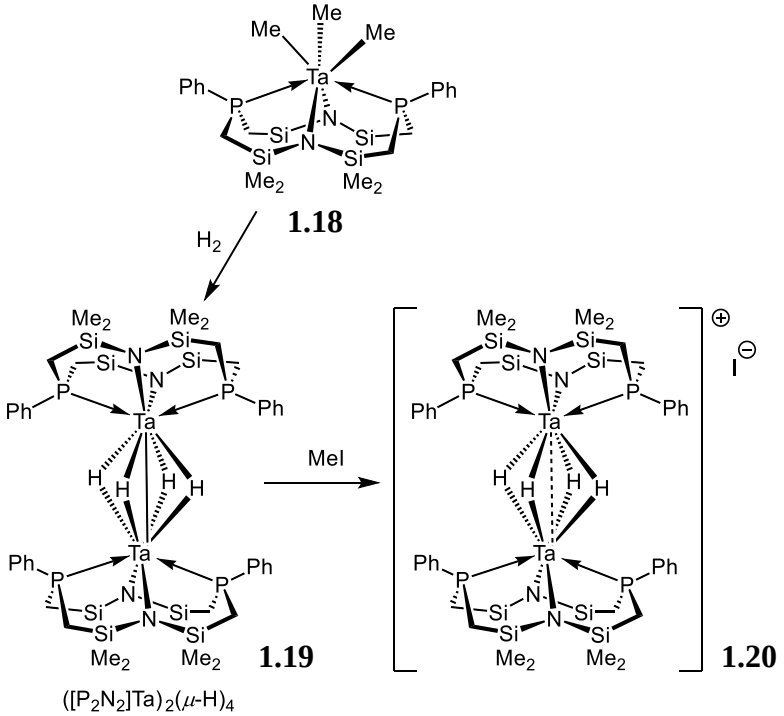

Scheme 1.7

1.3.5 Niobium [P_2N_2] complexes

Although a lack of access to low-valent tantalum starting materials prevented facile synthesis of reduced [P_2N_2] derived complexes, the ready availability of the niobium(III) reagent, $NbCl_3$(DME) (DME = 1,2-dimethoxyethane),[60] allowed us to explore dinitrogen activation with this second row group 5 metal. The reaction of *syn*-[P_2N_2]Li_2 with $NbCl_3$(DME) results in the formation of [P_2N_2]NbCl (**1.21**).[60] Reduction of **1.21** using KC_8 under N_2 generates the paramagnetic bimetallic dinitrogen complex ([P_2N_2]Nb)$_2$(μ-N_2) (**1.22**) (Scheme 1.8).[61] X-ray crystallographic data shows that the N–N bond length of **1.22** is 1.272(5) Å, similar to other end-

on bridging N_2 units; EPR data and variable-temperature magnetic studies are consistent with the presence of a formal hydrazido N_2^{4-} unit bridging between two Nb(IV) centres.[61]

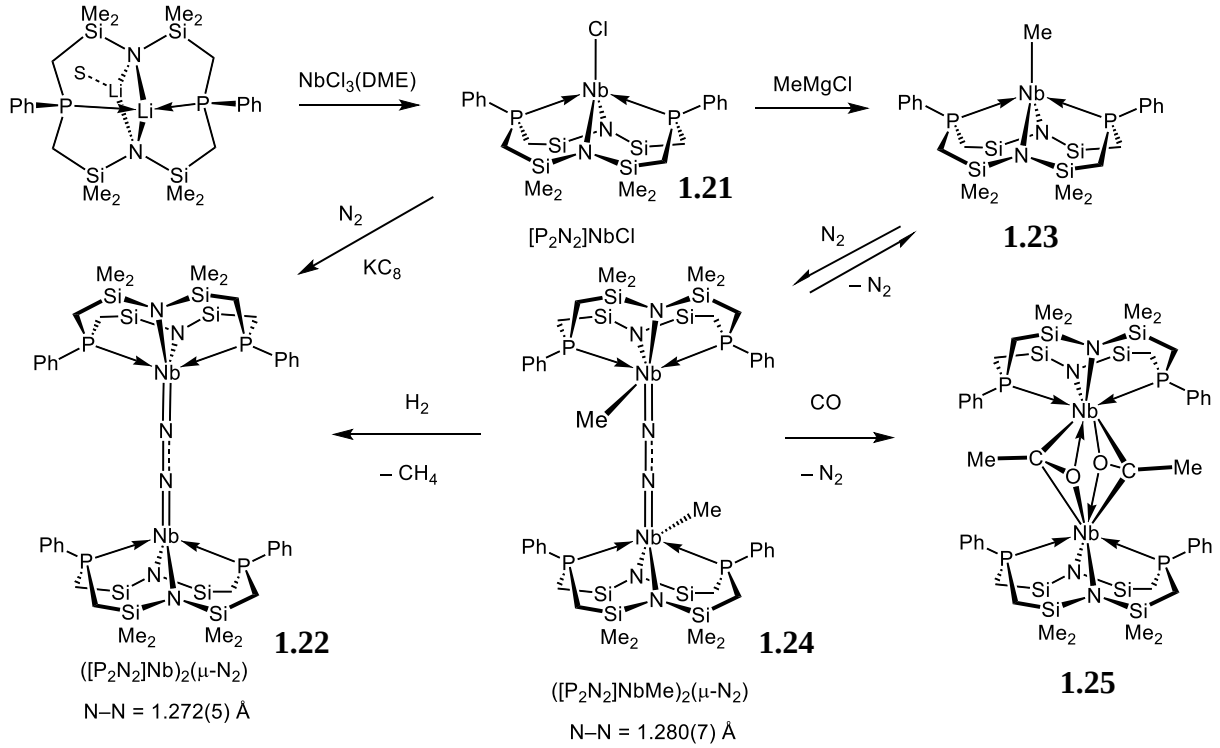

Scheme 1.8

Stable niobium alkyl complexes were also discovered upon exposure of **1.21** to alkyllithium reagents. In particular, the paramagnetic methyl complex $[P_2N_2]$NbMe (**1.23**), [60, 62] prepared by reaction of **1.21** with MeMgCl, coordinates dinitrogen to generate the diamagnetic dinuclear derivative **1.24**, which also reverts back to the starting species **1.23** when heated under partial vacuum (Scheme 1.8).[62] Although the N–N bond length of 1.280(7) Å in **1.24** is similar to other end-on bridging units, the lability of the coordinated N_2 fragment suggests that it is only weakly activated.[62] Interestingly, exposure of the methyl complex **1.24** to H_2 generates the previously described complex **1.22**.[62] Lastly, addition of CO to **1.24** results in loss of N_2 to

produce $[[P_2N_2]Nb]_2(\mu\text{-}\eta^2\text{-}COCH_3)_2$ (**1.25**), a bimetallic Nb species bridged by acyl groups bound in an η^2 fashion (Scheme 1.8).[62]

1.4 The $[NPN^{Si}]$ ligand system: $M[PhP(CH_2SiMe_2NPh)_2]$

The progression from monoanionic [PNP] to the dianionic macrocyclic $[P_2N_2]$ system allowed for new kinds of transformations involving coordinated N_2. The observed reactivity patterns were partially attributed to the stability imparted by the macrocycle, preventing phosphine dissociation. This design feature was extended into an acyclic tridentate ligand system by positioning a single phosphine donor between two formally anionic amido donors, which should also prevent phosphine dissociation. The synthesis of the $[NPN^{Si}]$ donor set is shown in Scheme 1.9.[63] Treatment of $ClSiMe_2CH_2Cl$ with 1 equivalent of lithium anilide results in the formation of chloromethyldimethylsilyl aniline. Subsequent addition of *n*-butyllithium and $PhPH_2$ in a 4:1 ratio provides good yields of the dilithio diamidophosphine, $[NPN^{Si}]Li_2$ (Scheme 1.9).

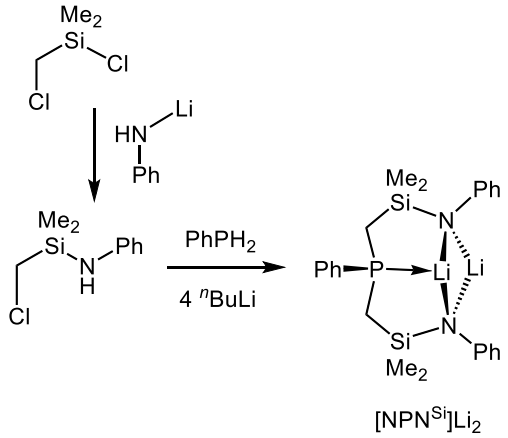

Scheme 1.9

1.4.1 Zirconium and titanium [NPN^{Si}] complexes

The Zr(IV) starting material [NPN^{Si}]$ZrCl_2$ (**1.26**) was prepared via the treatment of [NPN^{Si}]Li_2 with $ZrCl_4(THF)_2$. As described for related zirconium systems, reduction of **1.26** with KC_8 under dinitrogen (in the presence of THF) results in the formation of the dinuclear dinitrogen derivative ([NPN^{Si}]ZrTHF)$_2$(μ-η^2:η^2-N_2) (**1.27**) in which a side-on N_2 bridges the two Zr(IV) centres with a N–N bond distance of 1.503(3) Å (Scheme 1.10).[56] Both **1.10** (Section 1.3.1) and **1.27** have similar coordination geometries in that two amido and two neutral donors coordinate to each Zr(IV) centre. However, attempts to replicate the reactivity of **1.10** by addition of H_2, silanes and alkynes were not successful, highlighting the unpredictability of ligand changes on the reactivity of metal complexes. No reaction was observed upon addition of H_2 to **1.27**, even after extended reaction times. In contrast, the addition of alkynes and silanes to **1.27** led to multiple products that could not be identified or separated.[64]

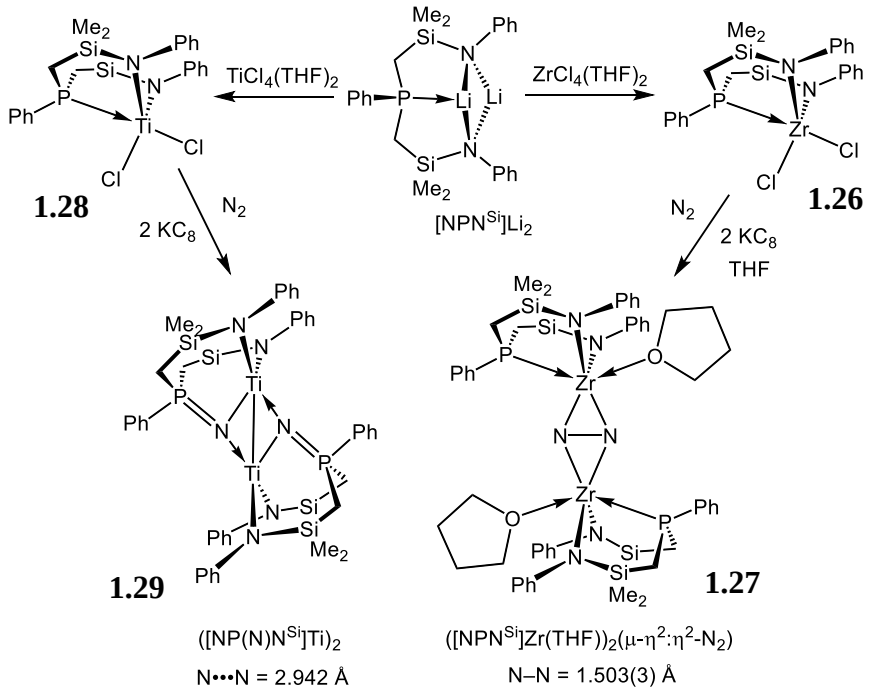

Scheme 1.10

As shown in Scheme 1.10, the analogous treatment of $[NPN^{Si}]Li_2$ with $TiCl_4(THF)_2$ provided good yields of $[NPN^{Si}]TiCl_2$ **1.28**, which was then reduced with 2 equivalents of KC_8 under dinitrogen. However, the final product was not the putative dinitrogen complex but rather the diphosphinimido complex $([NP(N)N^{Si}]Ti)_2$ (**1.29**). Each phosphine has been oxidized to a phosphinimide and the titanium centres have been formally reduced to Ti(III). A proposed mechanism involves an intermediate bimetallic Ti(IV) dinitrogen complex that is over-reduced to generate a bimetallic Ti(IV) species with two bridging nitrides, undergoing nucleophilic attack by the ligand phosphine; subsequent electron transfer reduces Ti(IV) to Ti(III).[56] The accessibility of the Ti(III) oxidation state could account for the difference in overall reduction pathways between the Zr and Ti complexes stabilized by the NPN^{Si} ligand.

1.4.2 Tantalum $[NPN^{Si}]$ complexes

As a result of the study of $[P_2N_2]$ tantalum complexes that led to tetrahydride **1.19**, exploration of the coordination chemistry of the $[NPN^{Si}]$ ligand toward tantalum, with the presumption that complexes of $[NPN^{Si}]$ would be more reactive by virtue of being coordinatively less saturated than the $[P_2N_2]$ systems. The reaction of $TaMe_3Cl_2$ and $[NPN^{Si}]Li_2$ produces $[NPN^{Si}]TaMe_3$ (**1.30**), which upon hydrogenation yields the corresponding ditantalum tetrahydride $([NPN^{Si}]Ta)_2(\mu\text{-}H)_4$ (**1.31**) (Scheme 1.11).[63, 65] Unexpectedly, it was found that a solution of **1.31** reacts spontaneously with dinitrogen via elimination of H_2 to generate the side-on end-on bound N_2 complex $([NPN^{Si}]Ta)_2(\mu\text{-}\eta^1{:}\eta^2\text{-}N_2)(\mu\text{-}H)_2$ (**1.32**). Not only was the bonding mode unique, the overall formation of an activated dinitrogen complex without the addition of strong reducing agents such as Na/Hg or KC_8 was an important breakthrough.[63, 65] The N–N

bond length is 1.319(4) Å, consistent with a strongly activated N_2 moiety assigned a formal N_2^{4-} oxidation state.[63, 65]

The reactivity of **1.32** is extremely rich, as the dinitrogen unit can be functionalized and the bridging hydrides can also undergo reactivity independently.[66] For example, the reaction of propene with **1.32** results in isomerization of the N_2 unit to generate the end-on bridging dinitrogen derivative ([NPN^{Si}]Ta($CH_2CH_2CH_3$))$_2$(μ-N_2) (**1.33**) (Scheme 1.11), highlighting the requirement of bridging hydrides to enforce the side-on end-on bonding mode.[65]

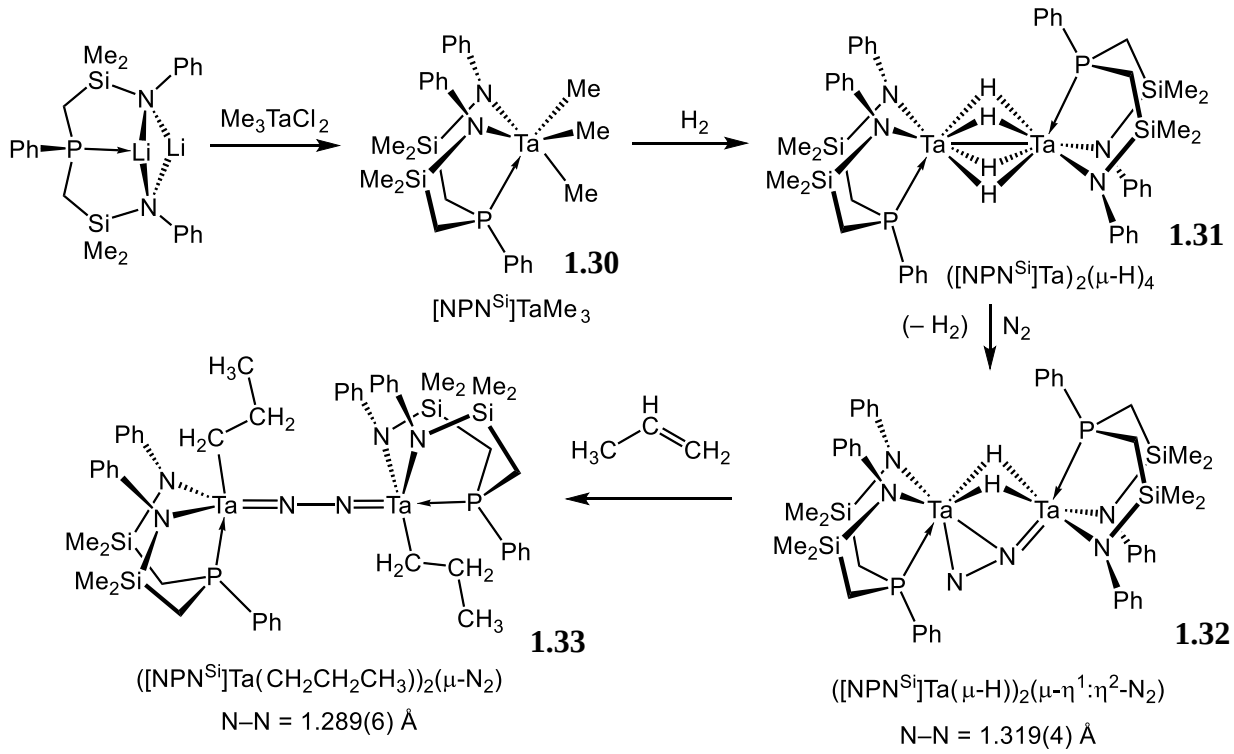

Scheme 1.11

Examining the treatment of **1.32** with a variety of neutral group 13 Lewis acids revealed that the exposed nitrogen of the side-on end-on N_2 unit readily forms Lewis acid adducts.[67] Specifically, trimethylaluminum (**1.34**), trispentafluorophenylborane (**1.35**) and trimethylgallium

(**1.36**) adducts were synthesized and characterized (Scheme 1.12). X-ray crystallographic data indicate a slight elongation of the N–N bond in each adduct compared to the parent species **1.32**, suggestive of some small further activation of the N_2 moiety.[67] The range of adducts possible illustrates the accessibility of the terminal nitrogen in the side-on end-on unit, which was explored further in [2+2] cycloadditions.

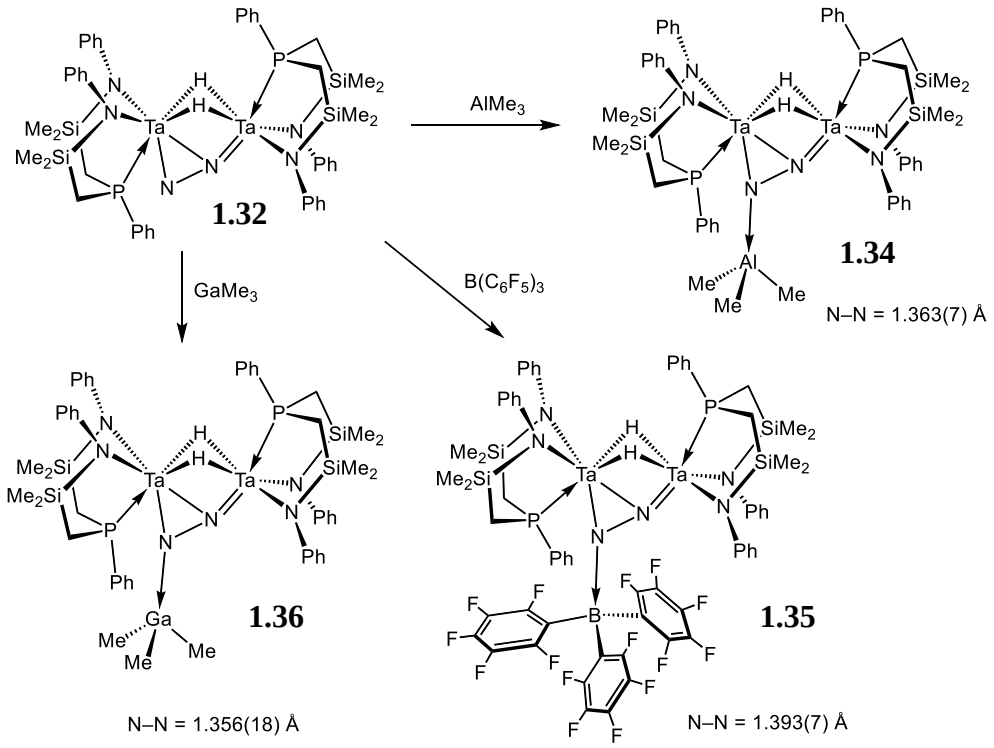

Scheme 1.12

In the interest of forming new N–C bonds towards functionalization of coordinated N_2, the possibility of cycloadditions using reagents with cumulated X=C=Y double bonds (where X, Y = S, N, O) was evaluated. Initial attempts with oxygen-containing 1,2-heterodienes X=C=O (where X = RN, S, O) resulted in complex mixtures and/or intractable solids.[68-69] However, reaction of **1.32** with the CO_2 analogue, N,N'-diphenylcarbodiimide, resulted in the clean

formation of the cycloaddition product ([NPN^{Si}]Ta)$_2$(μ-H)$_2$(μ-κ^3-PhNC(NPh)N$_2$) (**1.37**), shown in Scheme 1.13.[69] While no further chemistry was observed with this species, the formation of the [2+2] cycloadduct with a new N-C bond is noteworthy and provided the crucial underpinning for the reactions with other heterodienes.[69] In the reaction of **1.32** with phenylisothiocyanate (PhN=C=S) sulfur migration, H_2 elimination and N–N bond cleavage occurs to generate ([NPN^{Si}]Ta)$_2$(μ-S)(μ-N)(NCNPh) (**1.38**). A similar reaction is observed between **1.32** and *tert*-butylisothiocyanate (**1.39**), however, the final product is more complicated due to ligand rearrangement (**1.40**) (Scheme 1.13).

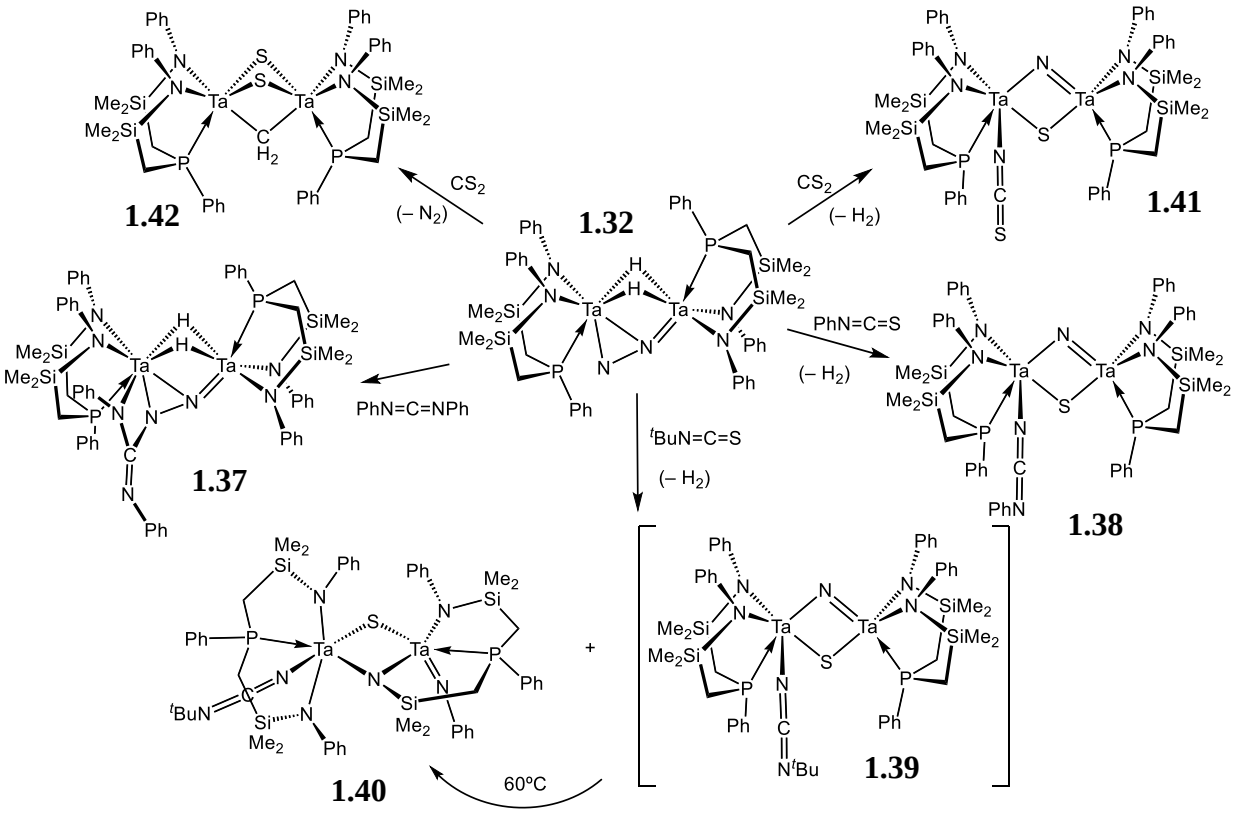

Scheme 1.13

The reaction of **1.32** with carbon disulfide generated two different products (**1.41** and **1.42**, shown in Scheme 1.13) in variable yields depending on specific reaction conditions.[68-69] Addition of CS_2 at low temperatures favours the product of sulfur migration, that is the isothiocyanato derivative ([NPN^{Si}]Ta)$_2$(μ-S)(μ-N)(NCS) (**1.41**) bearing bridging sulfide and nitride moieties, similar to that found for the reaction of phenylisothiocyanate. Changing the reaction conditions to higher temperatures appears to favour a different product that involves N_2 dissociation and complete disassembly of the CS_2 molecule to generate methylene and two bridging sulfides in ([NPN^{Si}]Ta)$_2$(μ-S)$_2$(μ-CH$_2$) (**1.42**). Recently, this reaction was revisited, revealing that CS_2 concentration, not temperature, is the important parameter in determining which product forms.[70]

Further modification of [NPN^{Si}] was undertaken in the interest of changing the phosphorus donor to arsenic to observe the effect on the reactivity pattern. The synthesis of the diamido-arsine adaptation [NAsN^{Si}] was carried out in an analogous manner and treated with $TaMe_3Cl_2$ to form the corresponding [NAsN^{Si}]$TaMe_3$ complex.[71] However, hydrogenation of this complex does not lead to the desired tetrahydride, but instead yields only protonated ligand precursor.[71] X-ray crystallography and DFT studies indicate that the arsine donor does not interact with tantalum, perhaps rationalizing the unproductive reactivity with dihydrogen.[71]

1.4.3 Niobium [NPN^{Si}] complexes

Concurrent with research involving the [NPN^{Si}] ligand system and tantalum, coordination of [NPN^{Si}] to niobium was explored. The reaction between [NPN^{Si}] and $NbCl_3$(DME) in the presence of N_2 results in the direct formation of a diamagnetic dinitrogen complex

($[NPN^{Si}]NbCl)_2(\mu\text{-}N_2)$ (**1.43**) (Equation 1.2) under ambient conditions.[65] In comparison to **1.32**, the N_2 moiety of **1.43** is bound end-on with a short N–N bond length of 1.237(4) Å.

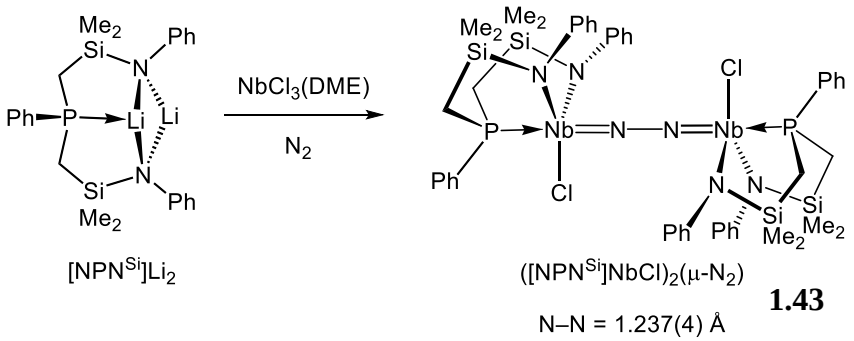

[1.2]

In an effort to replicate the method used to generate the tantalum tetrahydride and subsequent dinitrogen species of $[NPN^{Si}]$, the corresponding $NbMe_3Cl_2$ starting material was reacted with $[NPN^{Si}]$ to form the analogous $[NPN^{Si}]NbMe_3$, a highly light- and thermally-sensitive compound.[72] Attempts to hydrogenate $[NPN^{Si}]NbMe_3$ led to decomposition, suggesting that this complex is too unstable to withstand the hydrogenation process.[72]

1.5 The $[^{Mes}NPN^*]$ ligand system: $M[[(2,4,6\text{-}Me_3C_6H_2)N\text{-}2\text{-}(5\text{-}MeC_6H_3)]_2PPh]$

The discoveries made possible by the coordination environment of $[NPN^{Si}]$ illustrated the potential of this diamido-phosphine ligand set to facilitate dinitrogen activation and functionalization when coordinated to early transition metals. However, non-productive ligand rearrangements involving N–Si bond cleavage and phosphine oxidation[73] suggested that synthesis of a similar array of donors with increased thermal and kinetic stability could prevent these undesired rearrangements and perhaps allow release of a functionalized nitrogen fragment. To that end, the CH_2SiMe_2 linkers were replaced with *ortho*-phenylene linkers, reasoning that the basicity of the amine unit should not change too much; the known pK_a values of diaryl amine

(Ph_2NH = 24.95) and disilylamines ($(Me_3Si)_2NH$ = 25.8) are similar enough to suggest that substitution of an aryl for a silyl substituent would be appropriate.[44] Synthetic routes to these new [NPN*] systems have been reported; Scheme 1.14 summarizes the preparation of [^{Mes}NPN*]H_2, the diamine-phosphine derivative in which the amine and phosphine donors are linked by *ortho*-phenylene units.

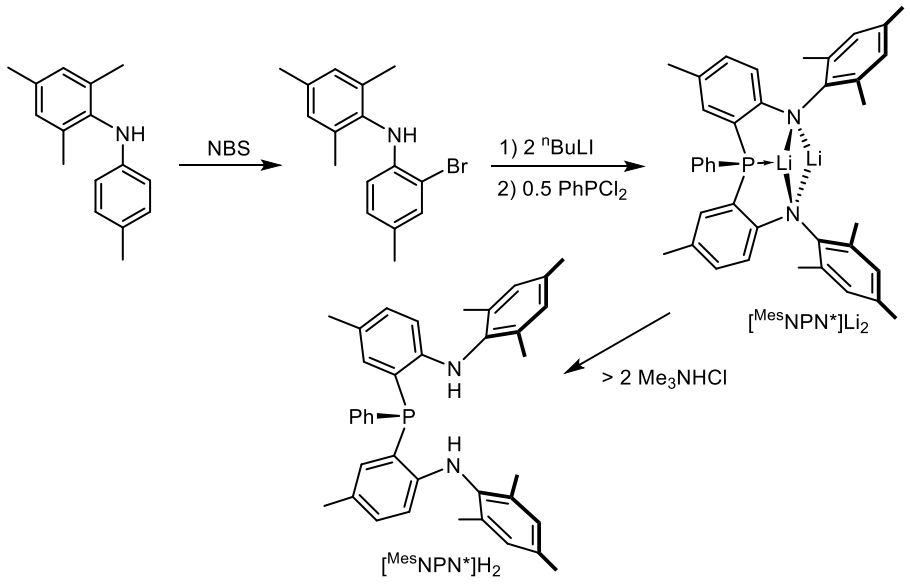

Scheme 1.14

Using *N*-mesityl-4-toluamine, the bromination occurs at the 2-position of the *p*-tolyl group in high yield. Subsequent lithium halogen exchange and amine deprotonation by *n*-butyllithium followed by dichlorophenylphosphine quench resulted in the desired lithiated ligand [^{Mes}NPN*]Li_2 in two steps from commercially available starting materials (Scheme 1.14).[74] The synthesis of [^{Mes}NPN*] was also modified by replacement of the mesityl groups on the amido donors with less sterically encumbering aryl groups such as N-*p*-Me-phenyl and N-*p*-isopropyl-phenyl to generate [^{tol}NPN*] and [^{iPr}NPN*].[75]

1.5.1 Zirconium [^{Mes}NPN*] complexes

Early studies with the [^{Mes}NPN*] ligand initially focused on zirconium chloride precursors as a means to evaluate the similarities with [NPN^{Si}]. Direct salt metathesis with $ZrCl_4$ resulted in complex mixtures rather than the desired complex. To circumvent this, the protonated ligand, [^{Mes}NPN*]H_2, was treated with $Zr(NMe_2)_4$, resulting in quantitative formation of [^{Mes}NPN*]$Zr(NMe_2)_2$. Subsequent treatment with excess Me_3SiCl [74] generated the dichloro complex [^{Mes}NPN*]$ZrCl_2$ (**1.44**), which was reduced with 2 equivalents of KC_8 under excess N_2 in THF (Scheme 1.15) to generate the side-on dinitrogen complex ([^{Mes}NPN*]ZrTHF)$_2$(μ-η^2:η^2-N_2) (**1.45**).[76] Complex **1.45** displays a long N–N bond length of 1.503(6) Å, consistent with other side-on NPN-stabilized zirconium dinitrogen complexes.[44, 56, 76]

The THF ligands of **1.45** can be displaced by pyridine to generate the bis(pyridine) complex ([^{Mes}NPN*]Zrpy)$_2$(μ-η^2:η^2-N_2) (**1.46**), and by PMe_2Ph to produce the unsymmetrical monophosphine derivative ([^{Mes}NPN*]Zr)$_2$$PMe_2Ph$($\mu$-$\eta^2$:$\eta^2$-$N_2$) (**1.47**) (Scheme 1.15). This latter monophosphine derivative **1.47** adds H_2 similar to that found for complex **1.10**[53] to generate N–H bearing ([^{Mes}NPN*]Zr)$_2$$PMe_2Ph$($\mu$-$\eta^2$-$N_2H$)($\mu$-H) (**1.48**). To date, N-H bond formation in this manner has only been observed at zirconium supported by [P_2N_2] and [^{Mes}NPN*] demonstrating the rare and challenging nature of this transformation.

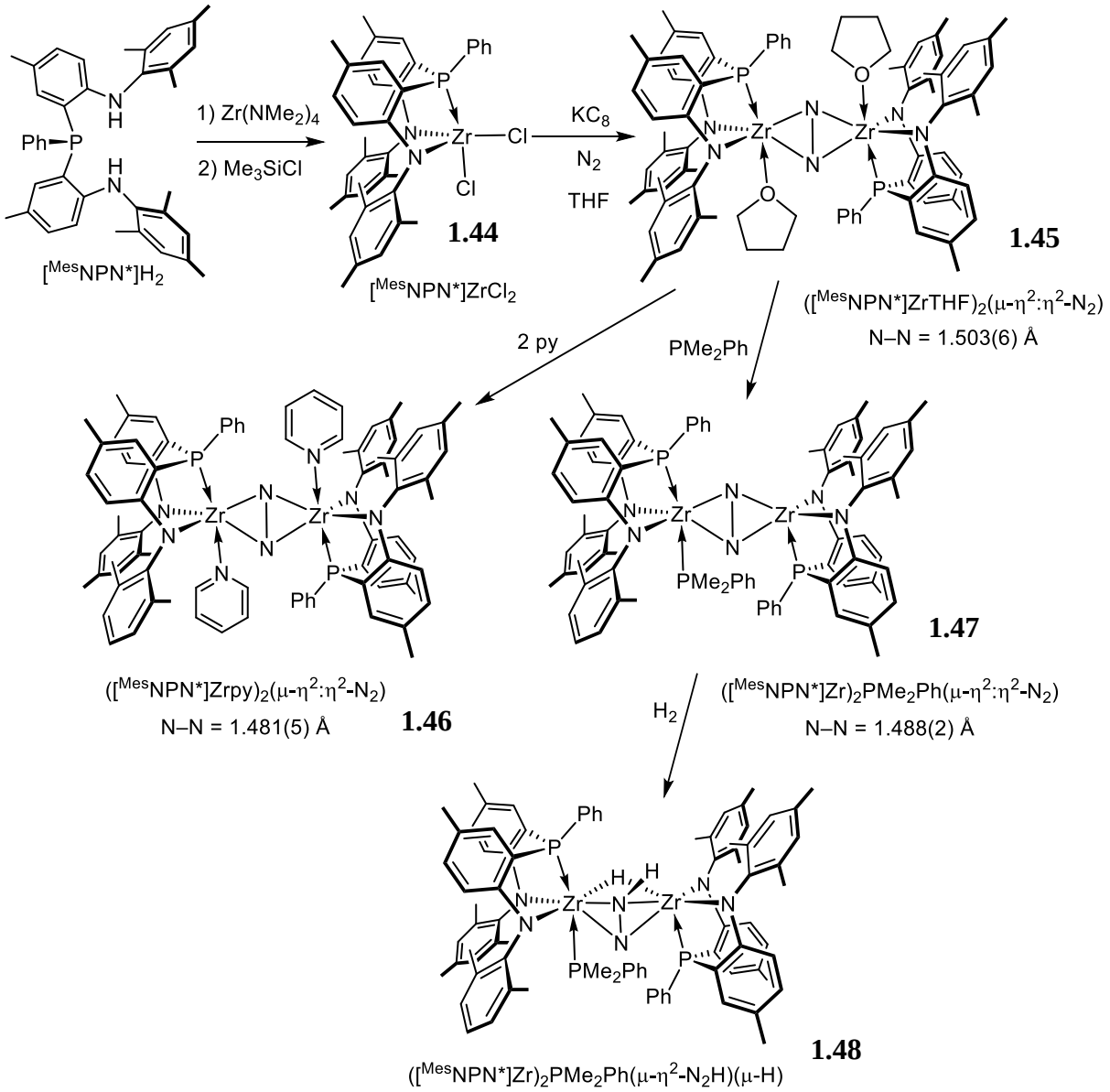

Scheme 1.15

In unpublished work, other *ortho*-phenylene tethered NPN ligands that have less bulky N-aryl substituents such as 4-isopropylphenyl have been explored, resulting in the [^{iPr}NPN*] donor set and 4-methylphenyl, represented as [^{tol}NPN*]; these are prepared via modifications of the route shown in Scheme 1.14. The zirconium dichloride complex [^{iPr}NPN*]$ZrCl_2$ (**1.49**) was

synthesized in an identical manner to **1.44** (Scheme 1.16).[75] Reduction under excess N_2 (in THF) resulted in the formation of the expected bimetallic, side-on N_2 bridged complex ([^{iPr}NPN*]ZrTHF)$_2$(μ-η^2:η^2-N_2) (**1.50**) (Scheme 1.16). Similar to **1.45**, the THF donors of **1.50** are labile and the N–N bond is comparable in length (1.542(4) Å).[75]

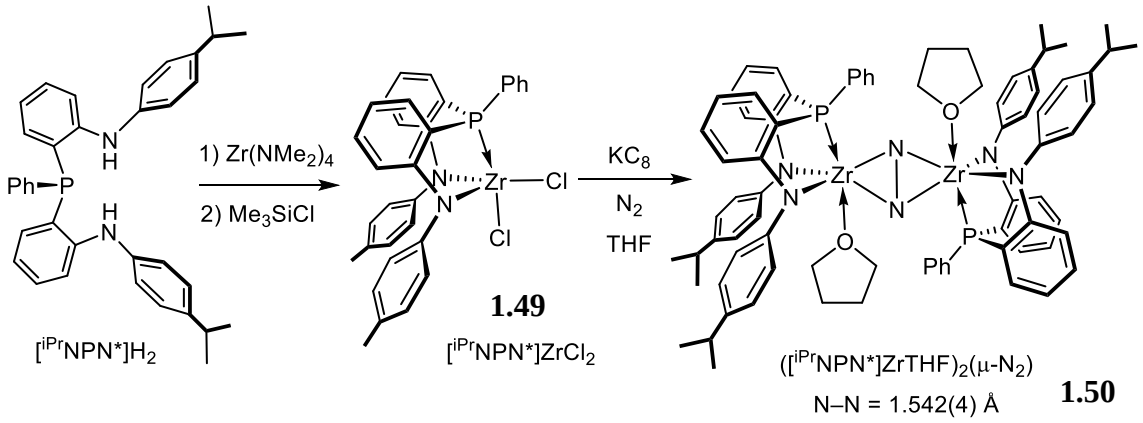

Scheme 1.16

1.5.2 Titanium [^{tol}NPN*] complexes

Coordination of [^{tol}NPN*] to titanium was achieved by treatment of $Ti(NMe_2)_2Cl_2$ with protonated proligand [(4-MeC_6H_4)NH-2-(5-MeC_6H_3)]$_2$PPh for concomitant release of Me_2NH. Reduction of the resulting titanium dichloride complex [^{tol}NPN*]$TiCl_2$ (**1.51**) under excess N_2 generated end-on dinitrogen bridged bimetallic ([^{tol}NPN*]TiTHF)$_2$(μ-N_2) (**1.52)** in moderate yield (Scheme 1.17). The solid-state structure of this dititanium N_2 complex revealed an end-on bridging dinitrogen moiety. An observed N–N bond length of 1.260(4) Å is typical for end-on bridging N_2 units implying an N_2^{4-} moiety.[75] Beyond ligand substitution reactions replacing the supporting THF ligands with pyridine and bipyridine bases, the reactivity of **1.52** was not explored. It should also be noted that ligand substitution in this manner has little to no effect on the N–N bond distance.[75]

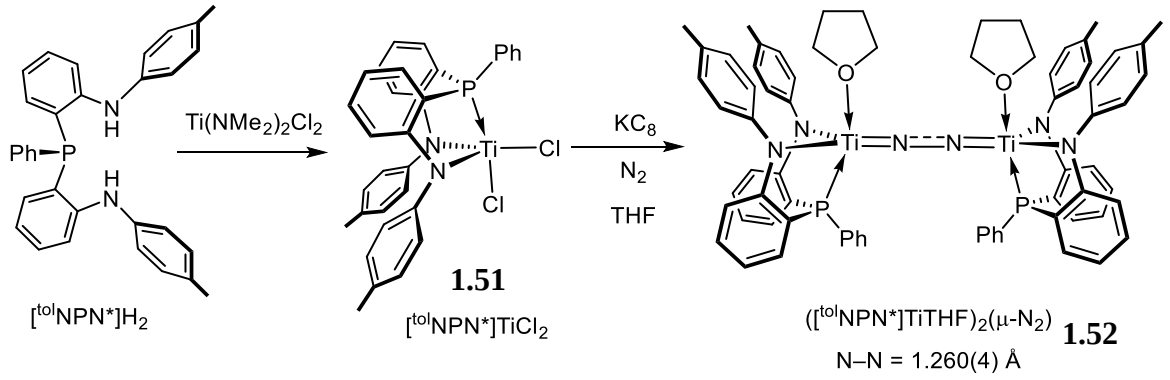

Scheme 1.17

1.5.3 Tantalum [^{Mes}NPN*] complexes

As mentioned above, the syntheses of the *ortho*-aryl linked NPN donor systems was developed to explore the formation of tantalum dinitrogen complexes via the "hydride route", analogous to the preparation of **1.32** via reaction of N_2 with **1.31** (Scheme 1.11). To that end, the corresponding [^{Mes}NPN*] bound trimethyl derivative [^{Mes}NPN*]$TaMe_3$ (**1.53**) was prepared and exposed to 4 atm of H_2 to generate the ditantalum tetrahydride complex ([^{Mes}NPN*]Ta)$_2$(μ-H_4) (**1.54**) with no detectable intermediates (Scheme 1.18).[77] Unfortunately, activation of dinitrogen by **1.54** was not observed even under forcing conditions.[77]

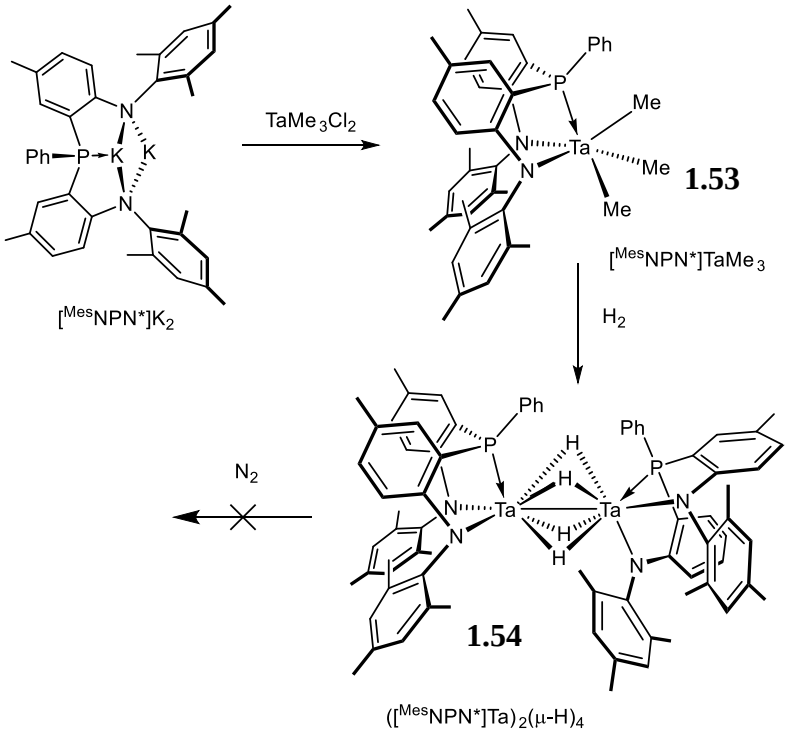

Scheme 1.18

1.6 The [NPN^{S}] and [NPN^{cp}] ligand systems: M[[(2,4,6-Me$_3$C$_6$H$_2$)N-2-(C$_4$H$_2$S)]$_2$PPh] and M[[(2,6-Me$_2$C$_6$H$_3$)N-2-(C$_5$H$_6$)]$_2$PPh] and coordination to zirconium(IV)

Given that the change to *ortho*-phenylene linkers (shown in Schemes 1.14 to 1.16) still allowed access to activated dinitrogen complexes via reduction under N_2, variants of unsaturated two-carbon backbones between the amido and phosphine donors in NPN arrays were examined. A natural extension of the aryl linker to a thiophenyl unit was explored as well as simplifying to an alkenyl linker.

Starting from commercially available 3,4-dibromothiophene, Hartwig-Buchwald amination with mesitylamine resulted in exclusively mono N–C coupling. As shown in Scheme 1.19, the remaining synthetic steps are in line with previous related ligand syntheses involving lithium halogen exchange followed by a $PhPCl_2$ quench for the desired NPN array; however, as

previously reported, there is a clean rearrangement that occurs from the expected 3,4-substitution to generate the 2,3-pattern found in the [^{Mes}NPN^{S}] ligand.[78] Protonolysis and reaction with $Zr(NMe_2)_4$ followed by treatment with excess Me_3SiCl resulted in the formation of the zirconium dichloride complex [^{Mes}NPN^{S}]$ZrCl_2$ (**1.55**). Unfortunately, while reduction did result in consumption of complex **1.55**, intractable mixtures resulted.

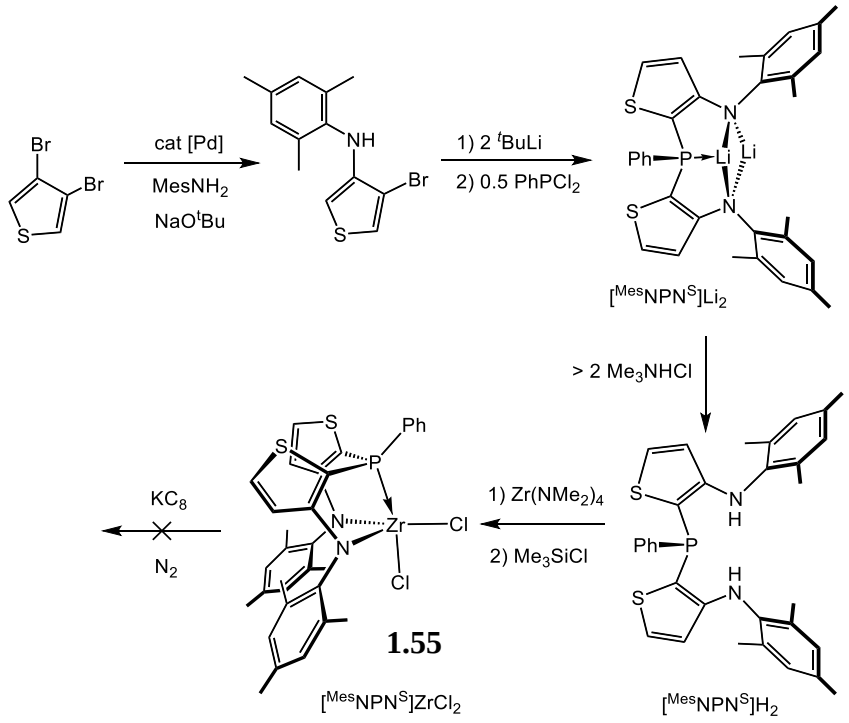

Scheme 1.19

A condensation, deprotonation sequence to assemble a related NPN donor set was also investigated. Deprotonation of *N*-2,6-dimethylphenylcyclopentylidene imine by LDA followed by quenching with 0.5 equiv $PhPCl_2$ resulted in a mixture of imine-enamine tautomers [^{xyl}NPN^{cp}]H_2 that reacted smoothly with $Zr(NMe_2)_4$. As before, reaction with excess Me_3SiCl provided the dichloride derivative [^{xyl}NPN^{cp}]$ZrCl_2$ (**1.56**).[79] In this case, reduction under dinitrogen did result in the formation of a dinuclear side-on bridging N_2 complex [^{xyl}NPN^{cp}]Zr(μ-

η^2:η^2-N_2) (**1.57**) (Scheme 1.20). An observed N–N bond distance of 1.508(5) Å shows considerable N_2 activation, comparable to the zirconium chemistry demonstrated with the [NPN^{Si}] and **[**^{Mes}NPN*] ligands.[79] In this particular context, functionalization of the hydrazido ligand was not explored.

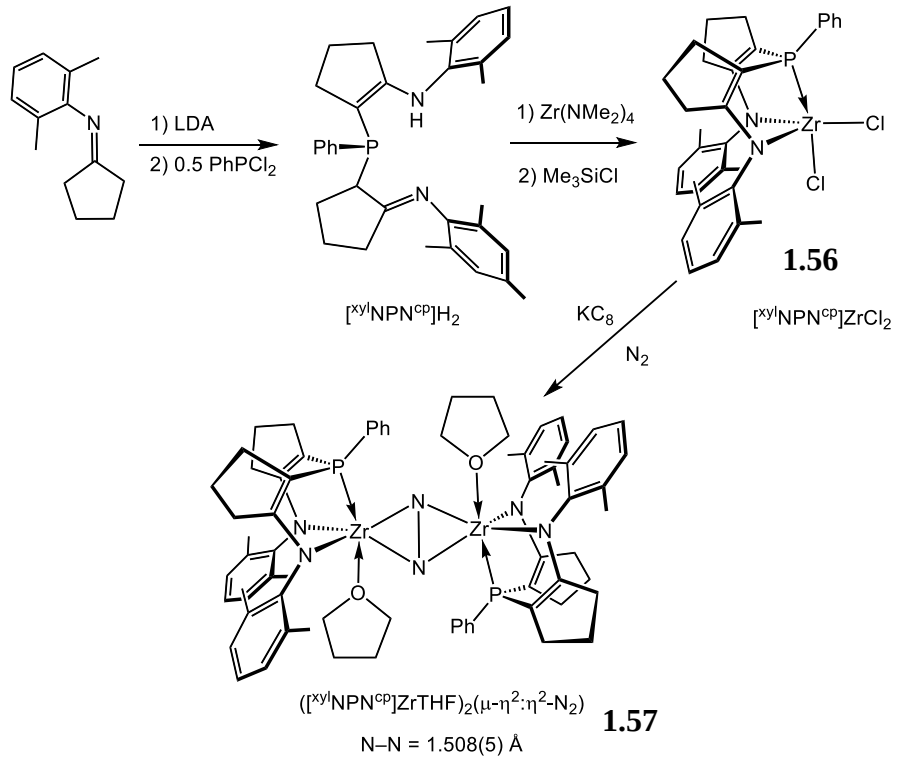

Scheme 1.20

1.7 Cobalt and rhodium coordination chemistry

While interest in ligand design and coordination to early metals towards dinitrogen activation is a principal focus, late metal coordination chemistry using the group 9 metals cobalt and rhodium continues to be an important endeavour in the Fryzuk lab. Previous reports show the synthesis of an alternate [PNP] ligand containing phenyl substituents on the phosphorus donors, generating the lithium salt of [^{Ph}PNP] (where [^{Ph}PNP] = [N(SiMe$_2$CH$_2$PPh$_2$)$_2$]) in an

analogous manner to Li[PNP], using lithium diphenylphosphide.[37] Early work examined the coordination of [PNP] ligands to rhodium,[80-82] followed by investigation of paramagnetic [^{Ph}PNP] cobalt complexes.[83] Later work on the [^{xyl}NPN^{cp}] ligand explored coordination chemistry with rhodium.[84] More recently designed ligand scaffolds have also been utilized to investigate paramagnetic cobalt complexes.[85-86]

1.7.1 Cobalt and rhodium [^{Ph}PNP] complexes

Synthesis of various rhodium [^{Ph}PNP] complexes was accomplished by reaction of Li[^{Ph}PNP] with a number of rhodium starting materials, as shown in Scheme 1.21.[80-81]

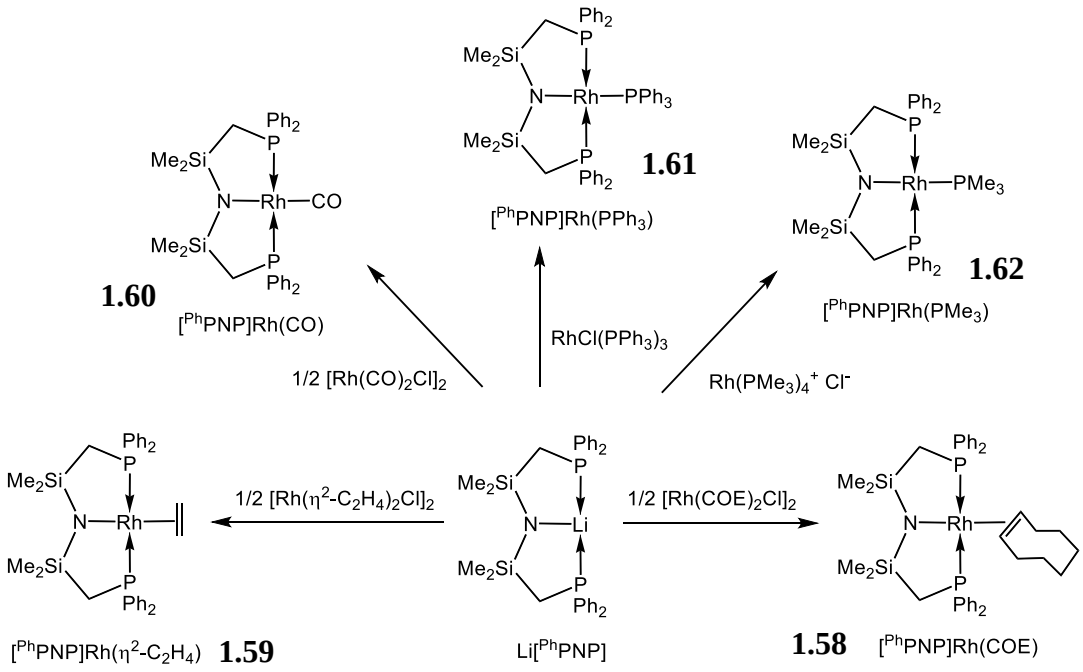

Scheme 1.21

The Rh(I) complexes [^{Ph}PNP]Rh(COE) (**1.58**), [^{Ph}PNP]Rh(η^2-C_2H_4) (**1.59**), [^{Ph}PNP]Rh(CO) (**1.60**), [^{Ph}PNP]Rh(PPh_3) (**1.61**) and [^{Ph}PNP]Rh(PMe_3) (**1.62**) were generated

and subsequent reactivity was explored.[81-82] The labile cyclooctene ligand in **1.58** is easily displaced by other neutral ligands, such that complexes **1.59–1.62** can be also be formed via treatment of **1.58** with the appropriate donor reagent (Scheme 1.22).

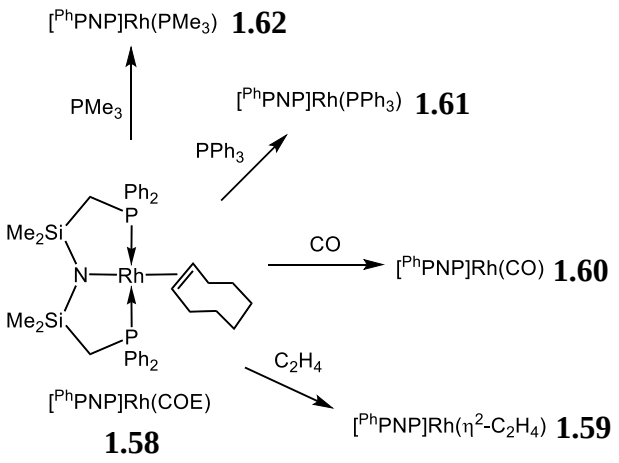

Scheme 1.22

Paramagnetic cobalt complexes of [^{Ph}PNP] were later synthesized and studied, more than a decade after the [PNP] rhodium chemistry was initiated. The cobalt halide complex [^{Ph}PNP]CoCl (**1.63**) was prepared via addition of Li[^{Ph}PNP] to a suspension of $CoCl_2$ in THF (Scheme 1.23).[83] Complex **1.63**, a high-spin tetrahedral Co(II) species, undergoes reactivity with organolithium and potassium reagents to generate low-spin square planar Co(II) alkyl species.[83] Scheme 1.23 shows the formation of [^{Ph}PNP]CoMe (**1.64**), [^{Ph}PNP]$CoCH_2SiMe_3$ (**1.65**) and [^{Ph}PNP]$CoCH_2Ph$ (**1.66**) via the treatment of **1.63** with MeLi, $LiCH_2SiMe_3$ and KCH_2Ph respectively. Addition of excess benzyl chloride ($PhCH_2Cl$) to **1.63** results in a one-electron oxidation to produce the paramagnetic Co(III) dichloride species [^{Ph}PNP]$CoCl_2$ (**1.67**).[83] Reduction of complex **1.63** was not explored.

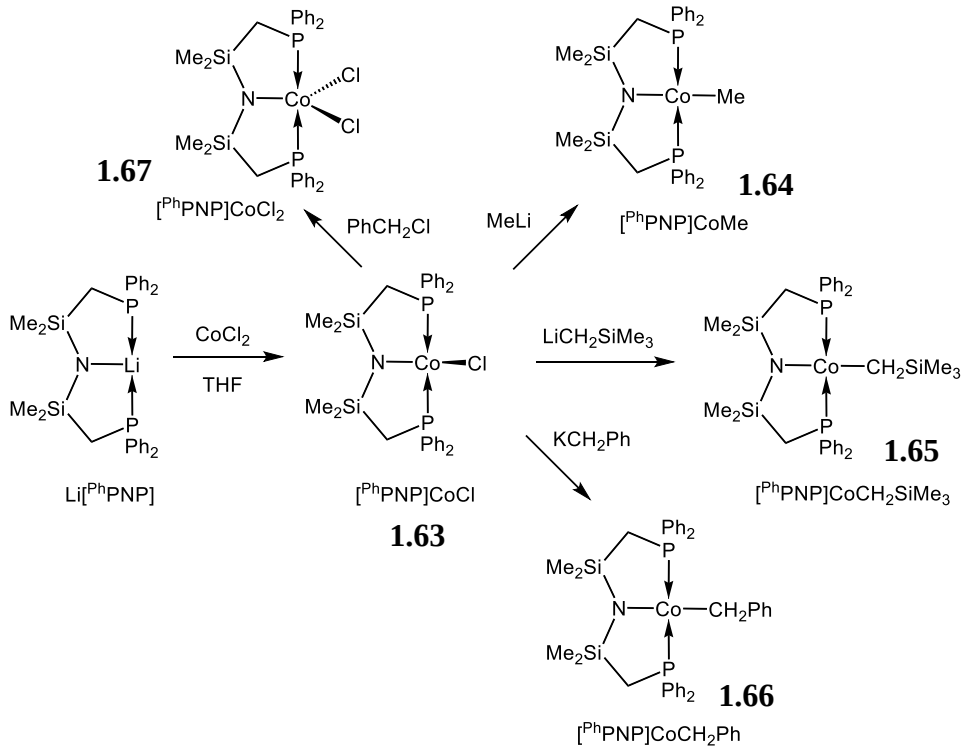

Scheme 1.23

1.7.2 Rhodium [^{xyl}NPN^{cp}] complexes

Coordination of rhodium to [^{xyl}NPN^{cp}] has also been investigated, producing [^{xyl}NPN^{cp}]RhCl(COE) (**1.68**) via reaction of [^{xyl}NPN^{cp}]H_2 of with [Rh(COE)$_2$Cl]$_2$ (Scheme 1.24).[84] While both of the ligand arms in **1.68** have assumed the imine tautomeric form, only one of the imine nitrogen donors is coordinated to rhodium, leaving an open site for coordination of a COE ligand. Displacement of the COE occurs upon exposure of **1.68** to CO, generating the Rh(I) monocarbonyl complex [^{xyl}NPN^{cp}]RhCl(CO) (**1.69**),[84] as shown in Scheme 1.24. Reaction of **1.68** with H_2 leads to the formation of a Rh(III) monohydride species [^{xyl}NPN^{cp}]Rh(H)Cl$_2$ (**1.70**), with both nitrogen donors coordinated to rhodium from the meso-diimine form of the ligand.[84]

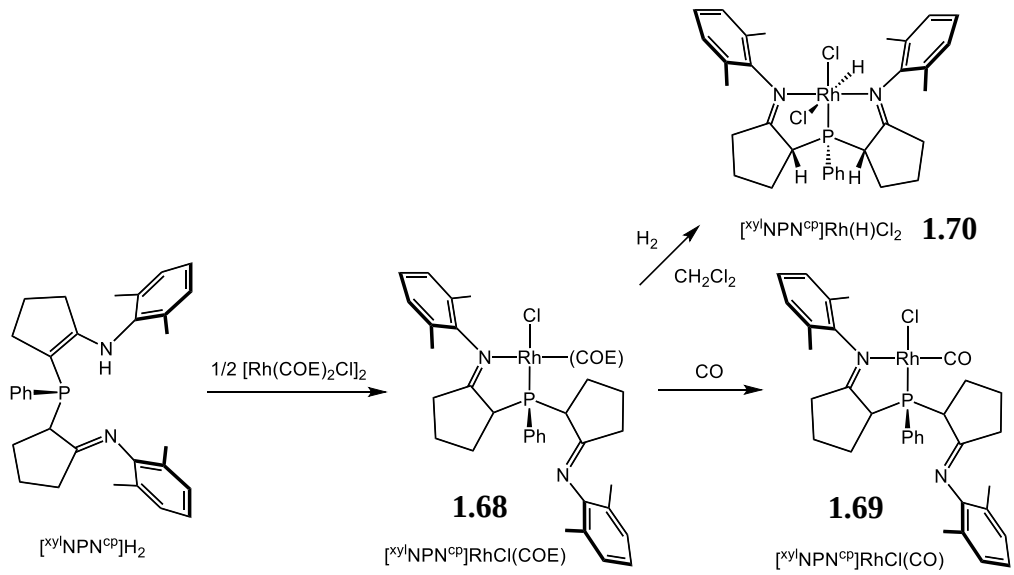

Scheme 1.24

1.7.3 Cobalt complexes with alternative ligand scaffolds

More recently reported work explored the coordination chemistry of ligands containing phosphinoamide donors with no linker between the amido and phosphine donor.[86-88] Utilizing a ferrocene diamine scaffold, synthesis of a diphosphinoamido ligand, [fc(NP)$_2$] (where NP = NP^{i}Pr$_2$) was accomplished. The polymeric dipotassium salt of [fc(NP)$_2$], K$_2$[fc(NP)$_2$], is formed from deprotonation of 1,1′-ferrocene bis(diisopropylphosphinoamine) with potassium hydride (KH), shown in Scheme 1.25.[86] The salt metathesis reaction of K$_2$[fc(NP)$_2$] with CoCl$_2$(py)$_4$ results in the formation of a paramagnetic, dimeric cobalt complex ([fc(NP)$_2$]Co)$_2$ (**1.71**),[86] as shown in Scheme 1.25. The geometry about the Co(II) centres of **1.71** is square planar, due to weak but significant Fe–Co interactions with the ferrocene backbone, as evidenced by X-ray crystallography, Mössbauer spectroscopy, VT-magnetometry and DFT studies.[86]

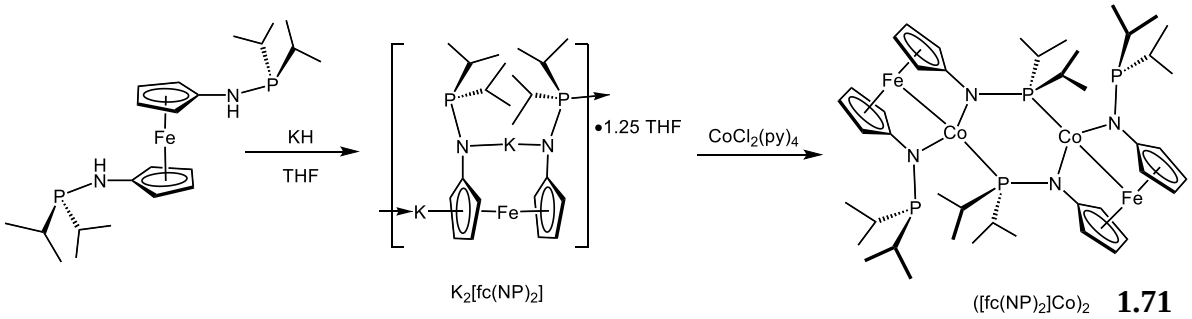

Scheme 1.25

Other recent work details the synthesis of the enamido-phosphinimine ligands [NNpN^{DIPP}] and [NNpN^{TMS}] (where NNpN = $Et_2NCH_2CH_2N$-2-(C_5H_6)P($^iPr_2$)NR; R = DIPP, 2,6-diisopropylphenyl; R = TMS, trimethylsilyl) and their subsequent coordination chemistry with cobalt.[85] The lithium salt Li[NNpN^{DIPP}] undergoes salt metathesis with $CoCl_2$ to produce the cobalt chloride species κ^3-[NNpN^{DIPP}]CoCl (**1.72**), shown in Scheme 1.26. The cobalt alkyl complex κ^3-[NNpN^{DIPP}]$CoCH_2SiMe_3$ (**1.73**) was also generated via metathesis of **1.72** with $LiCH_2SiMe_3$ (Scheme 1.26). With the aim of producing a dinitrogen complex, **1.72** was reduced with KC_8 under N_2 atmosphere, resulting in formation of the π-arene complex **1.74**, κ^2:η^6-[NNpN^{DIPP}]Co (Scheme 1.26).

In an effort to avoid the arene coordination that occurs upon reduction of **1.72**, replacement of the DIPP substituent with a TMS substituent was examined.[85] Metathesis of the lithium salt Li[NNpN^{TMS}] with $CoCl_2THF_{1.5}$ resulted in the formation of κ^3-[NNpN^{TMS}]CoCl (**1.75**), shown in Scheme 1.26. The reaction of **1.75** with $LiCH_2SiMe_3$ also generated the analogous complex **1.76**, κ^3-[NNpN^{TMS}]$CoCH_2SiMe_3$ (Scheme 1.26). However, treatment of **1.75** with KC_8 under N_2 failed to generate a dinitrogen complex, instead producing the C–H activated complex κ^4-[NNpN$SiMe_2CH_2$]Co (**1.77**), as shown in Scheme 1.26. The formation of

1.74 and **1.77** instead of the desired N_2 complexes underlines the unpredictability of pursuing dinitrogen activation chemistry.

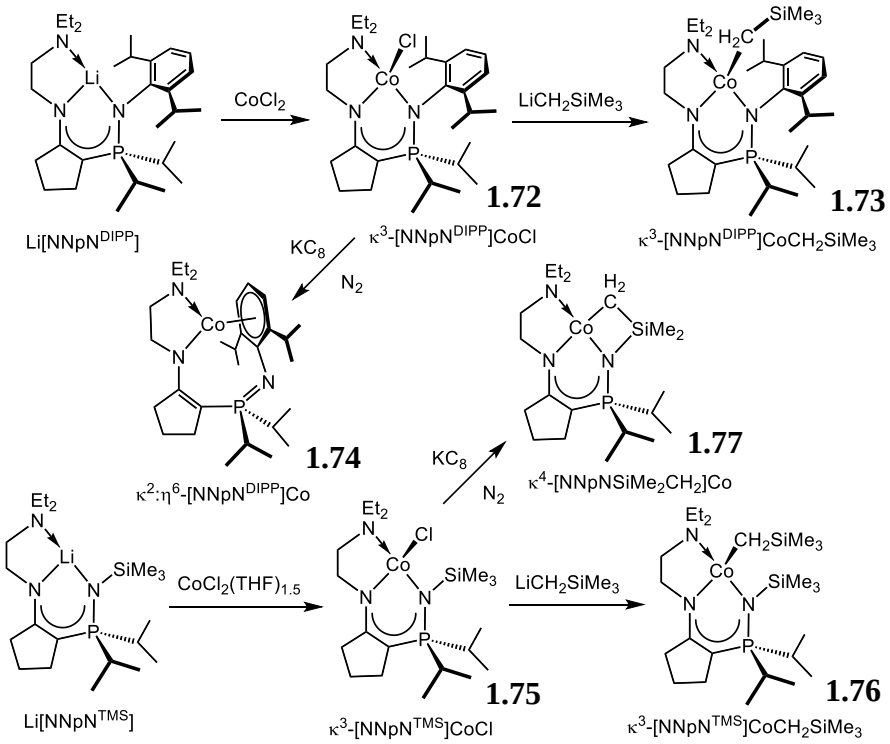

Scheme 1.26

1.8 Scope of thesis

The lofty goal of catalytic dinitrogen reduction/functionalization continues to be an important focus of the Fryzuk lab, even after more than 25 years of research, spanning numerous transition metals and uncovered novel N_2 bonding modes and new reactivity patterns for coordinated dinitrogen. Although the design and synthesis of new ligand arrays continues, there is still much to be learned from existing systems. The work in this thesis is focused on exploration of novel coordination chemistry and dinitrogen functionalization of transition metal

complexes, using the previously described ligand frameworks with group 5 (V, Nb, Ta) and group 9 (Co, Rh) metals.

Chapter 2 details the hydrosilylation of a tantalum dinitrogen complex, an analogue of complex **1.32** that contains a modified [NPN^{Si}] ligand framework. Chapter 3 examines the reactivity of paramagnetic [P_2N_2] niobium and vanadium dinitrogen complexes with electrophiles and oxidants. Chapter 4 describes the synthesis and reactivity of paramagnetic cobalt complexes containing the [P_2N_2] ligand. Chapter 5 explores the synthesis and reactivity of [P_2N_2] complexes of rhodium. Chapter 6 provides an overview of the work presented in this thesis, as well as briefly mentioning alternate projects that were pursued and suggestions for future work.

Chapter 2: Hydrosilylation of side-on end-on coordinated dinitrogen

2.1 Introduction

One of the "blue-sky" goals in chemistry is to discover a homogeneous catalyst that can convert molecular nitrogen into a high value nitrogen-containing material.[1, 31, 89] While some interesting results have been achieved with systems that produce ammonia (NH_3) using soluble transition metal complexes and various sources of protons and electrons, the turnovers have been disappointing and extension to large-scale processes is not realistic.[23, 25, 90] Nevertheless, these systems represent remarkable synthetic achievements that help further understanding of the necessary requirements.[2]

The Haber-Bosch process of ammonia production utilizes N_2 and H_2 to form NH_3 at high pressures and temperatures.[13] It is estimated that the whole process consumes more than 1% of the total energy produced globally.[11, 91] Such an investment in energy is considered essential, as the ammonia produced is used to increase agricultural production.[92] Because of the huge energy cost, it is desirable to find ways to improve the efficiency of this process; for this reason, developing a homogeneous nitrogen fixation catalyst is of interest.[93]

Previous work towards finding a catalytic system for the functionalization of N_2 originated from the discovery that an [NPN^{Si}] supported ditantalum tetrahydride species (**1.31**) reacts spontaneously with N_2 to generate a reactive ditantalum dinitrogen complex (**1.32**).[65] Perhaps this transformation could be the first step in a potential catalytic cycle, whereby multiple additions of the ideal element–hydride (E–H) reagent would form N–E bonds and release a functionalized N_2E_4 moiety, with concomitant regeneration of **1.31** (Scheme 2.1).[73]

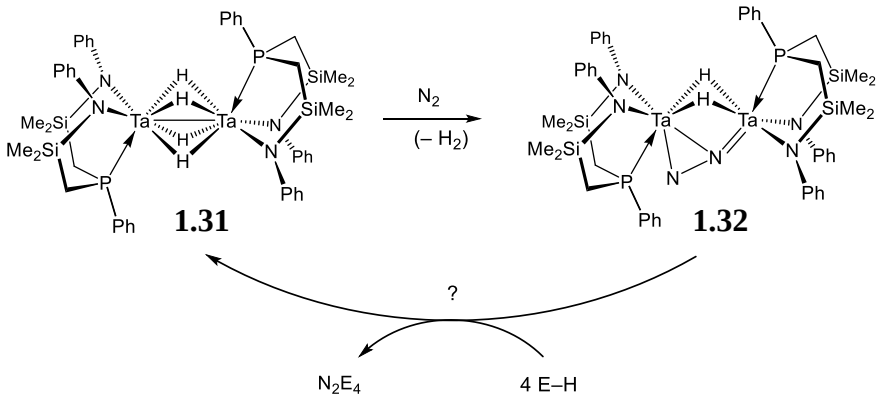

Scheme 2.1

Unfortunately, this potential catalytic cycle was not realized, but in the process of this investigation, the extraordinary reactivity of **1.32** with E–H reagents was revealed. For example, previous reports show that **1.32** is capable of undergoing hydroboration,[94-95] hydroalumination,[96] hydrosilylation,[97-99] and zirconocene insertion[100] reactions, all of which result in new N–E bond formation.[44, 73, 101] An overview of the reactivity of **1.32** towards these reagents is illustrated in Scheme 2.2. Although N–N bond cleavage and N–E bond formation was accomplished, further reactivity was eventually negated by ancillary ligand rearrangements, hindering the liberation of any dinitrogen-derived products. The limitations of the [NPN^{Si}] ligand system in these reactions prompted investigation of further ligand modifications.[101]

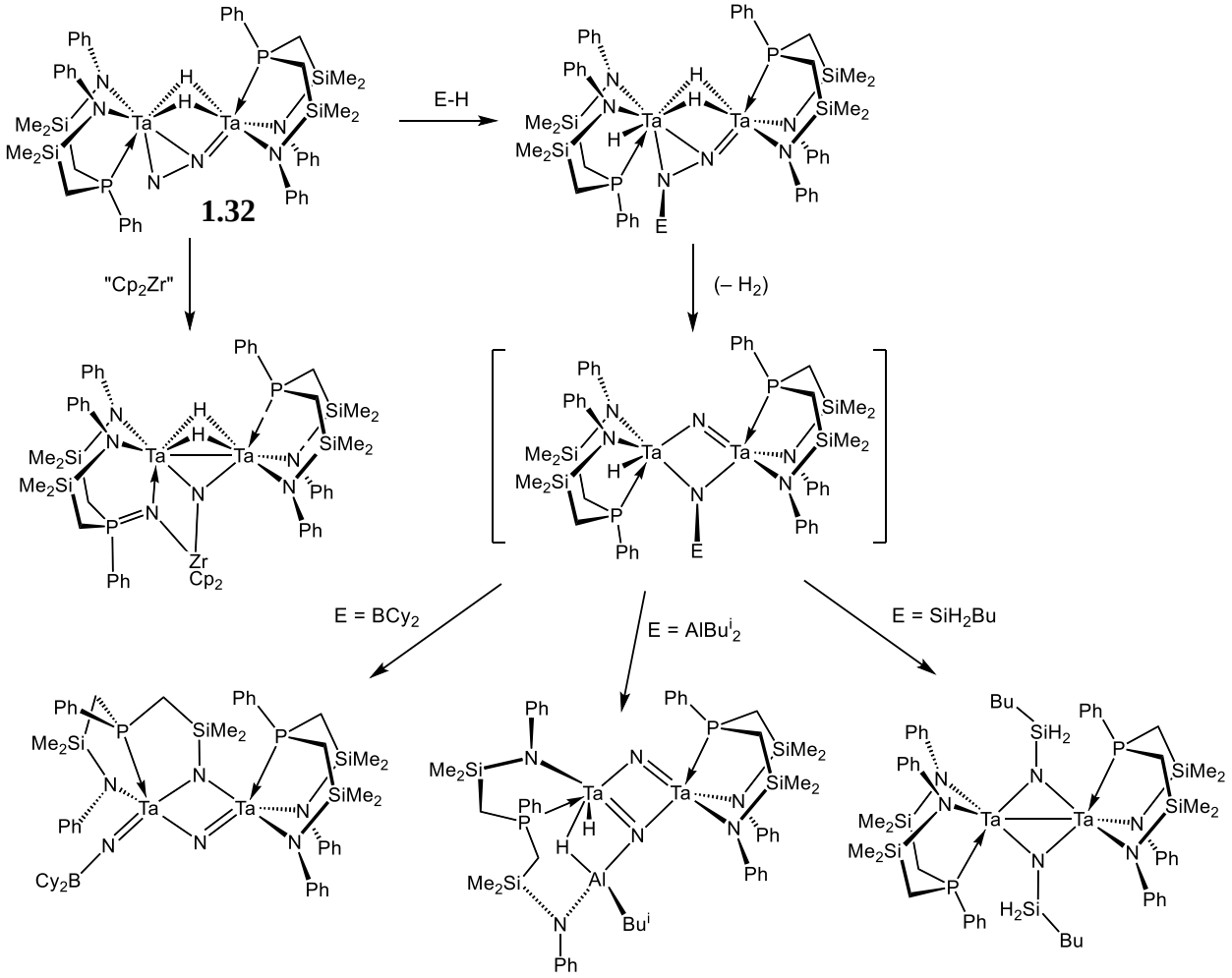

Scheme 2.2

In the previously reported hydrosilylation of $([NPN^{Si}]Ta)_2(\mu\text{-}\eta^2{:}\eta^1\text{-}N_2)(\mu\text{-}H)_2$ (**1.32**) with butylsilane ($BuSiH_3$),[97-98] one of the isolated products is the disilylimido-bridged ditantalum complex **2.1**, when strict control of stoichiometry (2 equivalents of $BuSiH_3$) is maintained (Scheme 2.3). The mechanism of the formation of **2.1** has been proposed[98] on the basis of variable temperature NMR studies and labeling experiments, and further supported by DFT evaluation.[99] The possibility that the addition of excess butylsilane could result in the elimination

of tris(butylsilyl)amine and the formation of a silylhydride derivative of tantalum was also investigated. Upon addition of more $BuSiH_3$ to **2.1**, an unusual transformation was observed that involves one ancillary ligand rearrangement and loss of H_2, as shown in Scheme 2.3. The mechanism of this transformation remains elusive, as no intermediates were observed; however, it is noteworthy that the reaction is promoted by the presence of excess $BuSiH_3$ regardless of the fact that the excess silane is not incorporated into the product.

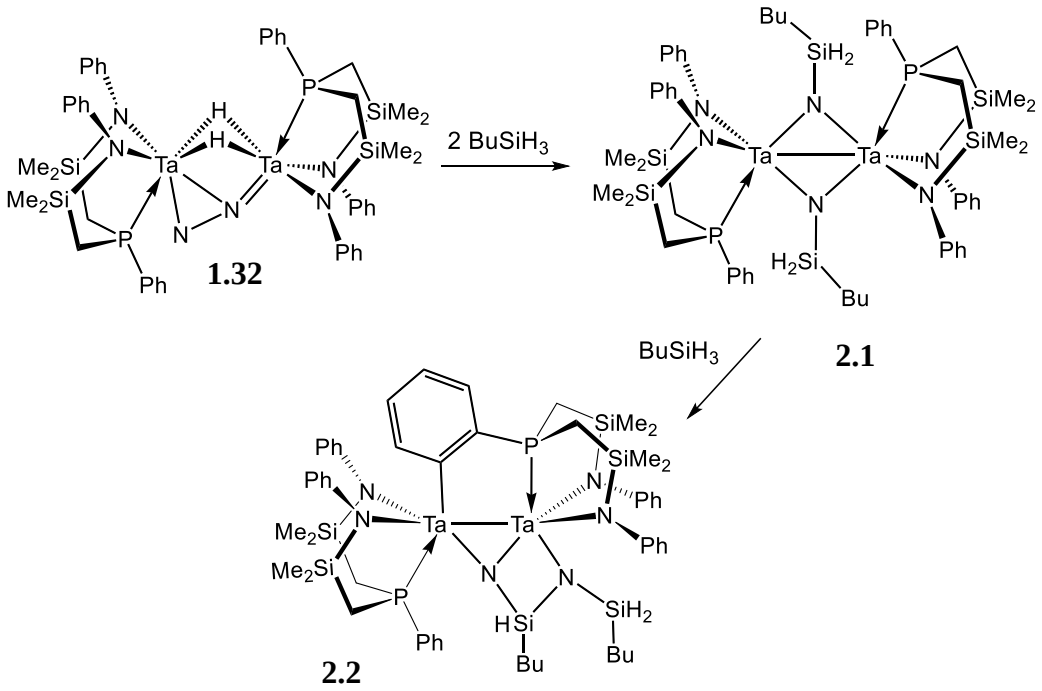

Scheme 2.3

Given that the P-phenyl substituent of the [NPN^{Si}] ligand orthometallates to generate a bridging interaction between the two central tantalum atoms, a modified [NPN^{Si}] ligand containing a different substituent on phosphorus could preclude cyclometallation and ideally push the reaction forward to the desired outcome of tris(butylsilyl)amine elimination.

Modification of [NPN^{Si}] to include P-cyclohexyl as a replacement for the P-phenyl substituents has previously been reported.[102] In this chapter, the synthesis and hydrosilylation of the P-cyclohexyl analogue of ([NPN^{Si}]Ta)$_2$(μ-η^2:η^1-N$_2$)(μ-H)$_2$ is examined.

2.2 Synthesis and molecular structure of (^{Cy}[NPN^{Si}]Ta)$_2$(μ-η^2:η^1-N$_2$)(μ-H)$_2$

The preparation of the P-cyclohexyl ditantalum tetrahydride, (^{Cy}[NPN^{Si}]Ta)$_2$(μ-H)$_4$ (**2.3**) (where Cy denotes the P-cyclohexyl substituent) was previously reported.[102] In analogy to the formation of **1.32**, reaction of **2.3** with molecular nitrogen results in the formation of the analogous side-on end-on dinitrogen complex, (^{Cy}[NPN^{Si}]Ta)$_2$(μ-η^2:η^1-N$_2$)(μ-H)$_2$ (**2.4**) (Equation 2.1).[103]

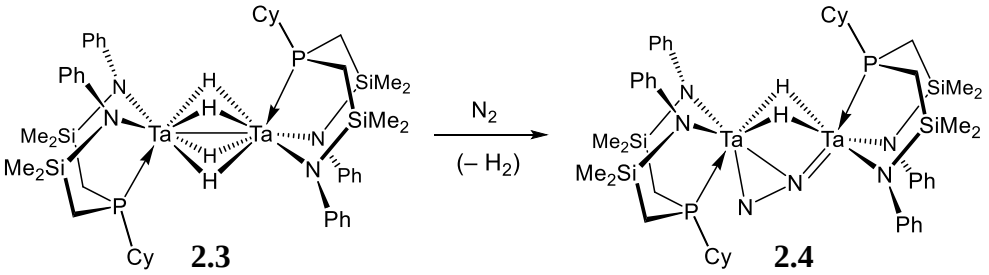

[2.1]

Although the solid-state molecular structure of this dinitrogen complex was previously determined,[103] the bridging hydrides were not located. During this investigation, single crystals of **2.4** were obtained and the structure is included here for completeness; the bridging hydrides were located in the difference map. Figure 2.1 shows the molecular structure of **2.4** and relevant bond lengths are shown in Table 2.1. The overall metrical parameters are very similar to the P-phenyl dinitrogen complex **1.32**; in particular the N1–N2 bond length is 1.328(7) Å in **2.4** as compared to 1.319(2) Å in **1.32**, and the Ta1⋯Ta2 separation is largely unchanged at 2.8333(4) in **2.4** and 2.830(4) in **1.32**. It is curious to note that the Ta–P bond lengths do not vary much

from the P-phenyl upon introduction of the more electron-rich cyclohexyl substituent: in **2.4**, Ta1–P1 and Ta2–P2 are 2.5956(19) and 2.609(2) Å, respectively, compared to 2.573(5) and 2.596(5) Å in **1.32**.

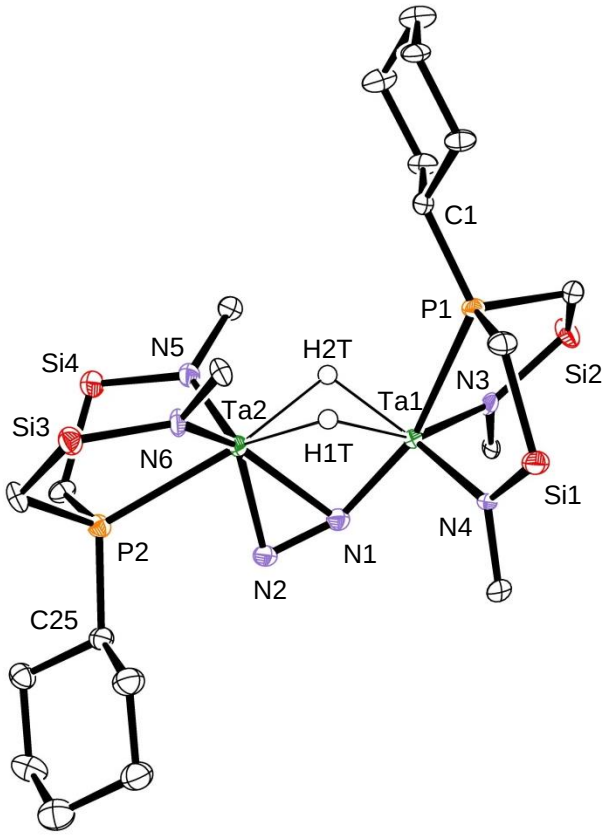

Figure 2.1 ORTEP depiction (ellipsoids at 50 % probability) of (^{Cy}[NPN^{Si}]Ta)$_2$(μ-η^2:η^1-N$_2$)(μ-H)$_2$ (**2.4**). Silyl methyl and N-phenyl ring carbons other than ipso are omitted for clarity.

Table 2.1 Selected bond distances (Å) of **2.4**

Atoms	Distance	Atoms	Distance
N(1)–N(2)	1.328(7)	Ta(1)···Ta(2)	2.8333(4)
Ta(2)–N(1)	2.144(5)	Ta(1)–H(1T)	1.87(6)
Ta(2)–N(2)	1.987(6)	Ta(1)–H(2T)	1.76(7)
Ta(1)–N(1)	1.880(6)	Ta(2)–H(1T)	1.85(7)
Ta(1)–P(1)	2.5956(19)	Ta(2)–H(2T)	1.92(7)
Ta(2)–P(2)	2.609(2)		

The formation of **2.4** is also supported by NMR spectroscopy. Diagnostic resonances in the ^{1}H NMR spectrum include a singlet at δ 10.5 that integrates to 2H, corresponding to two hydrides bridging the two tantalum centres, as well as four silyl methyl resonances at δ –0.03, 0.11, 0.14 and 0.19, supporting the expected lack of symmetry in this side-on end-on dinitrogen complex. In the ^{31}P{^{1}H} NMR spectrum there are two resonances: a doublet at δ 27.9 that is coupled to the second ^{31}P environment and a broad multiplet at δ 15.8 that is coupled to an ^{14}N quadrupolar nucleus. Tracking these characteristic resonances via NMR spectroscopic studies has proven useful in examining the reactivity of this dinitrogen complex.

2.3 Hydrosilylation of $(^{Cy}[NPN^{Si}]Ta)_2(\mu\text{-}\eta^2{:}\eta^1\text{-}N_2)(\mu\text{-}H)_2$ with $BuSiH_3$

2.3.1 Monitoring hydrosilylation by ^{31}P{^{1}H} and ^{1}H NMR spectroscopy

The reaction of $BuSiH_3$ with **2.4** was monitored by ^{31}P{^{1}H} NMR spectroscopy in an effort to detect intermediates and compare this process to the hydrosilylation of the P-phenyl analogue with $BuSiH_3$. Upon treatment of **2.4** with excess $BuSiH_3$, the slow formation of several new species can be observed in the ^{31}P{^{1}H} NMR spectra, resulting in clean conversion to a single complex over a 72 hour period. (Figure 2.2). This reaction proceeds through two intermediates, as evidenced by the appearance of two new doublet signals at δ 16.5 and 30.8 , and two small resonances at δ 1.8 and –0.4 in the ^{31}P{^{1}H} NMR spectrum after 48 h. These signals correspond to two different species due to the inequivalent phosphorus donors on the ligands. After 72 h, both the starting material and intermediate species resonances disappeared and two new resonances at δ 27.8 and 22.1 were observed. By analogy to the P-phenyl system, the first intermediate is likely the monosilylated N_2 complex (**2.5**). Figure 2.3 shows the hydride region in the ^{1}H NMR spectrum, providing evidence of two signals that can be assigned as two

inequivalent bridging hydrides (multiplet signals at δ 11.0 and 11.1) and a third signal indicative of a terminal hydride (δ 14.3 ppm). These resonances are in agreement with the assignment of **2.5** as the first intermediate. Another signal at δ 16.8 in the ^{1}H NMR spectrum can be assigned to a terminal tantalum hydride, belonging to the other intermediate species. The second intermediate is proposed to be the imide-nitride species **2.6**, on the basis of its similar spectral parameters to the previously reported analogue.[97]

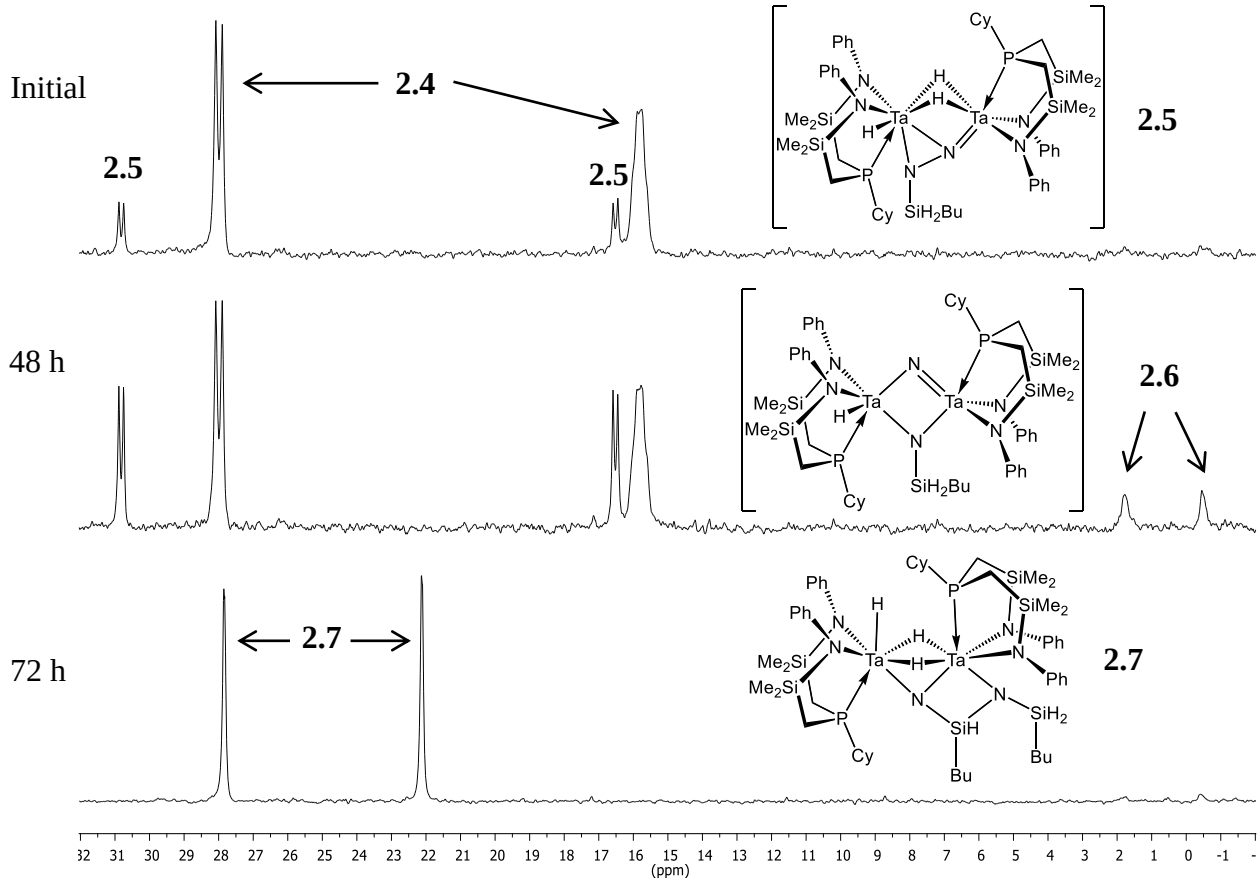

Figure 2.2 ^{31}P{^{1}H} NMR spectra (121.4 MHz, C_6D_6) recorded after treatment of **2.4** with excess $BuSiH_3$.

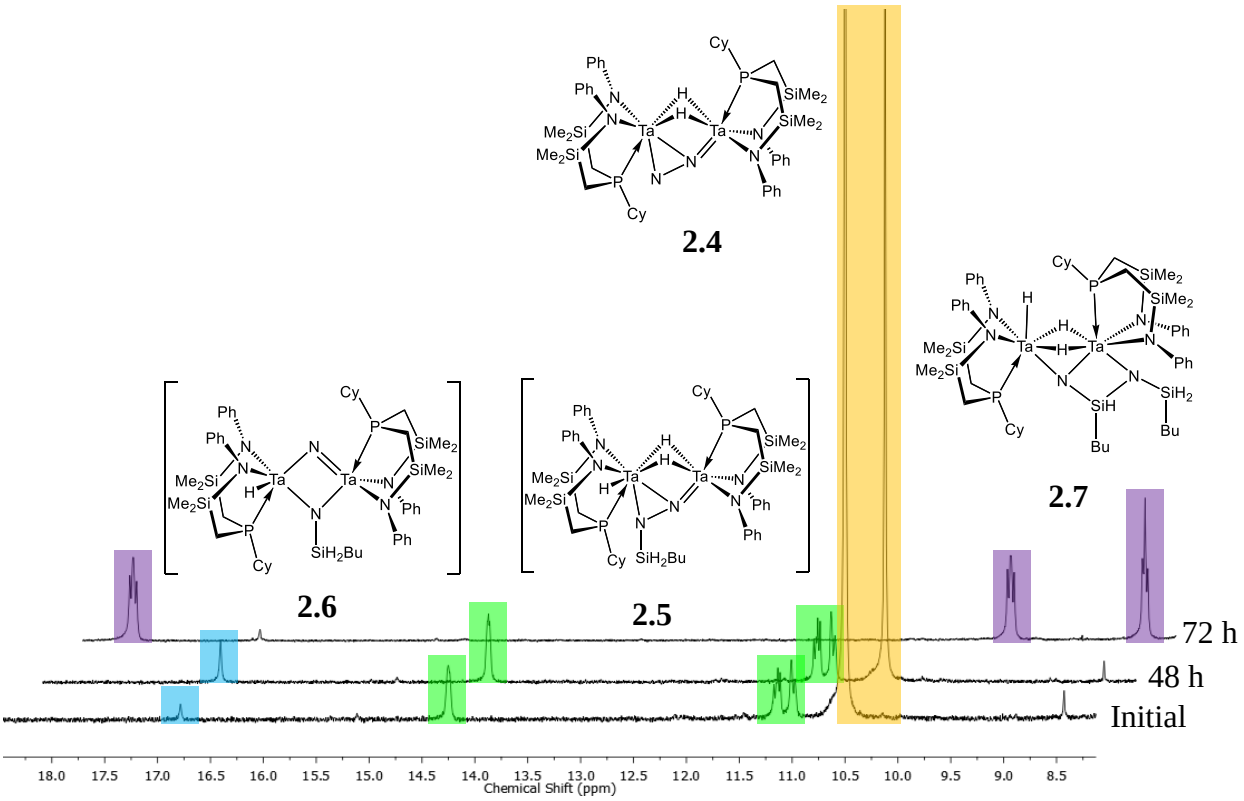

Figure 2.3 Stack plot of $^{1}H\{^{31}P\}$ NMR spectra (300 MHz, C_6D_6) in the Ta hydride region, during the reaction of **2.4** (yellow) with excess $BuSiH_3$ in C_6D_6 over the course of 72 h. The hydrides of the two reaction intermediates, **2.5** (green) and **2.6** (blue) are observed, as well as the final product, **2.7** (purple).

Reaction of **2.6** with excess $BuSiH_3$ was expected to produce the disilylimide analogue of **2.1** (Scheme 2.3).[98] However, while in situ evidence for **2.5** and **2.6** was observed, the analogous disilylimide species with P-cyclohexyl substituents was not detected. The final complex (**2.7**) gives rise to two doublet signals in the $^{31}P\{^{1}H\}$ NMR spectrum at δ 22.1 and 27.8 ppm, and three hydride multiplet signals in the ^{1}H NMR spectrum at δ 8.4, 9.7 and 18.0. These hydride resonances clearly suggest that a different species is being formed for the P-cyclohexyl analogue, compared to compound **2.2** in the P-phenyl reaction (Scheme 2.3). Complex **2.7** was isolated as

single crystals, and its solid-state molecular structure determined. The overall reaction outcome is shown in Scheme 2.4.

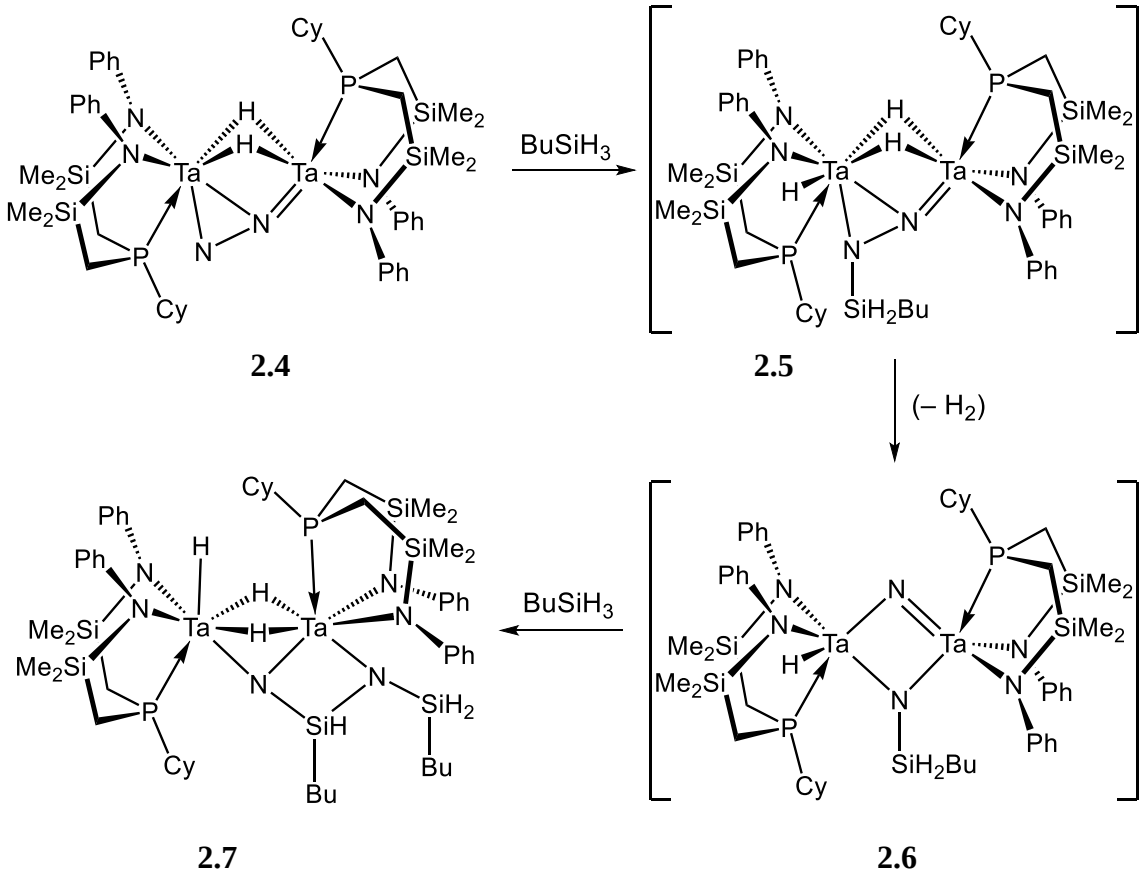

Scheme 2.4

In an effort to further explore the mechanism and develop a reaction timeline to aid in isolation of the intermediates, a series of consecutive timed $^{31}P\{^{1}H\}$ NMR experiments were conducted. Figure 2.4 shows a stacked plot of $^{31}P\{^{1}H\}$ NMR spectra recorded during the reaction of **2.4** with four equivalents of $BuSiH_3$ over the course of 46 h. The resonances of **2.4** (yellow) slowly disappear as resonances of the first intermediate species **2.5** (green) appear, but remain minor, suggesting that this species is undergoing further reactivity shortly after being produced.

Resonances of the second intermediate species **2.6** (blue) appear soon after, followed by the resonances of the final product **2.7** (purple), confirming that there are three species present for several hours during the course of the reaction. Attempts to isolate and further characterize these intermediates proved challenging and were ultimately unsuccessful. Characteristic NMR resonances for **2.4**, **2.5**, **2.6** and **2.7** are summarized in Table 2.2.

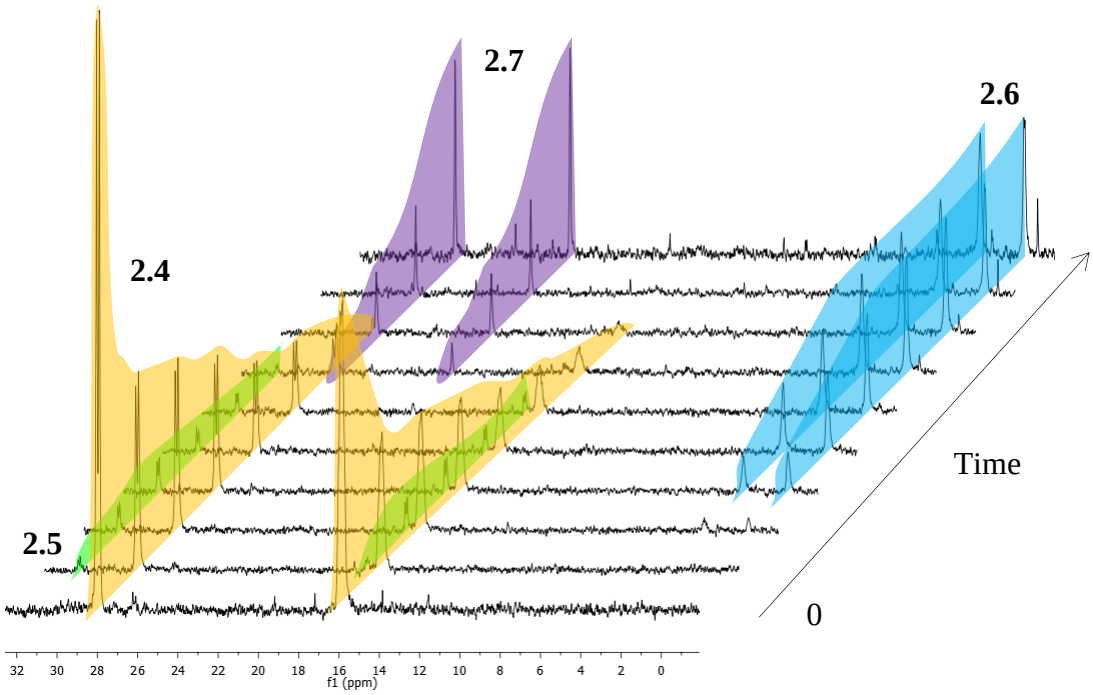

Figure 2.4 Stack plot of $^{31}P\{^{1}H\}$ NMR spectra (161.9 MHz, C_6D_6) during reaction of **2.4** (yellow) with four equivalents of $BuSiH_3$ in C_6D_6 over the course of 46 h. The two reaction intermediates, **2.5** (green) and **2.6** (blue) are observed, as well as the final product, **2.7** (purple).

Table 2.2 Selected $^{31}P\{^{1}H\}$ and ^{1}H NMR spectroscopy chemical shifts for **2.4**, **2.5**, **2.6** and **2.7**.

Nuclei	Chemical Shift (δ)	Structure
^{31}P ^{1}H	27.9 15.8 10.5 (H_b)	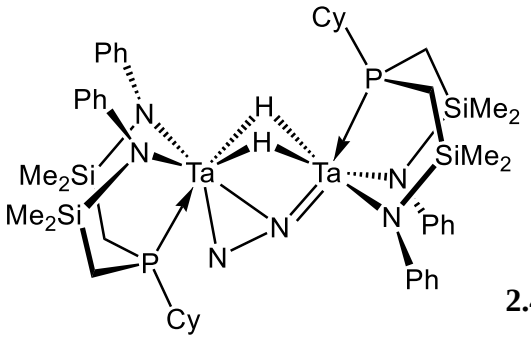 **2.4**
^{31}P ^{1}H	30.8 16.5 11.0 (H_b) 11.1 (H_b) 14.2 (H_t)	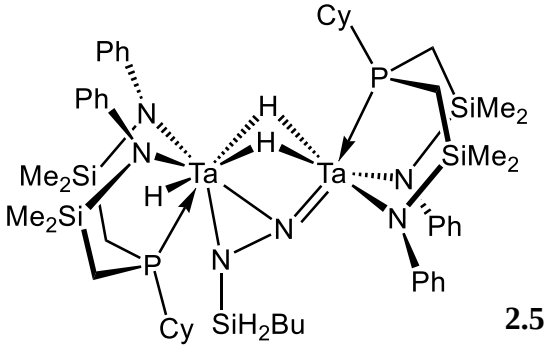 **2.5**
^{31}P ^{1}H	1.8 -0.4 16.8 (H_t)	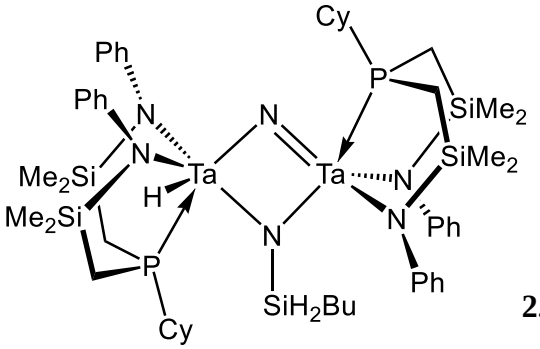 **2.6**
^{31}P ^{1}H	27.8 22.1 8.4 (H_t) 9.7 (H_b) 18.0 (H_b)	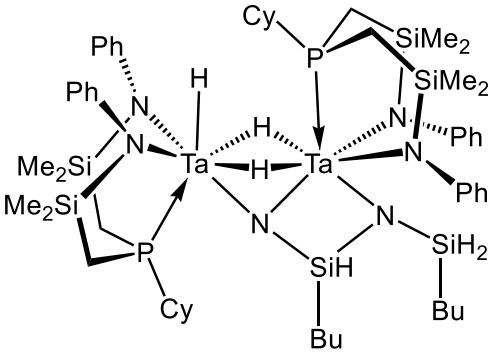 **2.7**

2.3.2 Molecular structure of $^{Cy}[NPN^{Si}]TaH(BuSiN\text{-}\mu\text{-}Si(H)Bu\text{-}\mu\text{-}N)(\mu\text{-}H)_2Ta[NPN^{Si}]^{Cy}$

X-ray quality crystals were grown from slow evaporation of a hexane solution of $^{Cy}[NPN^{Si}]TaH(BuSiN\text{-}\mu\text{-}Si(H)Bu\text{-}\mu\text{-}N)(\mu\text{-}H)_2Ta[NPN^{Si}]^{Cy}$ (**2.7**) and the solid-state molecular structure was determined. In Figure 2.5, the molecular structure of **2.7** is shown; although related to the structure of the P-phenyl reaction product **2.2**, the structure of **2.7** exhibits some striking differences.

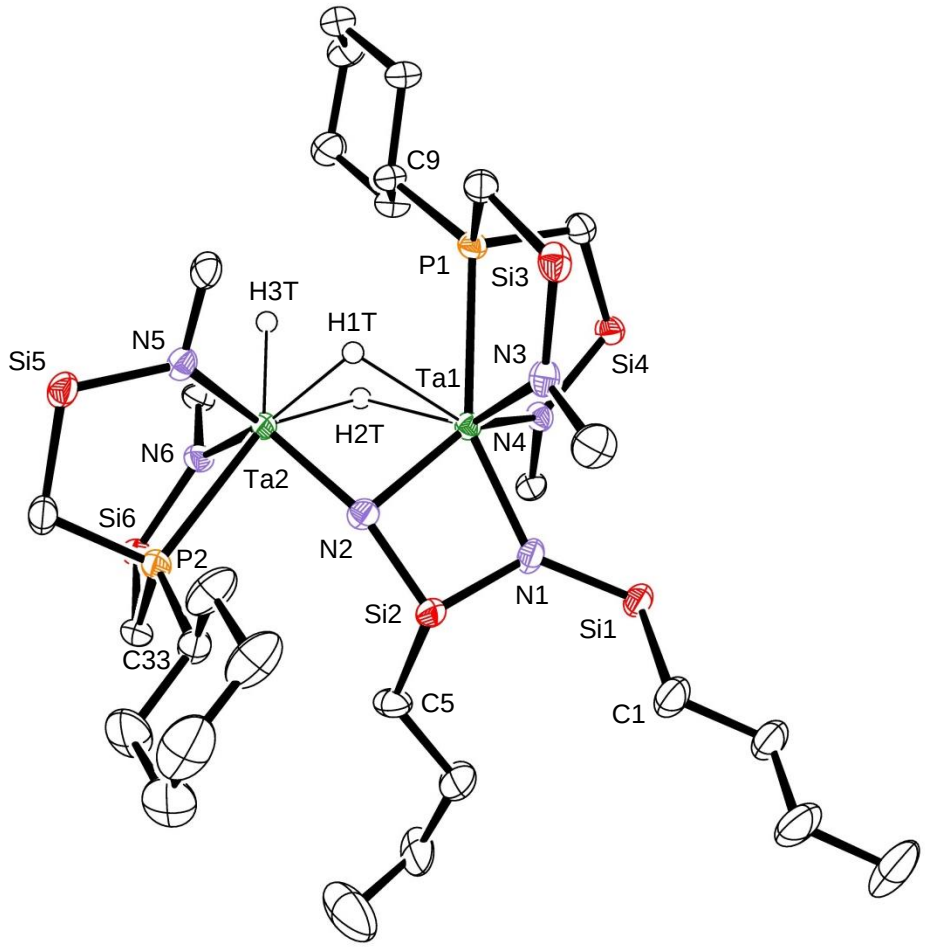

Figure 2.5 ORTEP depiction (ellipsoids at 50 % probability) of **2.7**. Silyl methyl and N-phenyl ring carbons other than ipso are omitted for clarity.

Table 2.3 Selected bond distances (Å) and angles (°) of **2.7**.

Atoms	Distance	Atoms	Distance
Ta(1)–N(1)	2.096(3)	Ta(1)···Ta(2)	2.9667(4)
Ta(1)–N(2)	2.044(3)	Ta(1)–H(1T)	2.14(4)
Ta(2)–N(2)	1.976(3)	Ta(1)–H(2T)	1.98(4)
Ta(1)–N(3)	2.056(3)	Ta(2)–H(1T)	1.78(4)
Ta(1)–N(4)	2.105(3)	Ta(2)–H(2T)	1.77(5)
Ta(2)–N(5)	2.074(3)	Ta(2)–H(3T)	1.69(4)
Ta(2)–N(6)	2.051(3)	N(1)–Si(1)	1.710(3)
Ta(1)–P(1)	2.6624(10)	N(1)–Si(2)	1.713(3)
Ta(2)–P(2)	2.6288(10)	N(2)–Si(2)	1.721(3)
Atoms	Angle	Atoms	Angle
Si(1)–N(1)–Si(2)	129.24(19)	N(1)–Ta(1)–N(2)	74.98(12)
N(1)–Si(2)–N(2)	94.38(15)	Ta(1)–N(2)–Ta(2)	95.10(12)
Ta(2)–Ta(1)–P(1)	91.64(2)	Ta(1)–Ta(2)–P(2)	125.35(2)

The most obvious feature is that neither of the P-cyclohexyl substituents is cyclometalated or in any way altered in **2.7**. In addition, there are hydrides that have been located that bridge the two central tantalum atoms and one terminal hydride is also present. The silylimido-amido unit that results from a rearrangement of the putative bridging imides of the unobserved analogue of **2.1** remains unchanged. Selected bond lengths and angles of **2.7** are shown in Table 2.3. A comparison of the two structures (**2.2** and **2.7**) shows that most of the metrical parameters in the silylimido-amido unit are virtually identical in both structures. Most diagnostic is the Ta1⋯Ta2 separation in the P-phenyl cyclometalated product **2.2** is 2.9511(5) Å, which is similar to that found in the dihydride bridged structure **2.7**, where the Ta⋯Ta2 distance is 2.9667(4) Å.

2.3.3 Characterization of ^{Cy}[NPN^{Si}]TaH(BuSiN-μ-Si(H)Bu-μ-N)(μ-H)$_2$Ta[NPN^{Si}]^{Cy}

Further NMR spectroscopic characterization of **2.7** was carried out to substantiate the molecular structure determined by X-ray crystallography. Assignment of the three hydride resonances of **2.7** was made by a series of NMR experiments. Numerous 2D NMR experiments (^{1}H–^{1}H COSY, ^{1}H–^{13}C HSQC and ^{1}H–^{29}Si HSQC) confirmed that the hydride resonances all correlate to each other and do not correlate to carbon or silicon, suggesting that they are hydrides bound to tantalum. Critical analysis of a ^{1}H – ^{31}P HMBC experiment provided insight into the assignment of the hydride resonances as bridging or terminal, based on their coupling to phosphorus. Both phosphorus resonances correlate to the bridging hydrides as expected, while the unique terminal hydride correlates to only one of the phosphine donors (Figure 2.6). The ^{1}H NMR chemical shifts of the two bridging hydrides are quite disparate, at δ 9.7 and 18.0, and the assignment of the terminal hydride resonance at δ 8.4 is somewhat counterintuitive; the terminal Ta–H resonances in **2.5** and **2.6** (as well as their P-phenyl analogues) are typically the furthest downfield. However, the coupling patterns are consistent with these assignments. Although there is some asymmetry in the bonding of the bridging hydrides in the X-ray structure, this is not conclusive enough to rationalize the disparate chemical shifts.

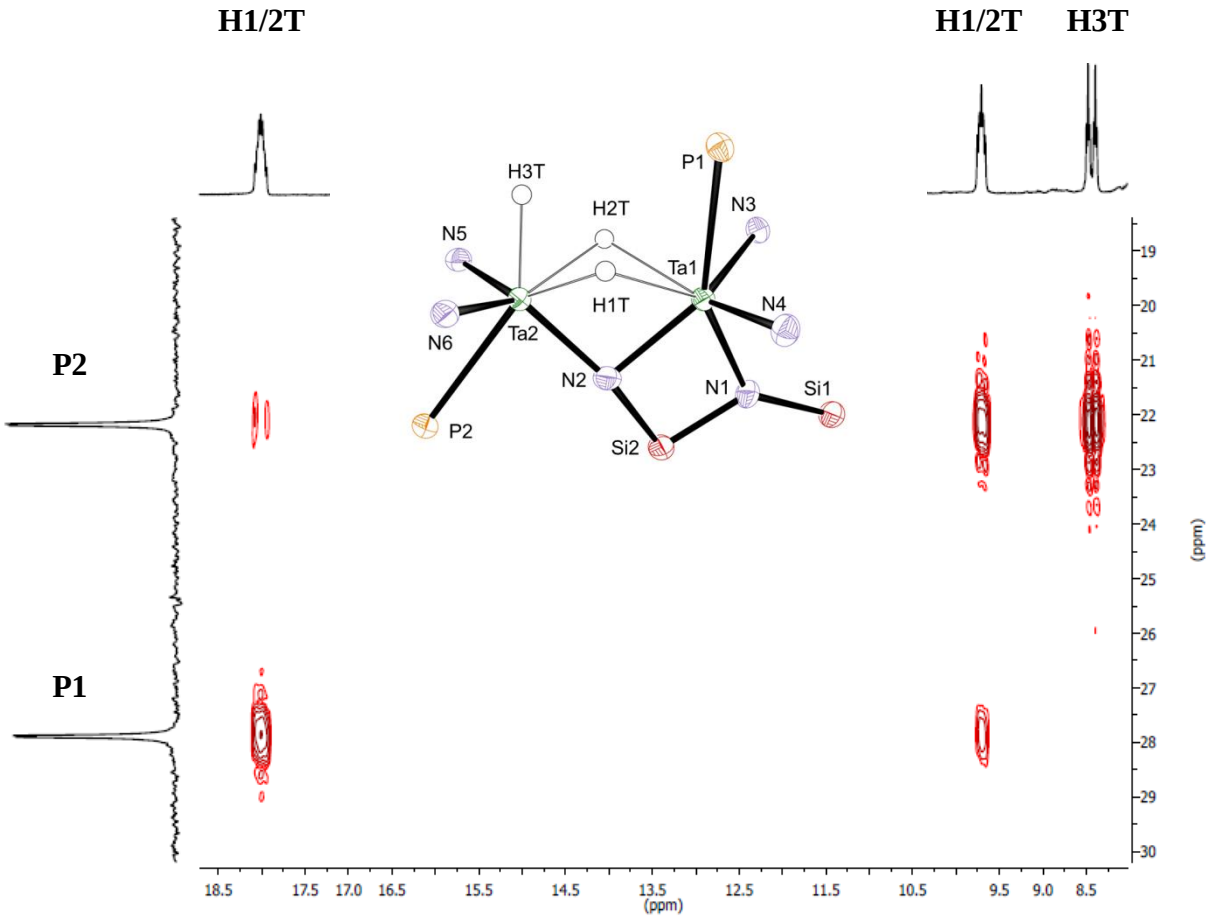

Figure 2.6 Analysis of the ^{1}H – ^{31}P HMBC spectrum (400 MHz, ^{1}H and 161.9 MHz, ^{31}P external projections) of **2.7** (in C_6D_6).

The presence of six silicon atoms in **2.7** was confirmed by ^{29}Si NMR spectroscopy; the ^{1}H–^{29}Si HSQC experiment correlated two silicon atoms to their corresponding Si–H resonances in the silylimido-amido unit and the other four silicon atoms correlated to the eight silyl methyl environments of the ligands (Figure 2.7).

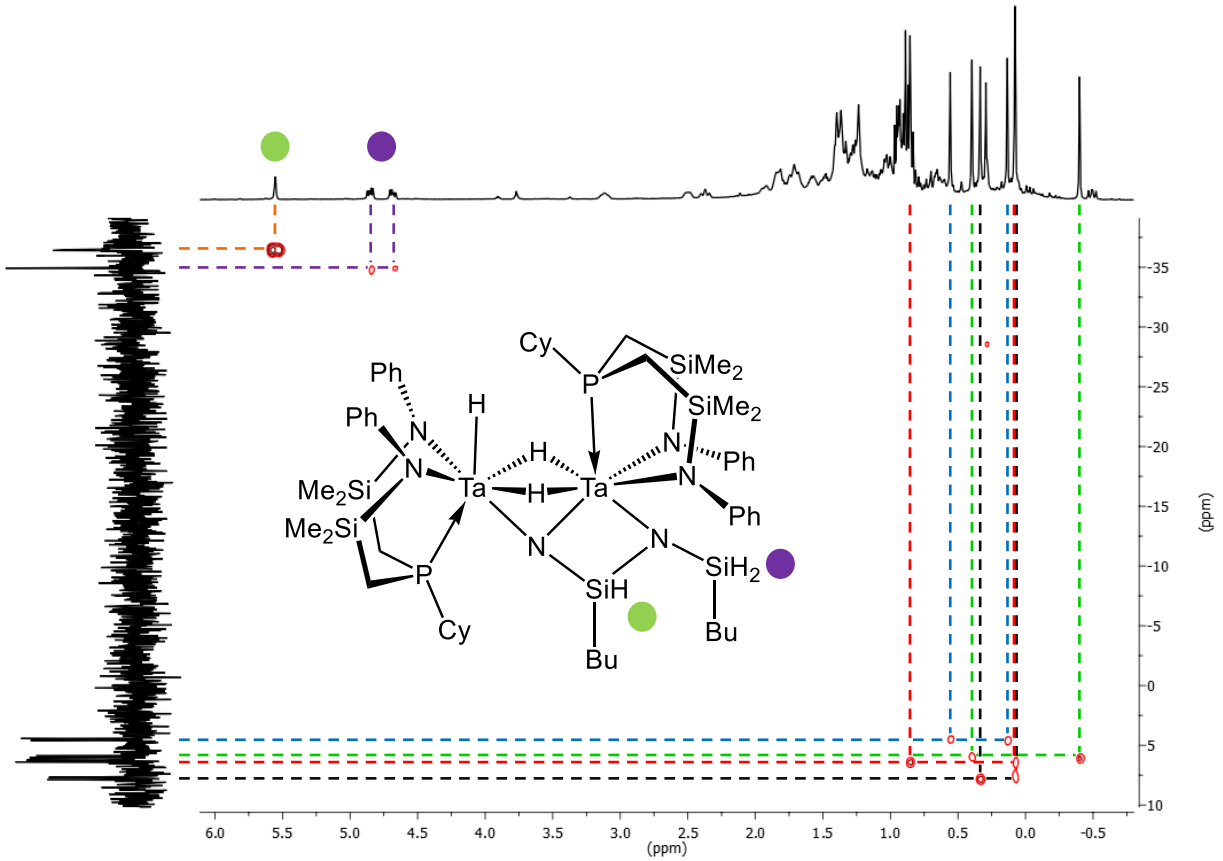

Figure 2.7 ^{1}H–^{29}Si HSQC spectrum (400 MHz, ^{1}H and 79.5 MHz, ^{29}Si external projections) of **2.7** in C_6D_6. The cross peak at 0.29 in ^{1}H and –28.5 in ^{29}Si is due to a silicone grease impurity.

2.3.4 Synthesis of $(^{Cy}[NPN]Ta)_2(\mu\text{-}\eta^2\text{:}\eta^1\text{-}N_2)(\mu\text{-}D)_2$ and ^{2}H NMR spectroscopic studies

Given that the presence of the tantalum hydrides are a defining feature of **2.7** in comparison to the structure of the P-phenyl analogue **2.2**, determining the origin of these hydrides was of great interest. Prior to assigning the identity of the second intermediate as the imide-nitride species **2.6**, a key observation was made that aided this determination. When the hydrosilylation experiment is carried out in a sealed J. Young NMR tube, a singlet at δ 4.47 is observed in the ^{1}H NMR spectra, which is the characteristic chemical shift for H_2. This indicated

that reductive elimination of the bridging hydrides as H_2 does occur, forming **2.6** as the second intermediate species. While this says little about where the bridging hydrides in **2.7** originate from, it gave rise to the idea of tracking the hydrides through deuterium labelling studies. Synthesis of the deuterated dinitrogen complex $(^{Cy}[NPN^{Si}]Ta)_2(\mu\text{-}\eta^2\text{:}\eta^1\text{-}N_2)(\mu\text{-}D)_2$, **2.4-d$_2$** was proposed as a means to track the deuterium atoms via ^{2}H NMR spectroscopy. Analogous to formation of $(^{Cy}[NPN^{Si}]Ta)_2(\mu\text{-}H)_4$ (**2.3**), synthesis of $(^{Cy}[NPN^{Si}]Ta)_2(\mu\text{-}D)_4$ (**2.3-d$_4$**) was accomplished via treatment of $^{Cy}[NPN^{Si}]TaMe_3$ with D_2 gas. Reaction of **2.3-d$_4$** with N_2 results in the formation of the analogous dinitrogen complex **2.4-d$_2$**, containing bridging deuterides instead of hydrides.

The reaction of **2.4-d$_2$**, with excess $BuSiH_3$ was examined through sequential ^{2}H and ^{1}H NMR spectroscopic studies. In the ^{2}H NMR spectra, the signal corresponding to the bridging deuterides (δ 10.4) slowly diminished into the baseline as the reaction progressed. However, the elimination of the bridging deuterides as D_2 was not observed as predicted; there was no trace of a signal corresponding to D_2 present in any of the ^{2}H NMR spectra recorded over the course of the reaction. Instead, a new peak at δ 3.6 was observed that was attributed to $BuSiD_3$, indicating there is some deuterium exchange with the excess $BuSiH_3$ present. Furthermore, the ^{1}H NMR spectra showed the presence of H_2 (δ 4.47), suggesting that H_2 is eliminated instead of D_2, as a result of H/D exchange between **2.4-d$_2$** and butylsilane. As a complimentary experiment, the reaction of trideuterobutylsilane, ($BuSiD_3$) with **2.4** was also investigated. In this case, the presence of D_2 was observed in the ^{2}H NMR spectra, but there was no evidence of H_2 found in the ^{1}H NMR spectra, suggesting D_2 is eliminated instead of H_2 as a result of H/D exchange between **2.4** and $BuSiD_3$. Signals observed in the hydride region of the ^{2}H NMR spectra correspond to the known chemical shifts of the tantalum hydrides of **2.5**, **2.6** and **2.7**, confirming

the presence of tantalum deuterides. In the hydride region of the ^{1}H NMR spectra, only trace signals of the tantalum hydrides are observed. Although the process is complicated by fast exchange between the butylsilane hydrides and the tantalum hydrides early in the reaction, the evidence suggests that the hydrides present in **2.7** arise from the excess butylsilane present.

2.4 Hydrosilylation of (^{Cy}[NPN]Ta)$_2$(μ-η^2:η^1-N$_2$)(μ-H)$_2$ with PhSiH$_3$

Since isolation and characterization of the intermediates in the reaction between **2.4** and BuSiH$_3$ proved challenging, the reaction between **2.4** and excess phenylsilane (PhSiH$_3$) was investigated in order to gain understanding of the mechanism by which **2.4** reacts with silanes. Initial ^{31}P{^{1}H} NMR studies indicated that **2.4** reacts rapidly with PhSiH$_3$ to form the analogous monosilylated species **2.8** (Scheme 2.5), as evidenced by the appearance of two new doublets at δ 29.7 and 15.5 and the complete disappearance of the resonances of **2.4**. In the ^{1}H NMR spectrum, there are two new hydride resonances at δ 14.3 and 11.0 which integrate to 1H and 2H respectively, corresponding to one terminal hydride and two bridging hydrides. This is consistent with the spectral properties of the analogous P-phenyl monosilylated species found in the reaction between **1.32** and one equivalent of PhSiH$_3$.[98] A second intermediate species is also rapidly formed, giving rise to a broad resonance at δ -1.0 in the ^{31}P{^{1}H} NMR spectrum and a signal at δ 16.5 in the ^{1}H NMR spectrum that could correspond to a tantalum hydride. In all likelihood, this second intermediate is the imide-nitride (**2.9**) that forms analogously to **2.6**. The presence of a peak at δ 4.47 in the ^{1}H NMR spectrum suggests that H$_2$ has been eliminated, (arising from conversion of **2.8** to **2.9**), further supporting the assignment of **2.9** as the analogous imide-nitride species (Scheme 2.5). Within several hours, two new singlets at δ 22.0 and –4.9 appear in ^{31}P{^{1}H} NMR spectrum, suggesting a third species in the reaction mixture. During the

reaction, all three species are present simultaneously for some time, eventually leading to complete conversion into the third species within 16 hours. The ^{1}H NMR spectrum for the final product (**2.10**) is quite messy and complicated; peaks that are suggestive of eight silyl methyl environments indicate this complex has C_1 symmetry in solution. The spectral properties of this complex are reminiscent of the product of the reaction between the P-phenyl dinitrogen complex **1.32** and 2 equivalents of $PhSiH_3$, resulting in migration of one of the amido donors of the [NPN] ligand.[98] The structure of **2.10** is proposed on the basis of similar spectral parameters to the previously reported P-phenyl analogue. Scheme 2.5 shows the overall reaction of **2.4** with excess phenylsilane. Attempts to isolate the intermediate species were unsuccessful and crystals suitable for X-ray diffraction experiments were elusive, so this study was not pursued further.

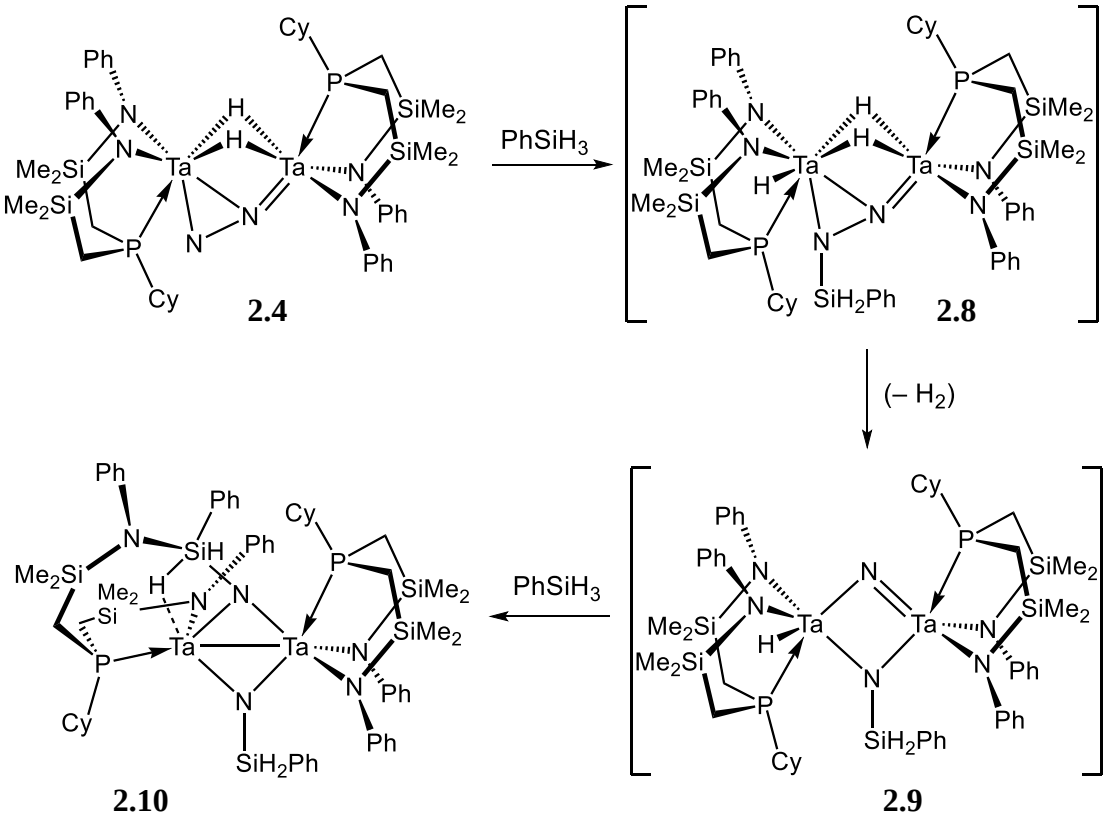

Scheme 2.5

2.5 Conclusions

The P-cyclohexyl dinitrogen complex **2.4** was prepared and its reaction with excess butylsilane was explored. Upon monitoring the reaction by multinuclear NMR spectroscopy, a number of intermediate species were observed. The final product is a hydride-bridged imido-amido silylated species (**2.7**) that has the imido bridging between the two central tantalum atoms. The origin of the bridging hydrides in the product is proposed to arise from the excess silane present, on the basis of deuterium labelling studies. The reaction of **2.4** with excess $PhSiH_3$ was also examined and monitored via $^{31}P\{^1H\}$ and ^1H NMR spectroscopy. This process appears to proceed similarly to the reaction between the P-phenyl dinitrogen complex **1.32** and $PhSiH_3$, producing analogous species.

Although the strategy to change the substituent on the phosphine from phenyl to cyclohexyl did not result in release of tris(butylsilyl)amine, cyclometallation of the phosphine substituent was circumvented. Nevertheless, both of the final products display the same rearranged silylimido-amido unit, which suggests that this bonding arrangement is the thermodynamic sink in this system, as it forms in two separate reactions. While understanding the operative mechanism for both processes would be of interest, the fact that in neither case the cleaved and functionalized dinitrogen fragment can be eliminated from the ditantalum core is disappointing. Although both of these processes get us close to the lofty goal of converting dinitrogen to a higher value organonitrogen product with the potential for turnover, it is clear that these systems are flawed. Elimination via hydrolysis[104] is an additional method that could lead to liberation of a desirable product.

Chapter 3: Reactivity of paramagnetic niobium and vanadium dinitrogen complexes

3.1 Introduction

Dinitrogen complexes are commonly accessed via reduction of a metal complex with a strong reducing agent in the presence of molecular nitrogen. Previously reported work has demonstrated that numerous early transition metal dinitrogen complexes can be obtained using this method (see Chapter 1). The reduction of $[P_2N_2]NbCl$ (**1.21**) using KC_8 in the presence of N_2 lead to formation of a paramagnetic end-on bridged dinitrogen complex $([P_2N_2]Nb)_2(\mu\text{-}N_2)$ (**1.22**).[61] Similarly, the reduction of $[P_2N_2]VCl$ under the same conditions generated the analogous paramagnetic dinitrogen complex $([P_2N_2]V)_2(\mu\text{-}N_2)$.[105] It is worth noting that the use of strong reducing agents in these systems does not always lead to formation of a dinitrogen complex. For example, the reduction of $[P_2N_2]NbCl$ using KC_8 in the presence of aromatic substrates has generated some interesting arene complexes.[106-107] Under an H_2 atmosphere, toluene or benzene solutions of $[P_2N_2]NbCl$ and KC_8 undergo hydrogenation of the respective aromatic solvent to produce $[P_2N_2]$ niobium cyclohexadienyl complexes[106] (Scheme 3.1). Reduction of $[P_2N_2]NbCl$ with KC_8 under argon resulted in phosphorus-phenyl group activation,[107] shown in Scheme 3.1. Although there was a deliberate absence of N_2 in both of these systems, they still serve to demonstrate the complex reactivity that can arise when generating highly reduced complexes supported by P- and N- containing arrays.

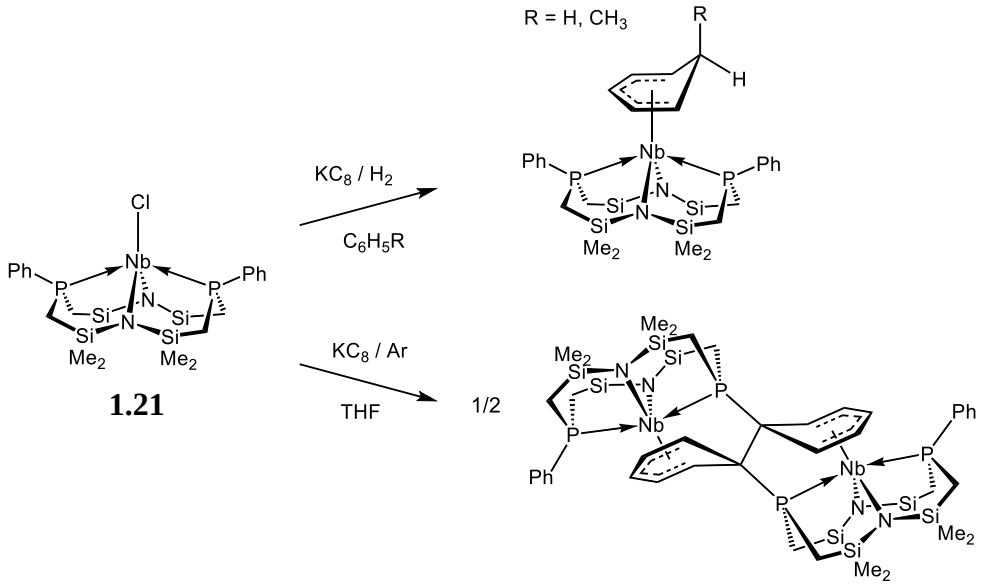

Scheme 3.1

While the N_2 complexes $([P_2N_2]Nb)_2(\mu\text{-}N_2)$ and $([P_2N_2]V)_2(\mu\text{-}N_2)$ have previously been reported,[61, 105] exploration of reactivity studies are limited. Treatment of $([P_2N_2]Nb)_2(\mu\text{-}N_2)$ with H_2 and primary silanes was previously examined, however no reactivity was observed.[61] When $([P_2N_2]Nb)_2(\mu\text{-}N_2)$ was exposed to phenylacetylene, formation of an alkyne complex $[P_2N_2]Nb(\eta^2\text{–}HCCPh)$[61] occurred via displacement of the coordinated dinitrogen (Scheme 3.2). Cleavage of the N_2 unit via nitride formation was also previously investigated; as each Nb(IV) center in $([P_2N_2]Nb)_2(\mu\text{-}N_2)$ is formally d^1, each metal could theoretically supply one electron to further reduce the hydrazido N_2^{4-} to two nitrido N^{3-} species. Previous reports show that the thermolysis of a toluene solution of $([P_2N_2]Nb)_2(\mu\text{-}N_2)$ resulted in formation of the paramagnetic, bimetallic bridging-nitride complex, $[P_2N_2]Nb(\mu\text{-}N)Nb[PN_3]$ (**3.1**), where $[PN_3]$ = $PhPMe(CHSiMe_2NSiMe_2CH_2P(Ph)CH_2SiMe_2NSiMe_2N)$ (Scheme 3.2). A single nitride bridges the two Nb centers, while the other nitrogen atom of the hydrazido ligand has been incorporated

into the backbone of the P_2N_2 macrocycle. Despite the complications of a ligand rearrangement, this result is significant in that it demonstrates not only the formation of N_2 derived nitrides, but also nitride functionalization, as evidenced by N–P and N–Si bond formation.

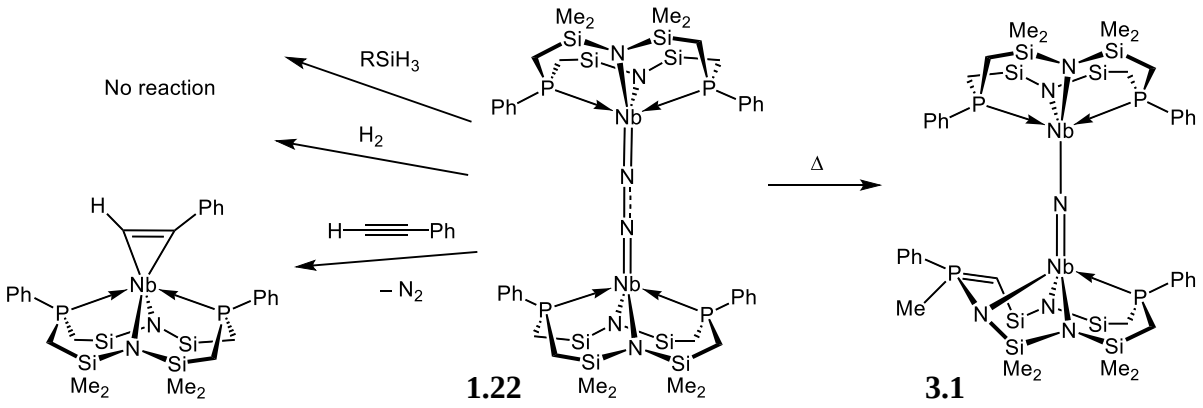

Scheme 3.2

In an attempt to trap the potential niobium nitride intermediate species, the thermolysis of $([P_2N_2]Nb)_2(\mu\text{-}N_2)$ in the presence of Lewis acids was proposed. Prior examination using two equivalents of trimethylaluminum ($AlMe_3$) revealed that $AlMe_3$ does not act as a Lewis acid; instead, loss of a methyl group occurred to form a bis(organo)aluminum imide species[108] $([P_2N_2]NbN)_2(AlMe_2)_2$ (**3.2**) (Scheme 3.3). The N_2 unit was cleaved and the formation of N–Al bonds indicates functionalization of the coordinated dinitrogen. The observation of 1,2-diphenylethane in the ^1H NMR spectrum is suggestive of a radical mechanism, whereby a methyl radical abstracts a proton from toluene to form CH_4 and 1,2-diphenylethane.[108]

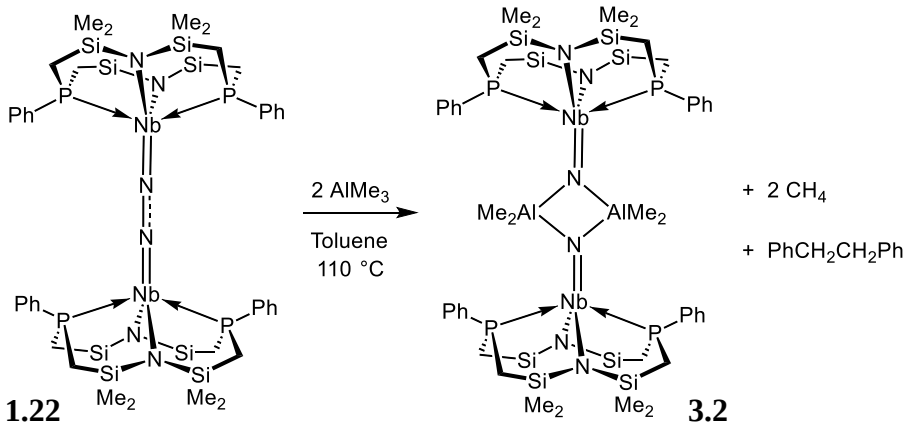

Scheme 3.3

In this chapter, the thermolysis of $([P_2N_2]Nb)_2(\mu\text{-}N_2)$ in the presence of Lewis acids is further investigated and novel reactivity of $([P_2N_2]Nb)_2(\mu\text{-}N_2)$ and $([P_2N_2]V)_2(\mu\text{-}N_2)$ with electrophiles/oxidants is also explored.

3.2 Reactivity of $([P_2N_2]Nb)_2(\mu\text{-}N_2)$ with Lewis acids

The thermolysis of $([P_2N_2]Nb)_2(\mu\text{-}N_2)$ in the presence of various Lewis acids was explored in an effort to determine if similar reactivity to that of the $AlMe_3$ example could be observed (forming species analogous to **3.2**). Initially, the reproducibility of **3.2** from the reported reaction between $AlMe_3$ and $([P_2N_2]Nb)_2(\mu\text{-}N_2)$[108] was examined. When a toluene solution of $([P_2N_2]Nb)_2(\mu\text{-}N_2)$ and $AlMe_3$ was heated at 110 °C overnight, a colour change from dark brown to maroon was observed, consistent with the previous report.[108] A maroon paramagnetic material was isolated, showing broad resonances in the paramagnetic ^{1}H NMR spectrum at differing chemical shifts from the starting $([P_2N_2]Nb)_2(\mu\text{-}N_2)$ complex. The previous report stated that a large crop of green crystalline material was isolated; despite numerous

attempts, only a few green crystals suitable for X-ray diffraction were obtained. Figure 3.1 shows the molecular structure determined from these crystals, confirming **3.2** as a product of this reaction.

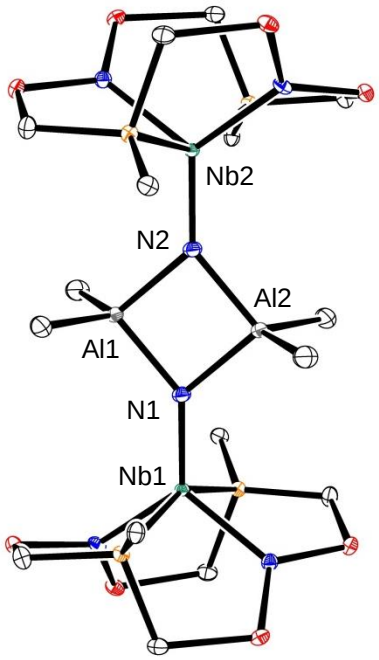

Figure 3.1 ORTEP depiction (ellipsoids at 50 % probability) of $([P_2N_2]NbN)_2(AlMe_2)_2$ (**3.2**). Silyl methyl and P-phenyl ring carbons other than ipso are omitted for clarity.

The thermolysis of $([P_2N_2]Nb)_2(\mu\text{-}N_2)$ in the presence of triethylaluminum ($AlEt_3$) was examined next, in order to observe the effect of using an organoaluminum reagent with bulkier alkyl groups. Upon heating a toluene solution of $([P_2N_2]Nb)_2(\mu\text{-}N_2)$ and $AlEt_3$ overnight, a colour change from dark brown to maroon was observed. The resultant maroon compound is tentatively assigned as $([P_2N_2]NbN)_2(AlEt_2)_2$ (**3.3**), formed analogously to complex **3.2**. A

comparison of the paramagnetic ^{1}H NMR spectra of **3.2** versus **3.3** is shown in Figure 3.2. Similar resonances are observed at relatively similar chemical shifts in the spectra of both compounds. Unfortunately, the structure of **3.3** is unsubstantiated, due to failure to obtain X-ray quality crystals of this material.

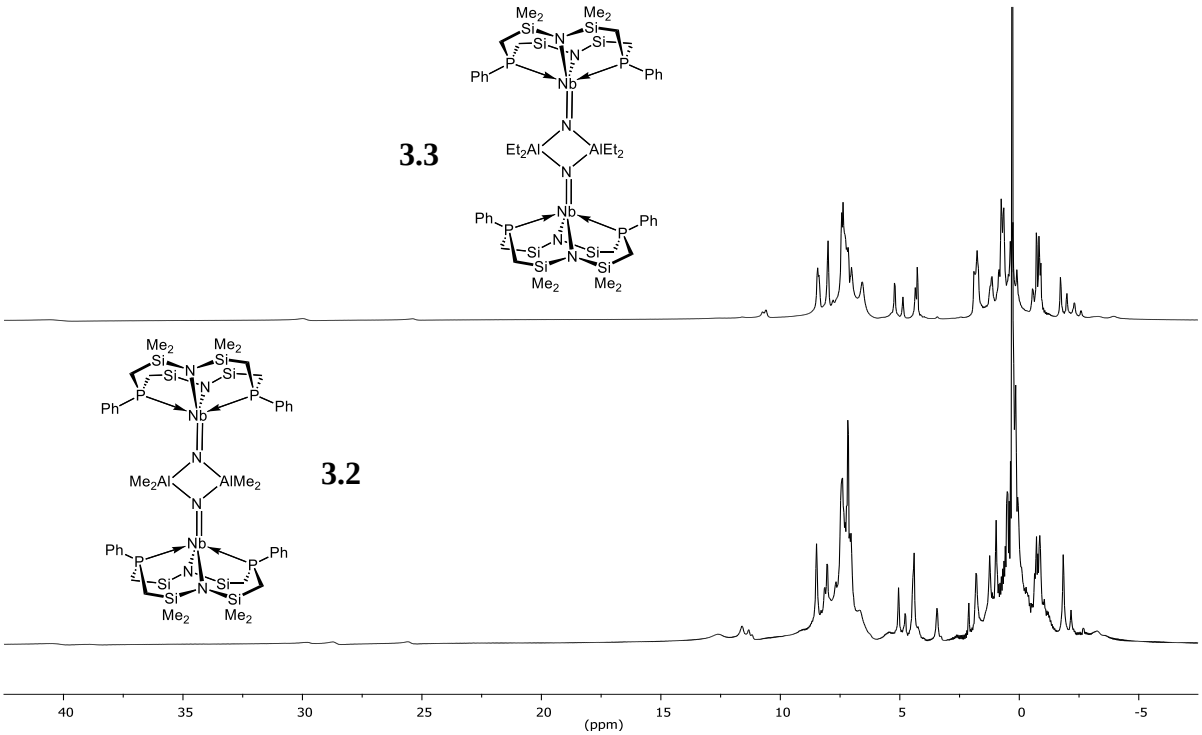

Figure 3.2 Comparison of the paramagnetic ^{1}H NMR (400 MHz, C_6D_6) spectra of **3.2** (bottom) versus **3.3** (top).

In contrast, thermolysis of $([P_2N_2]Nb)_2(\mu\text{-}N_2)$ in the presence of triethylborane (BEt_3) did not lead to N_2 functionalization. A colour change from dark brown to dark blue was observed after heating a toluene solution of $([P_2N_2]Nb)_2(\mu\text{-}N_2)$ and BEt_3 overnight, reminiscent of the thermolysis of $([P_2N_2]Nb)_2(\mu\text{-}N_2)$ that forms the nitride species **3.1**. Formation of **3.1** was confirmed by comparative paramagnetic ^{1}H NMR spectra, in addition to single crystal X-ray

diffraction studies (Figure 3.3). No interaction with BEt_3 was observed, even when the experiment was conducted with excess (8 equivalents) BEt_3 present.

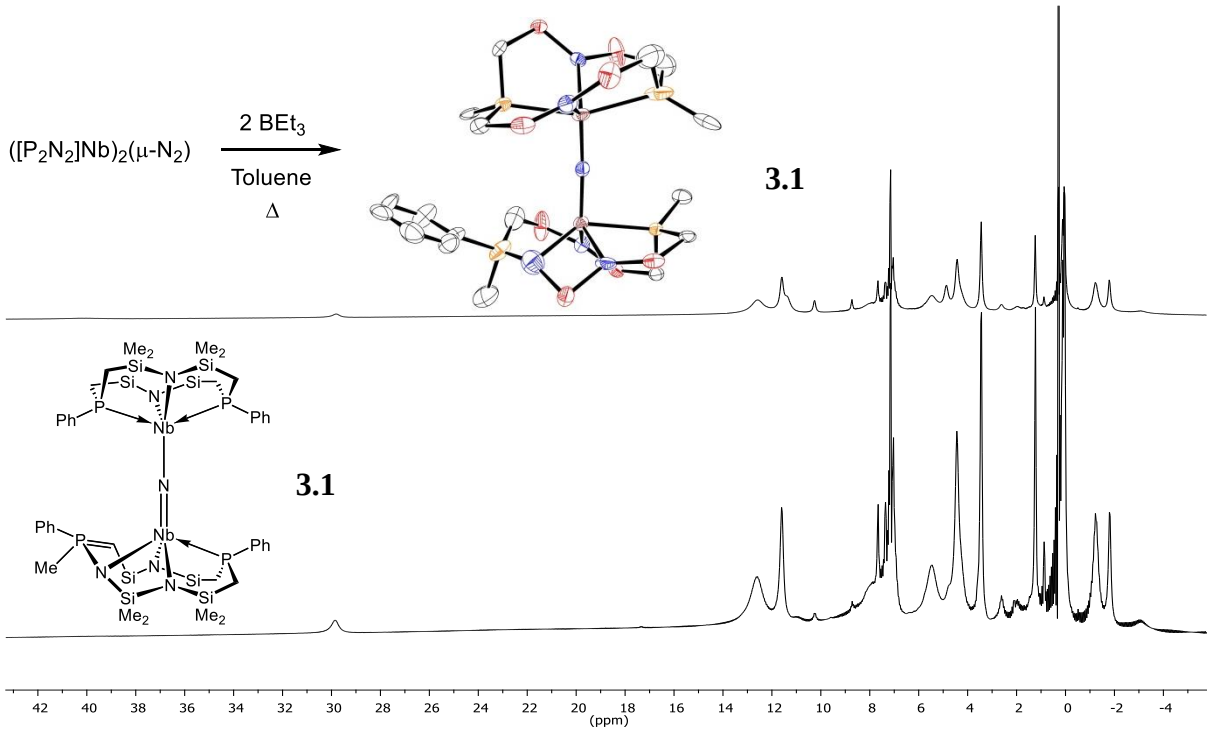

Figure 3.3 Comparison of the paramagnetic ^{1}H NMR (400 MHz, C_6D_6) spectrum of **3.1** (bottom) to that of the material isolated from the thermolysis of $([P_2N_2]Nb)_2(\mu\text{-}N_2)$ in the presence of BEt_3 (top). ORTEP depiction (ellipsoids at 50 % probability) of the material, verified as **3.1**. Silyl methyl and P-phenyl ring carbons other than ipso are omitted for clarity.

When a toluene solution of $([P_2N_2]Nb)_2(\mu\text{-}N_2)$ was thermolyzed in the presence of tris(pentafluorophenyl)borane $[B(C_6F_5)_3]$, a colour change from dark brown to dark red was observed. A dark red paramagnetic material was isolated, displaying very broad, unresolved peaks in the paramagnetic ^{1}H NMR spectrum. Attempts to grow X-ray quality crystals from this

material were ultimately unsuccessful, thus the structure and identity of the product remains elusive.

Similar to the above reaction, the thermolysis of $([P_2N_2]Nb)_2(\mu\text{-}N_2)$ with bis(pentafluorophenyl)borane (Piers' borane, $HB(C_6F_5)_2$) yields a dark red paramagnetic material that shows broad peaks in the paramagnetic ^{1}H NMR spectrum. In an effort to observe the effect of reduced temperature, a toluene solution of $([P_2N_2]Nb)_2(\mu\text{-}N_2)$ and $HB(C_6F_5)_2$ was left to stir at room temperature overnight. The resulting dark red solution also yielded a dark red paramagnetic material, showing broad peaks in the paramagnetic ^{1}H NMR spectrum. A small amount of single crystals suitable for X-ray diffraction were isolated and the solid-state molecular structure was determined. Initially, the structure was assigned as the starting materials, $([P_2N_2]Nb)_2(\mu\text{-}N_2)$ and Piers' borane, co-crystallized with diethyl ether. However, after further scrutiny of the crystallographic data, two hydrides associated with the borane moiety were located and the C–B–C bond angle was more acute than the expected 121.6(4) ° seen in the starting Piers' borane.[109] Hydridoborate formation suggests a novel complex, $[([P_2N_2]Nb)_2(\mu\text{-}N_2)][H_2B(C_6F_5)_2]$ (**3.4**), was formed, as shown in Figure 3.4. The C49–B1–C55 bond angle of 114.7(4) ° in **3.4** is consistent with complexes containing the $H_2B(C_6F_5)_2$ anion.[110-111] The counter cation must then be the $[([P_2N_2]Nb)_2(\mu\text{-}N_2)]$ fragment, indicating a loss of one or two electrons has occurred. The metrical parameters for the $[([P_2N_2]Nb)_2(\mu\text{-}N_2)]$ fragment in **3.4** are essentially the same as the parent $([P_2N_2]Nb)_2(\mu\text{-}N_2)$ species. The N1–N2 bond length of 1.265(4) Å in **3.4** is slightly contracted compared to the $([P_2N_2]Nb)_2(\mu\text{-}N_2)$ complex at 1.272(5) Å.

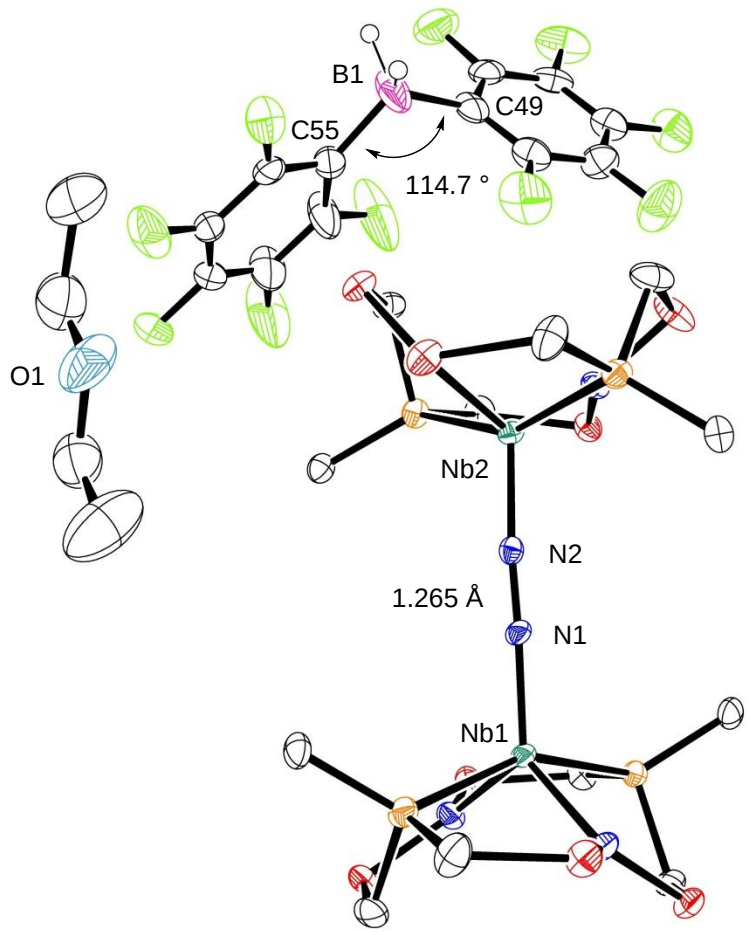

Figure 3.4 ORTEP depiction (ellipsoids at 50 % probability) of $[([P_2N_2]Nb)_2(\mu\text{-}N_2)]$ $[H_2B(C_6F_5)_2]$ (**3.4**). Silyl methyl and P-phenyl ring carbons other than ipso are omitted for clarity. Significant bond length (Å) and angle (°): N1–N2, 1.265(4); C49–B1–C55, 114.7(4).

The overall summary of the thermolysis of $([P_2N_2]Nb)_2(\mu\text{-}N_2)$ in the presence of various Lewis acids is shown in Scheme 3.4. With the exception of triethylborane, some indication of reactivity of $([P_2N_2]Nb)_2(\mu\text{-}N_2)$ with each Lewis acid was observed, although several of the products eluded characterization. Investigating the reactivity of $([P_2N_2]Nb)_2(\mu\text{-}N_2)$ with Lewis acids provided the inspiration for exploring the treatment of $([P_2N_2]Nb)_2(\mu\text{-}N_2)$ with other electrophiles and oxidants.

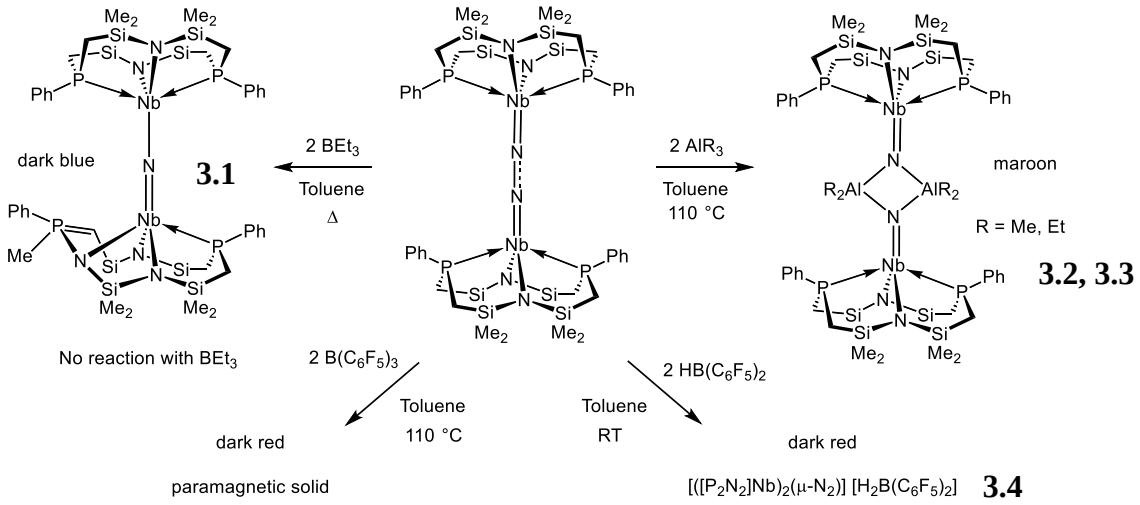

Scheme 3.4

3.3 Reactivity of $([P_2N_2]Nb)_2(\mu\text{-}N_2)$ with electrophiles and oxidants

In order to generate the positively charged $[([P_2N_2]Nb)_2(\mu\text{-}N_2)]$ fragment in complex **3.4**, it was postulated that the electron loss could occur as a result of oxidation of the N_2 unit. While this particular reaction pathway is an imprecise example of how to accomplish this, it has served as a stepping stone for considering oxidation reactions of $([P_2N_2]Nb)_2(\mu\text{-}N_2)$. Treatment of N_2 complexes with chemical oxidants is known to produce oxidized N_2 species that are salts of the reagent anion.[112-114] Commonly used oxidants include silver salts, ferrocenium salts, halogens and diphenyliodonium salts.[115] Some of these reagents can act as either an electrophile or oxidant, dependent on the chemical environment and species involved.[115] In this section, treatment of $([P_2N_2]Nb)_2(\mu\text{-}N_2)$ with a variety of electrophiles/oxidants is discussed.

3.3.1 Treatment of $([P_2N_2]Nb)_2(\mu\text{-}N_2)$ with iodine-containing reagents

The reactivity of $([P_2N_2]Nb)_2(\mu\text{-}N_2)$ with different iodine containing reagents was first explored. Diphenyliodonium salts can act as oxidants towards transition metal complexes, although they are typically used in electrophilic arylation reactions.[115-116] Addition of a toluene solution of diphenyliodonium triflate ($[Ph_2I][OTf]$) to a toluene solution of $([P_2N_2]Nb)_2(\mu\text{-}N_2)$ resulted in a colour change from dark brown to clear yellow within 30 minutes. The isolated yellow paramagnetic material showed broad resonances in the paramagnetic ^{1}H NMR spectrum at differing chemical shifts from the starting $([P_2N_2]Nb)_2(\mu\text{-}N_2)$ complex (Figure 3.5). Crystallization efforts were ultimately unsuccessful; the identity of this material remains elusive due to failure to determine the solid-state molecular structure.

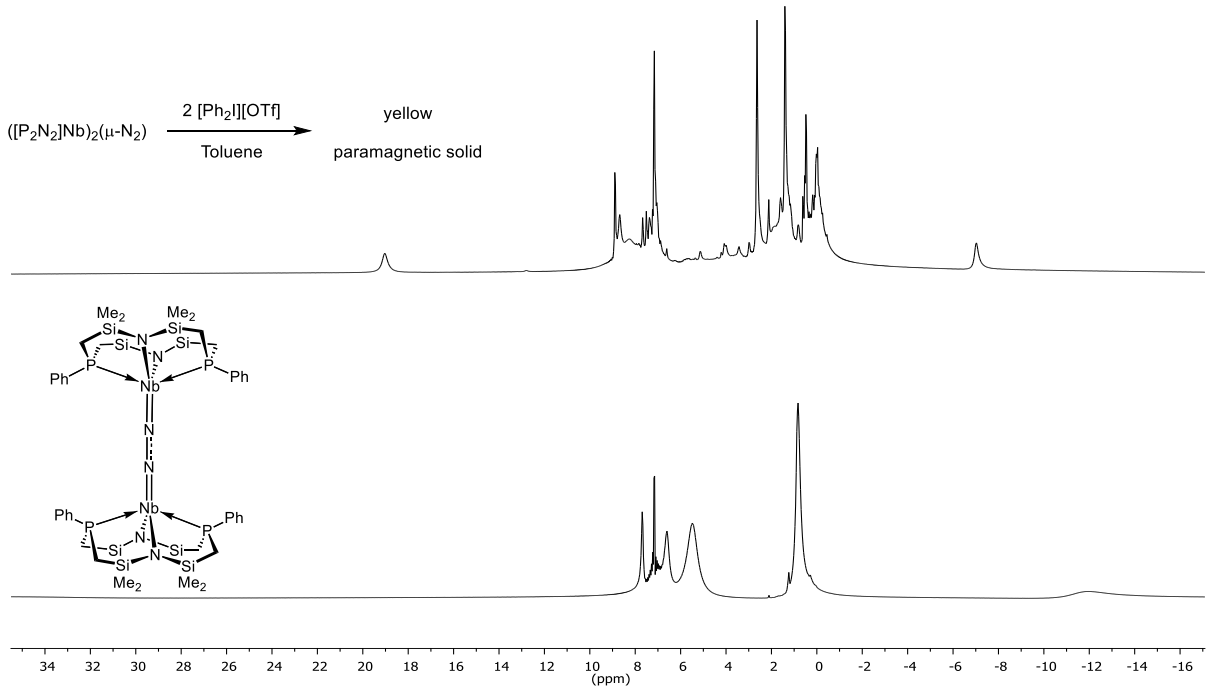

Figure 3.5 Comparison of the paramagnetic ^{1}H NMR (400 MHz, C_6D_6) spectrum of $([P_2N_2]Nb)_2(\mu\text{-}N_2)$ (bottom) to that of the material isolated from the reaction of $([P_2N_2]Nb)_2(\mu\text{-}N_2)$ with $[Ph_2I][OTf]$ (top).

In addition to possessing electrophilic character, alkyl halides act as weak one-electron oxidants.[115] A gradual colour change from dark brown to clear yellow was observed upon addition of methyl iodide (MeI) to a toluene solution of $([P_2N_2]Nb)_2(\mu\text{-}N_2)$. The dark yellow material showed broad resonances in the paramagnetic ^{1}H NMR spectrum. The material resisted all crystallization attempts, thus crystals suitable for X-ray diffraction studies were not accessible and the structure remains undetermined.

The reaction of 1,2-diiodoethane with $([P_2N_2]Nb)_2(\mu\text{-}N_2)$ yields a dark yellow-brown paramagnetic material (**3.5**), showing broad peaks in the paramagnetic ^{1}H NMR spectrum. Single crystals of **3.5** were obtained and the solid-state molecular structure was determined. Figure 3.6 illustrates the structure of **3.5** as $([P_2N_2]NbI)_2(\mu\text{-}N_2)$. The N_2 unit remains intact, with an N1–N1' bond distance of 1.09(2) Å, considerably shorter than the parent $([P_2N_2]Nb)_2(\mu\text{-}N_2)$ N–N bond length of 1.272(5) Å. The Nb1–N1 bond length of 1.943(12) Å is longer than the Nb–N bond lengths (1.853(4), 1.850(4) Å) in $([P_2N_2]Nb)_2(\mu\text{-}N_2)$. In contrast to the distorted trigonal bipyramidal geometry around the niobium centres in $([P_2N_2]Nb)_2(\mu\text{-}N_2)$, both niobium atoms in **3.5** have formed a Nb–I bond, generating a distorted octahedral geometry about each niobium centre. The $[P_2N_2]NbI$ units are staggered with respect to each other along the Nb–N_2–Nb axis, such that the niobium iodides are rotated about 45° from one another. The magnetic moment of **3.5** was found to be 2.99 μ_B (indicating 2 unpaired electrons) consistent with the presence of two d^1 Nb(IV) centres. Accordingly, the dinitrogen moiety in **3.5** can be considered a diazenido type N_2^{2-} unit.

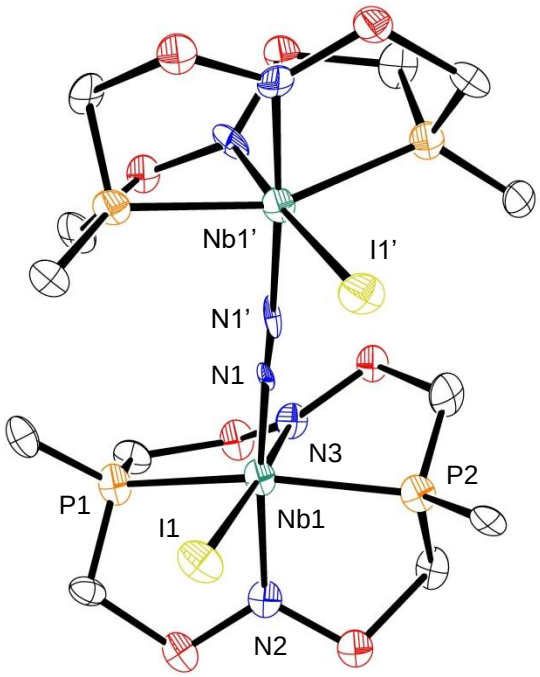

Figure 3.6 ORTEP depiction (ellipsoids at 50 % probability) of $([P_2N_2]NbI)_2(\mu\text{-}N_2)$ (**3.5**). Silyl methyl and P-phenyl ring carbons other than ipso are omitted for clarity. Selected bond lengths (Å) and angles (°): N–N', 1.09(2); Nb1–N1, 1.943(12); Nb1–I1, 2.835(2); Nb1–N1–N1', 175.9(14); N1–Nb1–N2, 169.6(5); N3–Nb1–I1, 175.5(4); P1–Nb1–P2, 157.84(15).

3.3.2 Treatment of $([P_2N_2]Nb)_2(\mu\text{-}N_2)$ with silver salts and ferrocenium salts

Silver (I) salts are broadly used as oxidants with transition metal complexes,[115] in addition to acting as halide abstraction agents. The reactivity of $([P_2N_2]Nb)_2(\mu\text{-}N_2)$ with silver tetraphenylborate ($AgBPh_4$) and silver triflate (AgOTf) was studied in order to determine if oxidation of $([P_2N_2]Nb)_2(\mu\text{-}N_2)$ would take place. The addition of a THF solution of $AgBPh_4$ to a solution of $([P_2N_2]Nb)_2(\mu\text{-}N_2)$ in THF produced a colour change from dark brown to dark red.

Red needle crystals were isolated, showing broad peaks in the paramagnetic ^{1}H NMR spectrum (Figure 3.7). Although the red crystalline product could be consistently isolated, single crystals suitable for X-ray diffraction studies remain elusive; the solid state molecular structure is undetermined and thus the identity of the product is unknown.

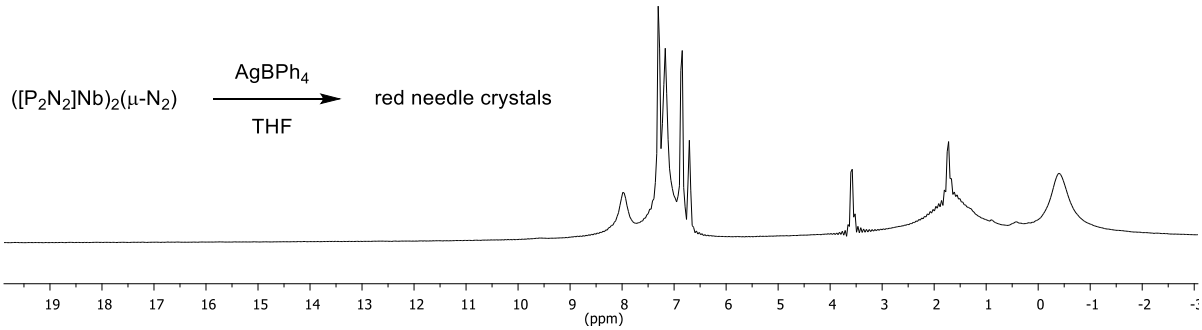

Figure 3.7 Paramagnetic ^{1}H NMR (400 MHz, THF-d_8) spectrum of red needle crystals isolated from the reaction between $AgBPh_4$ and $([P_2N_2]Nb)_2(\mu\text{-}N_2)$.

Upon addition of a THF solution of AgOTf to a solution of $([P_2N_2]Nb)_2(\mu\text{-}N_2)$ in THF, a colour change from dark yellow-brown to dark red-brown was observed. The dark brown residue isolated was extracted into minimal toluene and filtered to remove some insoluble dark solids, likely Ag^0 produced from the reaction. Broad peaks were visible in the paramagnetic ^{1}H NMR spectrum. Slow evaporation of a toluene solution yielded a small amount of crystals that were suitable for X-ray diffraction studies. The solid-state molecular structure obtained from these crystals is shown in Figure 3.8. Complex **3.6** demonstrates that loss of the N_2 unit and coordination of a toluene solvent molecule has occurred to form a niobium arene complex. The coordinated toluene appears to be slightly distorted from planarity, bound η^6 to the niobium

centre. Two triflate molecules are also present in the structure (one triflate is incompletely modelled due to disorder). This is consistent with the formal assignment of a Nb(IV) centre.

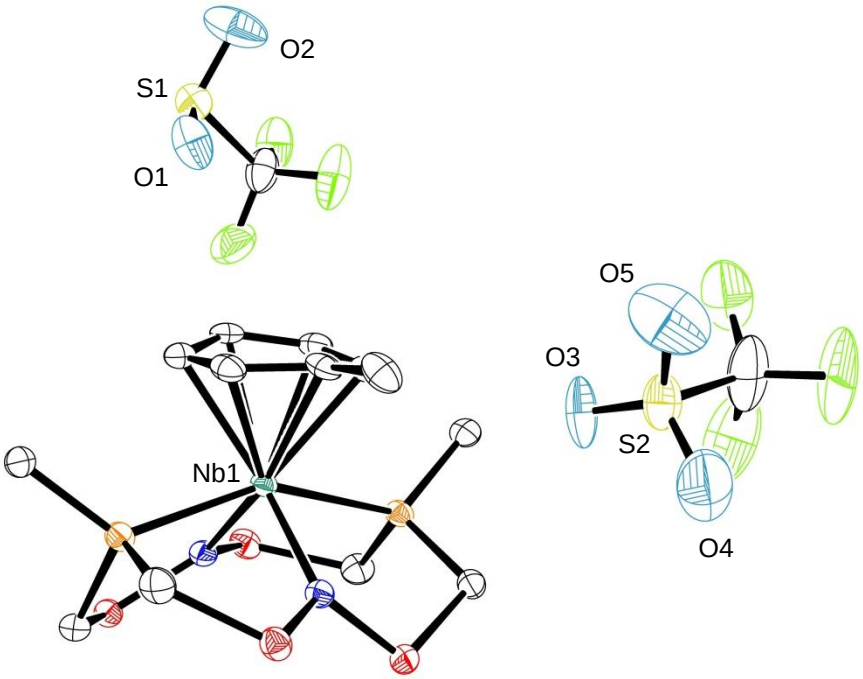

Figure 3.8 ORTEP depiction (ellipsoids at 50 % probability) of **3.6**. Silyl methyl and P-phenyl ring carbons other than ipso are omitted for clarity. One triflate molecule is missing an oxygen atom (incomplete model due to disorder).

Unfortunately, it is unclear if **3.6** is the major product in the reaction between AgOTf and $([P_2N_2]Nb)_2(\mu\text{-}N_2)$. Upon repeating the reaction, paramagnetic ^{1}H NMR spectra matching that of **3.6** failed to be obtained. In addition, crystals of **3.6** were never isolated again. The experiment was also repeated in the absence of aromatic solvents, in an effort to observe how the reaction outcome would differ. After filtering out the insoluble solids (Ag^0), crystal growth was observed upon concentrating a THF solution of the reaction mixture. However, when the crystals were

taken for X-ray diffraction studies, the solid-state molecular structure showed $([P_2N_2]Nb)_2(\mu\text{-}N_2)$ co-crystallized with THF. The remaining dark red-brown material (isolated from the mother liquor) shows broad peaks in the paramagnetic ^{1}H NMR spectrum. Figure 3.9 shows a comparison of the paramagnetic ^{1}H NMR spectra of **3.6** to that of the dark red-brown material produced in this reaction. Repeated attempts to produce crystals from the reaction of AgOTf and $([P_2N_2]Nb)_2(\mu\text{-}N_2)$ in the absence of aromatic solvent failed, thus the identity of any new species remains undetermined.

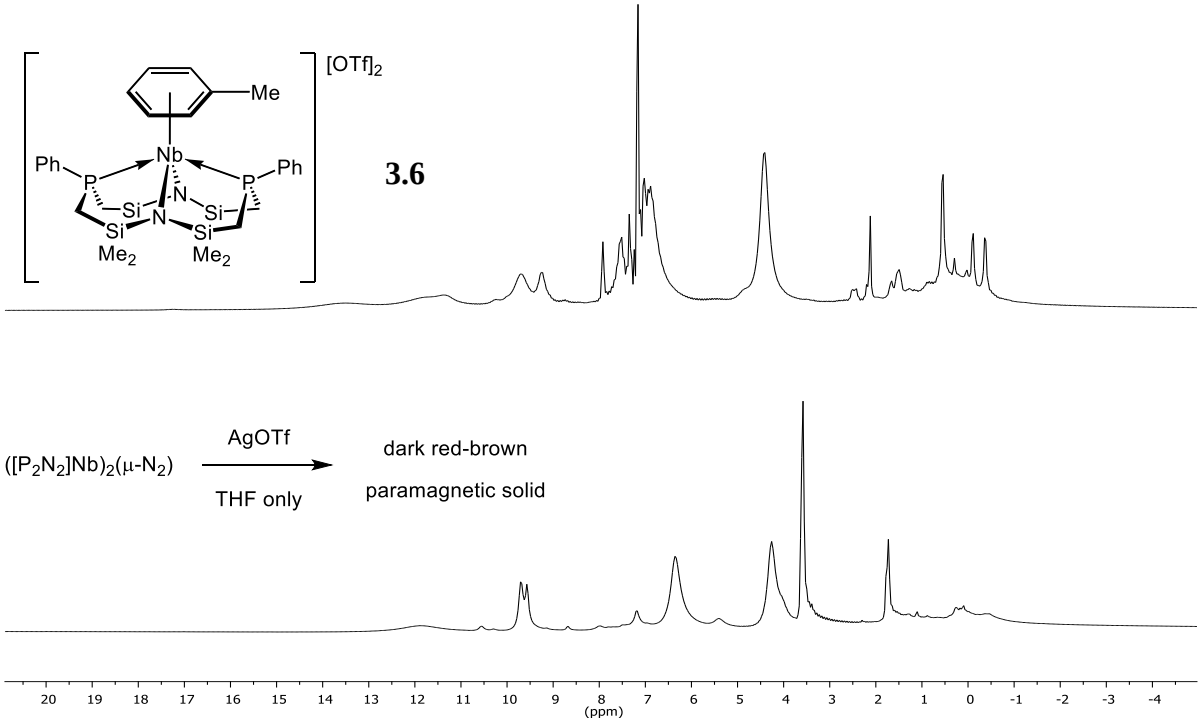

Figure 3.9 Comparison of the paramagnetic ^{1}H NMR (400 MHz) spectrum of **3.6** (top, C_6D_6) to that of the dark red-brown material isolated from the reaction of AgOTf and $([P_2N_2]Nb)_2(\mu\text{-}N_2)$ in the absence of aromatic solvent (bottom, THF-d_8).

Ferrocenium salts are considered mild one-electron oxidants that are easily handled. The ferrocene ($FeCp_2$) byproduct (observed in ^{1}H NMR spectroscopy as a singlet at 4.0 ppm) can be

removed by simply washing the product with nonpolar solvent such as hexane. Treatment of $([P_2N_2]Nb)_2(\mu\text{-}N_2)$ with oxidants such as ferrocenium tetraphenylborate ($[FeCp_2][BPh_4]$) and ferrocenium tetrafluoroborate ($[FeCp_2][BF_4]$) was explored. After stirring a THF solution of $([P_2N_2]Nb)_2(\mu\text{-}N_2)$ and $[FeCp_2][BPh_4]$ for 20 hours with no obvious colour change observed, the mixture was heated to 90 °C for 12 h. The presence of ferrocene in the ^{1}H NMR spectrum of the reaction mixture indicated that some oxidation/reduction occurred. The isolated maroon solid showed broad resonances in the paramagnetic ^{1}H NMR spectrum. The structure and identity of this material was not realized due to failure to obtain crystals for X-ray diffraction studies.

The reaction between $([P_2N_2]Nb)_2(\mu\text{-}N_2)$ and $[FeCp_2][BF_4]$ produced a dark yellow-brown solid that showed broad peaks in the paramagnetic ^{1}H NMR spectrum. The resulting solid residue was washed with hexane and yellow solid isolated from the hexane wash was assigned as ferrocene on the basis of ^{1}H NMR spectroscopy. Crystals isolated from a THF/hexane solution of the remaining material were subjected to X-ray diffraction studies (Figure 3.10). Loss of coordinated N_2 has occurred to form $[([P_2N_2]Nb)_2((\mu\text{-}F)_3)][BF_4]$ (**3.7**), with three fluorides bridging the two Nb centres. Each Nb centre is seven-coordinate, displaying a distorted, capped trigonal prismatic geometry. This structural motif has been observed in NbF_7^{2-} complexes.[117-118] The Nb–F bond lengths in **3.7** are comparable to those observed for a dinuclear niobium oxide NHC complex containing two bridging fluorides (Nb–F bonds of 1.9952(12), 2.3193(12), 1.9915(12) and 2.3632(13) Å),[119] one of the few crystallographic examples of a complex with a related bonding arrangement. Both Nb centres in **3.7** are formally assigned as Nb(IV), each having one unpaired d electron, supporting the spectroscopically observed paramagnetic nature of this complex.

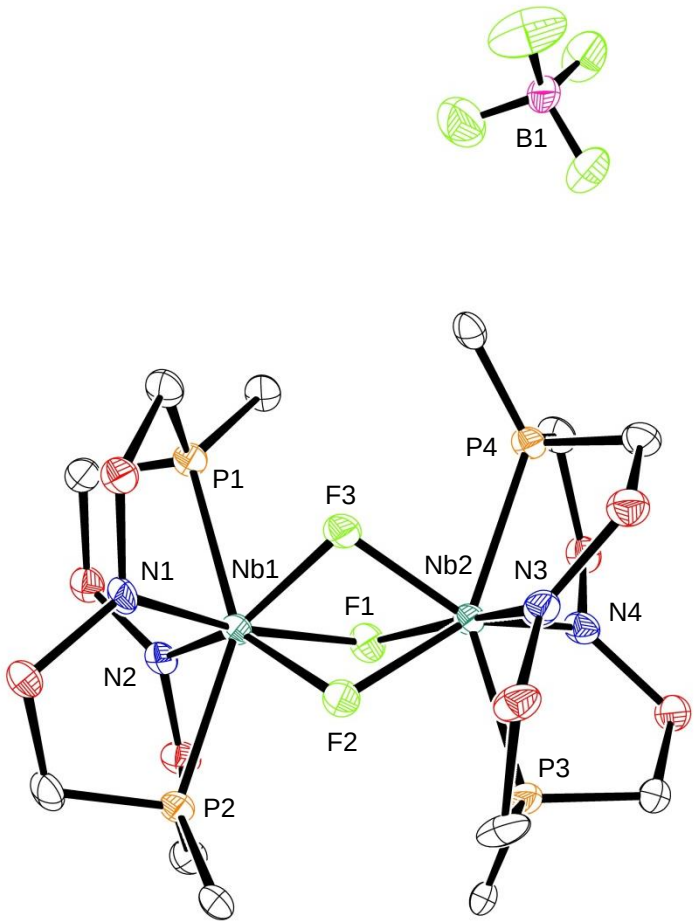

Figure 3.10 ORTEP depiction (ellipsoids at 50 % probability) of $[([P_2N_2]Nb)_2(\mu\text{-}F)_3][BF_4]$ (**3.7**). Silyl methyl and P-phenyl ring carbons other than ipso are omitted for clarity. Selected bond lengths (Å) and angles (°): Nb1–F1, 2.144(4); Nb1–F2, 2.133(4); Nb1–F3, 2.153(4); Nb2–F1, 2.175(4); Nb2–F2, 2.172(3); Nb2–F3, 2.143(4); F1–Nb1–F2, 69.91(13); F1–Nb1–F3, 69.47(13); F2–Nb1–F3, 65.78(13); F1–Nb2–F2, 68.62(13); F1–Nb2–F3, 69.08(14); F2–Nb2–F3, 65.28(13); Nb1–F1–Nb2, 99.11(14); Nb1–F2–Nb2, 99.52(14); Nb1–F3–Nb2, 99.82(14).

3.3.3 Treatment of $([P_2N_2]Nb)_2(\mu\text{-}N_2)$ with oxygen-containing reagents

Investigation into the reactivity of $([P_2N_2]Nb)_2(\mu\text{-}N_2)$ toward oxygen-containing oxidants was also pursued. Pyridine N-oxide is a known oxidizing agent that has shown utility in organic synthesis reactions.[120-121] Upon addition of a THF solution of pyridine n-oxide to a solution of

$([P_2N_2]Nb)_2(\mu\text{-}N_2)$ in THF, a colour change from dark brown to dark blue was observed. Upon removal of the volatiles, a dark blue solid was isolated, exhibiting broad resonances in the paramagnetic ^{1}H NMR spectrum. Crystals isolated from a hexane solution of the blue material were subjected to X-ray diffraction studies, revealing a disordered structure of the starting $([P_2N_2]Nb)_2(\mu\text{-}N_2)$. Given the failure to produce other crystalline material and identify the structure of a new product, this experiment was not pursued further.

DMSO is another commonly known oxidant that is also often employed as an oxygen donor.[121-123] Addition of a THF solution of DMSO to a solution of $([P_2N_2]Nb)_2(\mu\text{-}N_2)$ in THF produced a colour change from dark brown to dark magenta. Broad peaks were observed in the paramagnetic ^{1}H NMR spectrum of the dark magenta material isolated. Multiple repetitions of this reaction and various crystallization strategies failed to produce X-ray quality crystals, thus the structure and identity of this material remains elusive.

The free radical 2,2,6,6-tetramethyl-1-piperidinyloxy (TEMPO) is broadly utilized in a number of organic oxidation reactions.[124] Transition metal TEMPO complexes are known, including one derived from treatment of an N_2 complex with TEMPO.[125-126] Treatment of $([P_2N_2]Nb)_2(\mu\text{-}N_2)$ with TEMPO generated a dark red-brown material that was found to be diamagnetic. A very broad resonance at δ 11.5 was observed in the $^{31}P\{^1H\}$ NMR spectrum. The ^{1}H NMR spectrum showed eight silyl methyl resonances, indicating this species has low symmetry. Slow evaporation of a THF solution of this material yielded a small amount of crystals suitable for X-ray diffraction studies; the solid state molecular structure was determined (Figure 3.11). The bonding arrangement of the N_2 unit has changed from bridging end-on to bridging side-on in $([P_2N_2]Nb)_2(\mu\text{-}\eta^2\text{:}\eta^2\text{-}N_2)(\mu\text{-}O)$ (**3.8**), with the addition of an oxo ligand bridging the two niobium centres. The N5–N6 bond length of 1.352(5) Å in **3.8** is elongated

from the N–N bond length of 1.272(5) Å in $([P_2N_2]Nb)_2(\mu\text{-}N_2)$. The Nb1⋯Nb2 distance of 2.9673(4) Å is outside the bonding range that is typically observed in complexes containing Nb–Nb bonds,[127-128] indicating that a Nb–Nb bond in **3.8** is unlikely. The N_2 moiety can be considered a N_2^{4-} unit, consistent with the formal assignment of each niobium centre as Nb(V).

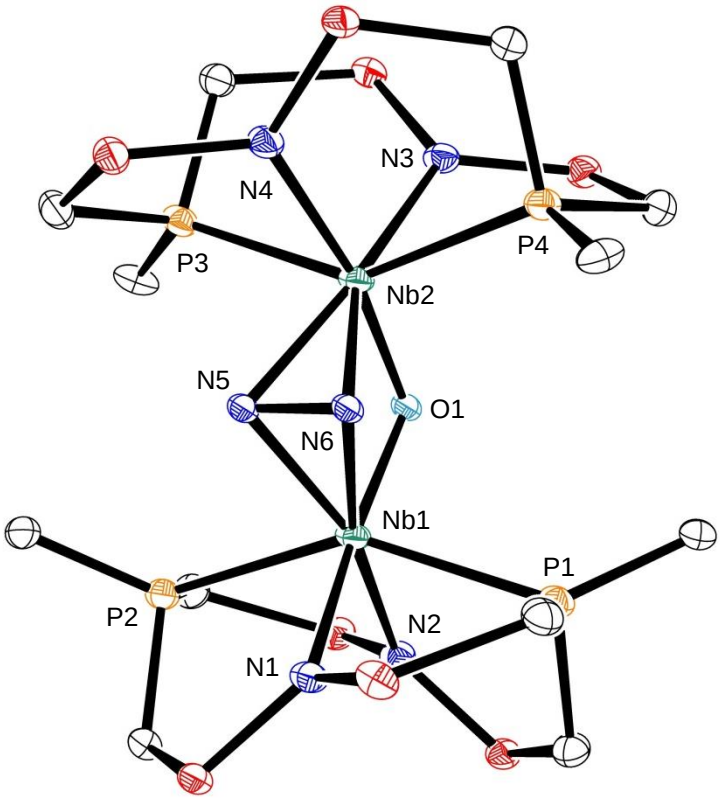

Figure 3.11 ORTEP depiction (ellipsoids at 50 % probability) of $([P_2N_2]Nb)_2(\mu\text{-}\eta^2{:}\eta^2\text{-}N_2)(\mu\text{-}O)$ (**3.8**). Silyl methyl and P-phenyl ring carbons other than ipso are omitted for clarity. Selected bond lengths (Å) and angles (°): Nb1⋯Nb2, 2.9673(4); N5–N6, 1.352(5); Nb1–N5, 2.123(4); Nb1–N6, 2.137(4); Nb2–N5, 2.140(3); Nb2–N6, 2.128(4); Nb1–O1, 1.957(3); Nb2–O1, 1.950(3); Nb1–O1–Nb2, 98.82(13); Nb1–N5–Nb2 88.22(14); Nb1–N6–Nb2, 88.18(15).

The bonding parameters in the Nb(μ-η^2:η^2-N_2)(μ-O)Nb unit of **3.8** are comparable to those observed in a Nb calix[4]arene complex that contains a similar bridging side-on N_2 and bridging oxo bonding arrangement (N−N bond length, 1.424(5) Å; Nb···Nb separation, 2.876(9) Å; Nb−N bond lengths, average 2.058(7) Å; Nb−O(oxo) bond lengths, 1.961(3) and 1.909(4) Å; Nb−O−Nb angle, 96.0(1)°).[129] Comparatively, pyridine N-oxide is the source of the oxo ligand in the analogous Nb calix[4]arene complex, which is also derived from a bridging end-on N_2 complex similar to $([P_2N_2]Nb)_2(\mu\text{-}N_2)$.

3.4 Synthesis of $([P_2N_2]V)_2(\mu\text{-}N_2)$

In a similar fashion to the preparation of $([P_2N_2]Nb)_2(\mu\text{-}N_2)$, the vanadium analogue $([P_2N_2]V)_2(\mu\text{-}N_2)$ has previously been synthesized.[105] The synthesis of $([P_2N_2]V)_2(\mu\text{-}N_2)$ and the antecedent $[P_2N_2]VCl$ is reported here with accompanying crystallographic data as supporting evidence that these paramagnetic complexes are isolable. Treatment of *syn*-$[P_2N_2]Li_2$ with $VCl_3(THF)_3$ afforded $[P_2N_2]VCl$ as an orange crystalline solid in good yield. Broad resonances were observed in the paramagnetic ^{1}H NMR spectrum. Single crystals of $[P_2N_2]VCl$ were obtained and the structure was confirmed via X-ray diffraction studies. The solid state molecular structure of $[P_2N_2]VCl$ (not previously reported) is illustrated in Figure 3.12. The structure of $[P_2N_2]VCl$ displays a distorted trigonal bipyramidal geometry about the vanadium centre.

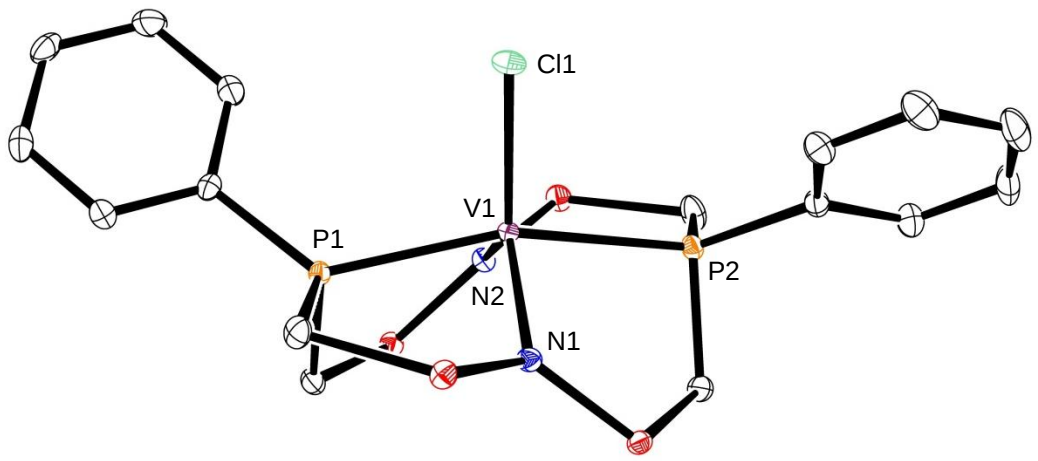

Figure 3.12 ORTEP depiction (ellipsoids at 50 % probability) of $[P_2N_2]VCl$. Silyl methyl carbons are omitted for clarity. Selected bond lengths (Å) and angles (°): V1–Cl1, 2.2945(6); V1–N1, 1.9731(18); V1–N2, 1.9755(17); V1–P1, 2.4907(7); V1–P2, 2.4578(7); N1–V1–Cl1, 124.54(6); N2–V1–Cl1, 119.00(6); N1–V1–N2, 116.39(8); P1–V1–P2, 161.45(2); N1–V1–P1, 82.07(6); N2–V1–P1, 89.17(5); N1–V1–P2, 87.01(5); N2–V1–P2, 82.29(5); P1–V1–Cl1, 100.88(2); P2–V1–Cl1, 97.66(2).

Reduction of $[P_2N_2]VCl$ with KC_8 under 4 atm of N_2 generates $([P_2N_2]V)_2(\mu\text{-}N_2)$ as a purple solid in good yield (Scheme 3.5). The paramagnetic ^{1}H NMR spectrum of $([P_2N_2]V)_2(\mu\text{-}N_2)$ displays broad resonances. The solid state molecular structure of $([P_2N_2]V)_2(\mu\text{-}N_2)$ was verified by X-ray diffraction studies (Figure 3.13). The bonding parameters of $([P_2N_2]V)_2(\mu\text{-}N_2)$ are analogous to those seen in $([P_2N_2]Nb)_2(\mu\text{-}N_2)$ and similar to observed metrics in a previously obtained structure of $([P_2N_2]V)_2(\mu\text{-}N_2)$.[105] The N–N bond length (1.206(14) Å) and V–N bond lengths (1.793(10) and 1.790(10) Å) in $([P_2N_2]V)_2(\mu\text{-}N_2)$ are consistent with those seen in dinuclear vanadium complexes containing an end-on bridging N_2 unit.[130-135]

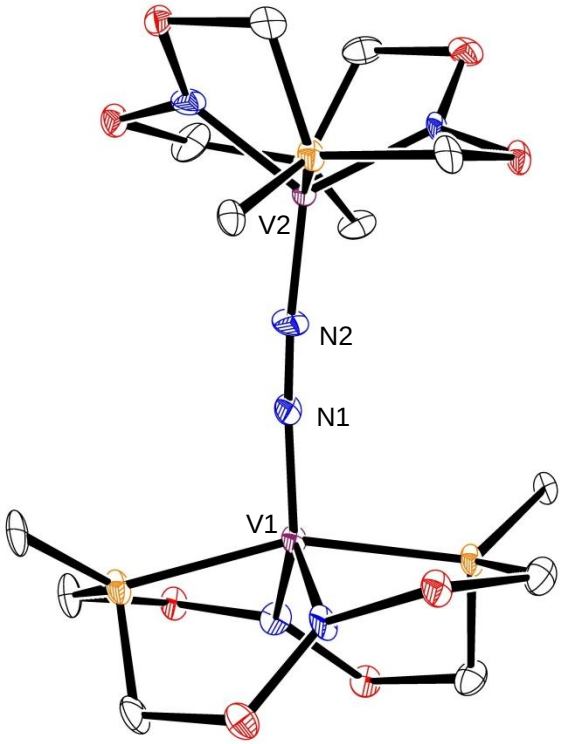

Figure 3.13 ORTEP depiction (ellipsoids at 50 % probability) of $([P_2N_2]V)_2(\mu\text{-}N_2)$. Silyl methyl and P-phenyl ring carbons other than ipso are omitted for clarity. Selected bond lengths (Å) and angles (°): N1–N2, 1.206(14); V1–N1, 1.793(10); V2–N2, 1.790(10); V1–N1–N2, 175.2(9); N1–N2–V2 172.9(9).

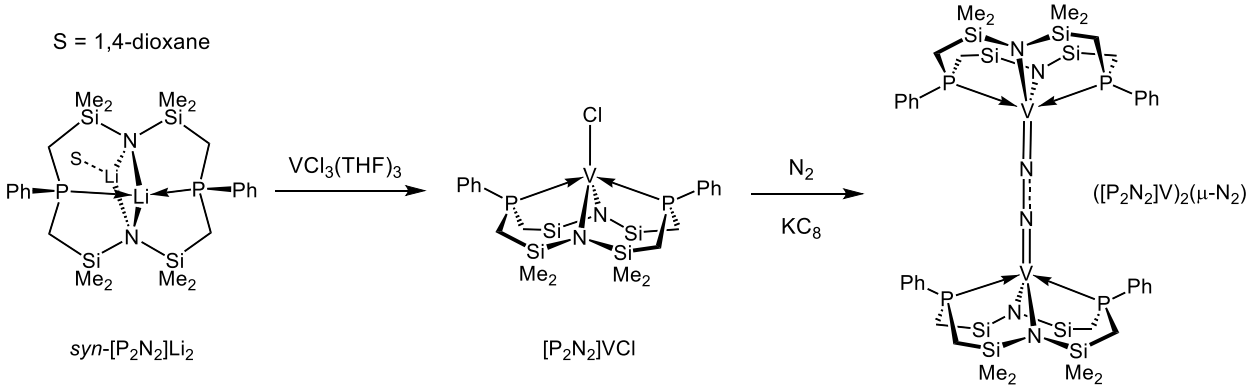

Scheme 3.5

3.5 Reactivity of $([P_2N_2]V)_2(\mu\text{-}N_2)$ with electrophiles and oxidants

By way of comparison, the thermolysis of $([P_2N_2]V)_2(\mu\text{-}N_2)$ was tested in the same manner as the thermolysis of $([P_2N_2]Nb)_2(\mu\text{-}N_2)$ that produces complex **3.1**, in an effort to observe the analogous vanadium nitride species. Upon heating a toluene solution of $([P_2N_2]V)_2(\mu\text{-}N_2)$ overnight at 110 °C, the solution appeared to change colour from dark purple to dark brown. However, upon cooling, the solution appeared dark purple once again. The resonances in the paramagnetic ^{1}H NMR spectrum of the isolated dark purple material matched that of the starting $([P_2N_2]V)_2(\mu\text{-}N_2)$ species. Given that $([P_2N_2]V)_2(\mu\text{-}N_2)$ did not prove reactive under these conditions, the thermolysis of $([P_2N_2]V)_2(\mu\text{-}N_2)$ in the presence of Lewis acids was not investigated. In analogy to the reactivity of $([P_2N_2]Nb)_2(\mu\text{-}N_2)$ with various electrophiles/oxidants, concurrent reactivity studies of $([P_2N_2]V)_2(\mu\text{-}N_2)$ with similar reagents was pursued. This section focuses on the treatment of $([P_2N_2]V)_2(\mu\text{-}N_2)$ with selected electrophiles/oxidants.

3.5.1 Treatment of $([P_2N_2]V)_2(\mu\text{-}N_2)$ with 1,2-diiodoethane

Treatment of $([P_2N_2]V)_2(\mu\text{-}N_2)$ with 1,2-diiodoethane ($I\text{-}CH_2CH_2\text{-}I$) was hypothesized to afford the vanadium analogue of **3.5**, $([P_2N_2]VI)_2(\mu\text{-}N_2)$. Addition of $I\text{-}CH_2CH_2\text{-}I$ to a toluene solution $([P_2N_2]V)_2(\mu\text{-}N_2)$ resulted in a slow colour change from dark purple to clear orange-pink. A light pink paramagnetic solid was isolated; crystals of this material were subjected to X-ray diffraction studies. Figure 3.14 shows the solid state molecular structure of this material as $[P_2N_2]VI$ (**3.9**). In contrast to the Nb congener **3.5**, N_2 loss has occurred to simply generate the vanadium iodide species **3.9** (Scheme 3.6). The bonding in **3.9** is similar to $[P_2N_2]VCl$, showing a distorted trigonal bipyramidal geometry around the vanadium centre. The magnetic moment of

3.9 (μ_{eff} = 2.64 μ_B) indicates the presence of 2 unpaired electrons, consistent with the formal assignment of a d^2 V(III) species.

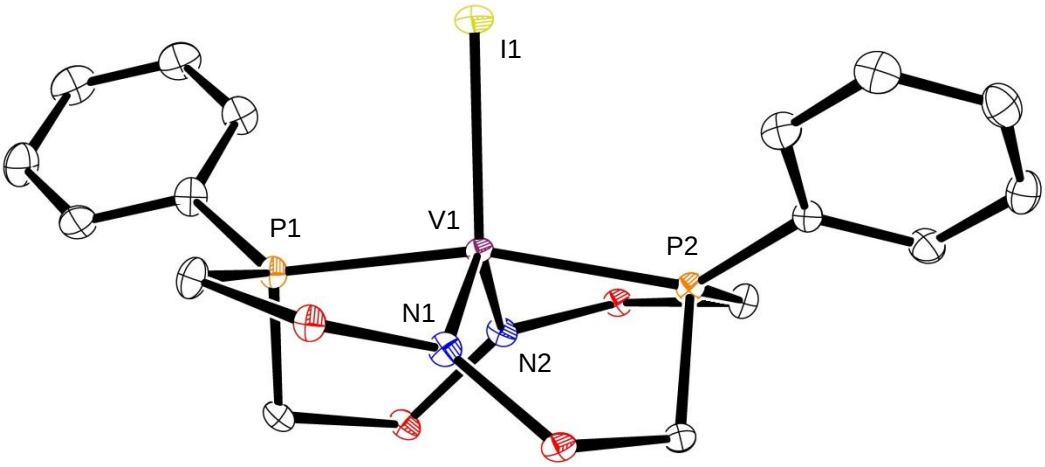

Figure 3.14 ORTEP depiction (ellipsoids at 50 % probability) of $[P_2N_2]$VI (**3.9**). Silyl methyl carbons are omitted for clarity. Selected bond lengths (Å) and angles (°): V1–I1, 2.6788(12); V1–N1, 1.965(6); V1–N2, 1.966(5); V1–P1, 2.4874(19); V1–P2, 2.4624(19); N1–V1–I1, 115.96(16); N2–V1–I1, 128.43(17); N1–V1–N2, 115.5(2); P1–V1–P2, 163.90(7); N1–V1–P1, 90.73(17); N2–V1–P1, 82.25(16); N1–V1–P2, 82.79(16); N2–V1–P2, 87.25(16); P1–V1–I1, 100.06(5); P2–V1–I1, 96.02(5).

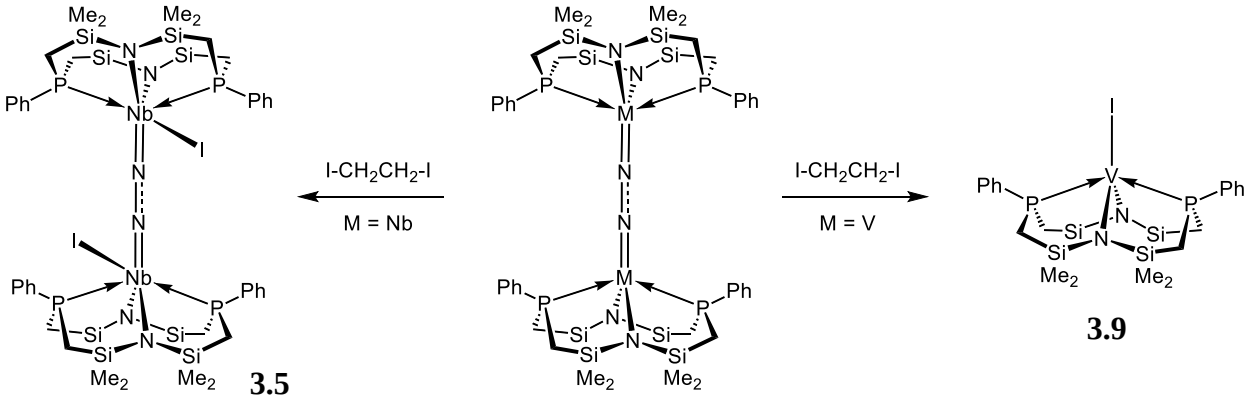

Scheme 3.6

3.5.2 Treatment of $([P_2N_2]V)_2(\mu\text{-}N_2)$ with silver tetraphenylborate

Addition of $AgBPh_4$ to $([P_2N_2]Nb)_2(\mu\text{-}N_2)$ consistently produced crystalline material, although the structure and identity of this material remains elusive. The treatment of $([P_2N_2]V)_2(\mu\text{-}N_2)$ with $AgBPh_4$ was investigated in an effort to produce some oxidized dinitrogen species such as $[([P_2N_2]V)_2(\mu\text{-}N_2)][BPh_4]$ that could be easily crystallized. The reaction of $AgBPh_4$ with $([P_2N_2]V)_2(\mu\text{-}N_2)$ in THF produced a cloudy green-brown solution. Removal of the insoluble solids (Ag^0) via filtration gave a clear green solution, affording isolation of a green paramagnetic solid in excellent yield. Green crystals of this material were obtained and X-ray diffraction studies revealed loss of the N_2 unit and coordination of two THF molecules to form $[([P_2N_2]V)(THF)_2][BPh_4]$ (**3.10**) (Equation 3.1).

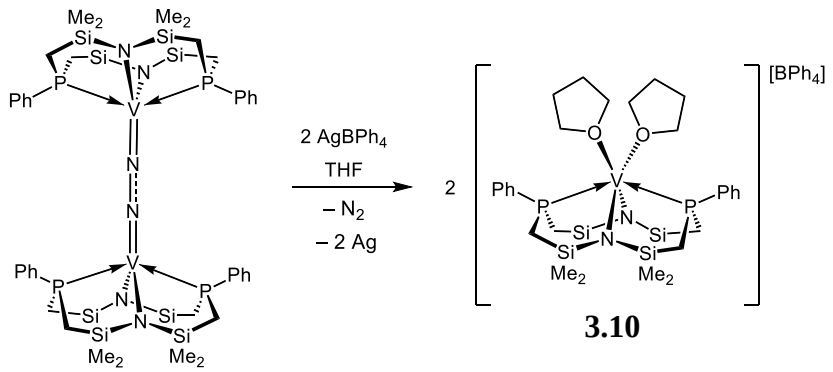

[3.1]

Similar reactivity has previously been observed with a dinuclear yttrium N_2 complex that showed loss of N_2 and coordination of THF upon reaction with $AgBPh_4$.[125] The solid state molecular structure of **3.10** is shown in Figure 3.15. Complex **3.10** has a distorted octahedral geometry about the vanadium centre. The N1–V1–O2, O1–V1–N2, and P1–V1–P2 bond angles (166.91(18)°, 167.78(18)° and 171.08(6)° respectively) demonstrate the distortion from idealized octahedral symmetry. The magnetic moment of 2.64 μ_B is consistent with the formal assignment of **3.10** as a d^2 V(III) species.

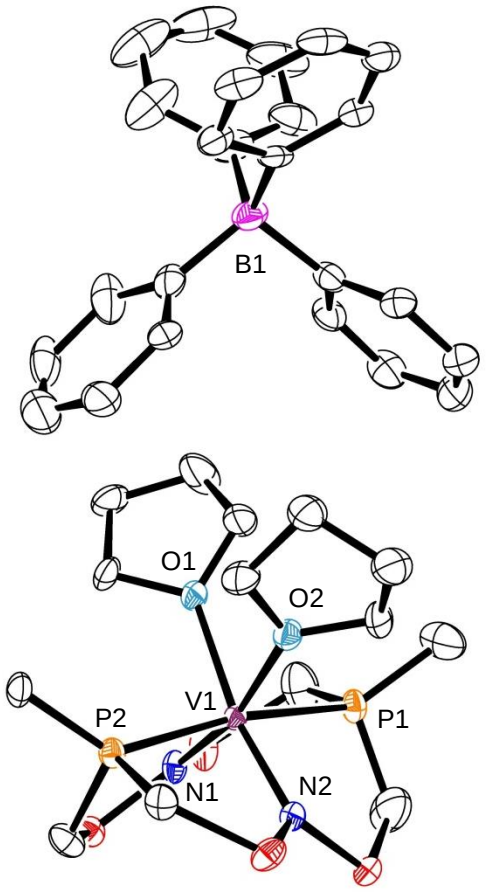

Figure 3.15 ORTEP depiction (ellipsoids at 50 % probability) of [([P_2N_2]V)(THF)$_2$][BPh_4] (**3.10**). Silyl methyl and P-phenyl ring carbons other than ipso are omitted for clarity. Selected bond lengths (Å) and angles (°): V1–N1, 2.008(5); V1–N2, 1.987(5); V1–P1, 2.5460(17); V1–P2, 2.5283(17); V1–O1, 2.194(4); V1–O2, 2.165(4); N1–V1–O2, 166.91(18); O1–V1–N2, 167.78(18); P1–V1–P2, 171.08(6).

3.5.3 Treatment of ([P_2N_2]V)$_2$(μ-N_2) with other oxidants

Exploration into the reactivity of ([P_2N_2]V)$_2$(μ-N_2) with other oxidants proved largely unfruitful. Upon addition of a suspension of [$FeCp_2$][BF_4] in THF to a THF solution of ([P_2N_2]V)$_2$(μ-N_2), a colour change from dark purple to dark yellow-green was observed. The green material isolated showed broad peaks in the paramagnetic ^{1}H NMR spectrum, differing

from the resonances of the starting $([P_2N_2]V)_2(\mu\text{-}N_2)$ (Figure 3.16). Attempts to grow crystals of this material were ultimately unsuccessful, thus the identity and structure remains undetermined.

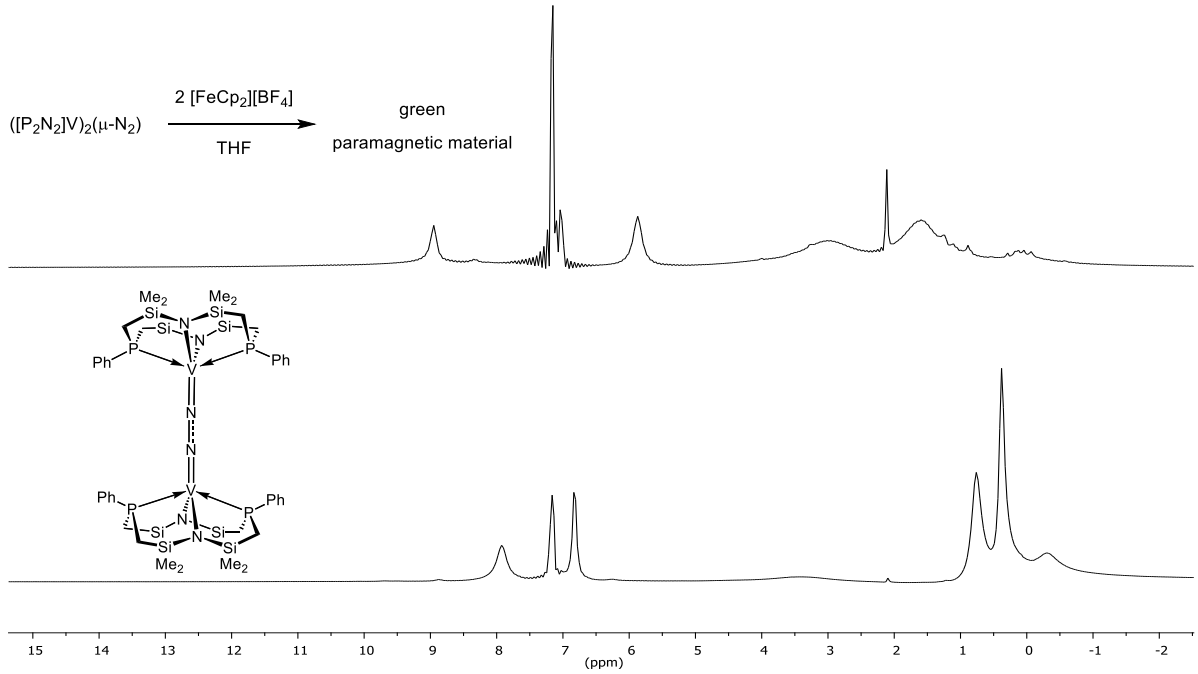

Figure 3.16 Comparison of the paramagnetic ^{1}H NMR (400 MHz, C_6D_6) spectrum of the material isolated from the reaction of $([P_2N_2]V)_2(\mu\text{-}N_2)$ with $[FeCp_2][BF_4]$ (top) to that of the starting $([P_2N_2]V)_2(\mu\text{-}N_2)$ (bottom).

Treatment of $([P_2N_2]V)_2(\mu\text{-}N_2)$ with pyridine N-oxide did not yield an obvious colour change, suggesting no reactivity occurred. However, the paramagnetic ^{1}H NMR spectrum of the dark purple material shows the appearance of different resonances from the starting $([P_2N_2]V)_2(\mu\text{-}N_2)$ (Figure 3.17). The identity of this material remains unverified, leaving the outcome of this experiment unclear. Futhermore, unlike the reaction of $([P_2N_2]Nb)_2(\mu\text{-}N_2)$ with TEMPO that produced complex **3.8**, the analogous $([P_2N_2]V)_2(\mu\text{-}N_2)$ showed no reaction when treated with TEMPO, even upon heating.

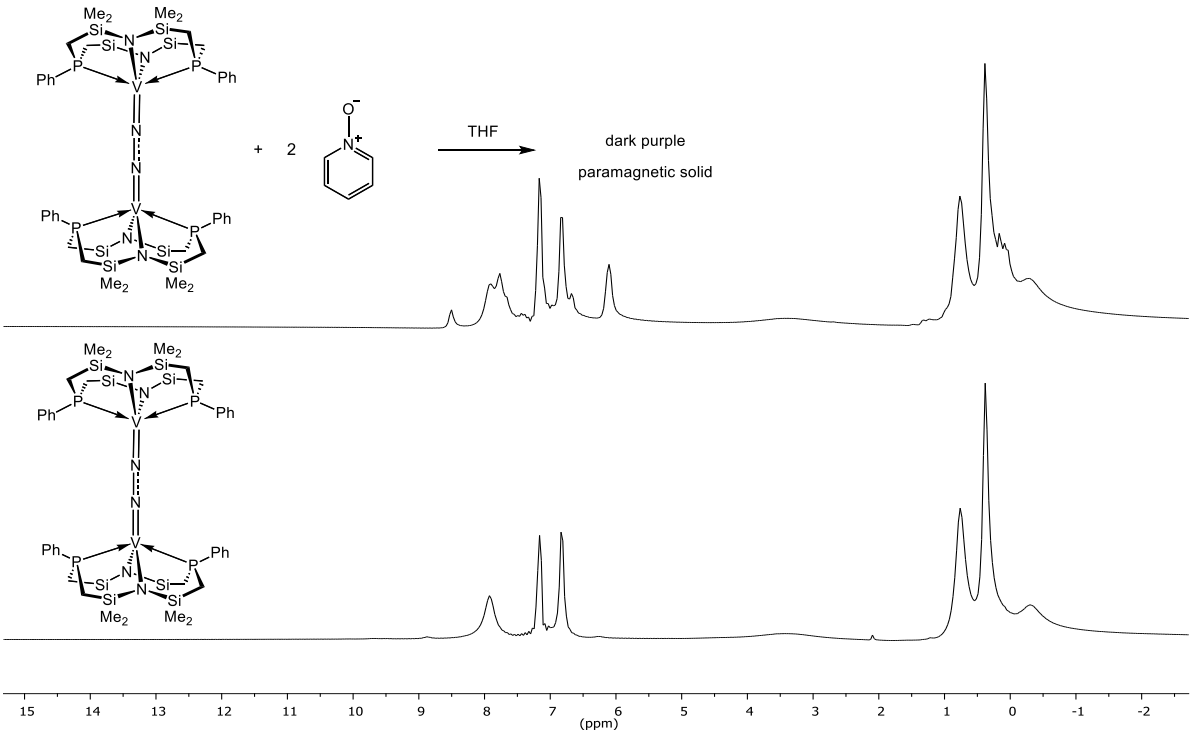

Figure 3.17 Comparison of the paramagnetic ^{1}H NMR (400 MHz, C_6D_6) spectrum of the dark purple material isolated from the treatment of $([P_2N_2]V)_2(\mu\text{-}N_2)$ with pyridine N-oxide (top) to that of the starting $([P_2N_2]V)_2(\mu\text{-}N_2)$ (bottom).

3.6 Synthesis of $[P_2N_2]VMe$

Previously reported work showed that $[P_2N_2]NbCl$ undergoes reactivity with methylmagnesium chloride (MeMgCl) to form the Nb methyl species $[P_2N_2]NbMe$.[62] Under dinitrogen atmosphere, $[P_2N_2]NbMe$ spontaneously reacts with N_2 to form the corresponding dinuclear niobium complex $([P_2N_2]NbMe)_2(\mu\text{-}N_2)$ (**1.24**) containing an end-on bridging N_2 unit (Scheme 3.7).[62] The formation of the analogous vanadium methyl species was investigated in an effort to determine if an oxidized vanadium N_2 species could be accessed by this method.

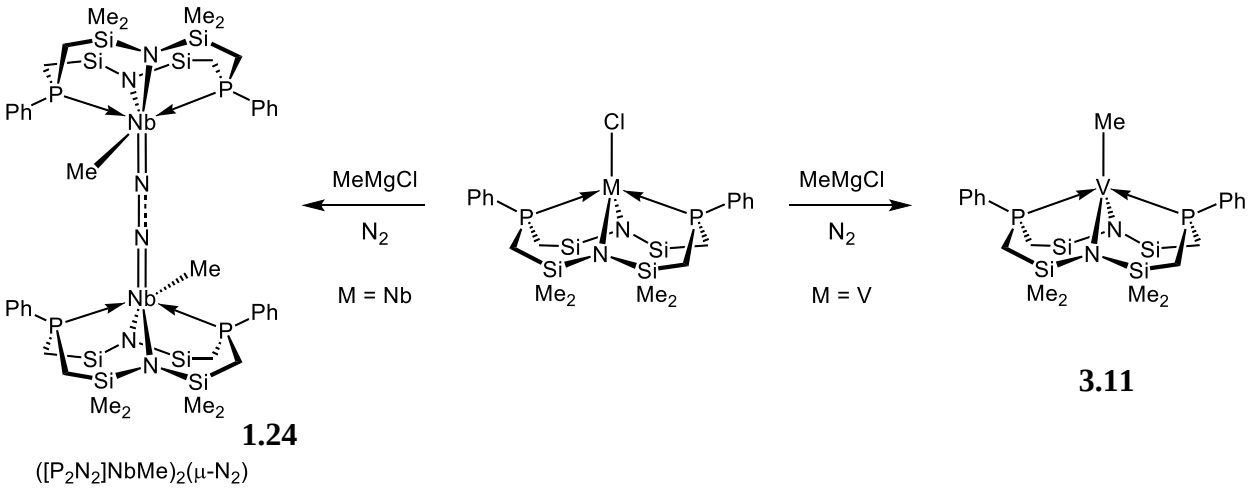

Scheme 3.7

The reaction of $[P_2N_2]$VCl with MeMgCl under N_2 generated an olive green paramagnetic material. Single crystals suitable for X-ray diffraction studies were isolated from a hexamethyldisiloxane (HMDSO) solution of this material and the structure was confirmed as $[P_2N_2]$VMe (**3.11**) (Scheme 3.7). The solid state molecular structure of **3.11** is illustrated in Figure 3.18. Complex **3.11** displays a distorted trigonal bipyramidal geometry around the vanadium centre, demonstrated by the P1–V1–P2 bond angle (162.956(16)°). The V1–C1 bond length of 2.1053(16) Å in **3.11** is consistent with other vanadium methyl species.[136-137] Magnetic moment measurements (μ_{eff} = 2.69 μ_B) indicate the presence of 2 unpaired electrons, supporting the formal assignment of **3.11** as a d^2 V(III) species. Although the $[P_2N_2]$VMe complex can be formed, spontaneous reactivity with N_2 was not observed. Exactly why $[P_2N_2]$-coordinated vanadium forms a stable methyl complex whereas the $[P_2N_2]$ niobium methyl complex is labile remains unclear.

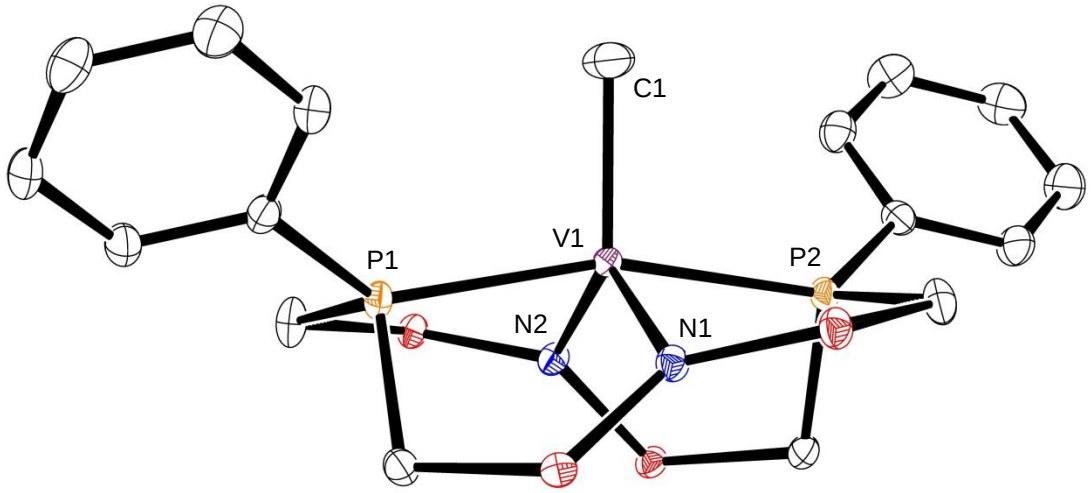

Figure 3.18 ORTEP depiction (ellipsoids at 50 % probability) of $[P_2N_2]VMe$ (**3.11**). Silyl methyl carbons are omitted for clarity. Selected bond lengths (Å) and angles (°): V1–C1, 2.1053(16); V1–N1, 2.0018(12); V1–N2, 2.0047(12); V1–P1, 2.4770(4); V1–P2, 2.4913(4); P1–V1–P2, 162.956(16); N1–V1–C1, 122.72(6); N2–V1–C1, 119.60(6); N1–V1–N2, 117.66(5); N1–V1–P1, 87.76(4); N2–V1–P1, 82.68(4); N1–V1–P2, 82.23(4); N2–V1–P2, 89.77(4); P1–V1–C1, 97.84(5); P2–V1–C1, 99.17(5).

3.7 Conclusions

The goal of this chapter was to explore reactivity of the paramagnetic niobium and vanadium dinitrogen complexes $([P_2N_2]Nb)_2(\mu\text{-}N_2)$ and $([P_2N_2]V)_2(\mu\text{-}N_2)$. Investigation of the thermolysis of $([P_2N_2]Nb)_2(\mu\text{-}N_2)$ in the presence of assorted Lewis acids has produced a variety of deeply coloured paramagnetic materials. Outcomes range from no reactivity with the Lewis acid (observed with BEt_3) to oxidation (found with Piers' borane) to N–N bond cleavage and functionalization, as seen with the organoaluminum reagents. Treatment of $([P_2N_2]Nb)_2(\mu\text{-}N_2)$ and $([P_2N_2]V)_2(\mu\text{-}N_2)$ with other electrophiles and oxidants also produced a variety of colourful paramagnetic materials. Reaction with $I\text{-}CH_2CH_2\text{-}I$ led to the formation of a new niobium N_2 complex $([P_2N_2]NbI)_2(\mu\text{-}N_2)$, in contrast to the formation of $[P_2N_2]VI$ in the case of vanadium.

Oxidation with silver salts generated a niobium arene complex **3.6** and a V(III) THF adduct $[([P_2N_2]V)(THF)_2][BPh_4]$. The ferrocenium salt $[FeCp_2][BF_4]$ reacts with $([P_2N_2]Nb)_2(\mu\text{-}N_2)$, displacing N_2 to produce a dinuclear Nb(IV)-Nb(IV) species (**3.7**) bridged by three fluorides. A vanadium methyl species (**3.11**) was produced in the pursuit of forming a new vanadium N_2 complex; however, no such N_2 species was realized. Affirming the identity of the products in these reactions has proven challenging and no discernible pattern of reactivity has emerged. Loss of the N_2 unit was commonly observed, far from the idealized outcome of observing oxidized N_2 species or cleavage and functionalization of the N_2 moiety as a result of further reactivity.

Treatment of $([P_2N_2]Nb)_2(\mu\text{-}N_2)$ with the oxygen-containing radical TEMPO resulted in a new diamagnetic niobium N_2 complex (**3.8**) whereby the N_2 unit is bound side-on, in addition to containing a bridging oxo ligand. While most single electron oxidants proved unfruitful or engaged in undesirable ligand exchange reactions, the 2 electron oxidant TEMPO achieved the desired goal of altering the electronic structure of the N_2 complex.

Chapter 4: Synthesis and reactivity of paramagnetic [P_2N_2] cobalt complexes

4.1 Introduction

Increasing interest in the chemistry of cobalt complexes can be attributed to the emergent focus on finding sustainable catalysts that incorporate earth-abundant base metals (such as Fe, Co, or Ni).[138] As an alternative to catalyst systems utilizing expensive precious metals (such as Ir, Ru, Rh, Pd, and Pt), base metals are more desirable from a sustainability perspective due to their abundance and effective low cost. Large-scale industrial applications of catalysis could thus benefit greatly from base-metal options, considering the low abundance and high cost associated with precious metals is ultimately prohibitive at that scale. In addition, differing electronic structural properties of base-metal complexes compared to precious metal complexes could prove advantageous and potentially lead to novel reactivity.[139-140]

Recent exploration into base metal catalysis has shown that cobalt complexes can be employed in a variety of catalytic transformations. For example, cobalt pyridine-diimine (PDI) complexes are active catalysts in olefin hydrogenation.[141] In particular, asymmetric hydrogenation of alkenes has been observed using PDI cobalt alkyl and cyclometalated complexes (Chart 4.1).[142]

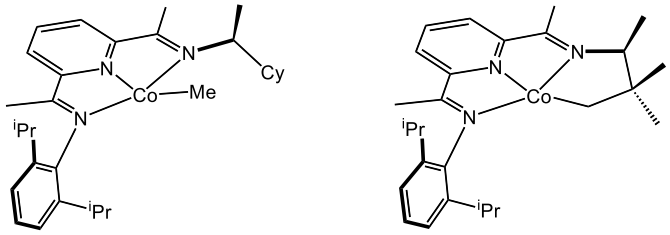

Chart 4.1 PDI cobalt precatalysts employed in asymmetric hydrogenation of alkenes.[142]

Catalytic alkene hydrogenation is also observed in a series of bis(phosphine)cobalt dialkyl complexes.[143] Hydrogenation of alkenes, ketones, aldehydes, and imines has been accomplished with cobalt alkyl and hydride complexes coordinated to a diphosphinoamine ligand (Chart 4.2).[144-145]

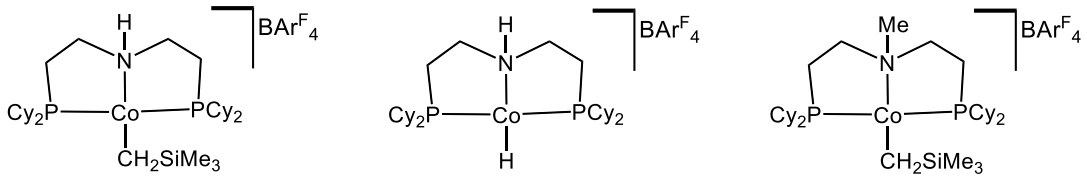

Chart 4.2 Diphosphinoamine cobalt alkyl and hydride complexes utilised as precatalysts.[144-145]

In addition to the hydrogenation of aldehydes and ketones,[146] a series of cobalt complexes stabilized by pincer ligands has proven active in the catalytic alkylation of aromatic amines and unactivated amides and esters by alcohols (Chart 4.3).[147-148] Lastly, a β-diketiminate cobalt(II) alkyl complex has been reported to selectively catalyze the isomerization of terminal alkenes to 2-alkenes with Z-stereochemistry, a rare transformation.[149]

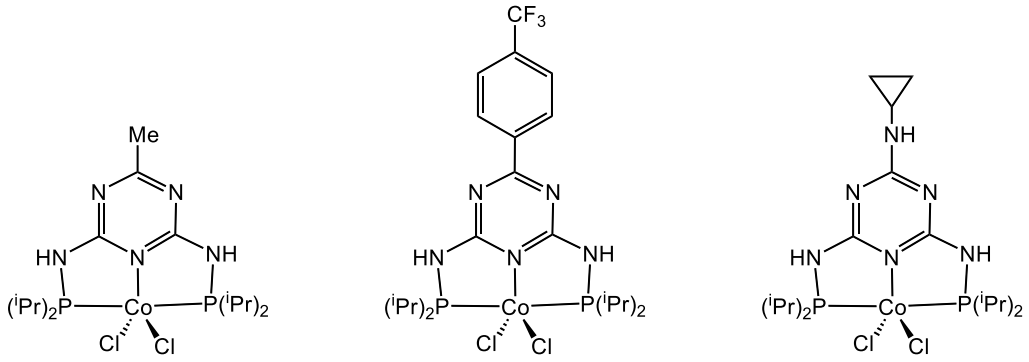

Chart 4.3 Cobalt dichloride precatalysts applied in hydrogenation and alkylation reactions.[146-148]

While these examples highlight success towards active cobalt catalyst systems, they also represent the challenges that one must overcome in pursuing base-metal research. Precious metal catalyst systems typically rely on two-electron oxidative addition and reductive elimination processes, which are less commonly observed using base-metals.[140] Furthermore, cobalt and iron complexes are frequently paramagnetic in nature,[83, 86, 150-151] introducing potential difficulties in the identification and characterization of active and intermediate species. In this respect, it is of interest to explore chemical space by pursuing the synthesis and characterization of novel paramagnetic cobalt complexes.

Although the exploration of catalytic processes utilizing cobalt was never a goal of this work, one-electron processes involving cobalt complexes was of interest. Investigation of paramagnetic cobalt complexes containing amidophosphine ligand sets has previously been pursued.[83, 152] Scheme 4.1 shows the synthesis of a [PNP] cobalt chloride complex and subsequent reactivity, generating [PNP] cobalt alkyl complexes and [PNP] cobalt halide complexes. One-electron oxidation of Co(II) to Co(III) by alkyl halides was observed, such as in the reaction of a [PNP] cobalt(II) chloride complex with benzyl chloride ($PhCH_2Cl$) that forms a [PNP] cobalt(III) dichloride complex.[83] In contrast, treatment of a [PNP] cobalt(II) methyl species with methyl iodide results in the formation of a [PNP] cobalt(II) iodide complex.[83] Reduction of Co(III) to Co(II) was also achieved via treatment of a [PNP] cobalt(III) dichloride complex with alkyllithium reagents, regenerating the antecedent [PNP] cobalt(II) chloride complex.[83]

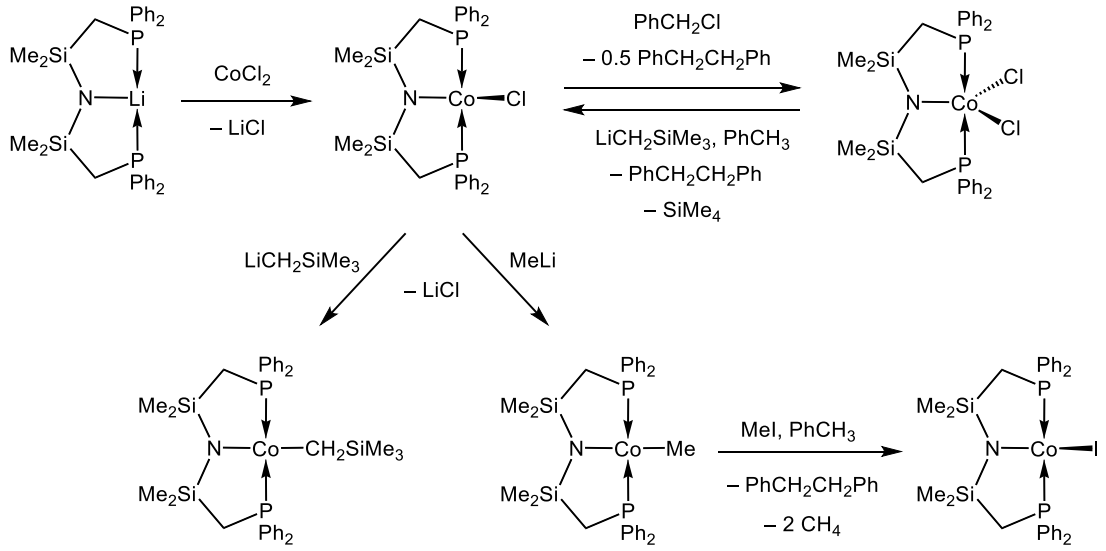

Scheme 4.1

The syntheses of *syn*-[P_2N_2]Co and *anti*-[P_2N_2]Co (Chart 4.4) were previously accomplished and some preliminary reactions involving *anti*-[P_2N_2]Co were explored, although never published in the literature.[152] Reactivity of *anti*-[P_2N_2]Co with iodine (I_2) and oxygen (O_2) has been investigated, yielding new *anti*-[P_2N_2]Co complexes.[152] The focus of this chapter is to follow up on these findings by exploring the synthesis and reactivity of *syn*-[P_2N_2]Co complexes.

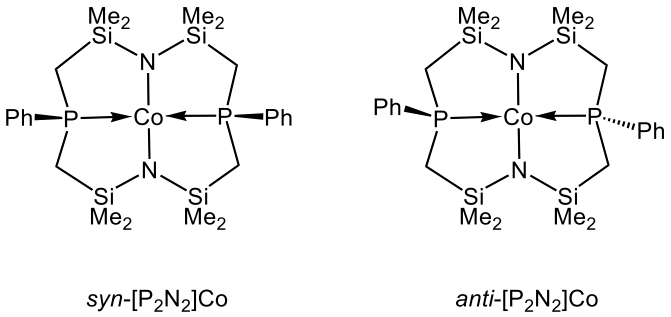

Chart 4.4 Structure of *syn*-[P_2N_2]Co compared to *anti*-[P_2N_2]Co

4.2 Synthesis and reactivity of *syn*-[P_2N_2]Co

In the previously described synthesis,[152] *syn*-[P_2N_2]Co was isolated as a paramagnetic solid and the solid-state molecular structure was not reported. In this work, treatment of *syn*-[P_2N_2]Li_2 with $CoCl_2(THF)_{1.5}$ afforded *syn*-[P_2N_2]Co (**4.1**) as an orange solid (Equation 4.1).

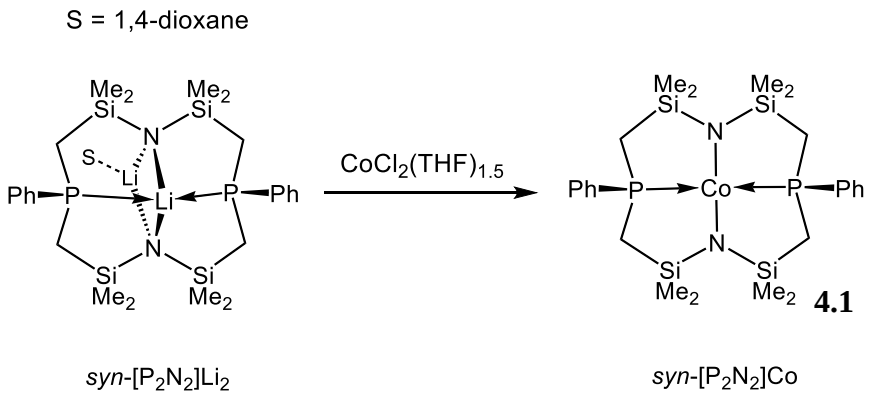

[4.1]

Orange crystals suitable for X-ray diffraction were isolated from a hexane solution of **4.1** and the solid-state molecular structure is shown in Figure 4.1. Complex **4.1** shows a distorted square planar geometry around the cobalt centre. The N1–Co1–N2 and P1–Co1–P2 bond angles (165.65(12)° and 176.82(4)° respectively) demonstrate the distortion from idealized square planar symmetry. The magnetic moment of **4.1** (μ_{eff} = 1.96 μ_B) indicates the presence of 1 unpaired electron, consistent with the formal assignment of a low-spin d^7 square planar Co(II) species.

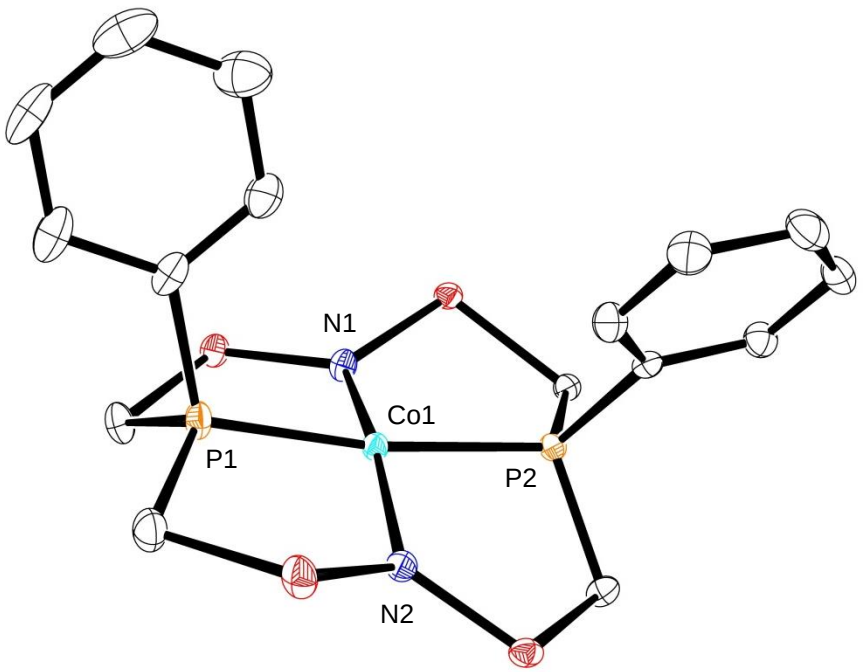

Figure 4.1 ORTEP depiction (ellipsoids at 50 % probability) of *syn*-[P_2N_2]Co (**4.1**). Silyl methyl carbons are omitted for clarity. Selected bond lengths (Å) and angles (°): Co1–N1, 1.934(3); Co1–N2, 1.933(3); Co1–P1, 2.1958(11); Co1–P2, 2.2087(10); N1–Co1–N2, 165.65(12); P1–Co1–P2, 176.82(4); N1–Co1–P1, 91.27(10); N1–Co1–P2, 89.19(10); N2–Co1–P2, 91.32(10); N2–Co1–P1, 89.01(10).

The treatment of *anti*-[P_2N_2]Co with oxygen has previously been described,[152] but the solid-state molecular structure of the proposed product, *anti*-[$(P{=}O)_2N_2$]Co, was not confirmed. Exposure of a solution of the syn isomer **4.1** to oxygen results in oxidation of the ligand phosphines, generating *syn*-[$(P{=}O)_2N_2$]Co (**4.2**) as a purple solid (Equation 4.2).

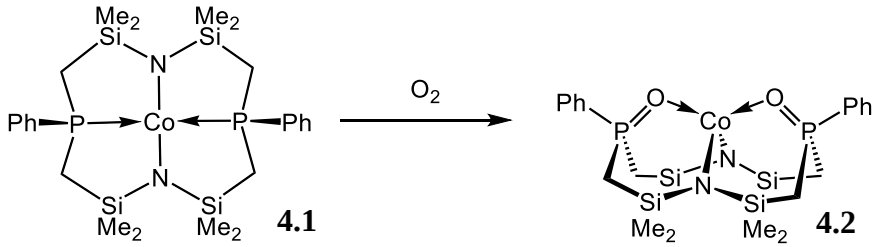

[4.2]

Purple crystals of **4.2** were isolated from a diethyl ether solution cooled to –40 °C. X-ray diffraction studies confirmed the solid-state molecular structure of **4.2** (Figure 4.2). Addition of oxygen has changed the geometry about the Co(II) centre from distorted square planar in **4.1** to slightly distorted tetrahedral symmetry in **4.2**. High-spin tetrahedral d^7 Co(II) species (such as **4.2**) contain 3 unpaired electrons, yet the magnetic moment of **4.2** (μ_{eff} = 4.49 μ_B) was found to be significantly higher than the expected $\mu_{(spin\ only)}$ value of 3.87 μ_B for 3 unpaired electrons; This can be attributed to a second-order orbital angular momentum contribution.[152] Complex **4.2** contains an interesting heterocyclic bonding arrangement in the ligand backbone, now comprised of four fused 6-membered rings (vs 5-membered rings in **4.1**), where every atom in the 6-membered ring is a different element.[153-154] A comparable bonding arrangement has previously been observed in oxidized cobalt complexes containing a similar PNP ligand.[155] Equation 4.3 illustrates the synthesis of a reported Co(II) compound with a similar molecular geometry and magnetic moment value (μ_{eff} = 4.50 μ_B) compared to **4.2** (μ_{eff} = 4.49 μ_B).[155] The P–O and Co–O bonds lengths (1.5277(15), 1.5210(16) and 1.9965(15), 2.0284(15) Å respectively) of **4.2** are comparable to those reported for similar complexes containing oxidized phosphines coordinated to cobalt.[150, 155]

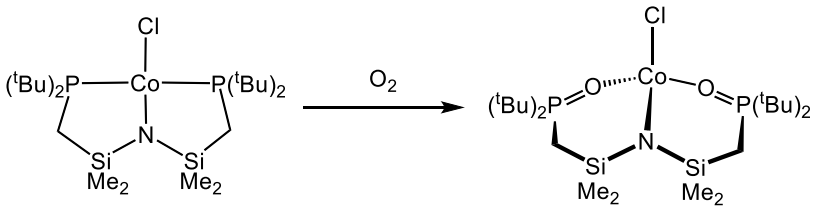

[4.3]

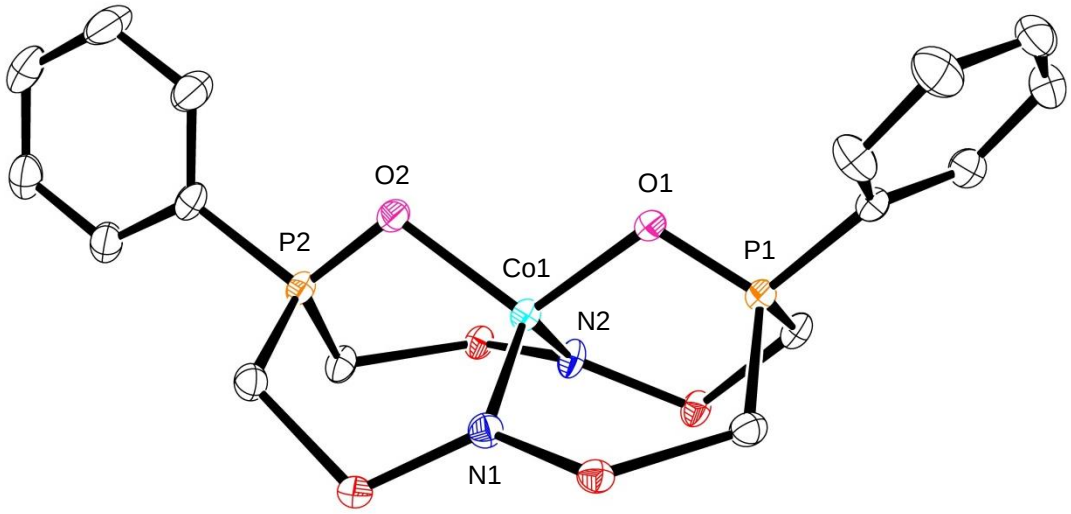

Figure 4.2 ORTEP depiction (ellipsoids at 50 % probability) of *syn*-[(P=O)$_2$N$_2$]Co (**4.2**). Silyl methyl carbons are omitted for clarity. Selected bond lengths (Å) and angles (°): Co1–N1, 1.9695(18); Co1–N2, 1.9707(18); Co1–O1, 1.9965(15); Co1–O2, 2.0284(15); P1–O1, 1.5277(15); P2–O2, 1.5210(16); O1–Co1–O2, 109.71(6); N1–Co1–O1, 102.70(7); N1–Co1–O2, 108.92(7); N1–Co1–N2, 121.38(8); N2–Co1–O1, 109.38(7); N2–Co1–O2, 104.52(7).

In an effort to pursue broader reactivity, oxidation to generate Co(III) bearing a formerly anionic ligand (such as a halide) was investigated. Previous work showed that treatment of the isomeric *anti*-[P$_2$N$_2$]Co with a stoichiometric amount of iodine (I$_2$) resulted in the formation of *anti*-[P$_2$N$_2$]CoI.[152] Synthesis of the analogous *syn*-[P$_2$N$_2$]CoI complex (**4.3**) was investigated by treating **4.1** with I-CH$_2$CH$_2$-I (Equation 4.4).

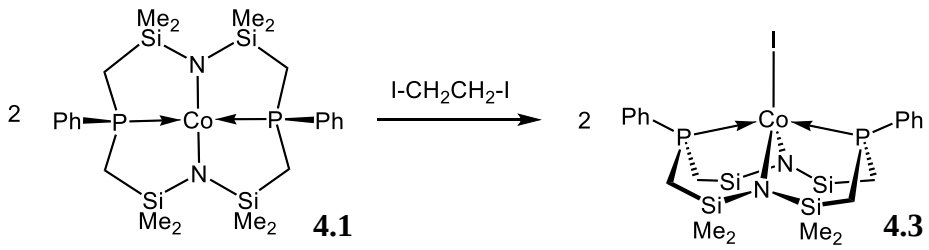

[4.4]

Dark maroon paramagnetic material was isolated in excellent yield. The magnetic moment of **4.3** is 2.81 μ_B (comparable to 3.0 μ_B for the *anti*-[P_2N_2]CoI isomer), indicating the presence of 2 unpaired electrons, consistent with the formal assignment of **4.3** as an intermediate-spin d^6 Co(III) species with 5-coordinate trigonal bipyramidal geometry. Crystals suitable for X-ray diffraction studies were examined, confirming the formation of *syn*-[P_2N_2]CoI (**4.3**). The solid-state molecular structure of **4.3** is shown in Figure 4.3. The geometry about the cobalt centre in **4.3** is slightly distorted from idealized trigonal bipyramidal symmetry. In comparison, the geometry of the solid-state molecular structure of the isomeric *anti*-[P_2N_2]CoI complex could be considered either distorted square pyramidal (with the iodine in the apical position) or distorted trigonal bypyramidal. The N1–Co1–N2 bond angle of 147.12(13)° for *anti*-[P_2N_2]CoI is much greater than the N1–Co1–N2 bond angle of 118.5(3)° observed for *syn*-[P_2N_2]CoI (**4.3**). Similarly, the N1–Co1–I1 and N2–Co1–I1 bond angles (110.70(9)° and 101.57(9)°, respectively) for *anti*-[P_2N_2]CoI are much lower than the expected 120° for idealized trigonal bypyramidal symmetry, whereas the N1–Co1–I1 and N2–Co1–I1 bond angles for **4.3** (115.9(2)° and 125.5(2)°, respectively) are less distorted from idealized trigonal bypyramidal symmetry. The P1–Co1–P2 bond angles for the *anti*-[P_2N_2]CoI and *syn*-[P_2N_2]CoI (**4.3**) isomers are comparable at 171.46(5)° and 171.09(11)°, respectively. The Co1–I1 bond length of 2.6107(13) Å in **4.3** is consistent with Co–I bond distances reported for similar cobalt iodide complexes,[155] compared to the unusually long Co1–I1 bond length of 2.7048(7) Å seen in the *anti*-[P_2N_2]CoI isomer.[152]

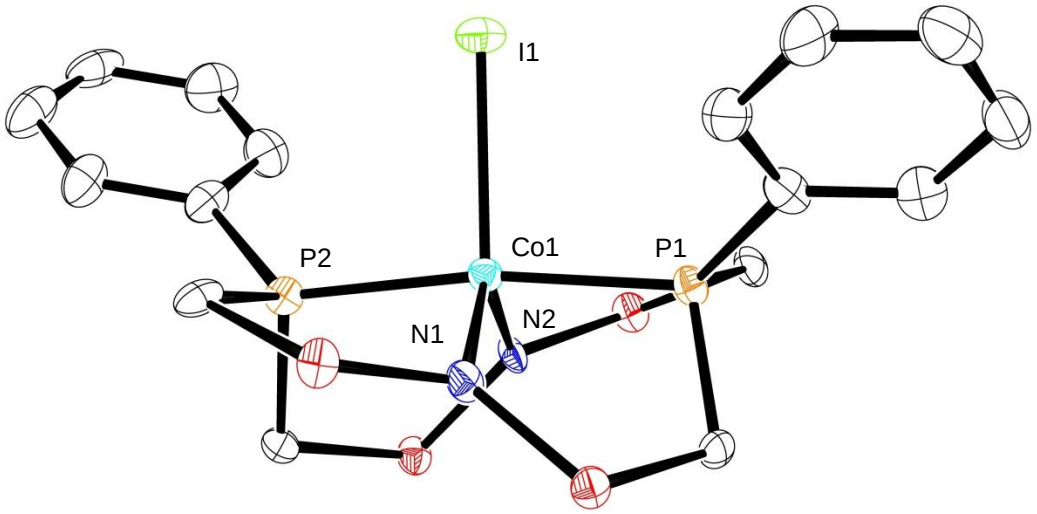

Figure 4.3 ORTEP depiction (ellipsoids at 50 % probability) of *syn*-[P_2N_2]CoI (**4.3**). Silyl methyl carbons are omitted for clarity. Selected bond lengths (Å) and angles (°): Co1–I1, 2.6107(13); Co1–N1, 1.953(8); Co1–N2, 1.958(7); Co1–P1, 2.231(3); Co1–P2, 2.238(3); P1–Co1–P2, 171.09(11); N1–Co1–N2, 118.5(3); N1–Co1–I1, 115.9(2); N2–Co1–I1, 125.5(2).

4.3 Reactivity of *syn*-[P_2N_2]CoI

Cobalt halide complexes often serve as precursors to cobalt hydride and alkyl species.[83, 85, 156] Furthermore, cobalt hydride species have been reported to react with N_2 to produce cobalt dinitrogen complexes.[157] A common method of preparing cobalt hydride species involves treatment of the cobalt halide complex with a hydride reagent, such as sodium or potassium triethylborohydride ($NaBEt_3H$ or $KBEt_3H$).[85, 156-158] In an effort to generate a [P_2N_2]Co hydride species, a solution of *syn*-[P_2N_2]CoI in THF was treated with a THF solution of $KBEt_3H$. The dark maroon solution changed colour to cloudy orange over the course of reaction. A dark orange paramagnetic material was isolated, showing broad peaks in the paramagnetic ^1H NMR spectrum that matched those of the *syn*-[P_2N_2]Co complex. Orange crystals were obtained and the structure of this material was confirmed as the *syn*-[P_2N_2]Co complex, via X-ray diffraction

studies. Equation 4.5 shows the overall transformation of *syn*-[P_2N_2]CoI to *syn*-[P_2N_2]Co upon treatment with $KBEt_3H$. It is not uncommon for reduction to occur from the use of hydride reagents; although the hydride complex forms, immediate reduction follows, liberating H_2 and preventing isolation of the desired hydride complex.[85, 156, 158]

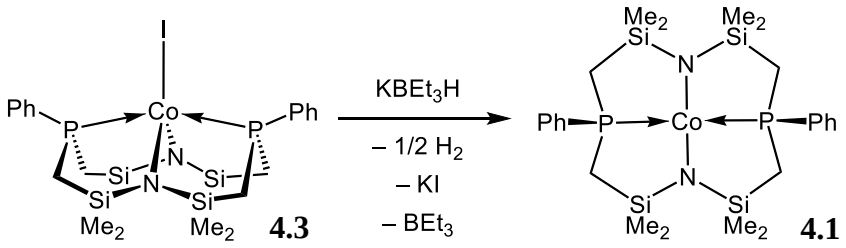

[4.5]

4.3.1 Synthesis of *syn*-[P_2N_2]Co alkyl complexes

Cobalt alkyl complexes are generally prepared via treatment of a cobalt halide species with an alkylithium or Grignard reagent.[83, 85, 142, 156, 158] Upon treatment of *syn*-[P_2N_2]CoI with one equivalent of methyllithium (MeLi), the anticipated *syn*-[P_2N_2]CoMe species was not isolated. A combination of paramagnetic and diamagnetic species was observed via ^{1}H NMR spectroscopic studies of the reaction mixture. A diamagnetic species observed in the ^{1}H NMR spectrum displayed a resonance in the alkyl region that integrated to 6H (relative to the silyl methyl resonances), suggesting two methyl substituents are coordinated to cobalt (Figure 4.4). Crystals suitable for X-ray diffraction studies were obtained, yet produced poor quality data that generated an incomplete structure. Surprisingly, a lithium atom coordinated to the ligand was observed in the model, although the presence of two methyl groups on cobalt was undetermined.

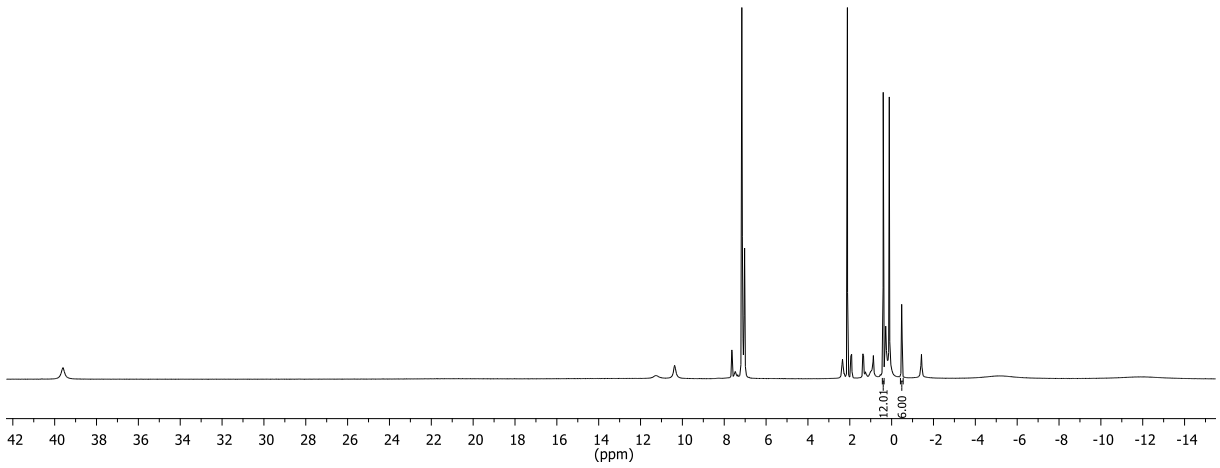

Figure 4.4 ^{1}H NMR (400 MHz, C_6D_6) spectrum of the material isolated from the reaction of *syn*-[P_2N_2]CoI with one equivalent of MeLi, showing a mixture of diamagnetic (strong, sharp signals) and paramagnetic (broad, weak signals) species. Integration of an alkyl resonance at -0.4 ppm (6H) relative to a silyl methyl resonance at 0.4 ppm (12H) suggests the presence of two methyl substituents.

Upon addition of two equivalents of MeLi to *syn*-[P_2N_2]CoI, resonances in the ^{1}H NMR spectrum indicated the presence of a mixture of paramagnetic and diamagnetic species, but with differing chemical shifts from the previous reaction. Attempts to isolate the supposed cobalt dimethyl species resulted in partial decomposition. It is plausible that the dimethyl species is stabilized by solvent coordinating to lithium, such that the absence of coordinating solvent (after removal under vacuum) could cause decomposition. Acetonitrile was added to a hexane solution of the crude material, in order to provide a strongly coordinating solvent. A mixture of orange and pink crystals was isolated, and the paramagnetic ^{1}H NMR spectrum of the crystals indicated the presence of the *syn*-[P_2N_2]Co complex as a decomposition product (Figure 4.5).

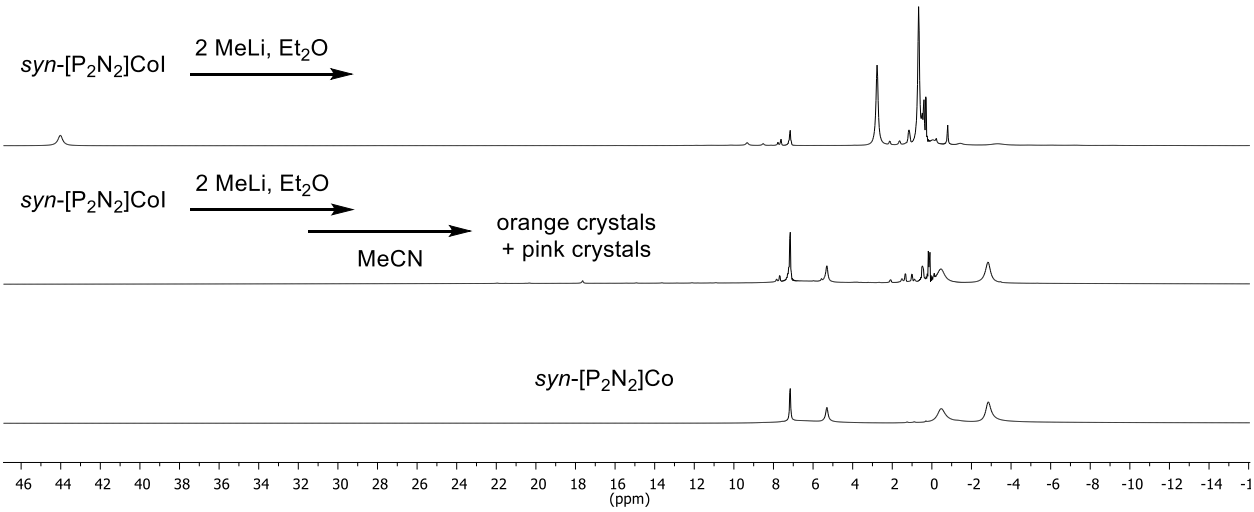

Figure 4.5 Comparison of the paramagnetic ^{1}H NMR (400 MHz, C_6D_6) spectra of the material isolated from the reaction of two equivalents of MeLi with *syn*-[P_2N_2]CoI (top) and the crystal mixture isolated after the addition of acetonitrile (middle) to the aforementioned material. Compared to the (bottom) spectrum of *syn*-[P_2N_2]Co, there is evidence of signals corresponding to *syn*-[P_2N_2]Co observed in the crystal mixture (middle spectrum).

X-ray diffraction studies of a single pink crystal revealed the solid-state molecular structure of **4.4-$_{\mathbf{MeCN}}$** (Figure 4.6). The reaction was also performed using 1,4-dioxane, yielding crystals suitable for X-ray diffraction; the solid-state molecular structure of **4.4-$_{\mathbf{dioxane}}$** was determined (Figure 4.6). Selected bond lengths and angles for **4.4-$_{\mathbf{MeCN}}$** and **4.4-$_{\mathbf{dioxane}}$** are shown in Table 4.1. The structures of both **4.4-$_{\mathbf{MeCN}}$** and **4.4-$_{\mathbf{dioxane}}$** are only slightly distorted from idealized octahedral symmetry, with P–Co–P and N–Co–C bond angles close to 180° (Table 4.1). The Co–C bond lengths (2.005(5), 2.004(5) Å for **4.4-$_{\mathbf{MeCN}}$** and 1.999(2), 2.005(3) Å for **4.4-$_{\mathbf{dioxane}}$**) are comparable with Co–C bond distances reported for cobalt methyl complexes.[156, 159] The Co–N bond distances (2.222(4), 2.229(4) Å for **4.4-$_{\mathbf{MeCN}}$** and 2.241(2), 2.240(2) Å for **4.4-$_{\mathbf{dioxane}}$**) are elongated from the Co–N bond lengths observed in the antecedent *syn*-[P_2N_2]CoI (1.972(15) and 1.953(15) Å) and *syn*-[P_2N_2]Co (1.935(4) and 1.913(3) Å).

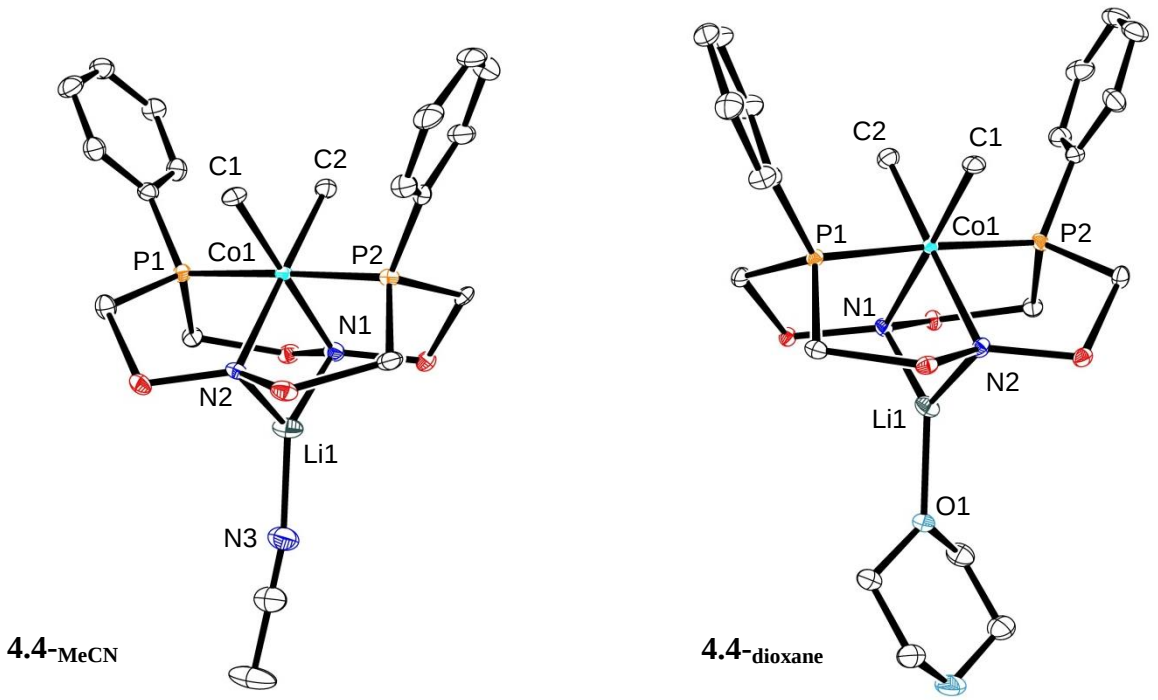

Figure 4.6 ORTEP depiction (ellipsoids at 50 % probability) of **4.4-$_{MeCN}$** (left) and **4.4-$_{dioxane}$** (right). Silyl methyl carbons are omitted for clarity.

Table 4.1 Selected bond lengths (Å) and angles (°) of **4.4-$_{MeCN}$** and **4.4-$_{dioxane}$**

4.4-$_{MeCN}$		**4.4-$_{dioxane}$**	
Atoms	Distance	Atoms	Distance
Co1–C1	2.005(5)	Co1–C1	1.999(2)
Co1–C2	2.004(5)	Co1–C2	2.005(3)
Co1–N1	2.222(4)	Co1–N1	2.241(2)
Co1–N2	2.229(4)	Co1–N2	2.240(2)
Co1–P1	2.1957(15)	Co1–P1	2.2004(9)
Co1–P2	2.1934(15)	Co1–P2	2.2108(9)
N1–Li1	1.986(10)	N1–Li1	1.994(5)
N2–Li1	1.969(10)	N2–Li1	1.994(5)
Li1–N3	2.026(10)	Li1–O1	1.990(5)
Atoms	Angle	Atoms	Angle
P1–Co1–P2	178.04(5)	P1–Co1–P2	176.82(8)
N1–Co1–C1	177.9(2)	N1–Co1–C1	177.08(9)
N2–Co1–C2	178.2(2)	N2–Co1–C2	178.65(9)

The diamagnetic nature of **4.4-$_{dioxane}$** is consistent with a low-spin d^6 Co(III) species, further supported by the octahedral geometry and coordinated lithium observed in the solid-state molecular structure. The $^{31}P\{^1H\}$ NMR spectrum of **4.4-$_{dioxane}$** displays a very broad resonance at 33.5 ppm (Figure 4.7). A singlet (δ 1.18) is observed in the ^7Li NMR spectrum of **4.4-$_{dioxane}$**, supporting the presence of lithium. In the ^1H NMR spectrum of **4.4-$_{dioxane}$** (Figure 4.7), the cobalt methyl resonance at δ -0.40 integrates to 6H, relative to the silyl methyl signals at δ 0.13 (12H) and δ 0.40 (12H), supporting the presence of two methyl substituents bonded to cobalt.

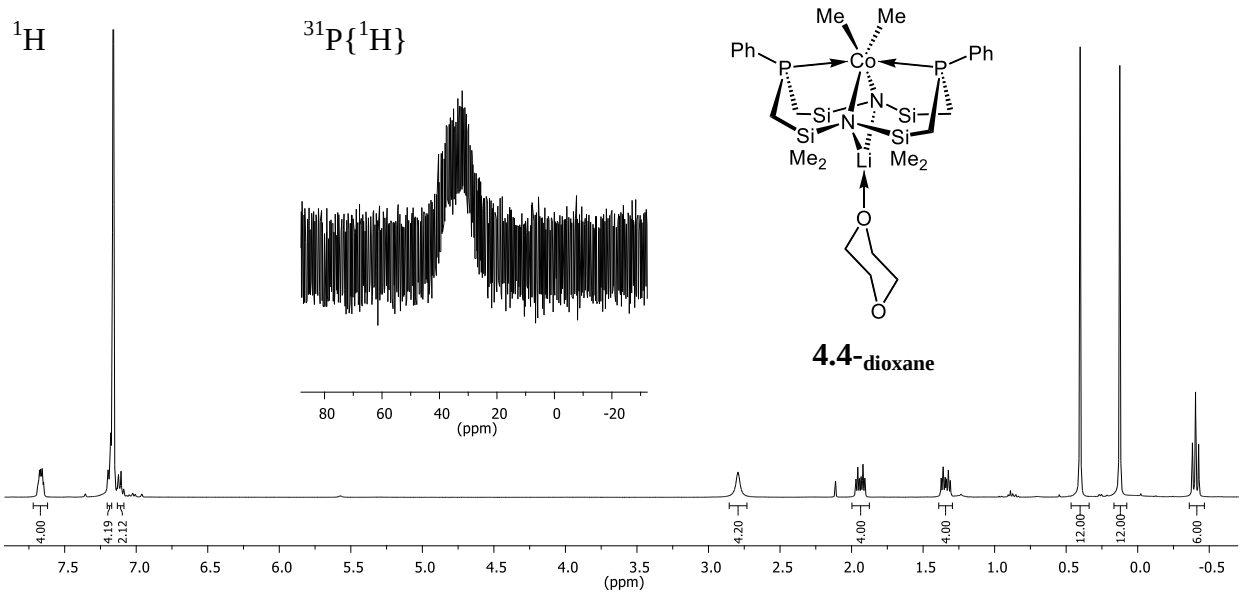

Figure 4.7 $^{31}P\{^1H\}$ NMR (161.9 MHz) spectrum (inset) and ^1H NMR (400 MHz) spectrum of **4.4-$_{dioxane}$** (in C_6D_6).

Synthesis of a *syn*-[P_2N_2] cobalt ethyl complex was also examined. Treatment of *syn*-[P_2N_2]CoI with one equivalent of ethylmagnesium chloride produced an orange paramagnetic material. Equation 4.6 shows the proposed transformation, producing a *syn*-[P_2N_2] Co(III) ethyl species (*syn*-[P_2N_2]CoEt). The paramagnetic ^1H NMR spectrum displays broad peaks with

differing chemical shifts from both the preceding *syn*-$[P_2N_2]$CoI species and the *syn*-$[P_2N_2]$Co complex (Figure 4.8). Attempts to grow crystals from this material (suitable for X-ray diffraction studies) were ultimately unsuccessful, thus the structure and identity of the product was not confirmed via X-ray crystallography.

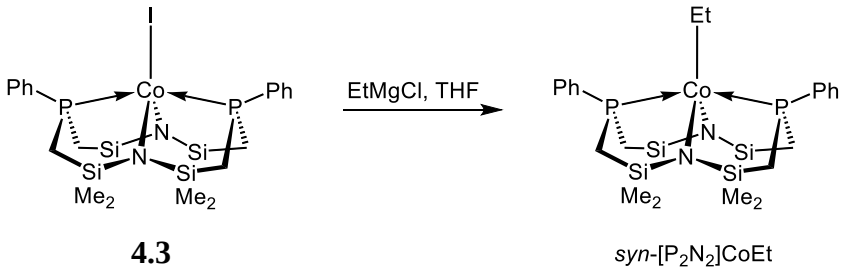

4.3 *syn*-$[P_2N_2]$CoEt **[4.6]**

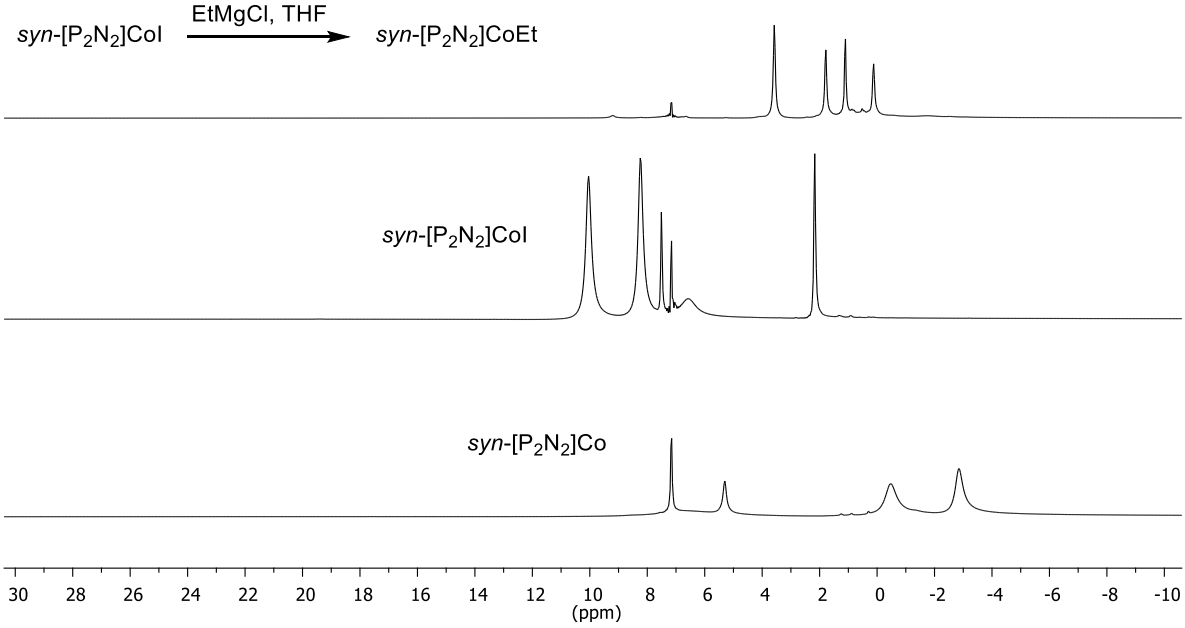

Figure 4.8 Comparison of the paramagnetic ^{1}H NMR (400 MHz, C_6D_6) spectra of the material generated from the treatment of *syn*-$[P_2N_2]$CoI with ethylmagnesium chloride (top spectrum), and the preceding *syn*-$[P_2N_2]$CoI species (middle spectrum) and *syn*-$[P_2N_2]$Co complex (bottom spectrum).

The treatment of *syn*-[P_2N_2]CoI with one equivalent of isopropyllithium was examined and proved unsuccessful in producing a stable *syn*-[P_2N_2] cobalt alkyl complex. Instead, the paramagnetic ^{1}H NMR spectrum of the final product matches that of the *syn*-[P_2N_2]Co complex. Crystals suitable for X-ray diffraction studies were also isolated and confirmed the presence of *syn*-[P_2N_2]Co. The formation of a *syn*-[P_2N_2] cobalt isopropyl complex is not observed during this transformation.

The reactivity of *syn*-[P_2N_2]CoI with (trimethylsilyl)methyllithium ($LiCH_2SiMe_3$) was explored in the interest of observing the effect of installing a bulkier alkyl substituent. Treatment of *syn*-[P_2N_2]CoI with $LiCH_2SiMe_3$ generated a dark green paramagnetic material. Single crystals suitable for X-ray diffraction studies were isolated and the solid-state molecular structure of *syn*-[P_2N_2]$CoCH_2SiMe_3$ (**4.5**) was confirmed (Figure 4.9). The structure of complex **4.5** shows a distorted trigonal bipyramidal geometry about the cobalt centre. The C1–Co1–N2 and N1–Co1–N2 bond angles (132.82(6)° and 108.18(5)° respectively) illustrate the distortion from idealized trigonal bipyramidal symmetry. The Co1–C1 bond length of 2.0320(16) Å is consistent with Co–C bond distances reported for cobalt complexes containing a CH_2SiMe_3 group.[85, 144, 159] The magnetic moment of **4.5** (μ_{eff} = 2.91 μ_B, indicating the presence of 2 unpaired electrons) supports the formal assignment of **4.5** as an intermediate-spin d^6 Co(III) species with 5-coordinate trigonal bipyramidal geometry.

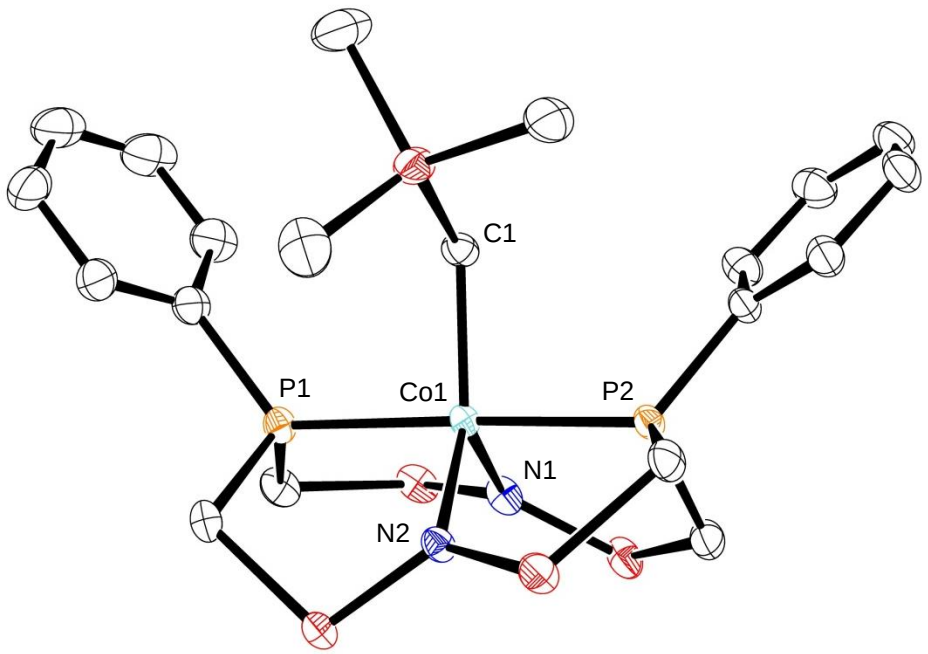

Figure 4.9 ORTEP depiction (ellipsoids at 50 % probability) of *syn*-$[P_2N_2]CoCH_2SiMe_3$ (**4.5**). Ligand silyl methyl carbons are omitted for clarity. Selected bond lengths (Å) and angles (°): Co1–C1, 2.0320(16); Co1–N1, 2.0193(12); Co1–N2, 2.0137(13); Co1–P1, 2.3051(4); Co1–P2, 2.2471(4); P1–Co1–P2, 177.096(16); C1–Co1–N1, 118.96(6); C1–Co1–N2, 132.82(6); N1–Co1–N2, 108.18(5).

Reactivity of $CoCH_2SiMe_3$ complexes with H_2 is reported to generate cobalt hydride complexes.[144, 156, 159] Exposure of a toluene solution of *syn*-$[P_2N_2]CoCH_2SiMe_3$ to H_2 resulted in a colour change from dark green to light orange. The paramagnetic ^{1}H NMR spectrum of the orange material isolated matched that of the *syn*-$[P_2N_2]$Co complex. Crystals suitable for X-ray diffraction studies were isolated and the structure of *syn*-$[P_2N_2]$Co was confirmed. Formation of a *syn*-$[P_2N_2]$Co hydride species was not observed, analogous to the reaction between $KBEt_3H$ and *syn*-$[P_2N_2]$CoI that also generated *syn*-$[P_2N_2]$Co as the final product. The formation of **4.5** and subsequent transformation to *syn*-$[P_2N_2]$Co upon exposure to H_2 is shown in Scheme 4.2.

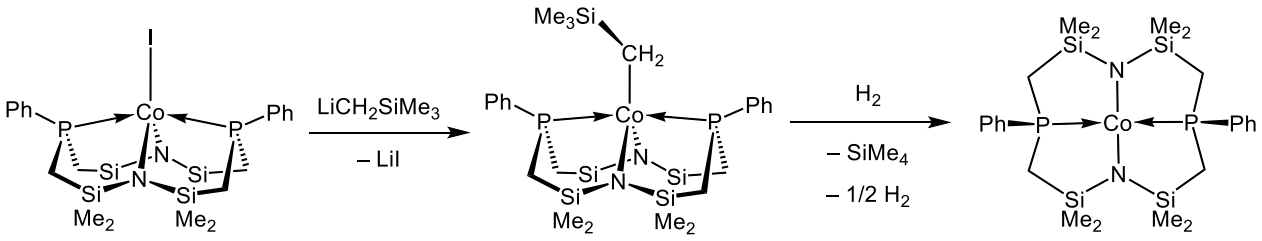

4.3 **4.5** **4.1**

Scheme 4.2

4.4 Conclusions

The paramagnetic *syn*-$[P_2N_2]$Co complex (**4.1**) was synthesized and further reactivity was explored. Exposure of *syn*-$[P_2N_2]$Co to oxygen results in oxidation of the ligand phosphines, forming *syn*-$[(P{=}O)_2N_2]$Co (**4.2**). Treatment of *syn*-$[P_2N_2]$Co with the oxidant I-CH_2CH_2-I generated the *syn*-$[P_2N_2]$CoI species (**4.3**). Reactivity of *syn*-$[P_2N_2]$CoI with alkyllithium and Grignard reagents was examined in an effort to generate *syn*-$[P_2N_2]$Co alkyl species. Interestingly, treatment of *syn*-$[P_2N_2]$CoI with methyllithium produced a diamagnetic *syn*-$[P_2N_2]$Co dimethyl species (**4.4-$_{\mathbf{dioxane}}$**). A new paramagnetic species was generated upon treatment of *syn*-$[P_2N_2]$CoI with ethymagnesium chloride, although the identity of the proposed *syn*-$[P_2N_2]$CoEt species remains unconfirmed by X-ray crystallography. The formation of a *syn*-$[P_2N_2]$Co isopropyl species was not observed during the reaction between isopropyllithium and *syn*-$[P_2N_2]$CoI; instead, *syn*-$[P_2N_2]$Co proved to be the final product. When the bulkier $LiCH_2SiMe_3$ was used, formation of the paramagnetic *syn*-$[P_2N_2]CoCH_2SiMe_3$ complex (**4.5**) was observed. Attempts to synthesize a *syn*-$[P_2N_2]$Co hydride species resulted in regeneration of the *syn*-$[P_2N_2]$Co complex. Both the treatment of *syn*-$[P_2N_2]$CoI with $KBEt_3H$ and the exposure

of *syn*-$[P_2N_2]CoCH_2SiMe_3$ to H_2 gave rise to *syn*-$[P_2N_2]Co$ as the final product. Scheme 4.3 summarizes the *syn*-$[P_2N_2]Co$ complexes synthesized in this chapter.

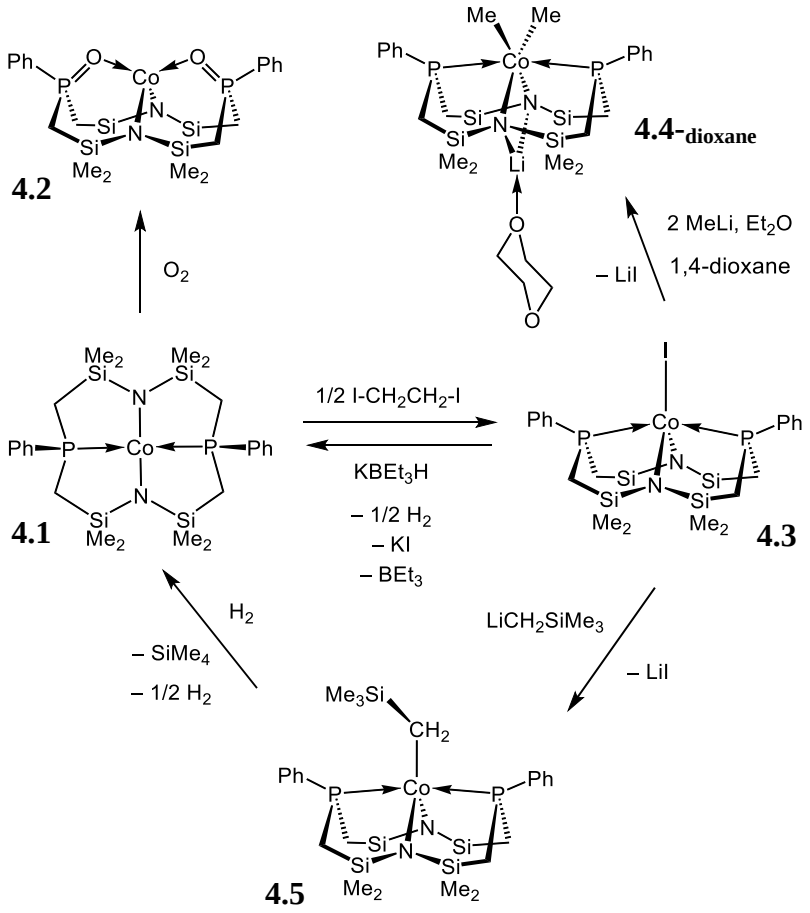

Scheme 4.3

Chapter 5: Synthesis and reactivity of [P_2N_2] rhodium complexes

5.1 Introduction

Exploration of chemistry involving rhodium is dominated by the design and study of rhodium complexes with respect to catalytic processes.[160] A large number of pincer complexes of rhodium have been developed, containing a variety of mixed-donor ligand arrays.[161-163] Several rhodium pincer complexes have proven useful in catalytic transformations, such as dimerization of terminal alkynes[164-165] and alkane transfer-dehydrogenation.[166] Other interesting transformations of PNP pincer rhodium complexes include C–H activation, addition of MeI and activation of H_2, N_2 and CO (Scheme 5.1).[167] In addition, a PNP rhodium hydride complex has been reported to cleave CO_2 to form a rhodium CO complex.[168] Upon subsequent UV irradiation, this rhodium CO complex C–H activates benzene to form a benzoyl complex, liberating benzaldehyde upon protonation.[168] Various catalytic transformations have also been observed with non-pincer rhodium complexes, such as hydrogenolysis of a titanium–amide bond yielding ammonia,[169] catalytic hydrogenation of CO_2[170] and intermolecular hydroalkoxylation of alkynes.[171]

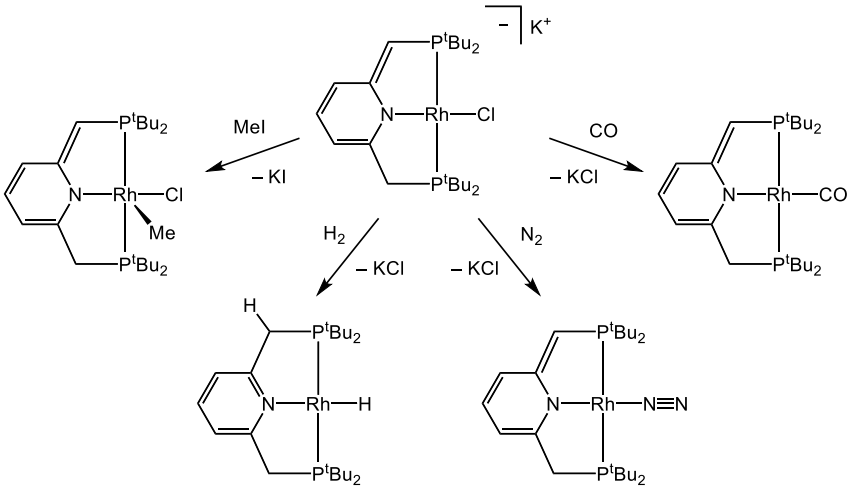

Scheme 5.1

A recurring characteristic amongst the aforementioned rhodium complexes is the use of P- and/or N-containing ligands. The synthesis of a number of rhodium complexes employing phosphorus- and/or nitrogen-containing ligand arrangements has previously been reported by the Fryzuk group.[80, 84, 172-175] In particular, early work focused on amidophosphine complexes of rhodium utilizing the [PNP] ligand framework.[81-82, 176] The synthesis of a [PNP] rhodium cyclooctene (COE) complex and subsequent reactivity with MeI,[81] CO[81] and H_2[82] is shown in Scheme 5.2. Although numerous group 9 (Co and Rh) metal complexes of the [PNP] and related [P_2N_2] ligand set are known, the synthesis of rhodium complexes of [P_2N_2] was not previously explored.

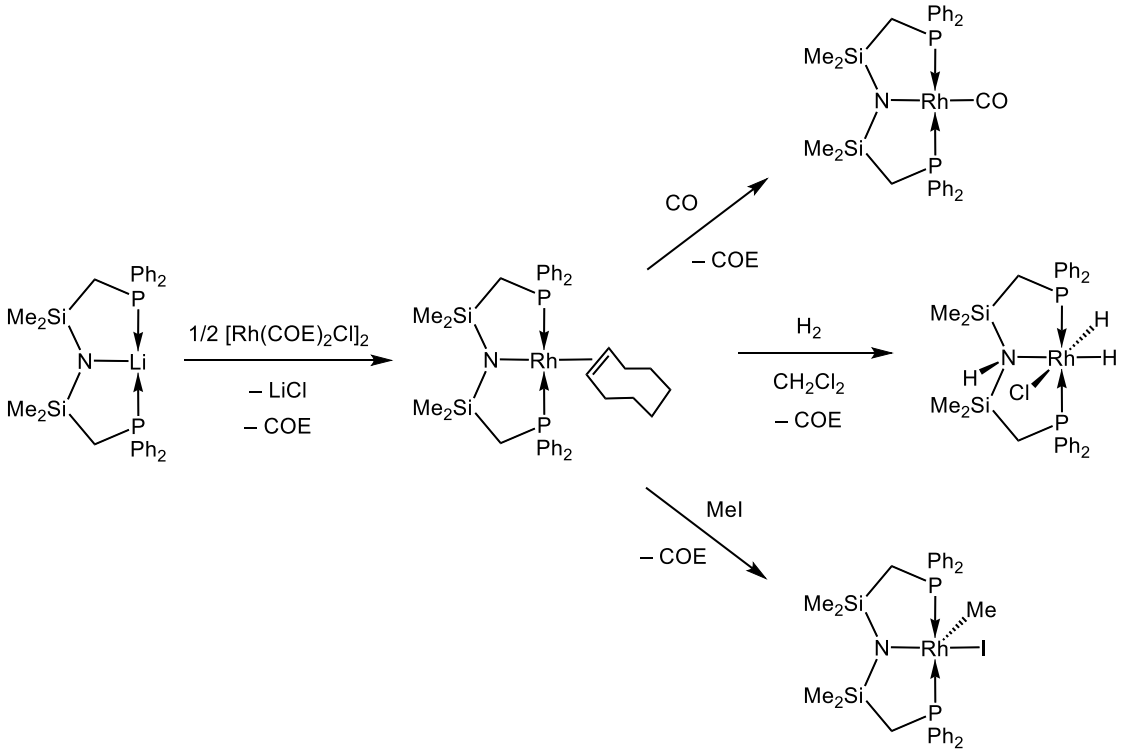

Scheme 5.2

Given the challenges presented in the synthesis and characterization of paramagnetic $[P_2N_2]$ cobalt complexes seen in Chapter 4, pursuit of diamagnetic $[P_2N_2]$ rhodium complexes that could be more reliably characterized using NMR spectroscopy was a logical avenue. The 100% abundant ^{103}Rh isotope has the same nuclear spin (S = ½) as that of protons and phosphorus, such that Rh coupling with these nuclei can be observed, proving advantageous for characterization via multinuclear NMR spectroscopic techniques. In this chapter, the synthesis and reactivity of $[P_2N_2]$ rhodium complexes are investigated; exploration of the ability of these systems to undergo oxidative addition with alkyl halides and H_2 is of particular interest. Such studies would set the stage towards utilizing these macrocyclic rhodium derivatives in catalytic processes.

5.2 Synthesis and reactivity of $[P_2N_2][Rh(COD)]_2$

Initial exploration into coordinating $[P_2N_2]$ to rhodium began with treatment of *syn*-$[P_2N_2]Li_2$ with half an equivalent of the readily available Rh(I) starting material $[Rh(COD)Cl]_2$, anticipating the formation of a Rh(I) species such as $Li[P_2N_2]Rh$. Surprisingly, upon examination of the $^{31}P\{^1H\}$ NMR spectrum of the reaction mixture, peaks corresponding to unreacted *syn*-$[P_2N_2]Li_2$ were observed along with a new doublet at δ 20.0 indicating a new complex was generated. The Rh–P coupling (143 Hz) observed in the $^{31}P\{^1H\}$NMR spectrum is indicative of a Rh(I) species.[177] The ^{1}H NMR spectrum of the material isolated from the reaction also revealed resonances suggestive of two coordinated COD molecules (via integration relative to the silyl methyl protons). As a result, it was proposed that the new species contains two rhodium COD units per $[P_2N_2]$ ligand. Treatment of *syn*-$[P_2N_2]Li_2$ with one equivalent of $[Rh(COD)Cl]_2$ afforded yellow crystalline material, giving rise to the same resonances observed in the previous

NMR spectra, absent of unreacted *syn*-$[P_2N_2]Li_2$ (Figure 5.1). Equation 5.1 shows the formation of this new rhodium species as $[P_2N_2][Rh(COD)]_2$ (**5.1**).

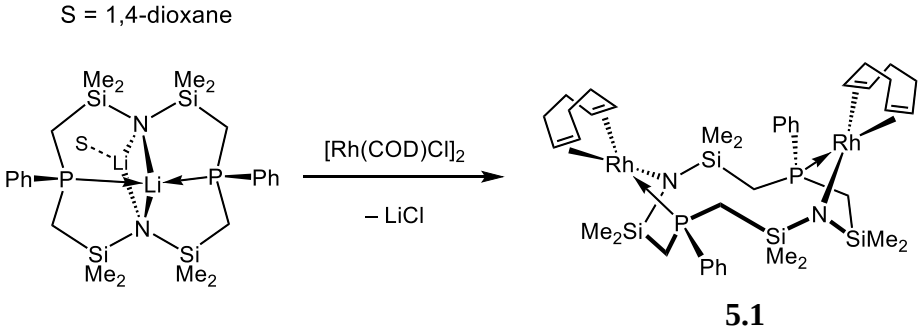

[5.1]

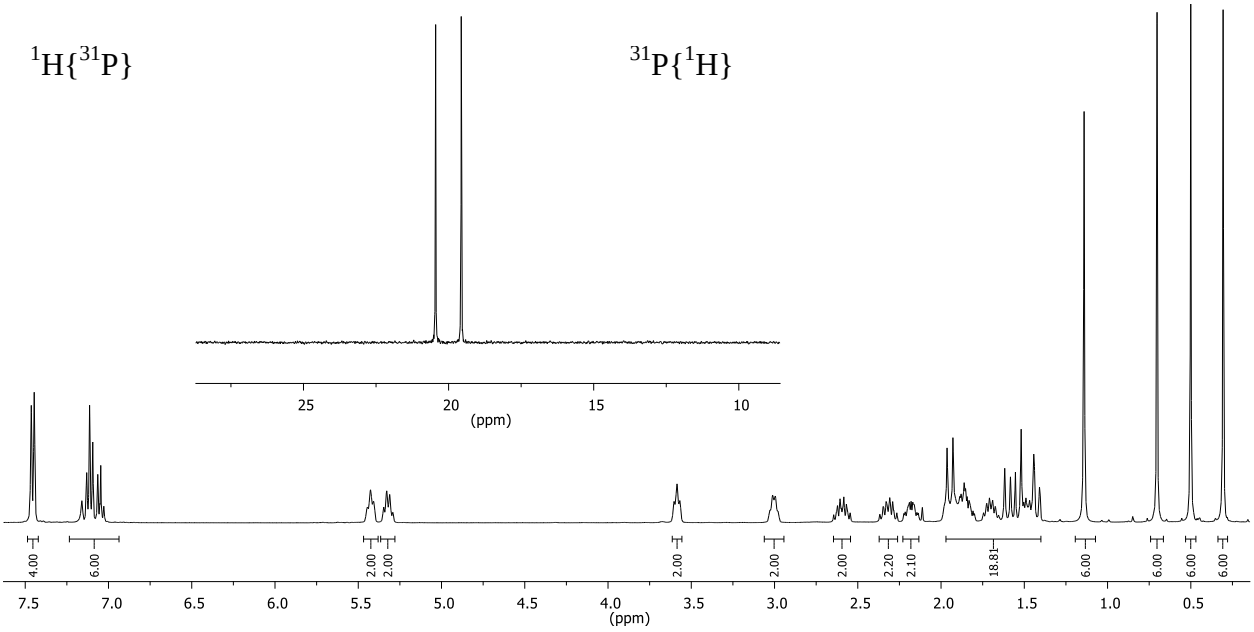

Figure 5.1 $^{31}P\{^1H\}$ NMR (161.9 Hz) spectrum (inset) and $^1H\{^{31}P\}$ NMR (400 MHz) spectrum of **5.1** (in C_6D_6).

Single crystals of **5.1** were isolated and subjected to X-ray diffraction studies. The solid-state molecular structure of **5.1** is shown in Figure 5.2 and Table 5.1 shows selected bond lengths and angles. Both rhodium atoms in **5.1** are coordinated on the same side of the $[P_2N_2]$ macrocycle.

The environments around Rh1 and Rh2 are essentially identical, with each Rh(I) centre coordinated to one amido and one phosphine donor on $[P_2N_2]$, as well as one COD molecule, generating a distorted square planar geometry. The Rh–P and Rh–N bond distances (2.3082(10), 2.2834(10) Å and 2.163(3), 2.143(3) Å respectively) in **5.1** are consistent with those reported for rhodium COD complexes coordinated to P,N-donor ligands.[178] The Rh–COD bond distances differ with respect to the C=C moiety coordinating in either a *cis* or *trans* position relative to the phosphine. The Rh–COD(*trans*) bond distances of 2.108 and 2.101 Å are longer than the Rh–COD(*cis*) bond distances of 2.005 and 1.984 Å. In addition, the C–C bond lengths of the *trans* C=C moieties (1.373(6) and 1.361(6) Å) are slightly shorter than the bond lengths of the cis C=C moieties (1.398(6) and 1.405(5) Å). This inequivalence in bond distances suggests that the *trans* disposed C=C moieties are less activated and less strongly bound to the rhodium centres, as a result of the *trans*-influence from the phosphines.[174, 179]

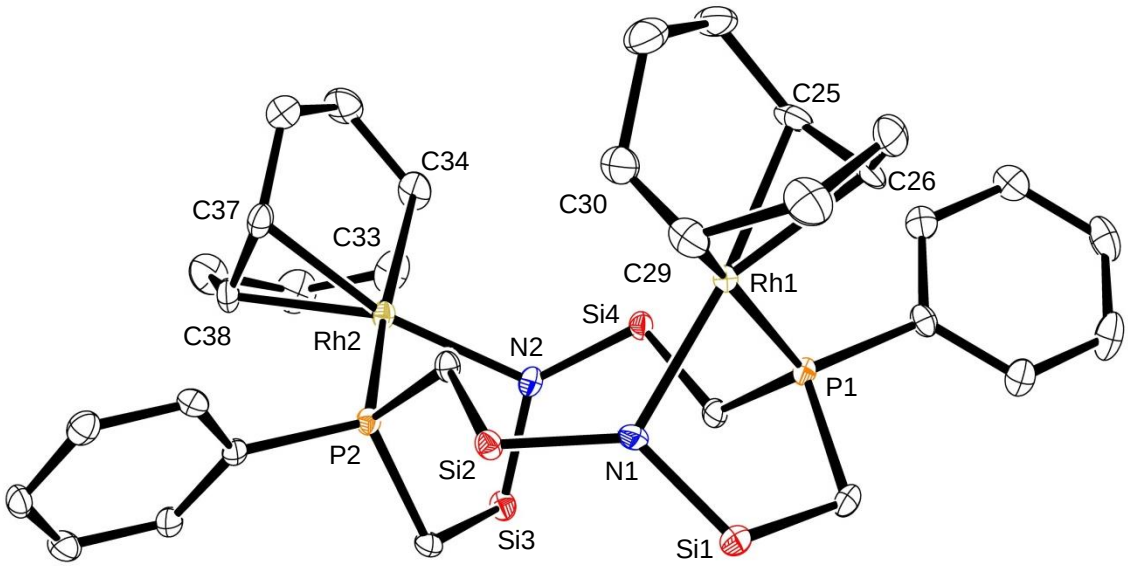

Figure 5.2 ORTEP depiction (ellipsoids at 50 % probability) of $[P_2N_2][Rh(COD)]_2$ (**5.1**). Silyl methyl carbons are omitted for clarity.

Table 5.1 Selected bond lengths (Å) and angles (°) of **5.1**

Atoms	Distance	Atoms	Distance
Rh1–N1	2.163(3)	Rh2–N2	2.143(3)
Rh1–P1	2.3082(10)	Rh2–P2	2.2834(10)
C29–C30 (*trans*) *	1.373(6)	C33–C34 (*trans*)	1.361(6)
C25–C26 (*cis*) *	1.398(6)	C37–C38 (*cis*)	1.405(5)
Rh1–COD(*trans*)$_{cent}$ ǂ	2.108	Rh2–COD(*trans*)$_{cent}$	2.101
Rh1–COD(*cis*)$_{cent}$ ǂ	2.005	Rh2–COD(*cis*)$_{cent}$	1.984
Atoms	**Angle**	**Atoms**	**Angle**
N1–Rh1–P1	82.07(9)	N2–Rh2–P2	82.37(9)
N1–Rh1–COD(*cis*)$_{avg}$	160.7	N2–Rh2–COD(*cis*)$_{avg}$	160.4
N1–Rh1–COD(*trans*)$_{avg}$	94.4	N2–Rh2–COD(*trans*)$_{avg}$	94.2
P1–Rh1–COD(*cis*)$_{avg}$	96.0	P2–Rh2–COD(*cis*)$_{avg}$	95.6
P1–Rh1–COD(*trans*)$_{avg}$	161.9	P2–Rh2–COD(*trans*)$_{avg}$	161.8

*(*trans*) or (*cis*) denotes *trans* or *cis* to the phosphine (P1 or P2)

ǂRh–COD$_{cent}$ distances calculated as the distance between the rhodium and the centroid of the C=C fragment

In an effort to drive the reaction of *syn*-[P_2N_2]Li_2 with [Rh(COD)Cl]$_2$ towards formation of a complex with only one rhodium coordinated to [P_2N_2] (potentially Li[P_2N_2]Rh via displacement of COD), a THF solution of *syn*-[P_2N_2]Li_2 with half an equivalent of [Rh(COD)Cl]$_2$ was heated at 60 °C for 12 h. In the $^{31}P\{^1H\}$NMR spectrum of the reaction mixture, three new doublet resonances at δ 13.2, 22.8 and 32.8 (with Rh–P coupling constants of 202, 127, and 108 Hz, respectively) were observed, in addition to the doublet at δ 20.0 for complex **5.1**. Attempts to isolate these species were unsuccessful and crystals suitable for X-ray diffraction remain elusive. Postulating that these new species could arise from thermal rearrangement of **5.1**, the thermal stability of **5.1** was also explored. After heating a solution of **5.1** at 60 °C for 12 h, there was no difference observed in the $^{31}P\{^1H\}$NMR and ^1H NMR spectra, indicating that **5.1** is not prone to thermal rearrangement or decomposition under these conditions. Accordingly, the addition of heat in the treatment of *syn*-[P_2N_2]Li_2 with [Rh(COD)Cl]$_2$ gave rise to new rhodium complexes independently of **5.1**.

5.2.1 Reactivity of $[P_2N_2][Rh(COD)]_2$ with alkyl halides

In order to investigate the ability of $[P_2N_2][Rh(COD)]_2$ (**5.1**) to undergo oxidative addition, treatment of **5.1** with MeI was attempted. Surprisingly, there was no reaction between **5.1** and MeI. Similarly, no reaction was observed between **5.1** and I-CH_2CH_2-I at room temperature. However, upon heating a toluene solution of **5.1** and one equivalent of I-CH_2CH_2-I at 110 °C for 5 h, a colour change from yellow to green-yellow was observed. Several new species were observed in the $^{31}P\{^1H\}$NMR spectrum of the reaction mixture. Complex **5.2**, $[P_2N_2]Rh(\mu\text{-}I)_2Rh(COD)$, was isolated from the reaction mixture as a green solid in fair yield, giving rise to a doublet in the $^{31}P\{^1H\}$NMR spectrum at δ 24.8 with a Rh–P coupling of 83 Hz, indicative of a Rh(III) centre bonded to phosphorus (Figure 5.3).

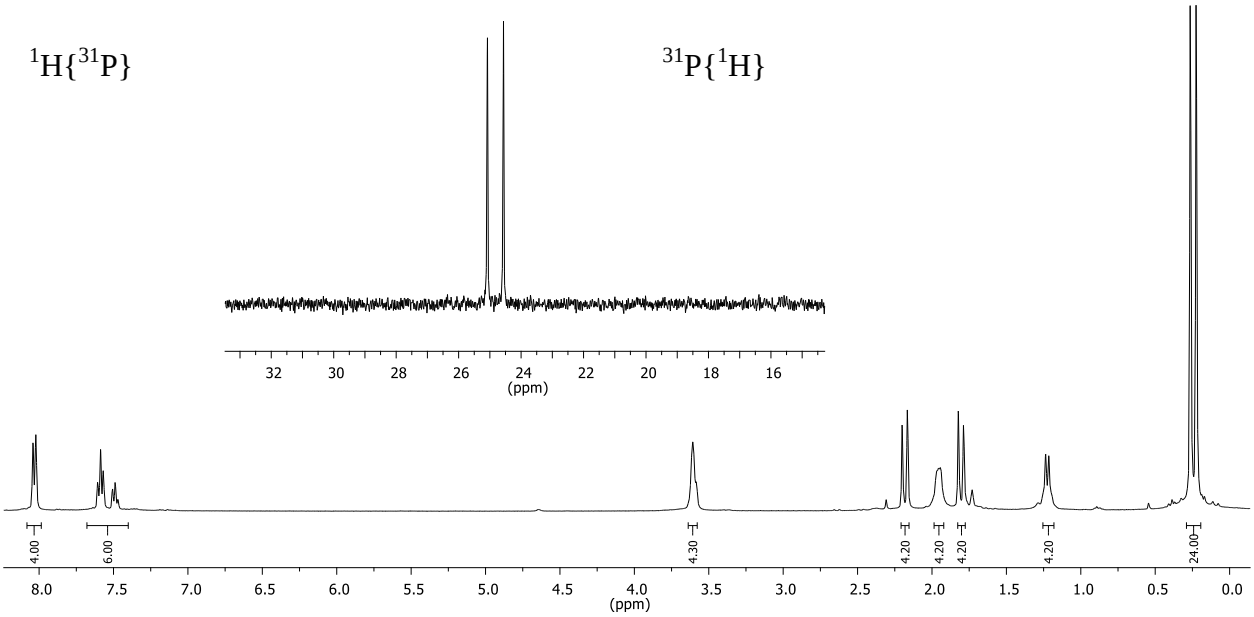

Figure 5.3 $^{31}P\{^1H\}$ NMR (161.9 MHz) spectrum (inset) and $^1H\{^{31}P\}$ NMR (400 MHz) spectrum of **5.2** (in THF-d_8).

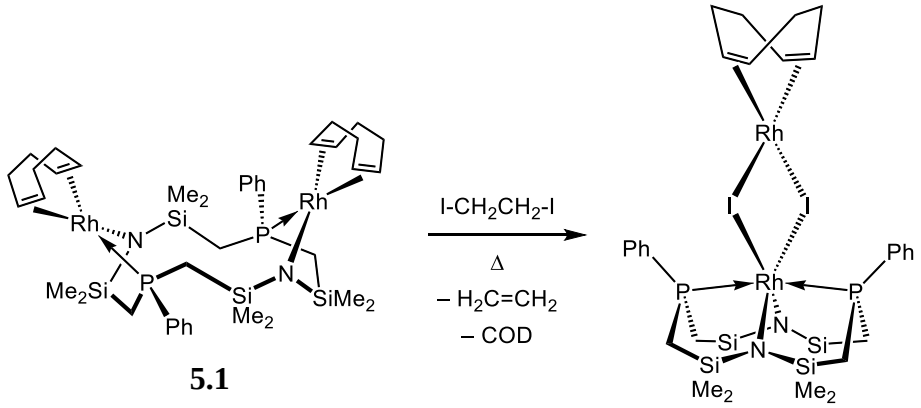

5.1 **5.2**

[5.2]

The transformation of $[P_2N_2][Rh(COD)]_2$ into $[P_2N_2]Rh(\mu\text{-}I)_2Rh(COD)$ (**5.2**) is shown in Equation 5.2. Although heat was required, oxidative addition has clearly occurred; only one of the two Rh(I) centres of **5.1** was involved, likely due to the strong bond between rhodium and the COD unit, providing stabilization for the lower oxidation state of Rh(I). Green crystals were isolated and the solid state molecular structure of **5.2** was determined (Figure 5.4). Complex **5.2** is a Rh(III)–Rh(I) species bridged by two iodides, with Rh–I bond distances (2.6890(9) and 2.6684(9) Å) comparable to those reported for rhodium iodide complexes.[180-181] The geometry about the Rh(III) centre is slightly distorted from idealized octahedral symmetry, as evidenced by the P1–Rh1–P1' and N1–Rh1–I1 bond angles of 174.41(12)° and 173.6(2)° respectively. The Rh(I) centre displays a distorted square planar geometry, with an I1–Rh2–I1' bond angle of 85.47(4)° (similar to the I1–Rh1–I1' bond angle of 84.66(4)° at the Rh(III) centre).

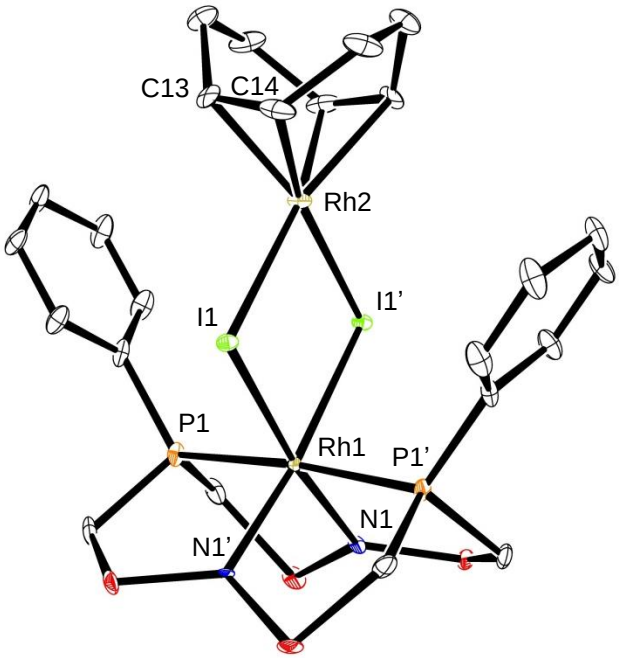

Figure 5.4 ORTEP depiction (ellipsoids at 50 % probability) of $[P_2N_2]Rh(\mu\text{-}I)_2Rh(COD)$ (**5.2**). Silyl methyl carbons are omitted for clarity. Selected bond lengths (Å) and angles (°): Rh1–I1, 2.6890(9); Rh2–I1, 2.6684(9); Rh1–N1, 2.119(7); Rh1–P1, 2.335(2); C13–C14, 1.400(16); Rh–COD_{cent}, 2.012; P1–Rh1–P1', 174.41(12); N1–Rh1–I1, 173.6(2); I1–Rh1–I1', 84.66(4); I1–Rh2–I1', 85.47(4).

5.2.2 Reactivity of $[P_2N_2][Rh(COD)]_2$ with H_2 and CO

Further investigation into the ability of $[P_2N_2][Rh(COD)]_2$ (**5.1**) to undergo oxidative addition was explored via treatment of **5.1** with H_2. Exposure of a toluene solution of **5.1** to 4 atm of H_2 resulted in the appearance of new resonances in the $^{31}P\{^1H\}$NMR spectrum of the reaction mixture. However, after stirring under 4 atm of H_2 at RT for 3 days, the starting $[P_2N_2][Rh(COD)]_2$ complex was still present in a significant amount. Interestingly, upon heating the reaction mixture at 80 °C, both in the presence and absence of H_2, the remaining $[P_2N_2][Rh(COD)]_2$ complex is consumed. Unfortunately, the reaction does not proceed cleanly; a

mixture of products is observed via NMR spectroscopy. The major species present displays a doublet resonance at δ 33.6 in the $^{31}P\{^{1}H\}$NMR spectrum, with a Rh–P coupling of 96 Hz suggestive of a Rh(III) species. In the ^{1}H NMR spectrum, resonances corresponding to the coordinated COD in $[P_2N_2][Rh(COD)]_2$ have disappeared and new resonances at δ –14 and –18 have appeared, suggesting the presence of rhodium hydrides. Attempts to isolate species for further NMR spectroscopy and X-ray crystallography studies were unsuccessful and the identity of the products remains elusive.

Treatment of $[P_2N_2][Rh(COD)]_2$ with CO was also explored, in an effort to prove displacement of the COD units with CO ligands. Upon exposure of a toluene solution of $[P_2N_2][Rh(COD)]_2$ to 4 atm of CO, a colour change from yellow to orange was initially observed, followed by another colour change to yellow, suggesting an intermediate species is formed before conversion to the final product. The $^{31}P\{^{1}H\}$NMR spectrum of the yellow solid isolated shows clean conversion to a new species, displaying a doublet at δ 30.1, with a Rh–P coupling of 84 Hz suggestive of a Rh(III) species (Figure 5.5). Transformation of $[P_2N_2][Rh(COD)]_2$ to this new species, $[P_2N_2]Rh(CO)[Rh(CO)_2]$ (**5.3**) is shown in Equation 5.3. The IR spectrum of complex **5.3** displays three ν_{CO} stretches at 1938, 1988, and 2020 cm^{-1}, supporting the presence of three CO moieties.

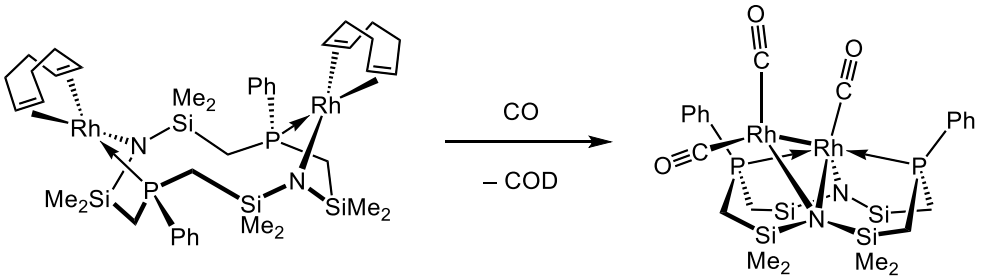

5.1 **5.3**

[5.3]

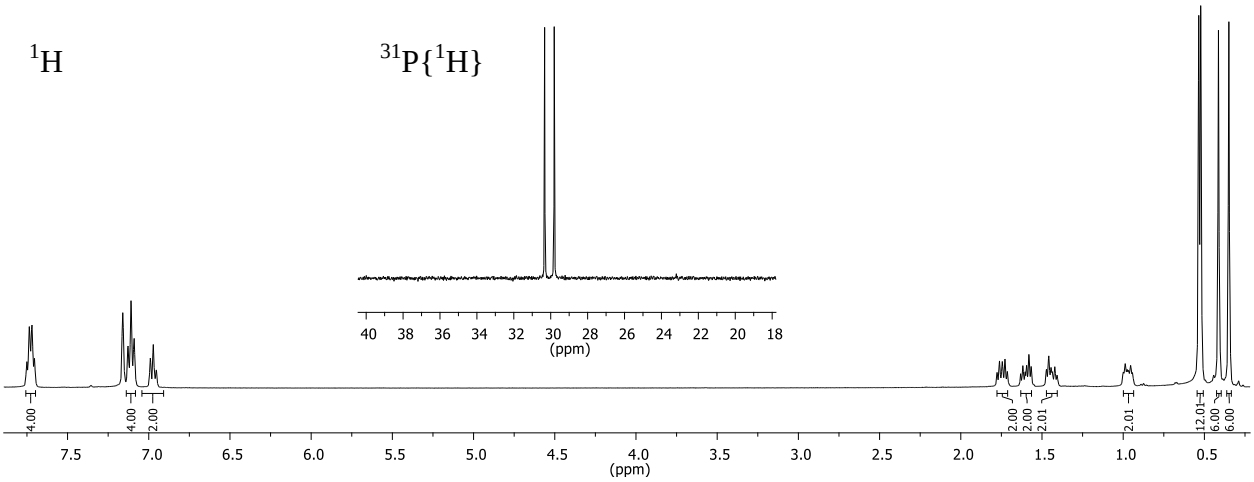

Figure 5.5 $^{31}P\{^{1}H\}$ NMR (161.9 MHz) spectrum (inset) and ^{1}H NMR (400 MHz) spectrum of **5.3** (in C_6D_6).

Single crystals suitable for X-ray diffraction were isolated and the solid-state molecular structure of **5.3** was determined (Figure 5.6). The starting Rh(I)–Rh(I) species **5.1** has been transformed to complex **5.3**, containing a $[P_2N_2]$-bound Rh(III) centre (with one CO substituent) connected to a Rh(-I) centre (with two CO ligands) via an amido bridge and a Rh–Rh bond (with a Rh1–Rh2 bond distance of 2.5675(3) Å). Coordination of three CO molecules has occurred to generate **5.3**, forming three new Rh–C bonds. The Rh1–C1, Rh2–C2 and Rh2–C3 bond lengths (1.843(3), 1.845(3) and 1.874(2) Å respectively) are comparable to those reported for rhodium carbonyl complexes.[161-163, 171] The Rh(III) centre (Rh1) in **5.3** exhibits distorted octahedral geometry, with the P1–Rh1–P2, N1–Rh1–Rh2 and C1–Rh1–N2 bond angles (173.38(2)°, 155.24(6)° and 149.34(9)° respectively) demonstrating the deviation from idealized octahedral symmetry. The geometry about Rh2 in **5.3** is distorted square planar, with C2–Rh2–N2 and C3–Rh2–Rh1 bond angles of 161.08(9)° and 162.19(8)° respectively.

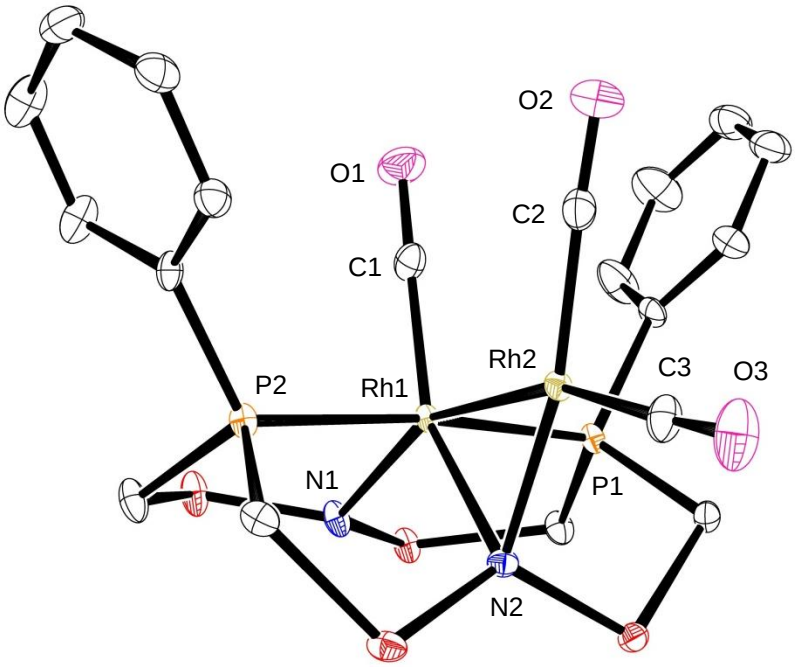

Figure 5.6 ORTEP depiction (ellipsoids at 50 % probability) of $[P_2N_2]Rh(CO)[Rh(CO)_2]$ (**5.3**). Silyl methyl carbons are omitted for clarity. Selected bond lengths (Å) and angles (°): Rh1–Rh2, 2.5675(3); Rh1–C1, 1.843(3); Rh2–C2, 1.845(3); Rh2–C3, 1.874(2); Rh1–N1, 2.217(2); Rh1–N2, 2.216(2); Rh2–N2, 2.1034(19); Rh1–P1, 2.3234(6); Rh1–P2, 2.3338(7); P1–Rh1–P2, 173.38(2); N1–Rh1–Rh2, 155.24(6); C1–Rh1–N2, 149.34(9); C2–Rh2–N2, 161.08(9); C3–Rh2–Rh1, 162.19(8).

5.3 Synthesis and reactivity of $([Rh(COE)][P_2N_2]Li)_2$(dioxane)

Oxidative addition with the $[P_2N_2][Rh(COD)]_2$ system proved challenging, perhaps due to difficulty in displacing the strongly-coordinated COD. In the interest of synthesizing a $[P_2N_2]$ rhodium species with a more labile substituent than COD, coordination of $[P_2N_2]$ to rhodium using $[Rh(COE)_2Cl]_2$ was investigated. Treatment of *syn*-$[P_2N_2]Li_2$ with $[Rh(COE)_2Cl]_2$ afforded a yellow solid, giving rise to two new doublet of doublets at δ 11.5 and δ 23.1 in the $^{31}P\{^1H\}$NMR spectrum (Figure 5.7). The phosphines are inequivalent, coupling to each other

(J_{PP} = 384 Hz), and coupling to rhodium (J_{RhP} = 123 Hz and 114 Hz, suggestive of a Rh(I) species). In the $^{1}H\{^{31}P\}$ NMR spectrum, a strong singlet was observed at δ 3.6, suggestive of the presence of a coordinated dioxane molecule (Figure 5.7).

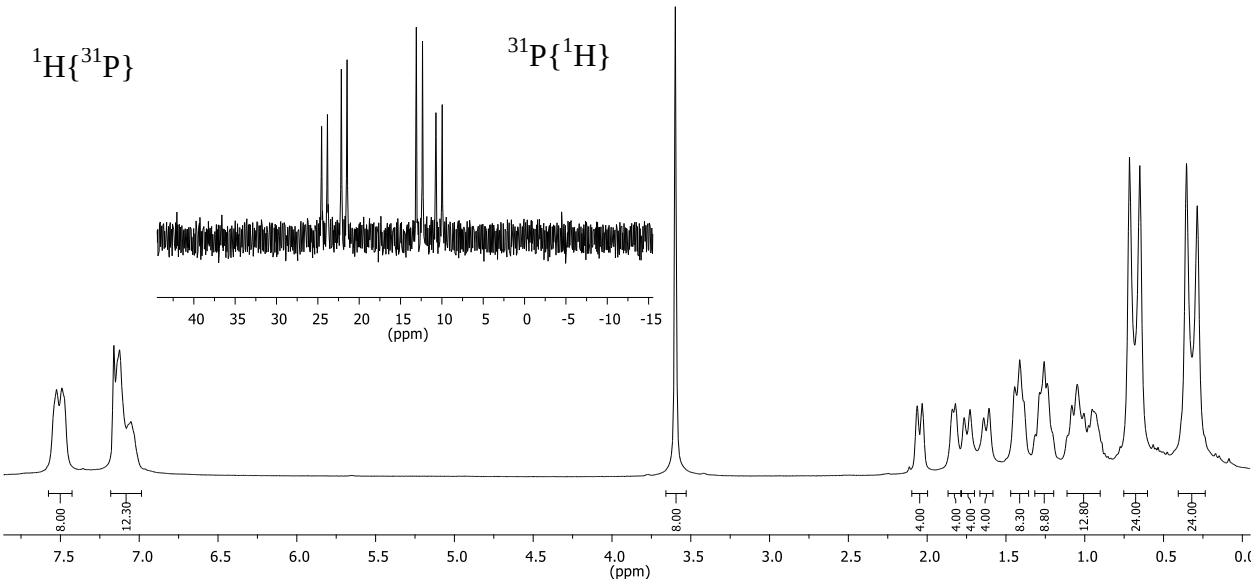

Figure 5.7 $^{31}P\{^{1}H\}$ NMR (161.9 MHz) spectrum (inset) and $^{1}H\{^{31}P\}$ NMR (400 MHz) spectrum of **5.4** (in C_6D_6).

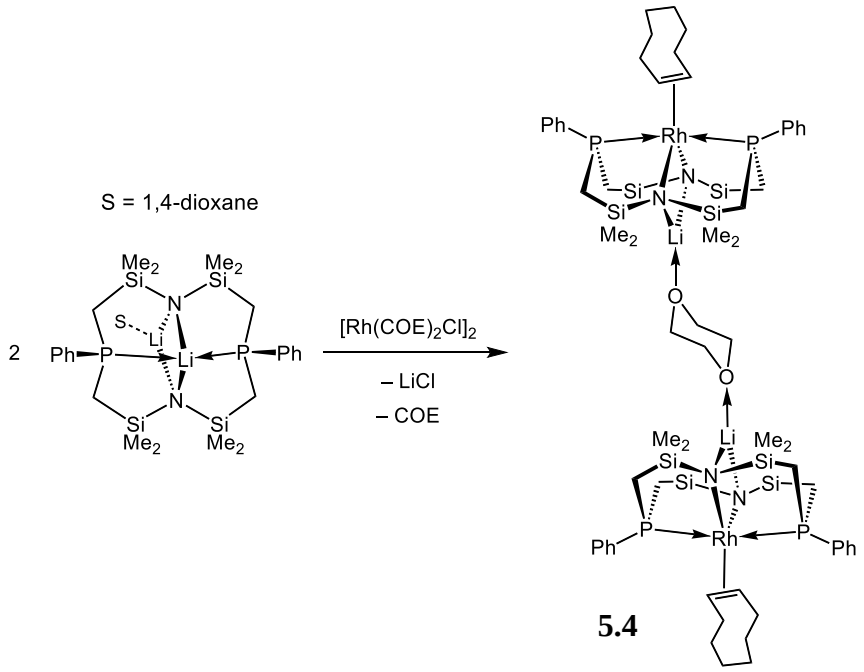

[5.4]

Equation 5.4 shows the formation of a new rhodium complex, ([Rh(COE)][P_2N_2]Li)$_2$(dioxane) **(5.4)**. X-ray diffraction studies confirmed the structure of a single complex that matches the NMR spectroscopy data. The solid-state molecular structure of **5.4** is shown in Figure 5.8. Complex **5.4** contains two [P_2N_2] rhodium units bridged by a Li-coordinated dioxane molecule.

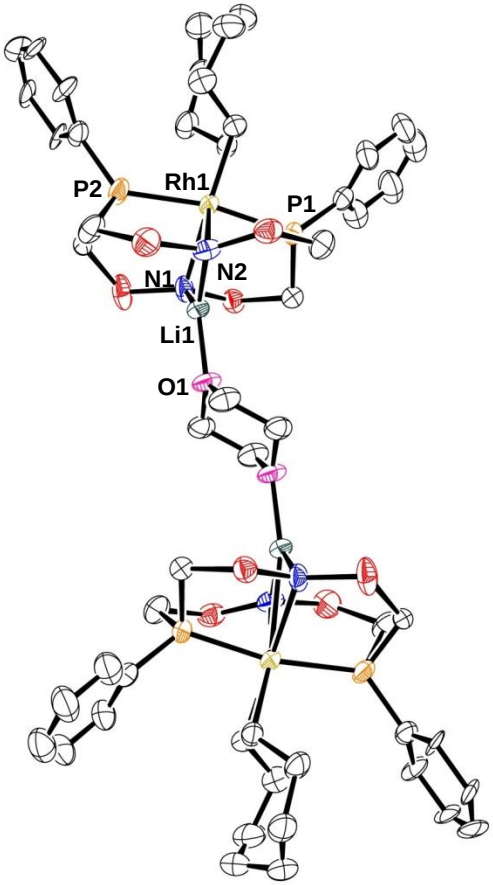

Figure 5.8 ORTEP depiction (ellipsoids at 50 % probability) of ([Rh(COE)][P_2N_2]Li)$_2$(dioxane) (**5.4**). Silyl methyl carbons are omitted for clarity. Selected bond lengths (Å) and angles (°): Rh1–N1, 2.453(4); Rh1–N2, 2.452(4); Rh1–P1, 2.2998(12); Rh1–P2, 2.3506(14); N1–Li1, 1.949(8); N2–Li1, 1.973(9); P1–Rh1–P2, 168.32(5); N1–Rh1–N2, 85.46(12).

The geometry about each Rh(I) centre is distorted trigonal bipyramidal, with one COE coordinated to each rhodium; the P1–Rh1–P2 and N1–Rh1–N2 bond angles (168.32(5)° and 85.46(12)°, respectively) demonstrate the distortion from idealized trigonal bipyramidal symmetry.

5.3.1 Reactivity of ([Rh(COE)][P_2N_2]Li)$_2$(dioxane) with alkyl halides

To explore the ability of ([Rh(COE)][P_2N_2]Li)$_2$(dioxane) **(5.4)** to undergo oxidative addition, in comparison to the [P_2N_2][Rh(COD)]$_2$ system, treatment of **5.4** with alkyl halides was investigated. Upon treatment of **5.4** with 1 equivalent of MeI, multiple peaks were observed in the ^{31}P{^{1}H}NMR spectrum. The resonances of the starting complex **5.4** disappeared and two new doublets appeared at δ 16.6 and 27.1, with Rh–P coupling constants of 99 Hz and 101 Hz respectively. Addition of excess (2-4 equivalents) MeI to **5.4** was also examined, leading to formation of the same species. Isolation of these species proved challenging and was ultimately unsuccessful, hindering further characterization and identification via NMR spectroscopy and X-ray crystallography.

Treatment of **5.4** with I-CH_2CH_2-I resulted in formation of a mixture of species, observed via ^{31}P{^{1}H}NMR spectroscopy. New doublet resonances appear at δ 16.6 and 63.8, with Rh–P couplings of 85 Hz and 133 Hz respectively, suggestive of a Rh(III) and a Rh(I) species. Attempts to isolate these species for further NMR spectroscopy and X-ray crystallography studies were unsuccessful and the identity of the products remain elusive.

5.3.2 Reactivity of ([Rh(COE)][P_2N_2]Li)$_2$(dioxane) with H_2 and CO

Oxidative addition of H_2 to complex **5.4** was also investigated, yielding a new rhodium hydride complex. Exposing a toluene solution of **5.4** to 4 atm of H_2 gas results in conversion to a new species (**5.5)**, giving rise to a doublet at δ 32.9 in the $^{31}P\{^1H\}$NMR spectrum with a Rh–P coupling of 108 Hz (Figure 5.9). In the ^1H NMR spectrum, a new resonance at δ -17.5, that integrates to 2H (relative to the silyl methyl signals), suggests the presence of two rhodium hydrides (Figure 5.9). Interestingly, there is another new resonance at δ 2.0 in the ^1H NMR spectrum that integrates to 1H (relative to the silyl methyl signals). Various 2D NMR experiments (^1H–^{13}C HSQC, ^1H–^{31}P HMBC, and ^1H–^1H COSY) confirmed that the hydride resonance (δ -17.5) does not correlate to carbon or phosphorus (or any other protons), supporting evidence of hydrides bound to rhodium. Similarly, the proton resonance at δ 2.0 does not correlate to carbon or phosphorus, or any other protons (such as the rhodium hydride resonance), suggesting this proton is bound to a heteroatom other than rhodium. This evidence suggests that the proton signal at δ 2.0 corresponds to an N–H on [P_2N_2H]. Additionally, a ^1H–^{13}C HMBC experiment shows a correlation between the proton resonance at δ 2.0 and a silyl methyl resonance, further supporting the assignment of an N–H proton.

Numerous efforts towards synthesis and purification of complex **5.5** were met with inconsistent results, giving unexpected insight into the mechanism of formation of **5.5** and the origin of the N–H. Several attempts resulted in the appearance of an additional resonance (δ -16.8) in the hydride region of the ^1H NMR spectrum (with varying integration values relative to the silyl methyl resonances and the other hydride resonance at δ -17.5) as well as additional silyl methyl signals (Figure 5.10).

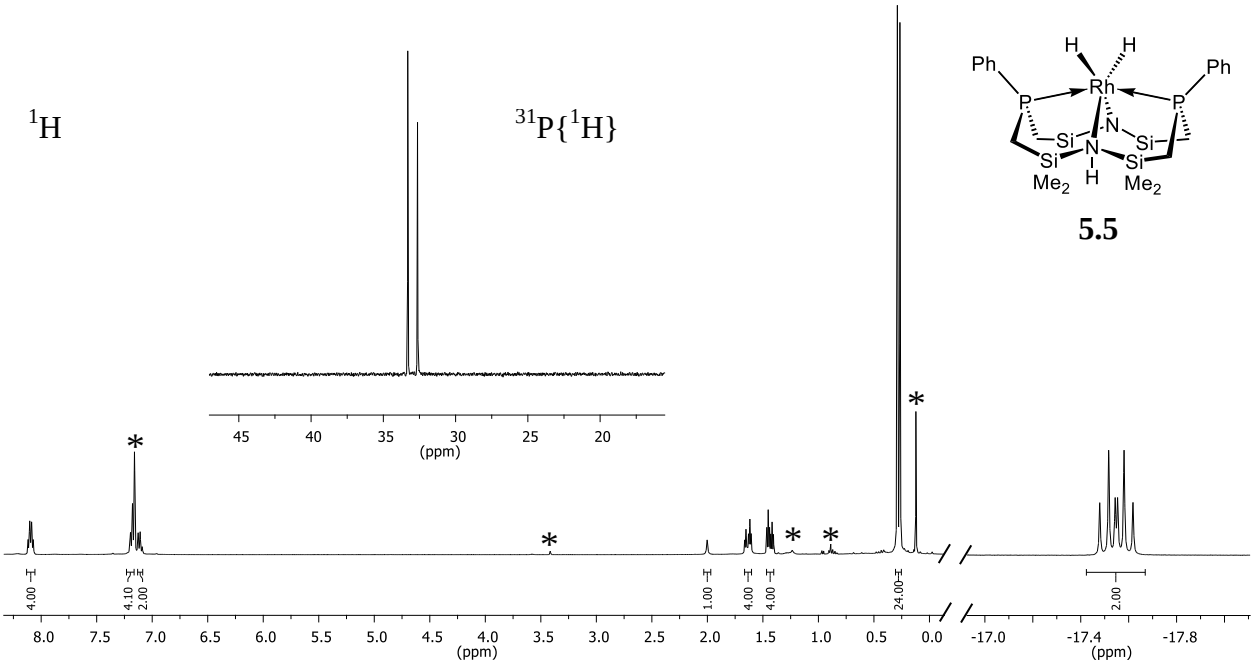

Figure 5.9 ^{31}P{^{1}H} NMR (161.9 MHz) spectrum (inset) and ^{1}H NMR (400 MHz) spectrum of complex **5.5** (in C_6D_6). (Resonances denoted with (*) indicate residual solvent impurities).

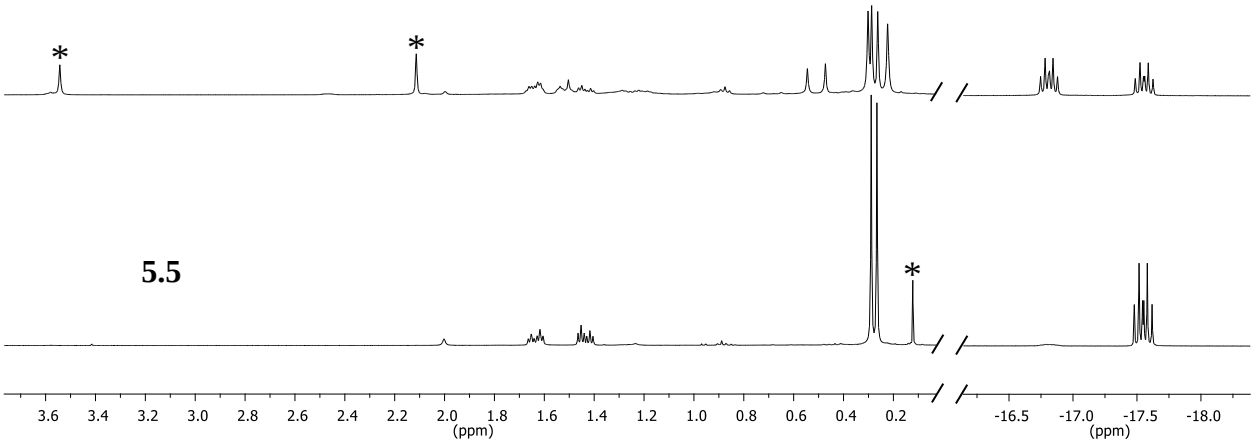

Figure 5.10 Comparison of the ^{1}H NMR spectra (400 MHz, C_6D_6) of the material generated from treatment of **5.4** with H_2 (top spectrum) and complex **5.5** isolated from the aforementioned reaction (bottom), focused on the alkyl and hydride regions of the spectra. (Resonances denoted with (*) correspond to dioxane, toluene and HMDSO.)

Upon extracting the reaction material with hexane, filtering the solution and removing the solvent under vacuum, the additional silyl methyl resonances and the hydride resonance at δ -16.8 disappeared from the ^{1}H NMR spectrum and the integration values were as expected. This evidence challenged the initial conjecture that the N–H originated from H_2, instead leading to speculation about the presence of adventitious water as a contributing factor. Given that the appearance of these additional resonances correlates with the presence of a strong dioxane signal in the ^{1}H NMR spectrum, it is probable that there is an intermediary species containing Li-coordinated dioxane (such as $(C_4H_8O_2)Li[P_2N_2]Rh(H)_2$) that is subsequently converted to $[P_2N_2H]Rh(H)_2$ (**5.5**). The proposed transformation of complex **5.4** to the rhodium hydride complex **5.5** via the intermediate species $(C_4H_8O_2)Li[P_2N_2]Rh(H)_2$ is shown in Scheme 5.3.

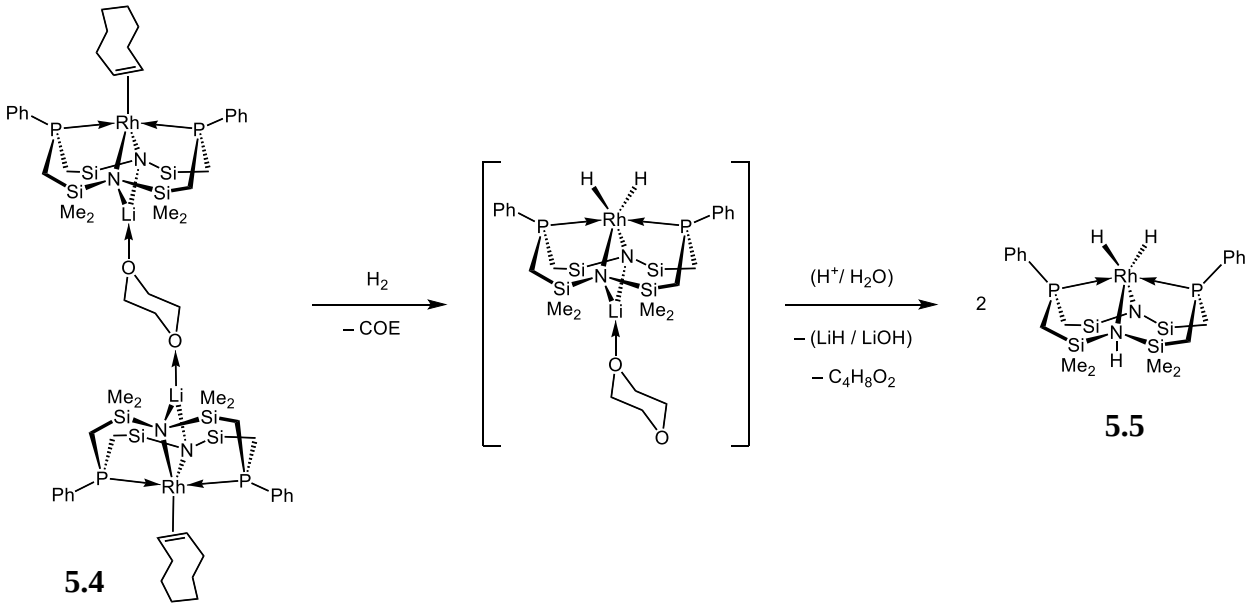

Scheme 5.3

Crystals suitable for X-ray diffraction studies were isolated and the solid state molecular structure of $[P_2N_2H]Rh(H)_2$ (**5.5**), was determined (Figure 5.11). The geometry about the Rh(III)

centre is distorted octahedral; the P1–Rh1–P2, N1–Rh1–H1R and N2–Rh1–H2R bond angles (172.076(14)°, 177.2(9)° and 178.4(9)° respectively) demonstrate the distortion from idealized octahedral symmetry. The Rh–H bond lengths (1.57(2) and 1.53(2) Å) are comparable to those reported for rhodium hydride complexes.[170, 182]

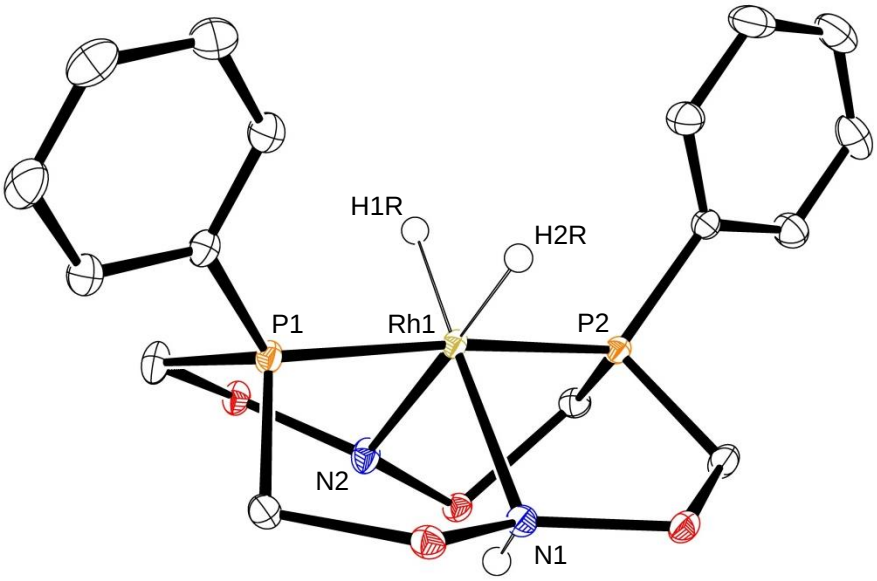

Figure 5.11 ORTEP depiction (ellipsoids at 50 % probability) of $[P_2N_2H]Rh(H)_2$ (**5.5**). Silyl methyl carbons are omitted for clarity. Selected bond lengths (Å) and angles (°): Rh1–N1, 2.3305(13); Rh1–N2, 2.2583(13); Rh1–P1, 2.2860(4); Rh1–P2, 2.2672(4); Rh1–H1R, 1.57(2); Rh1–H2R, 1.53(2); P1–Rh1–P2, 172.076(14); N1–Rh1–H1R, 177.2(9); N2–Rh1–H2R, 178.4(9).

Given the reactivity of the $[P_2N_2][Rh(COD)]_2$ system and CO, exposure of $([Rh(COE)][P_2N_2]Li)_2$(dioxane) (**5.4)** to CO gas was also explored for comparison. A toluene solution of complex **5.4** was treated with 4 atm of CO gas, affording complex **5.6** as a yellow solid. A doublet resonance at δ 22.8 was observed in the $^{31}P\{^1H\}$NMR spectrum (Figure 5.12), with a Rh–P coupling constant (127 Hz) suggestive of a Rh(I) species. In the ^1H NMR spectrum,

resonances corresponding to the COE and coordinated dioxane in **5.4** have disappeared. Similar to complex **5.5**, there is a new resonance at δ 1.1 in the ^{1}H NMR spectrum (Figure 5.12) that integrates to 1H (relative to the silyl methyl signals). Analogous 2D NMR experiments (^{1}H–^{13}C HSQC, ^{1}H–^{31}P HMBC, and ^{1}H–^{1}H COSY) confirmed that the proton resonance at δ 1.1 does not correlate to carbon or phosphorus, or any other protons, suggesting this proton is bound to a heteroatom. Similarly, a ^{1}H–^{13}C HMBC experiment shows a correlation between the proton resonance at δ 1.1 and silyl methyl resonances, suggesting that this proton signal corresponds to an N–H on [P_2N_2H], such as seen in complex **5.5**. However, in the synthesis of complex **5.6** (compared to **5.5**) there is no H_2 available to give rise to an N–H; adventitious water as a possible origin is speculative. The ^{13}C NMR spectrum of **5.6** shows a resonance at δ 193.2, typical of a carbonyl, suggesting the presence of a CO unit.

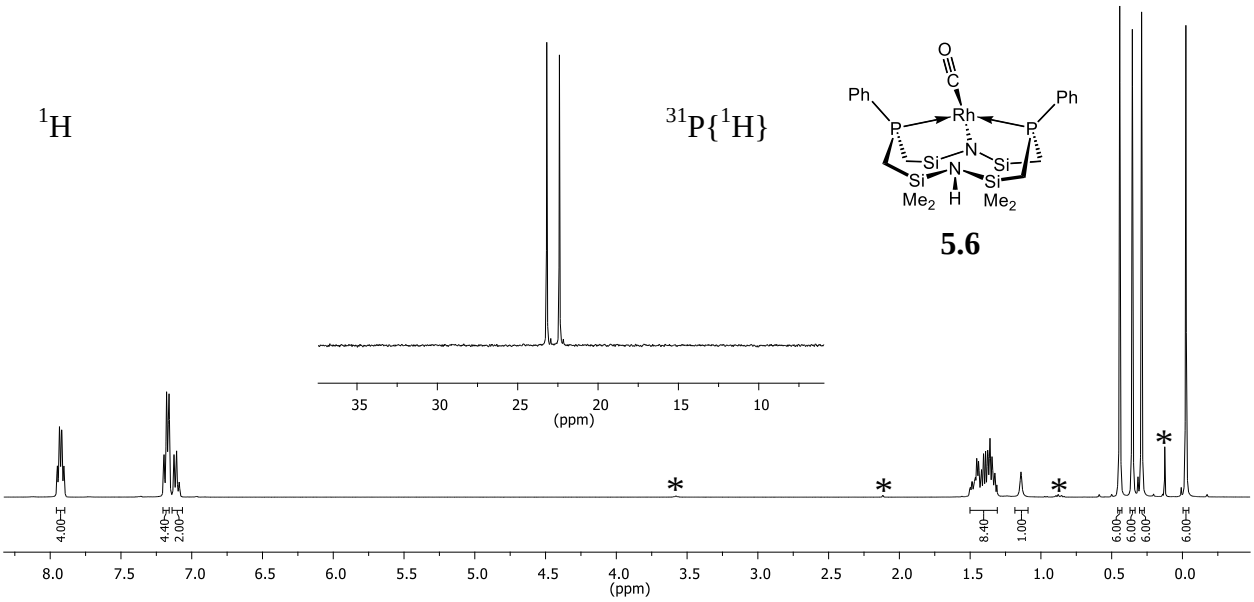

Figure 5.12 ^{31}P{^{1}H} NMR (161.9 MHz) spectrum (inset) and ^{1}H NMR (400 MHz) spectrum of **5.6** (in C_6D_6). (Resonances denoted with (*) indicate residual solvent impurities).

Complex **5.6** displays a ν_{CO} stretch at 1929 cm^{-1} in the IR spectrum, further supporting the presence of a CO moiety. Analysis of the various spectroscopic experiments lead to the assignment of complex **5.6** as a new rhodium carbonyl complex, $[P_2N_2H]Rh(CO)$.

Notable challenges were encountered in synthesizing and isolating pure **5.6**, leading to speculation about the role of coordinating solvent in this reaction. During various attempts to synthesize **5.6**, minor additional resonances were observed in the $^{31}P\{^1H\}$NMR spectrum of the material generated from the reaction, as well as additional silyl methyl resonances in the ^1H NMR spectrum. Postulating that these additional resonances may correspond to a species containing Li-coordinated solvent, an experiment was conducted using THF as the reaction solvent for comparison. An additional doublet resonance at δ 22.5 (with a Rh–P coupling constant of 127 Hz, suggestive of a Rh(I) species) was observed in the $^{31}P\{^1H\}$NMR spectrum of the material generated from the reaction of **5.4** with CO using THF as the solvent (Figure 5.13). In the $^1H\{^{31}P\}$ NMR spectrum (Figure 5.13), additional silyl methyl signals are observed, as well as a resonance at δ 3.6 that corresponds to THF. Analogous to what was observed in the $[P_2N_2H]Rh(H)_2$ system, the appearance of these additional resonances correlates with the presence of strong coordinating solvent signals in the $^1H\{^{31}P\}$ NMR spectra, suggestive of an intermediate species containing Li-coordinated solvent. Transformation of complex **5.4** to the rhodium carbonyl complex **5.6,** with a proposed intermediate species, is shown in Scheme 5.4.

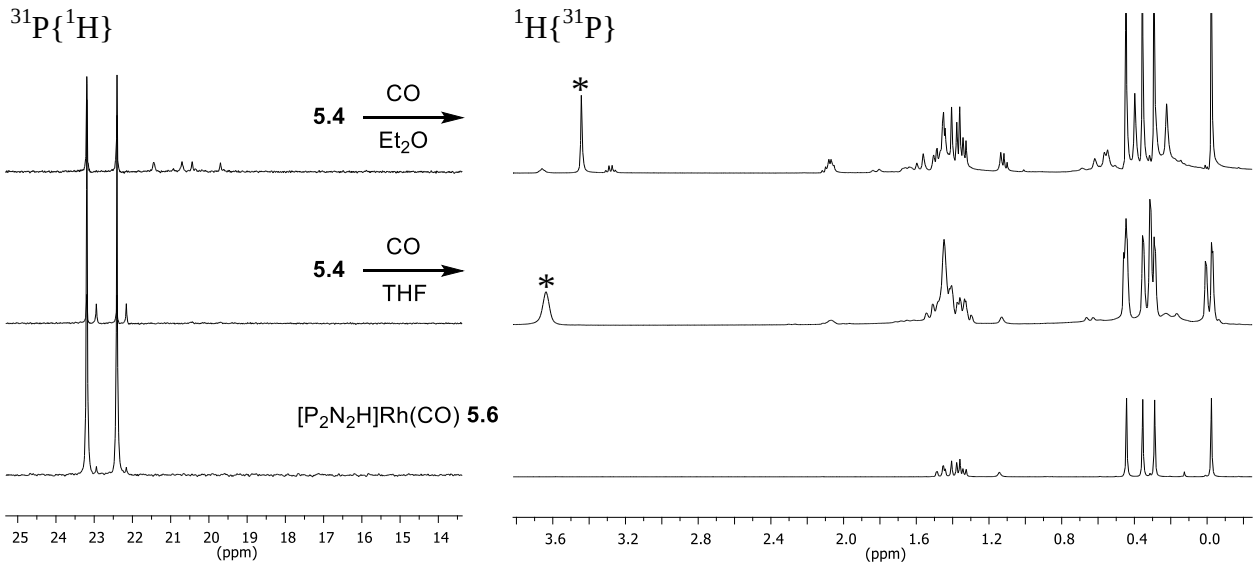

Figure 5.13 $^{31}P\{^{1}H\}$ NMR (161.9 MHz) spectra (left) and the alkyl region of the $^{1}H\{^{31}P\}$ NMR (400 MHz) spectra (right), all in C_6D_6, comparing the material generated from the reaction of CO with an Et_2O solution of **5.4** (top) and the material generated from the reaction of CO with a THF solution of **5.4** (middle) to complex **5.6** (bottom). (Resonances denoted with (*) correspond to dioxane and THF, respectively).

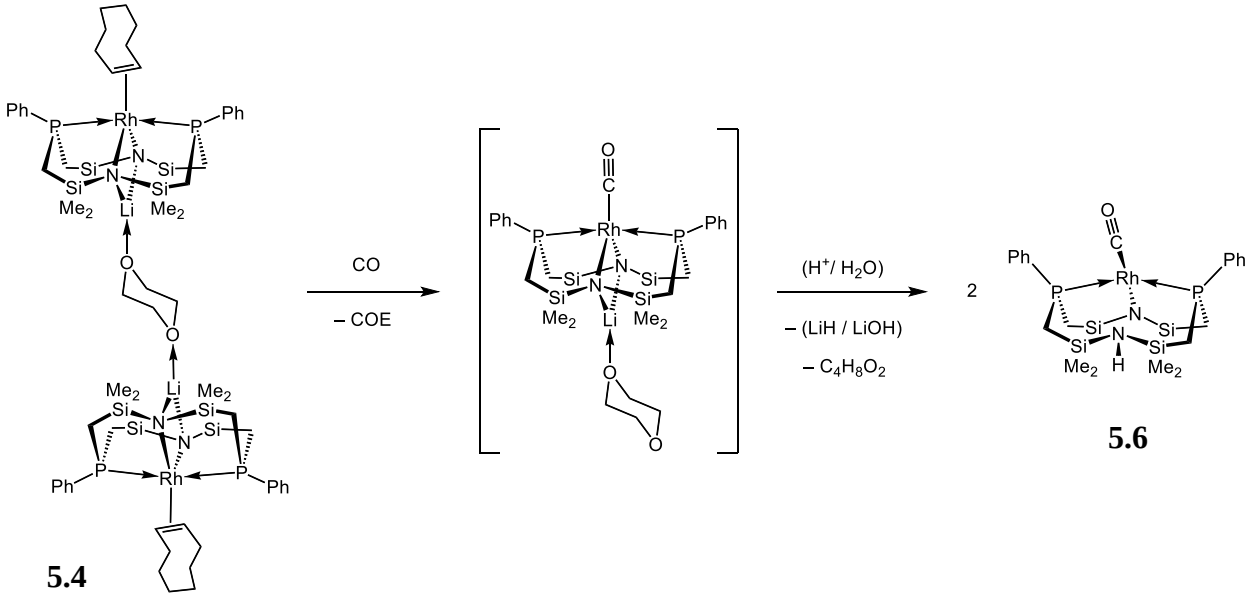

Scheme 5.4

Crystals suitable for X-ray diffraction were isolated from a concentrated HMDSO solution of **5.6** stored at –40 °C. The solid-state molecular structure of **5.6** is shown in Figure 5.14. The geometry about the Rh(I) centre in **5.6** is distorted square planar. The P1–Rh1–P2 and N2–Rh1–C1 bond angles (156.344(13)° and 176.89(6)° respectively) demonstrate the distortion from idealized square planar symmetry. The amino nitrogen (N1) is no longer coordinated to rhodium, with a Rh1···N1 interatomic distance of 3.561 Å.

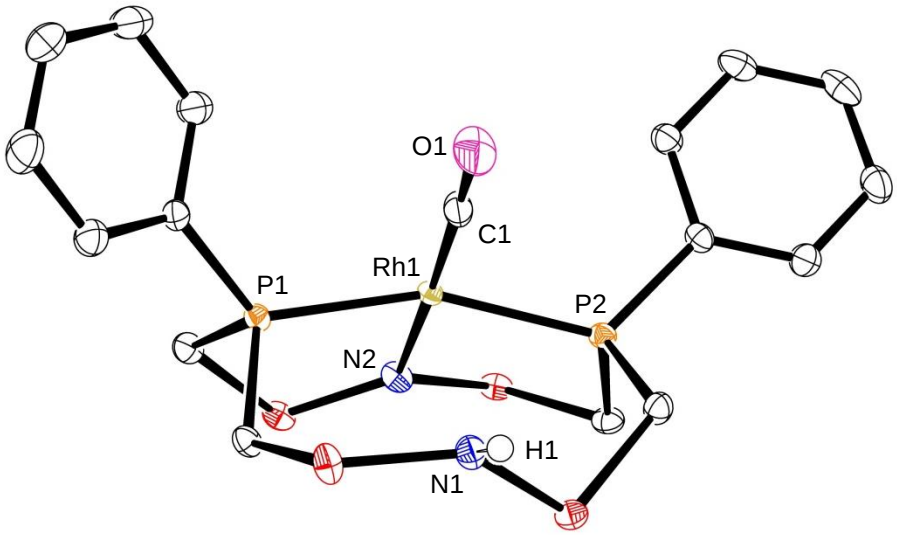

Figure 5.14 ORTEP depiction (ellipsoids at 50 % probability) of $[P_2N_2H]Rh(CO)$ (**5.6**). Silyl methyl carbons are omitted for clarity. Selected bond lengths (Å) and angles (°): Rh1–N2, 2.1034(11); Rh1–P1, 2.2909(4); Rh1–P2, 2.2968(4); Rh1–C1, 1.8109(14); P1–Rh1–P2, 156.344(13); N2–Rh1–C1, 176.89(6).

5.4 Conclusions

The novel $[P_2N_2]$ rhodium complexes, $[P_2N_2][Rh(COD)]_2$ (**5.1**) and $([Rh(COE)][P_2N_2]Li)_2$(dioxane) (**5.4**) were synthesized and their ability to undergo oxidative addition was investigated via treatment with alkyl halides and H_2. While no reactivity was observed between **5.1** and MeI, treatment of **5.4** with MeI produces a mixture of $[P_2N_2]$ rhodium

species that eluded characterization. Complex **5.1** shows reactivity with I-CH_2CH_2-I, generating the bridging iodide species $[P_2N_2]Rh(\mu\text{-}I)_2Rh[COD]$ (**5.2**). Reactivity between I-CH_2CH_2-I and **5.4** was also observed, forming a mixture of Rh(III) and Rh(I) species. Rhodium hydride species were observed upon exposure of both **5.1** and **5.4** to H_2 gas. Formation of the new $[P_2N_2]$ rhodium dihydride complex $[P_2N_2H]Rh(H)_2$ (**5.5)** results from reactivity of H_2 with complex **5.4**. Displacement of the COD units from **5.1** was accomplished via treatment with CO. Exposure of **5.1** to CO generates the new bimetallic rhodium carbonyl complex $[P_2N_2]Rh(CO)[Rh(CO)_2]$ (**5.3**). In comparison, reactivity of **5.4** with CO results in the formation of the rhodium carbonyl complex $[P_2N_2H]Rh(CO)$ **(5.6)**. Scheme 5.5 summarizes and compares the reactivity of complex **5.1** and complex **5.4**.

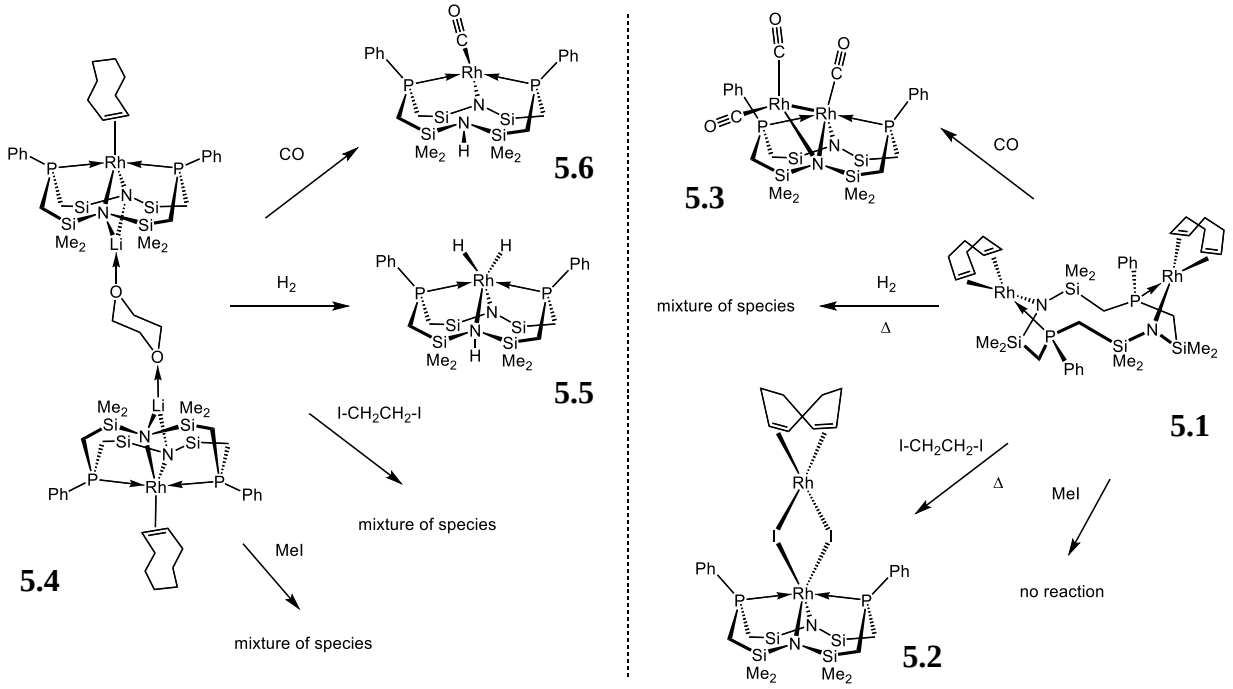

Scheme 5.5

Chapter 6: Thesis overview, diversions and future outlook

6.1 Overview

The overarching themes of ligand design/modification and dinitrogen activation/functionalization form the basis of the research that led to this work. Small molecule reactivity and exploration of chemical space also figure prominently in these pursuits. In Chapter 2, ligand modification was utilized to probe further functionalization of a dinitrogen complex. The hydrosilylation of the modified [NPN^{Si}] P–cyclohexyl tantalum N_2 complex **2.4** was investigated, resulting in N–N bond cleavage and N–Si bond formation to generate complex **2.7**. While the goal of avoiding cyclometallation of the phosphorus substituent was met, elimination of a functionalized nitrogen compound was not achieved.

With the aim of dinitrogen functionalization, reactivity of the paramagnetic [P_2N_2] niobium and vanadium N_2 complexes ([P_2N_2]Nb)$_2$(μ-N_2) and ([P_2N_2]V)$_2$(μ-N_2) was pursued in Chapter 3. Treatment of ([P_2N_2]Nb)$_2$(μ-N_2) and ([P_2N_2]V)$_2$(μ-N_2) with a number of electrophiles and oxidants resulted in the formation of a variety of new species. However, rather than realizing oxidized N_2 species or cleavage and functionalization of the N_2 moiety, loss of N_2 was the predominant outcome. The most notable finding was a diamagnetic niobium N_2 complex **3.8** containing a side-on bound N_2 unit and a bridging oxo ligand, resulting from the reactivity of ([P_2N_2]Nb)$_2$(μ-N_2) with the oxygen containing radical TEMPO. Alteration of the bonding arrangement from end-on to side-on bridging N_2 could lead to enhanced reactivity of the N_2 unit,[183] providing an opportunity for further reactivity studies with **3.8**.

Following up on previously reported work with paramagnetic cobalt species, the study of paramagnetic [P_2N_2] complexes of cobalt was continued in Chapter 4. In comparison to the previously observed reactivity of *anti*-[P_2N_2]Co, the analogous reactivity of the *syn*-[P_2N_2]Co

complex **4.1** was explored, producing an oxidized-phosphine species (**4.2**) and the cobalt iodide complex **4.3**. Investigating the reactivity of **4.3** with alkylithium and Grignard reagents lead to generation of cobalt alkyl complexes **4.4-$_{dioxane}$** and **4.5**. Regeneration of **4.1** was observed in the pursuit of isolating a cobalt hydride complex, underlining the labile nature of cobalt hydride species.

Further exploration of group 9 metal complexes of [P_2N_2] was initiated, with diamagnetic [P_2N_2] rhodium complexes becoming the focus of Chapter 5. Synthesis of the [P_2N_2] rhodium complexes **5.1** and **5.4** was accomplished and their ability to undergo oxidative addition was explored by treatment with alkyl halides and H_2. The bridging iodide species **5.2** results from reactivity of **5.1** with I-CH_2CH_2-I. Reactivity of **5.4** with H_2 was observed, leading to formation of the rhodium dihydride species **5.5**. Ligand exchange was accomplished upon exposure of both **5.1** and **5.4** to CO, generating the rhodium carbonyl complexes **5.3** and **5.6**.

6.2 Diversions

Several alternate projects were explored during the course of this work that proved challenging and unfruitful. Attempts to coordinate [NPN^{Si}] to group 6 metals (Mo and W) resulted in the production of paramagnetic materials that resisted characterization. Efforts to synthesize rhenium complexes of [NPN^{Si}] were also unsuccessful. Reactivity of the ditantalum tetrahydride species ([NPN^{Si}]Ta)(μ-H)$_4$ (**1.31**) with NO was explored, by way of comparison to the previously reported reactivity of ([NPN^{Si}]Ta)(μ-H)$_4$ with N_2 and CO (Scheme 6.1).[65, 184] Upon treatment of a diethyl ether solution of **1.31** with one equivalent of NO, the reaction mixture changed colour from deep purple to dark orange-brown. The isolated brown paramagnetic material showed a lack of resonances in the $^{31}P\{^1H\}$ NMR spectrum and very

broad signals evident in the ^{1}H NMR spectrum. Crystals suitable for X-ray diffraction studies remain elusive, hindering attempts to identify the species produced.

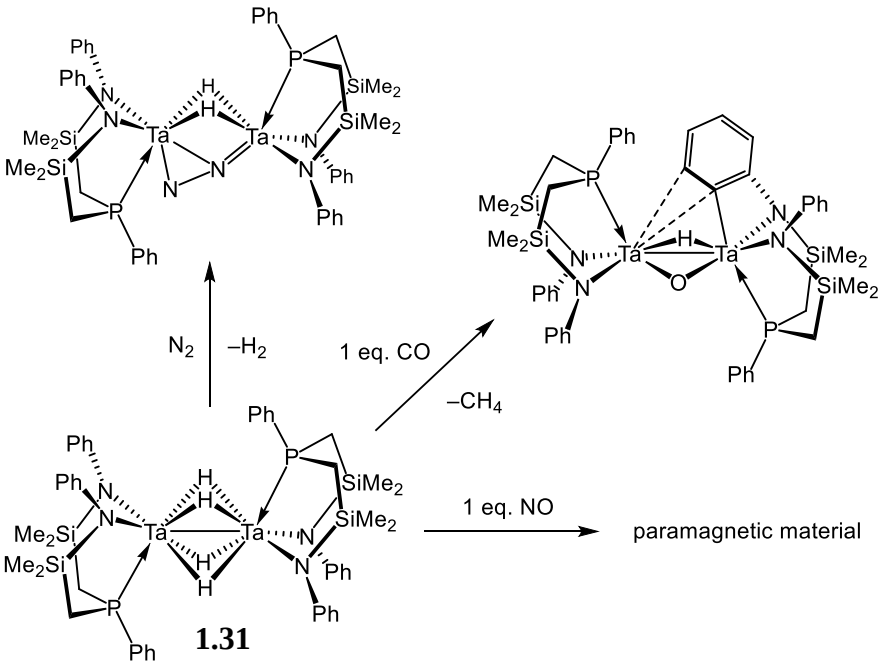

Scheme 6.1

Design of an alternative NPN pincer ligand was also pursued. An adaptation of the *ortho*-phenylene linked NPN* ligand system was proposed, containing benzylene linkers between the amine and phosphine donors (Scheme 6.2). Various strategies of installing the phosphine and amine donors were explored and proved unsuccessful. However, successful synthesis and coordination of the proposed ligand to Hf and Zr was later reported by another group.[185]

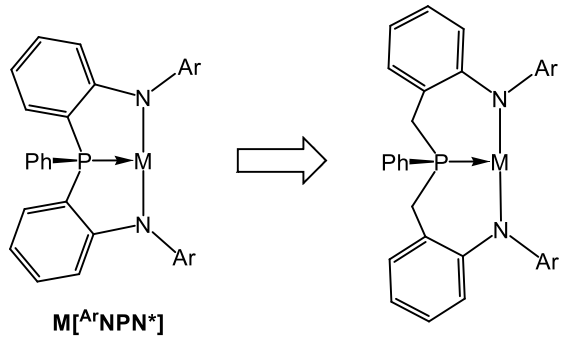

M[^{Ar}NPN*]

Ar = Ph, tol (4-MePh) iPr (4-^{i}PrPh)

Scheme 6.2

6.3 Future outlook

Expanding on the work in Chapter 3, reactivity studies of the side-on bridged N_2 complex $([P_2N_2]Nb)_2(\mu\text{-}\eta^2{:}\eta^2\text{-}N_2)(\mu\text{-}O)$ (**3.8**) could be investigated. In analogy to previous work showing reactivity of side-on bound N_2 complexes with various electrophiles (see Chapter 1), the treatment of **3.8** with electrophiles is of interest. Scheme 6.3 outlines the potential treatment of **3.8** with H_2, alkyl halide and E–H reagents. Preliminary exploration of the treatment of **3.8** with H_2 indicates no reactivity with 1 atm of H_2 at room temperature. Additional studies are warranted to observe if the difference in bonding arrangement of the N_2 moiety from end-on in $([P_2N_2]Nb)_2(\mu\text{-}N_2)$ to side-on in **3.8** promotes further reactivity.

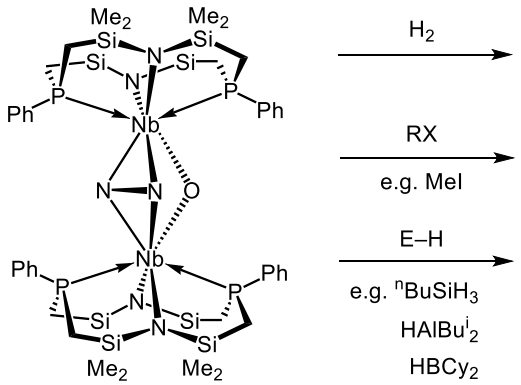

Scheme 6.3

In relation to the work covered in Chapter 3, the reactivity of $([P_2N_2]V)_2(\mu\text{-}N_2)$ with AgOTf was examined, producing intriguing results. Treatment of $([P_2N_2]V)_2(\mu\text{-}N_2)$ with two equivalents of AgOTf yielded a green paramagnetic material that displays broad peaks in the ^1H NMR spectrum. Single crystals suitable for X-ray diffraction studies were isolated from this material and a solid state molecular structure was determined. Figure 6.1 shows the structure of $[P_2N_2]V(OTf)_2NH_3$ (**6.1**), with two triflate molecules coordinated to the vanadium centre, and what appears to be an ammonia ligand. In addition, one of the $[P_2N_2]$ amine donors has been protonated and is no longer coordinated to the vanadium.

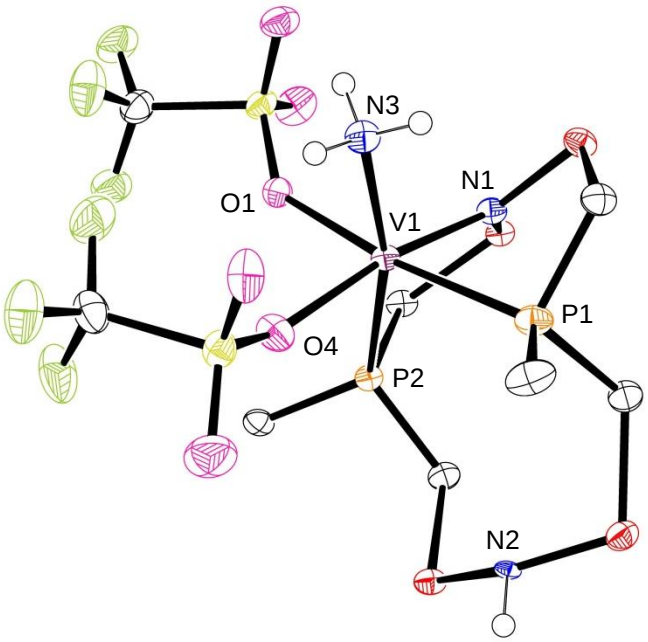

Figure 6.1 ORTEP depiction (ellipsoids at 50 % probability) of $[P_2N_2]V(OTf)_2NH_3$ (**6.1**). Silyl methyl and P-phenyl ring carbons other than ipso are omitted for clarity. Selected bond lengths (Å) and angles (°): V1–N3, 2.187(3); V1–N1, 1.940(3); V1–O1, 2.094(3); V1–O4, 2.093(3); V1–P1, 2.5894(13); V1–P2, 2.5692(12); P2–V1–N3, 165.66(10); P1–V1–O1, 171.93(9); N1–V1–O4, 170.92(14).

The possibility that **6.1** contains a nitrido instead of an ammonia ligand was considered, yet the V1–N3 bond distance of 2.187(3) Å is much longer than reported vanadium nitride bonds,[186-187] ruling out **6.1** as a vanadium nitride species. What is unclear is where the amine protons originate from or the fate of the remaining $[P_2N_2]$ vanadium fragment. Additional studies could substantiate the formation of **6.1** and aid in understanding how the reaction between $([P_2N_2]V)_2(\mu\text{-}N_2)$ and AgOTf proceeds.

Chapter 7: Experimental

7.1 General procedures

All experiments used oven- or flame-dried glassware cooled under vacuum and were performed under an atmosphere of dry, oxygen-free dinitrogen, using standard Schlenk techniques or glovebox (equipped with a -40°C freezer). Nitrogen gas was dried and deoxygenated by passage through a column containing activated molecular sieves and copper catalyst. Anhydrous diethyl ether, hexanes, toluene and THF were purchased from Aldrich, sparged with dinitrogen, passed through towers containing activated alumina and collected over activated molecular sieves. Pentane and acetonitrile were distilled from sodium benzophenone ketyl and collected over activated molecular sieves. DMSO was degassed and stored over activated molecular sieves. Benzene-d_6 was dried with sodium benzophenone ketyl, trap-to-trap distilled, and freeze-pump-thaw degassed. Tetrahydrofuran-d_8 was purchased from Aldrich (≥99.5 atom % D) in 1 mL ampoules and was dried over activated 4 Å molecular sieves. ^{1}H, ^{31}P, ^{29}Si, ^{7}Li and 2D NMR spectra were recorded on either a Bruker Avance 300 or 400 MHz spectrometer at room temperature. ^{1}H NMR spectra were referenced to residual proton signals in C_6D_6 (δ 7.16) or THF-d_8 (δ 1.72). The ^{31}P{^{1}H} NMR spectra were referenced to external 85% H_3PO_4 at 0.0 ppm. Solution magnetic susceptibilities were measured using the Evans method; the shift in frequency for the ^{1}H NMR signal of cyclooctane in a sealed capillary containing 1 mol% cyclooctane (in C_6D_6 or THF-d_8) was measured relative to a 1 mol% cyclooctane solution (in C_6D_6 or THF-d_8) containing the desired paramagnetic compound. IR spectra were recorded using a PerkinElmer Frontier FT-IR spectrometer with attenuated total reflectance (ATR), as solid samples. Elemental analyses (EA) were performed using a Thermo Flash 2000 Elemental Analyzer by Mr. Derek Smith or Ms. Jenny Lai, at the Department of Chemistry, University of

British Columbia. Multiple samples of each compound were submitted for EA and the best results are reported. For compounds containing a coordinated N_2 unit (**3.5**, **3.8**), the EA values for N are low, consistent with a labile N_2 ligand.[188]

Suitable single crystals were selected, coated in Fomblin oil and mounted on a glass loop. X-ray data was collected on a Bruker DUO or X8 Apex II diffractometer with a graphite-monochromated Mo Kα radiation (λ = 0.71073 Å) at a temperature of 90 or 100 K. Data was integrated using the Bruker SAINT software package.[189] The absorption corrections were performed using the multi-scan technique (SADABS).[190] The structures were solved by direct methods and refined using the WinGX[191] or Olex2[192] software package with the SHELX refinement program.[193] All non-hydrogen atoms were refined anisotropically. All hydrogen atoms (unless specified) were placed in calculated positions and assigned to an isotropic displacement parameter; other specified hydrogen atoms were located in the difference map and were refined isotropically. If no satisfactory model was obtained for a disordered solvent molecule, for further refinement, the contribution of this solvent molecule was subtracted from the reflection data using the SQUEEZE[194] algorithm in PLATON.[195] ORTEPs were generated using ORTEP-3.[191] Tables containing crystallographic structure and refinement data are located in Appendix C.

7.2 Starting materials and reagents

Unless otherwise noted, reagents were obtained from commercial sources and used as received. H_2 (99.99%), CO and Regen gas (10% H_2, 90% N_2) were purchased from Praxair and passed through activated molecular sieves prior to use. Butylsilane was purchased from Aldrich and distilled under vacuum. The deuterated butylsilane ($^{n}BuSiD_3$) was prepared analogous to

literature methods for the preparation of $^{n}BuSiH_3$,[196] except that $LiAlD_4$ was used instead of $LiAlH_4$. The ^{Cy}[NPN]$TaMe_3$[102] complex was prepared according to literature methods and (^{Cy}[NPN]Ta)$_2$(μ-H)$_4$[2] was prepared similar to literature methods, but was not isolated. The compounds *syn*-[P_2N_2]Li_2,[52] [P_2N_2]NbCl,[60] ([P_2N_2]Nb)$_2$(μ-N_2),[61] [P_2N_2]Nb(*μ*-N)Nb[PN_3],[61] ([P_2N_2]NbN)$_2$($AlMe_2$)$_2$,[108] [P_2N_2]VCl,[105] ([P_2N_2]V)$_2$(μ-N_2),[105] HB(C_6H_5)$_2$,[109] [Ph_2I][OTf],[197] $AgBPh_4$,[198] [$FeCp_2$][BPh_4],[199] [$FeCp_2$][BF_4],[200] $CoCl_2(THF)_{1.5}$,[201] were prepared according to reported procedures.

7.3 Synthesis of compounds and experimental procedures

7.3.1 Compounds pertaining to Chapter 2

(^{Cy}[NPN]Ta)$_2$(μ-η^2:η^1-N_2)(μ-H)$_2$ (2.4)

A solution of ^{Cy}[NPN]$TaMe_3$ (2.0 g, 3.0 mmol) in 60 mL of diethyl ether (Et_2O) was transferred into a thick-walled glass vessel equipped with a Teflon valve and thoroughly degassed via 3 freeze-pump-thaw cycles. The vessel was cooled under liquid N_2 and H_2 gas was added. The vessel was sealed, allowed to warm to room temperature and the mixture was stirred for 24 hours. During this time, the solution changed colour from yellow to deep purple. The (^{Cy}[NPN]Ta)$_2$(μ-H)$_4$ solution in Et_2O was then used to prepare (^{Cy}[NPN]Ta)$_2$(μ-η^2:η^1-N_2)(μ-H)$_2$ in a similar fashion, except with the addition of Regen gas. Over the 24 hour stirring period, the solution changed colour from deep purple to brown. The solvent was removed in vacuo and the remaining solids were dried, to afford 1.4 g (74% yield) of (^{Cy}[NPN]Ta)$_2$(μ-η^2:η^1-N_2)(μ-H)$_2$ as a brown powder. X-ray quality crystals were grown from slow evaporation of a hexane solution at –40 °C. ^{1}H{^{31}P} NMR (C_6D_6, 300 MHz) δ –0.03 (s, 6H, Si-C*H*$_3$), 0.10, 0.13, 0.19 (s, overlapping, 18H, Si-C*H*$_3$), 0.54–2.64 (m, broad, overlapping signals, approx. 30H, P–C*H*$_2$, P–

C_6H_{11}, protons from residual Et_2O), 6.83, 7.01, 7.19 (m, overlapping, approx. 20H, N–C_6H_5, residual protons in C_6D_6), 10.51 (s, 2H, Ta–H_b–Ta) $^{31}P\{^1H\}$ NMR (C_6D_6, 121.4 MHz) δ 27.9 (d, J_{PP} = 22.1 Hz) δ 15.8 (m). Anal. Calcd for $C_{48}H_{76}N_6P_2Si_4Ta_2$: C, 45.28; H, 6.00; N, 6.30. Found: C, 44.99; H, 6.00; N, 6.30.

(^{Cy}[NPN]Ta)$_2$(μ-η^2:η^1-N$_2$)(μ-D)$_2$ (2.4-*d*$_2$)

In manner analogous to the above procedure, (^{Cy}[NPN]Ta)$_2$(μ-D)$_4$ and (^{Cy}[NPN]Ta)$_2$(μ-η^2:η^1-N$_2$)(μ-D)$_2$ were prepared using D_2 gas and N_2 gas respectively.

^{Cy}[NPN]Ta(^{n}BuSiN-μ-Si(H)^{n}Bu-μ-N)Ta[NPN]^{Cy} (2.7)

To a stirred solution of **2.4** (203 mg, 0.16 mmol) in 20 mL Et_2O was added a solution of 0.20 mL $BuSiH_3$ (1.5 mmol, 10 equiv) in 5 mL Et_2O and the mixture was left to stir for 3 days. The solvent was removed under vacuum, yielding dark red-brown solids (155 mg, 67% yield). X-ray quality crystals were grown from slow evaporation of a hexane solution at -40 °C. ^1H NMR (C_6D_6, 400 MHz): δ –0.40, 0.14, 0.34, 0.40, 0.56, 0.85 (s, approx. 3H each, Si-CH_3), 0.08 (s, 6H Si-CH_3), 0.0–3.11 (m, broad, overlapping signals, approx. 48H, Si–C_4H_9), Si–CH_2–P, P–C_6H_{11}), 4.69, 4.86 (dd, 1H each, Si–H_2), 5.55 (s, 1H, Si–*H*), 6.72, 6.89, 6.98, 7.25, 7.62, 7.92 (overlapping, approx. 20H, N–C_6H_5, residual protons in C_6D_6), 8.44 (ddd, $^2J_{HP}$ = 33.1 Hz, 1H, Ta–H_t), 9.71, 18.01 (m, 1H each, Ta–H_b–Ta). $^{31}P\{^1H\}$ NMR (C_6D_6, 161.9 MHz): δ 27.89 (d, J_{PP} = 4.8 Hz), 22.18 (d, J_{PP} = 4.8 Hz). ^{29}Si (C_6D_6, 79.5 MHz): δ –36.45 (m, *Si*–H), –34.95 (d, J_{PSi} = 2.9 Hz, *Si*–H_2), 4.52 (d, J_{PSi} = 12.4 Hz, *Si*–$(CH_3)_2$), 5.96 (d, J_{PSi} = 11.4 Hz, *Si*–$(CH_3)_2$), 6.32 (d, J_{PSi} = 11.7 Hz, *Si*–$(CH_3)_2$), 7.78 (d, J_{PSi} = 15.3 Hz, *Si*–$(CH_3)_2$). Anal. Calcd for $C_{56}H_{98}N_6P_2Si_6Ta_2$: C, 46.46; H, 6.82; N, 5.80. Found: C, 46.19; H, 7.20; N, 5.75.

Reaction of (2.4) with $PhSiH_3$ (leading to formation of 2.8, 2.9 and 2.10)

To a J. Young NMR tube was added 0.40 mL of a 0.040 M solution (0.016 mmol) of **2.4** in C_6D_6 followed by 0.01 mL (0.08 mmol, 5 equiv) of neat $PhSiH_3$. The tube was sealed and shaken to mix. The reaction was monitored by $^{31}P\{^1H\}$ and $^1H\{^{31}P\}$ NMR spectroscopy over the course of 24h, during which time the solution changed colour from dark red to light orange. Characteristic peaks for **2.8**: $^1H\{^{31}P\}$ NMR (300 MHz): δ 14.3 (1H, Ta-H_t), 11.0 (2H, Ta-H_b-Ta). $^{31}P\{^1H\}$ NMR (121.4 MHz): δ 29.7 (d, J_{PP} = 15.7 Hz), 15.5 (d, J_{PP} = 15.7 Hz). Characteristic peaks for **2.9**: $^1H\{^{31}P\}$ NMR (300 MHz): δ 16.5 (Ta-H_t). $^{31}P\{^1H\}$ NMR (121.4 MHz): δ -1.0 (br). Characteristic peaks for **2.10**: $^1H\{^{31}P\}$ NMR (300 MHz): δ -0.65, -0.26, -0.22, -0.06, 0.22, 0.24, 0.42, 0.63 (s, 3H each, SiCH_3), 4.25 and 5.60 (d, 1H each, $^2J_{HH}$ = 12.8 Hz, PhSi(H)$_2$-N), 4.63 and 9.86 (d, 1H each, $^2J_{HH}$ = 9.2 Hz, N-PhSi(H)$_2$-N). $^{31}P\{^1H\}$ NMR (121.4 MHz): δ 22.0, –4.9 (s).

7.3.2 Experiments pertaining to Chapter 2

$^{31}P\{^1H\}$ NMR spectroscopic study of the reaction of (2.4) with excess $BuSiH_3$

To a 9” NMR tube was added 0.40 mL of a solution of **2.4** (0.040 mmol/mL, 0.016 mmol) in C_6D_6 and the tube was fitted with a rubber septum and wrapped with ParaFilm laboratory film. The tube was placed into a Bruker Avance 400 MHz spectrometer and initial calibrations were performed. The spectrometer was programmed to record delayed $^{31}P\{^1H\}$ NMR spectra over the course of 22 hours. Where t = total elapsed time, the experiments were delayed as follows: every 10 minutes, from t = 0-2 hours; every 15 minutes, from t = 2-5 hours; every 30 minutes, from t = 5-12 h; every 60 minutes, from t = 12-22 h. The tube was ejected and 0.1 mL of a solution of $BuSiH_3$ (0.72 mmol/mL, 0.072 mmol, 4.5 equiv) in C_6D_6 was added via syringe (fitted with a 20-gauge needle) through the septum. More ParaFilm was used to cover the septum and the tube

was inverted to mix the two solutions. The tube was then placed back into the spectrometer and the automated acquisition was initiated. Additional $^{31}P\{^{1}H\}$ NMR spectra were recorded manually at t = 28 h, 46 h, 74 h and 6 days.

^{1}H and ^{2}H NMR spectroscopic study of the reaction of (2.4-*d*$_2$) with excess BuSiH$_3$

To a J. Young NMR tube was added 0.40 mL of a solution of **2.4-*d*$_2$** (0.040 mmol/mL, 0.016 mmol) in benzene-d_6 and 0.40 mL of a solution of $BuSiH_3$ (0.72 mmol/mL, 0.29 mmol, 18 equiv) in benzene-d_6. The tube was inverted to mix the two solutions, just prior to placing it in a Bruker Avance 400 MHz spectrometer. The spectrometer was programmed to record delayed ^{1}H NMR spectra, every 15 minutes, over the course of 12 hours. Additional spectra were recorded manually after 14 h, 24 h and 6 days.

Another sample was prepared as stated above, using benzene instead of benzene-d_6 as the solvent, and the spectrometer was programmed to record delayed ^{2}H NMR spectra, every 10 minutes, over the course of 12 hours.

^{1}H and ^{2}H NMR spectroscopic study of the reaction of (2.4) with excess BuSiD$_3$

Experiments were carried out analogous to the above procedures, using **2.4** and $BuSiD_3$.

7.3.3 Compounds pertaining to Chapter 3

General procedure for thermolysis of ([P$_2$N$_2$]Nb)$_2$(μ-N$_2$) in the presence of Lewis acids

To a toluene solution of ([P_2N_2]Nb)$_2$(μ-N_2) in a thick-walled glass vessel fitted with a Teflon Kontes valve was added 2 equivalents of a solution of the desired Lewis acid ($AlMe_3$, 1.0 M in toluene, $AlEt_3$, 1.0 M in hexanes, BEt_3, 1.0 M in hexanes, $B(C_6F_5)_3$, solid dissolved in toluene). The solution was heated to 110 °C overnight. The resulting deeply coloured solution was cooled, filtered over Celite and the solvent removed under vacuum, leaving a deeply coloured solid.

Broad, messy resonances were consistently observed in the paramagnetic ^{1}H NMR spectra, giving no useful structural or identifying information.

[([P_2N_2]Nb)$_2$(μ-N_2)][$H_2B(C_6F_5)_2$] (3.4)

To a solution of ([P_2N_2]Nb)$_2$(μ-N_2) (22.6 mg, 0.0176 mmol) in 10 mL of toluene was added a solution of HB(C_6F_5)$_2$ (12.2 mg, 0.0352 mmol) in 10 mL of toluene. The dark brown solution was stirred at R.T. overnight, resulting in a colour change from dark brown to dark red. The dark red solution was filtered over Celite and the solvent was removed under vacuum. The red residue was washed with minimal pentane and the resulting red solid was dried under vacuum. A small amount of crystals were grown from a saturated toluene solution stored in the glovebox freezer. It was uncertain if these crystals were the major product and the yield was never determined. Paramagnetic ^{1}H NMR (C_6D_6, 400 MHz): δ -0.5, 0.7, 1.3 (br, overlapping), 4.9 (br), 6.8, 7.0, 7.6, 8.5 (br, overlapping).

([P_2N_2]NbI)$_2$(μ-N_2) (3.5)

To a solution of ([P_2N_2]Nb)$_2$(μ-N_2) (33 mg, 0.026 mmol) in 5 mL of toluene was added a solution of I-CH_2CH_2-I (7.0 mg, 0.026 mmol) in 5 mL of toluene. The solution changed colour from dark brown to dark yellow during the addition. The solvent was removed under vacuum, leaving a dark yellow-brown residue that was triturated with minimal hexane. The hexane was decanted and the solid was dried under vacuum. The dark yellow-brown solid was weighed (27 mg, 68% yield). A small amount of crystals were grown from a saturated toluene solution stored in the glovebox freezer. Paramagnetic ^{1}H NMR (C_6D_6, 400 MHz): δ 4.5, 8.8, 9.4, 11.9 (br). μ_{eff} (Evans method) = 2.99 μ_B. Anal. Calcd for $C_{48}H_{84}I_2N_6Nb_2P_4Si_8$: C, 37.60; H, 5.52; N, 5.48. Found: C, 37.38; H, 5.51; N, 3.49.

[([P_2N_2]Nb)(η^6-toluene)][OTf]$_2$ (3.6)

To a solution of ([P_2N_2]Nb)$_2$(μ-N_2) (29 mg, 0.023 mmol) in 10 mL of THF was added a solution of AgOTf (12 mg, 0.046 mmol) in 5 mL of THF. The mixture slowly changed colour from dark yellow-brown to cloudy dark red-brown and was left to stir overnight. The solvent was removed under vacuum, leaving a dark brown residue that was extracted into 5 mL of toluene and filtered to remove some insoluble dark solids (likely Ag^0). The dark brown filtrate was evaporated to dryness, leaving dark brown material. A small amount of crystals were grown from slow evaporation of a toluene solution stored in the glovebox freezer. The yield was not determined and consistent results could not be reproduced. Paramagnetic ^{1}H NMR (C_6D_6, 400 MHz): δ -0.4, -0.1, 0.5, 1.5, 2.5 (br, overlapping), 4.4 (br) 6.9, 7.0, 7.3, 7.5, 7.9 (br overlapping), 9.2, 9.7, 11.4 (br, overlapping).

[([P_2N_2]Nb)$_2$((μ-F)$_3$)][BF_4] (3.7)

To a blue solution of [$FeCp_2$][BF_4] (14 mg, 0.052 mmol) in 3 mL of acetonitrile was added a dark brown solution of ([P_2N_2]Nb)$_2$(μ-N_2) (34 mg, 0.026 mmol) in 5 mL of THF. The dark yellow-brown mixture was stirred for 30 minutes. The solvent was removed under vacuum and the dark yellow-brown solid was washed with 2 x 2 mL of hexane. The yellow hexane wash was decanted and dried under vacuum, leaving yellow solid. The ^{1}H NMR spectrum of this yellow solid displayed a peak at 4.0 ppm, indicating the presence of ferrocene. The remaining dark brown solids were dried under vacuum and weighed (25 mg, 69% yield). A small amount of crystals were grown from a THF/hexane solution stored in the glovebox freezer. Paramagnetic ^{1}H NMR (THF-d_8, 400 MHz): δ -8.1, -6.2 (br), 0.2, 2.4 (br, overlapping), 4.3 (br), 7.3, 7.6, 8.5 (br, overlapping), 45.9 (br). Anal. Calcd for $C_{48}H_{84}B_1F_7N_4Nb_2P_4Si_8$: C, 41.32; H, 6.07; N, 4.02. Found: C, 40.95; H, 6.14; N, 4.38.

$([P_2N_2]Nb)_2(\mu\text{-}\eta^2\text{:}\eta^2\text{-}N_2)(\mu\text{-}O)$ (3.8)

To a solution of $([P_2N_2]Nb)_2(\mu\text{-}N_2)$ (31 mg, 0.024 mmol) in 8 mL of toluene was added a solution of TEMPO (7.5 mg, 0.048 mmol) in 3 mL of toluene. The dark brown mixture was stirred for 30 minutes, changing colour to dark red-brown over this time. The solvent was removed under vacuum and the dark solid was washed with 2 mL of hexane. The solution was decanted and the remaining dark red-brown solid was dried under vacuum (13 mg, 42% yield). A small amount of crystals were grown from slow evaporation of a THF solution stored in the glovebox freezer. $^1H\{^{31}P\}$ NMR (THF-d_8, 400 MHz): δ -0.07, -0.06, -0.04, 0.21, 0.28, 0.61, (s, 6H each, Si-CH_3), 0.07 (s, 12H, Si-CH_3), 0.68, 0.75, 0.96, 1.65, 1.88 (d, 2H each, Si–CH_2–P), 1.06 - 1.17 (overlapping multiplets, 6H, Si–CH_2–P), 7.09, 7.27, 8.23 (m, 4H each, P–C_6H_5), 7.38 (m, 2H, P–C_6H_5), 7.54 (m, 6H, P–C_6H_5). $^{31}P\{^1H\}$ NMR (THF-d_8, 161.9 MHz): δ 11.5 (br). $^{13}C\{^1H\}$ NMR (THF-d_8, 100.6 MHz): δ 4.7, 4.9, 6.1, 6.7, 7.4, 7.7, 8.1, 8.4 (Si-CH_3), 13.2, 16.3, 24.0, 26.5 (Si–CH_2–P), 129.2, 129.4, 130.6, 133.6, 135.2, 138.6 (P–C_6H_5). Anal. Calcd for $C_{48}H_{84}N_6Nb_2O_1P_4Si_8$: C, 44.50; H, 6.49; N, 6.54. Found: C, 42.85; H, 6.42; N, 5.08.

$[P_2N_2]VI$ (3.9)

A solution of I-CH_2CH_2-I (4.8 mg, 0.017 mmol) in 2 mL of toluene was combined with a dark purple solution of $([P_2N_2]V)_2(\mu\text{-}N_2)$ (21 mg, 0.017 mmol) in 5 mL of toluene and the mixture was left to stir overnight. The solution changed colour from dark purple to light pink-orange over this time. The solvent was removed under vacuum and the remaining pink residue was washed with minimal hexane. The solution was decanted and the solid was dried under vacuum, affording a light pink powder (22 mg, 92% yield). Single crystals were grown from a toluene/hexane solution stored in the glovebox freezer. Paramagnetic ^1H NMR (C_6D_6, 400 MHz):

δ 1.6, 5.8, 9.0 (br). μ_{eff} (Evans method) = 2.64 μ_B. Anal. Calcd for $C_{24}H_{42}I_1N_2P_2Si_4V_1$: C, 40.56; H, 5.96; N, 3.94. Found: C, 40.88; H, 6.04; N, 3.85.

[([P_2N_2]V)(THF)$_2$][BPh$_4$] (3.10)

To a dark purple solution of ([P_2N_2]V)$_2$(μ-N_2) (30 mg, 0.025 mmol) in 5 mL of THF was added a suspension of $AgBPh_4$ in 10 mL of THF. The resulting cloudy dark brown mixture was left to stir overnight, changing colour to cloudy dark green-brown. The cloudy solution was filtered over Celite, removing a dark solid. The clear green filtrate was evaporated to dryness, affording a green powder (48 mg, 92% yield). A crop of green crystals was grown from a THF solution cooled to –40 °C. Paramagnetic ^{1}H NMR (THF-d_8, 400 MHz): δ 1.73, 3.57 (br, THF), 5.0, 6.6, 6.8, 7.2 (br). μ_{eff} (Evans method) = 2.64 μ_B. Anal. Calcd for $C_{56}H_{78}B_1N_2O_2P_2Si_4V_1$: C, 64.22; H, 7.51; N, 2.67. Found: C, 61.48; H, 7.33; N, 2.78.

[P_2N_2]VMe (3.11)

To an ice-cooled solution of [P_2N_2]VCl (75 mg, 0.12 mmol) in 10 mL hexane was added a solution of MeMgCl in THF (3.0 M, 40 μL, 0.12 mmol) via a micro-syringe. The solution became cloudy and changed colour from orange to olive green. After stirring for 5-10 minutes, the cloudy solution was filtered over Celite, removing a light powder. The olive green filtrate was evaporated to dryness and the green residue was extracted into 2 mL of HMDSO. The cloudy green solution was filtered over Celite and the clear green filtrate was stored in the freezer. Olive green crystals were isolated from the HMDSO solution and dried under vacuum (46 mg, 65% yield). Paramagnetic ^{1}H NMR (C_6D_6, 400 MHz): δ 1.7, 4.8, 6.3, 6.7, 8.9, 9.7 (br). μ_{eff} (Evans method) = 2.69 μ_B. Anal. Calcd for $C_{25}H_{45}N_2P_2Si_4V_1$: C, 50.14; H, 7.57; N, 4.68. Found: C, 48.77; H, 7.76; N, 5.16.

7.3.4 Compounds pertaining to Chapter 4

***syn*-[P_2N_2]Co (4.1)**

A solution of *syn*-[P_2N_2]Li_2(1,4-dioxane) (201 mg, 0.317 mmol) in 10 mL of THF and a suspension of $CoCl_2(THF)_{1.5}$ (75 mg, 0.317 mmol) in 20 mL THF was cooled in the glovebox freezer for 45 minutes. The $CoCl_2(THF)_{1.5}$ suspension was added to the *syn*-[P_2N_2]Li_2(1,4-dioxane) solution and the dark orange-brown mixture was stirred for 2 hours. The solvent was removed under vacuum and the remaining dark brown solids were extracted into 10 mL of hexane. The cloudy solution was filtered over Celite, removing dark blue solids. The clear orange filtrate was evaporated to dryness, leaving orange residue that was dissolved in minimal (2-3 mL) hexane and stored at –40 °C. Orange crystals were isolated from the hexane solution and dried under vacuum (134 mg, 72% yield). Paramagnetic ^{1}H NMR (C_6D_6, 400 MHz): δ 5.30, -0.47, -2.85 (br). μ_{eff} (Evans method) =1.96 μ_B. Anal. Calcd for $C_{24}H_{42}N_2P_2Si_4Co_1$: C, 48.71; H, 7.15; N, 4.73. Found: C, 48.70; H, 7.06; N, 4.91.

***syn*-[$(P{=}O)_2N_2$]Co (4.2)**

A stirred solution of *syn*-[P_2N_2]Co (46 mg, 0.078 mmol) in 10 mL of hexane in a bomb was freeze-pump-thaw degassed 3x under vacuum and kept frozen under liquid nitrogen. Using a glass adapter for gas addition, 1 equiv of dry O_2 gas was added and the bomb was sealed. Upon thawing, the solution changed colour from orange to dark green, to dark brown as the solution was stirred. The solution was stirred for 1 h, changing colour to dark purple. The solvent was removed under vacuum, leaving a dark purple solid. The dark purple solid was washed with minimal hexane and the dark brown solution was decanted. The remaining purple solid was extracted into minimal Et_2O and the purple solution was filtered. The purple filtrate was evaporated to dryness, leaving a purple solid (40 mg, 82% yield). A solution of the purple solid

in Et_2O was placed in the freezer to crystallize, resulting in X-ray quality crystals from slow evaporation of the solution. Paramagnetic ^{1}H NMR (C_6D_6, 400 MHz): δ -44.7, -19.5, -16.5, -13.2 (br), -8.5, -7.9 (br, overlapping), -6.8, -1.9, 0.2, (br), 1.3, 1.4, 1.7, 2.1 (br, overlapping), 4.7, 5.0 (br, overlapping), 7.7, 19.5, 30.9, 32.1, 49.4 (br). μ_{eff} (Evans method) = 4.49 μ_B. Anal. Calcd for $C_{24}H_{42}N_2O_2P_2Si_4Co_1$: C, 46.21; H, 6.79; N, 4.49. Found: C, 46.35; H, 6.85; N, 4.24.

***syn*-[P_2N_2]CoI (4.3)**

A solution of I-CH_2CH_2-I (12 mg, 0.043 mmol) in 5 mL of toluene was slowly added dropwise to a solution of *syn*-[P_2N_2]Co (51 mg, 0.086 mmol) in 5 mL of toluene. The solution rapidly changed colour from orange to dark maroon, and was left to stir for 15 minutes. The solvent was removed under vacuum and the dark maroon residue was extracted into 15 mL of hexane. The solution was evaporated to dryness under vacuum, affording a dark maroon solid (61 mg, 98% yield). Dark maroon crystals suitable for X-ray diffraction were isolated from a concentrated hexane solution cooled to –40 °C. Paramagnetic ^{1}H NMR (C_6D_6, 400 MHz): δ 2.2, 6.6, 7.5, 8.2, 10.0 (br). μ_{eff} (Evans method) = 2.81 μ_B. Anal. Calcd for $C_{24}H_{42}I_1N_2P_2Si_4Co_1$: C, 40.11; H, 5.89; N, 3.90. Found: C, 39.86; H, 5.97; N, 3.66.

***syn*-[P_2N_2](Li-dioxane)$CoMe_2$ (4.4-$_{dioxane}$)**

To an ice-cooled solution of *syn*-[P_2N_2]CoI (31 mg, 0.043 mmol) in 10 mL of toluene and a few drops of 1,4-dioxane, was added 0.05 mL of a solution of MeLi in Et_2O (1.6 M in Et_2O, 0.086 mmol). The mixture changed colour from dark maroon to dark orange after the addition was complete and was left to stir for 30 minutes. The cloudy orange solution was filtered over celite and the clear orange filtrate was evaporated to dryness. The remaining dark orange residue was extracted into minimal toluene and filtered to remove a dark solid, resulting in a clear orange filtrate. The solvent was removed under vacuum, leaving orange residue. The residue was

washed with minimal hexane and the solution was decanted. The remaining orange solid was dried under vacuum and weighed (21 mg, 68% yield). ^{1}H NMR (C_6D_6, 400 MHz): δ -0.40 (t, 6H, Co–C*H*$_3$), 0.13, 0.40 (s, 12H each, Si-C*H*$_3$), 1.33, 1.94 (m, 4H each, Si–C*H*$_2$–P), 2.79 (br, 4H (low on coordinated dioxane, should be 8H), $C_4H_8O_2$), 7.09 - 7.20, (m, approx. 6H, overlapping with residual proton signal from C_6D_6, P–C_6H_5), 7.67 (m, 4H, P–C_6H_5). ^{31}P{^{1}H} NMR (C_6D_6, 161.9 MHz): δ 33.5 (br). ^{7}Li NMR (C_6D_6, 155.5 MHz): δ 1.18 (s). ^{13}C{^{1}H} NMR (C_6D_6, 100.6 MHz): δ 6.1, 6.7 (Co–*C*H$_3$ and Si-**C**H$_3$), 24.7 (Si–*C*H$_2$–P), 66.8 (*C*$_4$H$_8$O$_2$), 127.8, 128.4, 131.9, 137.8 (P–*C*$_6$H$_5$). Anal. Calcd for $C_{30}H_{56}N_2O_2P_2Si_4Li_1Co_1$: C, 50.26; H, 7.87; N, 3.91. Found: C, 48.76; H, 7.78; N, 3.97.

***syn*-[P$_2$N$_2$]CoCH$_2$SiMe$_3$ (4.5)**

A solution of *syn*-[P$_2$N$_2$]Co (20 mg, 0.028 mmol) in 10 mL of hexane and a solution of LiCH$_2$SiMe$_3$ (2.6 mg, 0.028 mmol) in 5 mL of hexane were cooled to –40 °C in the glovebox freezer for 1 h. The LiCH$_2$SiMe$_3$ solution was added dropwise to the *syn*-[P$_2$N$_2$]Co solution and the dark maroon solution was left to stir. After 1 h, the solution was cloudy and had changed colour to dark green. The cloudy solution was filtered over celite, removing a white solid. The dark green filtrate was evaporated to dryness, yielding dark green solids (17 mg, 89% yield). X-ray quality crystals were isolated from a pentane-acetonitrile solution stored in the glovebox freezer. Paramagnetic ^{1}H NMR (C_6D_6, 400 MHz): δ -62.4, -45.9, -2.8, -0.5, 3.4, 4.6, 5.2, 5.9, 8.2, 17.8 (br). μ_{eff} (Evans method) = 2.91 μ_B. Anal. Calcd for $C_{28}H_{53}N_2P_2Si_5Co_1$: C, 49.53; H, 7.87; N, 4.13. Found: C, 48.54; H, 7.45; N, 4.13.

7.3.5 Compounds pertaining to Chapter 5

$[P_2N_2][Rh(COD)]_2$ (5.1)

Solid *syn*-$[P_2N_2]Li_2$(1,4-dioxane) (129 mg, 0.203 mmol) and $[Rh(COD)Cl]_2$ (100 mg, 0.203 mmol) were weighed into the same vial and put in the glovebox freezer for 30 minutes, along with another vial containing 10 mL of toluene. The cold toluene was added to the cold solids and the cloudy orange-yellow mixture was left to stir overnight. The solvent was removed under vacuum and the dark yellow residue was extracted into 4 mL of toluene. The resulting cloudy solution was filtered over Celite. The clear orange-yellow filtrate was condensed to a smaller volume (1-2 mL) and the concentrated solution was stored in the freezer until crystal growth was observed. The solution was decanted and the crystals were dried under vacuum. The yellow crystalline solid was weighed (132 mg, 68% yield) and stored in the freezer. $^{1}H\{^{31}P\}$ NMR (C_6D_6, 400 MHz): δ 0.3, 0.5, 0.7, 1.1 (s, 6H each, SiCH_3), 1.4–2.0 (m, overlapping signals, approx. 18 H, Si-CH_2-P, COD CH_2), 2.2, 2.3, 2.6, (m, 2 H each, COD CH_2), 3.0, 3.6, 5.3, 5.4 (m, 2H each, COD *H*C=C*H*), 7.0 (t, 2H, *p*-C_6H_5–P), 7.1 (t, 4H, *m*-C_6H_5–P), 7.5 (d, 4H, *o*-C_6H_5–P). $^{31}P\{^{1}H\}$ NMR (C_6D_6, 161.9 MHz): δ 20.0 (d, J_{RhP} = 143 Hz). $^{13}C\{^{1}H\}$ NMR (C_6D_6, 100.6 MHz): δ 6.4, 9.5, 9.6, 10.1 (Si*C*H_3), 18.8, 24.2, 28.3, 34.1 (COD *C*H_2), 30.5, 31.2, (Si-*C*H_2-P), 68.2, 71.1, 96.4, 100.9 (COD H*C*=*C*H), 128.2, 128.3, 129.0, 130.7 (*C*$_6$H$_5$–P). Anal. Calcd for $C_{40}H_{66}N_2P_2Si_4Rh_2$: C, 50.30; H, 6.97; N, 2.93. Found: C, 49.41; H, 7.12; N, 2.43.

$[P_2N_2]Rh(\mu\text{-}I)_2Rh(COD)$ (5.2)

To a solution of $[P_2N_2][Rh(COD)]_2$ (39 mg, 0.041 mmol) in 10 mL of toluene was added a solution of I-CH_2CH_2-I (11.6 mg, 0.041 mmol) in 5 mL of toluene. The solution was heated at 110 °C for 5 h. During this time, the solution changed colour from yellow to green-yellow. The solvent was removed under vacuum, leaving dark green-yellow residue. The residue was washed

with 2 mL of hexane and the dark yellow solution was decanted. The remaining green solids were dried under vacuum and weighed (32 mg, 71%). The solids were washed with minimal THF and the brown solution was decanted. The remaining bright green solid was dried under vacuum and weighed (22 mg, 49% yield). A small amount of green crystals (suitable for X-ray diffraction) were isolated from a THF solution stored at –40 °C. ^{1}H NMR (THF-d$_8$, 400 MHz): δ 0.22, 0.26 (overlapping, 24H, SiC*H*$_3$), 1.22 (m, 4H, COD C*H*$_2$), 1.80, 2.18 (m, 4H each, Si-C*H*$_2$-P), 1.94 (br, 4H, COD C*H*$_2$), 3.60 (br, approx. 4H, overlapping with residual proton signal from THF-d$_8$, COD *H*C=C*H*), 7.5 (m, 2H, C$_6$*H*$_5$–P), 7.6 (m, 4H, C$_6$*H*$_5$–P), 8.0 (m, 4H, C$_6$*H*$_5$–P). ^{31}P{^{1}H} NMR (THF-d$_8$, 161.9 MHz): δ 24.8 (d, J_{RhP} = 83 Hz). ^{13}C{^{1}H} NMR (THF-d$_8$, 100.6 MHz): δ 6.3, 7.6 (Si*C*H$_3$), approx. 25.4 (obscured by THF-d$_8$ solvent signal, COD *C*H$_2$), 31.2 (Si-*C*H$_2$-P), 79.4 (COD H*C*=*C*H), 127.6, 129.5, 129.8, 133.3 (*C*$_6$H$_5$–P). Anal. Calcd for $C_{32}H_{54}I_2N_2P_2Si_4Rh_2$: C, 34.92; H, 4.95; N, 2.55. Found: C, 35.56; H, 4.98; N, 2.36.

[P$_2$N$_2$]Rh(CO)[Rh(CO)$_2$] (5.3)

A solution of [P$_2$N$_2$][Rh(COD)]$_2$ (65 mg, 0.068 mmol) in 10 mL of toluene was transferred into a thick-walled glass vessel equipped with a Teflon valve and thoroughly degassed via 3 freeze-pump-thaw cycles. The vessel was cooled under liquid N$_2$ and CO gas was added. The vessel was sealed and the frozen solution was allowed to thaw slowly in a –78 °C (dry ice/acetone) bath, undergoing a colour change from yellow to orange. Once the solution had thawed, the CO and solvent was removed under vacuum, during which time the solution changed colour from orange to yellow. The remaining yellow solid was extracted into 5 mL of hexane and the cloudy solution was filtered over a glass filter pad, removing a small amount of dark solid. The clear yellow filtrate was evaporated to dryness, leaving a yellow residue. The residue was washed with minimal pentane and dried under vacuum, yielding a yellow solid (51 mg, 90% yield). X-ray

quality crystals were isolated from a concentrated hexane solution stored at –40 °C. $^{1}H\{^{31}P\}$ NMR (C_6D_6, 400 MHz): δ 0.35, 0.42 (s, 6 H each, SiCH_3), 0.52, 0.53 (s, overlapping, 12 H, SiCH_3), 0.98, 0.44, 1.60, 1.75 (d, 2H each, Si-CH_2-P), 7.0 (t, 2H, *p*-C_6H_5–P), 7.1 (t, 4H, *m*-C_6H_5–P), 7.7 (d, 4H, *o*-C_6H_5–P). $^{31}P\{^{1}H\}$ NMR (C_6D_6, 161.9 MHz): δ 30.1 (d, J_{RhP} = 84 Hz). $^{13}C\{^{1}H\}$ NMR (C_6D_6, 100.6 MHz): δ 4.7, 5.0, 5.6, 5.7 (SiCH_3), 25.4, 32.6 (Si-CH_2-P), 128.6, 130.0, 130.2, 137.8 (C_6H_5–P) 180.9, 195.7, 197.1 (Rh–*C*O). IR (cm^{-1}): ν_{CO} 1938 (s), ν_{CO} 1988 (s), ν_{CO} 2020 (s). Anal. Calcd for $C_{27}H_{42}N_2O_3P_2Si_4Rh_2$: C, 39.42; H, 5.15; N, 3.40. Found: C, 39.08; H, 5.21; N, 3.31.

([Rh(COE)][P_2N_2]Li)$_2$(dioxane) (5.4)

A solution of *syn*-[P_2N_2]Li_2(1,4-dioxane) (197 mg, 0.310 mmol) in 5 mL of toluene with 0.5 mL of dioxane and a solution of [Rh(COE)$_2$Cl]$_2$ (111 mg, 0.155 mmol) in 5 mL of toluene was prepared and cooled in the glovebox freezer for 1 h. The [Rh(COE)$_2$Cl]$_2$ solution was added dropwise to the *syn*-[P_2N_2]Li_2(1,4-dioxane) solution while stirring. After the addition was complete, the mixture was immediately put under vacuum to remove the solvent. The remaining solids were extracted into 2 mL of toluene and filtered through a glass filter pad within a pipette, to remove LiCl. The filtrate was evaporated to dryness and the remaining brown residue was triturated with 1 mL of cold hexane. The dark brown solution was decanted and the solids were washed with another 1 mL of cold hexane. The solution was decanted and the yellow-brown solid was dried under vacuum and weighed (199 mg, 81% yield). $^{1}H\{^{31}P\}$ NMR (C_6D_6, 400 MHz): δ 0.28, 0.36 (s, overlapping, 24 H, SiCH_3), 0.65, 0.72 (s, overlapping, 24 H, SiCH_3), 0.9-1.1 (m, overlapping signals, approx. 12H, COE CH_2, Si-CH_2-P), 1.2, 1.4 (m, overlapping signals, approx. 8H each, COE CH_2, Si-CH_2-P), 1.6, 1.7 (d, 4H each, Si-CH_2-P) 1.8 (m, 4H COE CH_2), 2.0 (br, 4H, COE *H*C=C*H*), 3.6 (s, 8H, $C_4H_8O_2$), 7.0 - 7.1 (m, approx. 12H, overlapping with

residual C_6D_6 proton signal, C_6H_5–P), 7.5 (m, 8H, C_6H_5–P). $^{31}P\{^1H\}$ NMR (C_6D_6, 161.9 MHz): δ 11.5 (dd, J_{RhP} = 123 Hz, J_{PP} = 384 Hz), 23.1 (dd, J_{RhP} = 114 Hz, J_{PP} = 384 Hz). ^7Li NMR (C_6D_6, 155.5 MHz): δ 1.31 (s). $^{13}C\{^1H\}$ NMR (C_6D_6, 100.6 MHz): δ 5.7 - 6.0 (overlapping signals, not well resolved, Si*C*H_3), 7.3 (Si*C*H_3), 26.7, 32.3 (Si-*C*H_2-P), 26.4, 29.5, 32.6 (COE *C*H_2), 43.0 (COE H*C*=*C*H), 67.4 ($C_4H_8O_2$), 127.4, 127.6, 131.2, 131.7 (C_6H_5–P). Anal. Calcd for $C_{68}H_{120}Li_2N_4O_2P_4Si_8Rh_2$: C, 51.24; H, 7.59; N, 3.51. Found: C, 50.56; H, 7.70; N, 3.46.

$[P_2N_2H]Rh(H)_2$ (5.5)

A solution of $([Rh(COE)][P_2N_2]Li)_2$(dioxane) (44 mg, 0.028 mmol) in 10 mL of toluene was transferred into a thick-walled glass vessel equipped with a Teflon valve and thoroughly degassed via 3 freeze-pump-thaw cycles. The vessel was cooled under liquid N_2 and H_2 gas was added. The vessel was sealed and the frozen solution was allowed to warm to RT. The solution was stirred overnight. The H_2 and solvent was removed under vacuum, leaving yellow solid. The solid was extracted into 2 mL hexane and filtered over a glass filter pad within a pipette, removing a light solid. The clear yellow filtrate was evaporated to dryness and the remaining yellow residue was triturated with minimal HMDSO, precipitating a yellow solid. The solution was decanted and the solid was dried under vacuum (26 mg, 74% yield). Single crystals suitable for X-ray diffraction were isolated from a concentrated pentane solution stored at –40 °C. ^1H NMR (C_6D_6, 400 MHz): δ -17.5 (dt, 2H, Rh–*H*, J_{HP} = 14 Hz, J_{HH} = 25 Hz), 0.27, 0.29, (s, overlapping, 24H, SiC*H*$_3$), 1.4, 1.6 (dt, 4H each, Si-C*H*$_2$-P, J_{HP} = 4 Hz, J_{HH} = 14 Hz), 2.0 (s, 1H, N–*H*), 7.1 (m, 2H, C_6H_5–P), 7.2 (m, approx. 4H, overlapping with C_6D_6 residual proton, C_6H_5–P), 8.1 (m, 4H, C_6H_5–P). $^{31}P\{^1H\}$ NMR (C_6D_6, 161.9 MHz): δ 32.9 (d, J_{RhP} = 108 Hz). $^{13}C\{^1H\}$ NMR (C_6D_6, 100.6 MHz): δ 3.6, 5.4 (Si*C*H_3), 28.2 (Si-*C*H_2-P), 128.3, 129.8, 132.8, 140.9

(C_6H_5–P). Anal. Calcd for $C_{24}H_{45}N_2P_2Si_4Rh_1$: C, 45.12; H, 7.10; N, 4.39. Found: C, 43.04; H, 7.12; N, 3.09.

[P_2N_2H]Rh(CO) (5.6)

A solution of ([Rh(COE)][P_2N_2]Li)$_2$(dioxane) (69 mg, 0.043 mmol) in 10 mL of toluene was transferred into a thick-walled glass vessel equipped with a Teflon valve and thoroughly degassed via 3 freeze-pump-thaw cycles. The vessel was cooled under liquid N_2 and CO gas was added. The vessel was sealed and the frozen solution was allowed to warm to RT. The solution was stirred overnight. The CO and solvent was removed under vacuum, leaving a yellow residue. The residue was extracted into minimal hexane and filtered over a glass filter pad in a pipette, removing some dark solid. The clear yellow filtrate was evaporated to dryness. The remaining residue was extracted into minimal hexane and filtered over a glass filter pad in a pipette. The filtrate was evaporated to dryness, leaving a yellow residue. Minimal HMDSO was used to triturate the residue, resulting in a solid precipitate. The suspension was stored in the freezer overnight to precipitate more solid. The solid was dried under vacuum for 1.5 h and weighed (52 mg, 91 % yield). Crystals suitable for X-ray diffraction were isolated from a concentrated HMDSO solution stored at –40 °C. ^{1}H NMR (C_6D_6, 400 MHz): δ -0.03, 0.29, 0.35, 0.44 (s, 6H each, SiCH_3), 1.1 (s, 1H, N–*H*), 1.4 (m, overlapping, approx. 8H, Si-CH_2-P), 7.1 (m, 2H, C_6H_5–P), 7.2 (m, overlapping with C_6D_6 residual proton, 4H, C_6H_5–P), 7.9 (m, 4H, C_6H_5–P). ^{31}P{^{1}H} NMR (C_6D_6, 161.9 MHz): δ 22.8 (d, J_{RhP} = 127 Hz). ^{13}C{^{1}H} NMR (C_6D_6, 100.6 MHz): δ 3.1, 3.2, 5.3, 6.4 (SiCH_3), 25.8, 26.0 (Si-CH_2-P), 128.6, 130.1, 132.4, 140.1 (C_6H_5–P), 193.1 (Rh–*C*O). IR (cm^{-1}): ν_{CO} 1929 (s). Anal. Calcd for $C_{25}H_{43}N_2O_1P_2Si_4Rh_1$: C, 45.17; H, 6.52; N, 4.21. Found: C, 43.36; H, 6.54; N, 4.02.

7.3.6 Compounds pertaining to Chapter 6

$[P_2N_2]V(OTf)_2NH_3$ (6.1)

To a solution of $([P_2N_2]V)_2(\mu\text{-}N_2)$ (19 mg, 0.015 mmol) in 8 mL of toluene was added a solution of AgOTf (8 mg, 0.03 mmol) in 6 mL of toluene. The mixture changed colour from dark purple to dark orange-brown during the addition and was left to stir overnight. The solvent was removed under vacuum and the remaining residue was extracted into minimal THF. The cloudy green solution was filtered over a glass filter pad in a pipette, removing a dark solid. The green filtrate was evaporated to dryness, leaving a dark red residue (yield not recorded). Green crystals suitable for X-ray diffraction were isolated from a concentrated THF solution stored at –40 °C. Paramagnetic ^{1}H NMR (C_6D_6, 400 MHz): δ 1.4, 4.3, 6.1, 9.1 (br).

References

1. Fryzuk, M. D. *The Chemical Record* **2003,** *3* (1), 2-11.
2. Hazari, N. *Chem. Soc. Rev.* **2010,** *39* (11), 4044-4056.
3. Köthe, C.; Limberg, C. *Z. Anorg. Allg. Chem.* **2015,** *641* (1), 18-30.
4. Tanaka, H.; Nishibayashi, Y.; Yoshizawa, K. *Acc. Chem. Res.* **2016,** *49* (5), 987-995.
5. Kim, J.; Rees, D. C. *Science* **1992,** *257* (5077), 1677-1682.
6. Lancaster, K. M.; Roemelt, M.; Ettenhuber, P.; Hu, Y.; Ribbe, M. W.; Neese, F.; Bergmann, U.; DeBeer, S. *Science* **2011,** *334* (6058), 974-977.
7. Einsle, O. *J. Biol. Inorg. Chem.* **2014,** *19* (6), 737-745.
8. Spatzal, T.; Aksoyoglu, M.; Zhang, L.; Andrade, S. L. A.; Schleicher, E.; Weber, S.; Rees, D. C.; Einsle, O. *Science* **2011,** *334* (6058), 940-940.
9. Einsle, O.; Tezcan, F. A.; Andrade, S. L. A.; Schmid, B.; Yoshida, M.; Howard, J. B.; Rees, D. C. *Science* **2002,** *297* (5587), 1696-1700.
10. Boal, A. K.; Rosenzweig, A. C. *Science* **2012,** *337* (6102), 1617-1618.
11. Smith, B. E. *Science* **2002,** *297* (5587), 1654-1655.
12. Appl, M., Ammonia: Principles and Industrial Practice. In *Ammonia*, Wiley-VCH Verlag GmbH: 1999.
13. Schlögl, R. *Angew. Chem. Int. Ed.* **2003,** *42* (18), 2004-2008.
14. Allen, A. D.; Senoff, C. V. *Chemical Communications (London)* **1965,** (24), 621-622.
15. Chatt, J.; Dilworth, J. R.; Richards, R. L. *Chem. Rev.* **1978,** *78* (6), 589-625.
16. Hidai, M.; Mizobe, Y. *Chem. Rev.* **1995,** *95* (4), 1115-1133.
17. Schrock, R. R. *Acc. Chem. Res.* **2005,** *38* (12), 955-962.
18. Chirik, P. J. *Dalton Transactions* **2007,** (1), 16-25.
19. McWilliams, S. F.; Holland, P. L. *Acc. Chem. Res.* **2015,** *48* (7), 2059-2065.
20. Lee, Y.; Mankad, N. P.; Peters, J. C. *Nat Chem* **2010,** *2* (7), 558-565.
21. Nishibayashi, Y.; Saito, M.; Uemura, S.; Takekuma, S.-i.; Takekuma, H.; Yoshida, Z.-i. *Nature* **2004,** *428* (6980), 279-280.
22. Andino, J. G.; Mazumder, S.; Pal, K.; Caulton, K. G. *Angew. Chem. Int. Ed.* **2013,** *52* (18), 4726-4732.
23. Yandulov, D. V.; Schrock, R. R. *Science* **2003,** *301* (5629), 76-78.
24. Yuki, M.; Tanaka, H.; Sasaki, K.; Miyake, Y.; Yoshizawa, K.; Nishibayashi, Y. *Nat Commun* **2012,** *3*, 1254.
25. Anderson, J. S.; Rittle, J.; Peters, J. C. *Nature* **2013,** *501* (7465), 84-87.
26. Fryzuk, M. D. *Chem. Commun.* **2013,** *49* (43), 4866-4868.
27. MacKay, B. A.; Fryzuk, M. D. *Chem. Rev.* **2004,** *104* (2), 385-402.
28. Ohki, Y.; Fryzuk, M. D. *Angew. Chem. Int. Ed.* **2007,** *46* (18), 3180-3183.
29. Rodriguez, M. M.; Bill, E.; Brennessel, W. W.; Holland, P. L. *Science* **2011,** *334* (6057), 780-783.
30. Pool, J. A.; Lobkovsky, E.; Chirik, P. J. *Nature* **2004,** *427* (6974), 527-530.
31. Fryzuk, M. D.; Johnson, S. A. *Coord. Chem. Rev.* **2000,** *200–202*, 379-409.
32. Gerard van Koten, D. M., *Organometallic Pincer Chemistry*. Springer Berlin Heidelberg: 2013; Vol. 40.
33. Gupta, M.; Hagen, C.; Flesher, R. J.; Kaska, W. C.; Jensen, C. M. *Chem. Commun.* **1996,** (17), 2083-2084.

34. Morales-Morales, D.; Lee, D. W.; Wang, Z.; Jensen, C. M. *Organometallics* **2001,** *20* (6), 1144-1147.
35. Zhao, J.; Goldman, A. S.; Hartwig, J. F. *Science* **2005,** *307* (5712), 1080-1082.
36. Morgan, E.; MacLean, D. F.; McDonald, R.; Turculet, L. *J. Am. Chem. Soc.* **2009,** *131* (40), 14234-14236.
37. Fryzuk, M. D. *Can. J. Chem.* **1992,** *70* (12), 2839-2845.
38. Fryzuk, M. D.; MacNeil, P. A. *J. Am. Chem. Soc.* **1981,** *103* (12), 3592-3593.
39. Fryzuk, M. D.; Haddad, T. S.; Rettig, S. J. *Organometallics* **1989,** *8* (7), 1723-1732.
40. Fryzuk, M. D.; MacNeil, P. A.; Rettig, S. J. *J. Am. Chem. Soc.* **1985,** *107* (23), 6708-6710.
41. Fryzuk, M. D.; Haddad, T. S.; Rettig, S. J. *Organometallics* **1988,** *7* (5), 1224-1226.
42. Fryzuk, M. D.; Haddad, T. S.; Berg, D. J. *Coord. Chem. Rev.* **1990,** *99*, 137-212.
43. Fryzuk, M. D.; Haddad, T. S.; Rettig, S. J. *J. Am. Chem. Soc.* **1990,** *112* (22), 8185-8186.
44. MacLachlan, E. A.; Fryzuk, M. D. *Organometallics* **2006,** *25* (7), 1530-1543.
45. Hirotsu, M.; Fontaine, P. P.; Zavalij, P. Y.; Sita, L. R. *J. Am. Chem. Soc.* **2007,** *129* (42), 12690-12692.
46. Fryzuk, M. D.; Haddad, T. S.; Mylvaganam, M.; McConville, D. H.; Rettig, S. J. *J. Am. Chem. Soc.* **1993,** *115* (7), 2782-2792.
47. Cohen, J. D.; Mylvaganam, M.; Fryzuk, M. D.; Loehr, T. M. *J. Am. Chem. Soc.* **1994,** *116* (21), 9529-9534.
48. Chow, P. C. Dinitrogen Complexes of Titanium and Vanadium Stabilized by Phosphine Ligands. University of British Columbia, Vancouver, 1993.
49. Fryzuk, M. D.; Hoffman, V.; Kickham, J. E.; Rettig, S. J.; Gambarotta, S. *Inorg. Chem.* **1997,** *36* (16), 3480-3484.
50. Cabbiness, D. K.; Margerum, D. W. *J. Am. Chem. Soc.* **1969,** *91* (23), 6540-6541.
51. Lindoy, L. F., *The Chemistry of Macrocyclic Ligand Complexes*. Cambridge University Press: Cambridge University, 1990.
52. Fryzuk, M. D.; Love, J. B.; Rettig, S. J. *Chem. Commun.* **1996,** (24), 2783-2784.
53. Fryzuk, M. D.; Love, J. B.; Rettig, S. J.; Young, V. G. *Science* **1997,** *275* (5305), 1445-1447.
54. Morello, L.; João Ferreira, M.; Patrick, B. O.; Fryzuk, M. D. *Inorg. Chem.* **2008,** *47* (4), 1319-1323.
55. Morello, L.; Love, J. B.; Patrick, B. O.; Fryzuk, M. D. *J. Am. Chem. Soc.* **2004,** *126* (31), 9480-9481.
56. Morello, L.; Yu, P.; Carmichael, C. D.; Patrick, B. O.; Fryzuk, M. D. *J. Am. Chem. Soc.* **2005,** *127* (37), 12796-12797.
57. Carmichael, C. D.; Fryzuk, M. D. *Dalton Transactions* **2005,** (3), 452-459.
58. Fryzuk, M. D.; Johnson, S. A.; Rettig, S. J. *Organometallics* **1999,** *18* (20), 4059-4067.
59. Fryzuk, M. D.; Johnson, S. A.; Rettig, S. J. *Organometallics* **2000,** *19* (19), 3931-3941.
60. Fryzuk, M. D.; Kozak, C. M.; Bowdridge, M. R.; Jin, W.; Tung, D.; Patrick, B. O.; Rettig, S. J. *Organometallics* **2001,** *20* (17), 3752-3761.
61. Fryzuk, M. D.; Kozak, C. M.; Bowdridge, M. R.; Patrick, B. O.; Rettig, S. J. *J. Am. Chem. Soc.* **2002,** *124* (28), 8389-8397.
62. Fryzuk, M. D.; Kozak, C. M.; Patrick, B. O. *Inorg. Chim. Acta* **2003,** *345*, 53-62.

63. Fryzuk, M. D.; Johnson, S. A.; Rettig, S. J. *J. Am. Chem. Soc.* **1998,** *120* (42), 11024-11025.
64. Morello, L. Amidophosphine complexes of zirconium and titanium for dinitrogen activation. University of British Columbia, Vancouver, 2006.
65. Fryzuk, M. D.; Johnson, S. A.; Patrick, B. O.; Albinati, A.; Mason, S. A.; Koetzle, T. F. *J. Am. Chem. Soc.* **2001,** *123* (17), 3960-3973.
66. Studt, F.; MacKay, B. A.; Fryzuk, M. D.; Tuczek, F. *J. Am. Chem. Soc.* **2004,** *126* (1), 280-290.
67. Studt, F.; MacKay, B. A.; Johnson, S. A.; Patrick, B. O.; Fryzuk, M. D.; Tuczek, F. *Chemistry – A European Journal* **2005,** *11* (2), 604-618.
68. Ballmann, J.; Yeo, A.; MacKay, B. A.; Rijt, S. v.; Patrick, B. O.; Fryzuk, M. D. *Chem. Commun.* **2010,** *46* (46), 8794-8796.
69. Ballmann, J.; Yeo, A.; Patrick, B. O.; Fryzuk, M. D. *Angew. Chem. Int. Ed.* **2011,** *50* (2), 507-510.
70. Burford, R. J.; Castro, L.; Maron, L.; Hein, J. E.; Fryzuk, M. D. *Dalton Transactions* **2018,** *47* (24), 7983-7991.
71. Carmichael, C. D.; Shaver, M. P.; Fryzuk, M. D. *Can. J. Chem.* **2006,** *84* (12), 1667-1678.
72. Shaver, M. P.; Thomson, R. K.; Patrick, B. O.; Fryzuk, M. D. *Can. J. Chem.* **2003,** *81* (12), 1431-1437.
73. Fryzuk, M. D. *Acc. Chem. Res.* **2009,** *42* (1), 127-133.
74. MacLachlan, E. A.; Fryzuk, M. D. *Organometallics* **2005,** *24* (6), 1112-1118.
75. Hess, F. M. o-phenylene bridged diamidophosphine complexes of group 4 and 5 metals for dinitrogen activation. University of British Columbia, Vancouver, 2015.
76. MacLachlan, E. A.; Hess, F. M.; Patrick, B. O.; Fryzuk, M. D. *J. Am. Chem. Soc.* **2007,** *129* (35), 10895-10905.
77. Parker, K. D. J.; Nied, D.; Fryzuk, M. D. *Organometallics* **2015**.
78. Ménard, G.; Jong, H.; Fryzuk, M. D. *Organometallics* **2009,** *28* (17), 5253-5260.
79. Zhu, T.; Wambach, T. C.; Fryzuk, M. D. *Inorg. Chem.* **2011,** *50* (21), 11212-11221.
80. Fryzuk, M. D.; MacNeil, P. A. *Organometallics* **1983,** *2* (2), 355-356.
81. Fryzuk, M. D.; MacNeil, P. A.; Rettig, S. J. *Organometallics* **1986,** *5* (12), 2469-2476.
82. Fryzuk, M. D.; MacNeil, P. A.; Rettig, S. J. *J. Am. Chem. Soc.* **1987,** *109* (9), 2803-2812.
83. Fryzuk, M. D.; Leznoff, D. B.; Thompson, R. C.; Rettig, S. J. *J. Am. Chem. Soc.* **1998,** *120* (39), 10126-10135.
84. Wambach, T. C. Cooperative Ligand Design for Late Transition Metal Coordination Compounds. University of British Columbia, Vancouver, 2015.
85. Suzuki, T.; Masuda, H.; Fryzuk, M. D. *Dalton Transactions* **2017,** *46* (20), 6612-6622.
86. Pick, F. S.; Thompson, J. R.; Savard, D. S.; Leznoff, D. B.; Fryzuk, M. D. *Inorg. Chem.* **2016,** *55* (8), 4059-4067.
87. Halcovitch, N. R.; Fryzuk, M. D. *Dalton Transactions* **2012,** *41* (5), 1524-1528.
88. Halcovitch, N. R.; Fryzuk, M. D. *Organometallics* **2013,** *32* (20), 5705-5708.
89. Mori, M. *J. Organomet. Chem.* **2004,** *689* (24), 4210-4227.
90. Arashiba, K.; Miyake, Y.; Nishibayashi, Y. *Nat Chem* **2011,** *3* (2), 120-125.
91. Smil, V., *Enriching the Earth*. MIT Press: Boston, 2001.
92. Leigh, G. J., *The World's Greatest Fix*. Oxford University Press: New York, 2004.

93. Gilbertson, J. D.; Szymczak, N. K.; Tyler, D. R. *J. Am. Chem. Soc.* **2005,** *127* (29), 10184-10185.
94. Fryzuk, M. D.; MacKay, B. A.; Johnson, S. A.; Patrick, B. O. *Angew. Chem. Int. Ed.* **2002,** *41* (19), 3709-3712.
95. MacKay, B. A.; Johnson, S. A.; Patrick, B. O.; Fryzuk, M. D. *Can. J. Chem.* **2005,** *83* (4), 315-323.
96. MacKay, B. A.; Patrick, B. O.; Fryzuk, M. D. *Organometallics* **2005,** *24* (16), 3836-3841.
97. Fryzuk, M. D.; MacKay, B. A.; Patrick, B. O. *J. Am. Chem. Soc.* **2003,** *125* (11), 3234-3235.
98. MacKay, B. A.; Munha, R. F.; Fryzuk, M. D. *J. Am. Chem. Soc.* **2006,** *128* (29), 9472-9483.
99. Studt, F.; MacKay, B. A.; Fryzuk, M. D.; Tuczek, F. *Dalton Transactions* **2006,** (9), 1137-1140.
100. Spencer, L. P.; MacKay, B. A.; Patrick, B. O.; Fryzuk, M. D. *Proceedings of the National Academy of Sciences* **2006,** *103* (46), 17094-17098.
101. Burford, R. J.; Yeo, A.; Fryzuk, M. D. *Coord. Chem. Rev.* **2017,** *334*, 84-99.
102. Shaver, M. P.; Fryzuk, M. D. *Organometallics* **2005,** *24* (7), 1419-1427.
103. Shaver, M. P. Small molecule activation by diamidophosphine complexes of vanadium, niobium and tantalum. University of British Columbia, Vancouver, 2004.
104. Semproni, S. P.; Lobkovsky, E.; Chirik, P. J. *J. Am. Chem. Soc.* **2011,** *133* (27), 10406-10409.
105. Giesbrecht, G. R. Amidophosphine complexes of electron-poor metals. University of British Columbia, Vancouver, 1998.
106. Fryzuk, M. D.; Kozak, C. M.; Bowdridge, M. R.; Patrick, B. O. *Organometallics* **2002,** *21* (23), 5047-5054.
107. Fryzuk, M. D.; Kozak, C. M.; Mehrkhodavandi, P.; Morello, L.; Patrick, B. O.; Rettig, S. J. *J. Am. Chem. Soc.* **2002,** *124* (4), 516-517.
108. Kozak, C. M. Activation of small molecules by medium valent niobium complexes stabilized by a bis(amidophosphine) macrocycle. University of British Columbia, Vancouver, 2002.
109. Parks, D. J.; Piers, W. E.; Yap, G. P. A. *Organometallics* **1998,** *17* (25), 5492-5503.
110. Yan, K.; Upton, B. M.; Zhu, J.; Ellern, A.; Sadow, A. D. *Organometallics* **2013,** *32* (22), 6834-6843.
111. Schnurr, A.; Samigullin, K.; Breunig, J. M.; Bolte, M.; Lerner, H.-W.; Wagner, M. *Organometallics* **2011,** *30* (10), 2838-2843.
112. Chatt, J.; Dilworth, J. R.; Gunz, H. P.; Leigh, G. J.; Sanders, J. R. *Journal of the Chemical Society D: Chemical Communications* **1970,** (2), 90-91.
113. Chatt, J.; Dilworth, J. R.; Leigh, G. J. *J. Chem. Soc., Dalton Trans.* **1973,** (6), 612-618.
114. Allen, A. D.; Harris, R. O.; Loescher, B. R.; Stevens, J. R.; Whiteley, R. N. *Chem. Rev.* **1973,** *73* (1), 11-20.
115. Connelly, N. G.; Geiger, W. E. *Chem. Rev.* **1996,** *96* (2), 877-910.
116. Colquhoun, H. M.; Henrick, K. *Inorg. Chem.* **1981,** *20* (12), 4074-4078.
117. Hoffmann, R.; Beier, B. F.; Muetterties, E. L.; Rossi, A. R. *Inorg. Chem.* **1977,** *16* (3), 511-522.

118. Brown, G. M.; Walker, L. A. *Acta Crystallographica* **1966,** *20* (2), 220-229.
119. Bortoluzzi, M.; Ferretti, E.; Marchetti, F.; Pampaloni, G.; Zacchini, S. *J. Coord. Chem.* **2016,** *69* (18), 2766-2774.
120. Cohen, T.; Song, I. H.; Fager, J. H.; Deets, G. L. *J. Am. Chem. Soc.* **1967,** *89* (19), 4968-4975.
121. Chen, D. X.; Ho, C. M.; Rudy Wu, Q. Y.; Wu, P. R.; Wong, F. M.; Wu, W. *Tetrahedron Lett.* **2008,** *49* (26), 4147-4148.
122. Wu, Y.; Huang, Z.; Luo, Y.; Liu, D.; Deng, Y.; Yi, H.; Lee, J.-F.; Pao, C.-W.; Chen, J.-L.; Lei, A. *Org. Lett.* **2017,** *19* (9), 2330-2333.
123. Siddaraju, Y.; Prabhu, K. R. *The Journal of Organic Chemistry* **2017,** *82* (6), 3084-3093.
124. Nguyen, T.-A. D.; Wright, A. M.; Page, J. S.; Wu, G.; Hayton, T. W. *Inorg. Chem.* **2014,** *53* (21), 11377-11387.
125. Farnaby, J. H.; Fang, M.; Ziller, J. W.; Evans, W. J. *Inorg. Chem.* **2012,** *51* (20), 11168-11176.
126. Mahanthappa, M. K.; Huang, K.-W.; Cole, A. P.; Waymouth, R. M. *Chem. Commun.* **2002,** (5), 502-503.
127. Akagi, F.; Matsuo, T.; Kawaguchi, H. *Angew. Chem. Int. Ed.* **2007,** *46* (46), 8778-8781.
128. Kurogi, T.; Ishida, Y.; Hatanaka, T.; Kawaguchi, H. *Dalton Transactions* **2013,** *42* (21), 7510-7513.
129. Caselli, A.; Solari, E.; Scopelliti, R.; Floriani, C.; Re, N.; Rizzoli, C.; Chiesi-Villa, A. *J. Am. Chem. Soc.* **2000,** *122* (15), 3652-3670.
130. Buijink, J. K. F.; Meetsma, A.; Teuben, J. H. *Organometallics* **1993,** *12* (6), 2004-2005.
131. Vidyaratne, I.; Gambarotta, S.; Korobkov, I.; Budzelaar, P. H. M. *Inorg. Chem.* **2005,** *44* (5), 1187-1189.
132. Desmangles, N.; Jenkins, H.; Ruppa, K. B.; Gambarotta, S. *Inorg. Chim. Acta* **1996,** *250* (1–2), 1-4.
133. Vidyaratne, I.; Crewdson, P.; Lefebvre, E.; Gambarotta, S. *Inorg. Chem.* **2007,** *46* (21), 8836-8842.
134. Kilgore, U. J.; Sengelaub, C. A.; Fan, H.; Tomaszewski, J.; Karty, J. A.; Baik, M.-H.; Mindiola, D. J. *Organometallics* **2009,** *28* (3), 843-852.
135. Edema, J. J. H.; Meetsma, A.; Gambarotta, S. *J. Am. Chem. Soc.* **1989,** *111* (17), 6878-6880.
136. Aharonian, G.; Feghali, K.; Gambarotta, S.; Yap, G. P. A. *Organometallics* **2001,** *20* (12), 2616-2622.
137. Feghali, K.; Harding, D. J.; Reardon, D.; Gambarotta, S.; Yap, G.; Wang, Q. *Organometallics* **2002,** *21* (5), 968-976.
138. Bullock, R. M., Ed., *Catalysis without Precious Metals*. Wiley-VCH: Weinheim, Germany, 2010.
139. Chirik, P. J. *Acc. Chem. Res.* **2015,** *48* (6), 1687-1695.
140. Chirik, P. J.; Wieghardt, K. *Science* **2010,** *327* (5967), 794.
141. Knijnenburg, Q.; Horton, A. D.; Heijden, H. v. d.; Kooistra, T. M.; Hetterscheid, D. G. H.; Smits, J. M. M.; Bruin, B. d.; Budzelaar, P. H. M.; Gal, A. W. *J. Mol. Catal. A: Chem.* **2005,** *232* (1–2), 151-159.
142. Monfette, S.; Turner, Z. R.; Semproni, S. P.; Chirik, P. J. *J. Am. Chem. Soc.* **2012,** *134* (10), 4561-4564.

143. Friedfeld, M. R.; Margulieux, G. W.; Schaefer, B. A.; Chirik, P. J. *J. Am. Chem. Soc.* **2014,** *136* (38), 13178-13181.
144. Zhang, G.; Scott, B. L.; Hanson, S. K. *Angew. Chem. Int. Ed.* **2012,** *51* (48), 12102-12106.
145. Zhang, G.; Vasudevan, K. V.; Scott, B. L.; Hanson, S. K. *J. Am. Chem. Soc.* **2013,** *135* (23), 8668-8681.
146. Rösler, S.; Obenauf, J.; Kempe, R. *J. Am. Chem. Soc.* **2015,** *137* (25), 7998-8001.
147. Deibl, N.; Kempe, R. *J. Am. Chem. Soc.* **2016,** *138* (34), 10786-10789.
148. Rösler, S.; Ertl, M.; Irrgang, T.; Kempe, R. *Angew. Chem. Int. Ed.* **2015,** *54* (50), 15046-15050.
149. Chen, C.; Dugan, T. R.; Brennessel, W. W.; Weix, D. J.; Holland, P. L. *J. Am. Chem. Soc.* **2014,** *136* (3), 945-955.
150. Jenkins, D. M.; Di Bilio, A. J.; Allen, M. J.; Betley, T. A.; Peters, J. C. *J. Am. Chem. Soc.* **2002,** *124* (51), 15336-15350.
151. Hayes, C. E.; Leznoff, D. B. *Dalton Transactions* **2012,** *41* (19), 5743-5753.
152. Leznoff, D. B. Paramagnetic Organometallic Complexes of Chromium, Iron and Cobalt. University of British Columbia, Vancouver, 1997.
153. Burford, N.; Spence, R. E. H.; Whalen, J. M.; Rogers, R. D.; Richardson, J. F. *Organometallics* **1990,** *9* (11), 2854-2856.
154. Drover, M. W.; Schafer, L. L.; Love, J. A. *Angew. Chem. Int. Ed.* **2016,** *55* (9), 3181-3186.
155. Ingleson, M. J.; Pink, M.; Fan, H.; Caulton, K. G. *Inorg. Chem.* **2007,** *46* (24), 10321-10334.
156. Semproni, S. P.; Milsmann, C.; Chirik, P. J. *J. Am. Chem. Soc.* **2014,** *136* (25), 9211-9224.
157. Ding, K.; Brennessel, W. W.; Holland, P. L. *J. Am. Chem. Soc.* **2009,** *131* (31), 10804-10805.
158. Schaefer, B. A.; Margulieux, G. W.; Small, B. L.; Chirik, P. J. *Organometallics* **2015,** *34* (7), 1307-1320.
159. Chomitz, W. A.; Arnold, J. *Inorg. Chem.* **2009,** *48* (7), 3274-3286.
160. Evans, P. A., Ed., *Modern Rhodium-Catalyzed Organic Reactions* Wiley-VCH Verlag GmbH & Co. KGaA: Weinheim, 2005.
161. Konrad, F.; Lloret Fillol, J.; Wadepohl, H.; Gade, L. H. *Inorg. Chem.* **2009,** *48* (17), 8523-8535.
162. Wang, Y.; Zheng, B.; Pan, Y.; Pan, C.; He, L.; Huang, K.-W. *Dalton Transactions* **2015,** *44* (34), 15111-15115.
163. Smith, J. D.; Logan, J. R.; Doyle, L. E.; Burford, R. J.; Sugawara, S.; Ohnita, C.; Yamamoto, Y.; Piers, W. E.; Spasyuk, D. M.; Borau-Garcia, J. *Dalton Transactions* **2016,** *45* (32), 12669-12679.
164. Weng, W.; Guo, C.; Celenligil-Cetin, R.; Foxman, B. M.; Ozerov, O. V. *Chem. Commun.* **2006,** (2), 197-199.
165. Pell, C. J.; Ozerov, O. V. *ACS Catalysis* **2014,** *4* (10), 3470-3480.
166. Bezier, D.; Guan, C.; Krogh-Jespersen, K.; Goldman, A. S.; Brookhart, M. *Chemical Science* **2016,** *7* (4), 2579-2586.

167. Schwartsburd, L.; Iron, M. A.; Konstantinovski, L.; Ben-Ari, E.; Milstein, D. *Organometallics* **2011,** *30* (10), 2721-2729.
168. Anaby, A.; Feller, M.; Ben-David, Y.; Leitus, G.; Diskin-Posner, Y.; Shimon, L. J. W.; Milstein, D. *J. Am. Chem. Soc.* **2016,** *138* (31), 9941-9950.
169. Pappas, I.; Chirik, P. J. *J. Am. Chem. Soc.* **2015,** *137* (10), 3498-3501.
170. Lilio, A. M.; Reineke, M. H.; Moore, C. E.; Rheingold, A. L.; Takase, M. K.; Kubiak, C. P. *J. Am. Chem. Soc.* **2015,** *137* (25), 8251-8260.
171. Lam, R. H.; Walker, D. B.; Tucker, M. H.; Gatus, M. R. D.; Bhadbhade, M.; Messerle, B. A. *Organometallics* **2015,** *34* (17), 4312-4317.
172. Fryzuk, M. D. *Inorg. Chim. Acta* **1981,** *54*, L265-L266.
173. Fryzuk, M. D. *Organometallics* **1982,** *1* (2), 408-409.
174. Jong, H.; Patrick, B. O.; Fryzuk, M. D. *Can. J. Chem.* **2008,** *86* (8), 803-810.
175. Shaw, B. K.; Patrick, B. O.; Fryzuk, M. D. *Organometallics* **2012,** *31* (3), 783-786.
176. Fryzuk, M. D.; MacNeil, P. A.; McManus, N. T. *Organometallics* **1987,** *6* (4), 882-884.
177. Meek, D. W.; Mazanec, T. J. *Acc. Chem. Res.* **1981,** *14* (9), 266-274.
178. Vasilenko, V.; Roth, T.; Blasius, C. K.; Intorp, S. N.; Wadepohl, H.; Gade, L. H. *Beilstein Journal of Organic Chemistry* **2016,** *12*, 846-853.
179. Appleton, T. G.; Clark, H. C.; Manzer, L. E. *Coord. Chem. Rev.* **1973,** *10* (3), 335-422.
180. Stevens, T. E.; Smoll, K. A.; Goldberg, K. I. *J. Am. Chem. Soc.* **2017,** *139* (23), 7725-7728.
181. König, A.; Fischer, C.; Alberico, E.; Selle, C.; Drexler, H.-J.; Baumann, W.; Heller, D. *Eur. J. Inorg. Chem.* **2017,** *2017* (13), 2040-2047.
182. Hu, Y.; Li, L.; Shaw, A. P.; Norton, J. R.; Sattler, W.; Rong, Y. *Organometallics* **2012,** *31* (14), 5058-5064.
183. Burford, R. J.; Fryzuk, M. D. **2017,** *1*, 0026.
184. Ballmann, J.; Pick, F.; Castro, L.; Fryzuk, M. D.; Maron, L. *Organometallics* **2012,** *31* (24), 8516-8524.
185. Batke, S.; Sietzen, M.; Merz, L.; Wadepohl, H.; Ballmann, J. *Organometallics* **2016,** *35* (13), 2294-2308.
186. Tran, B. L.; Pink, M.; Gao, X.; Park, H.; Mindiola, D. J. *J. Am. Chem. Soc.* **2010,** *132* (5), 1458-1459.
187. Critchlow, S. C.; Lerchen, M. E.; Smith, R. C.; Doherty, N. M. *J. Am. Chem. Soc.* **1988,** *110* (24), 8071-8075.
188. Del Castillo, T. J.; Thompson, N. B.; Suess, D. L. M.; Ung, G.; Peters, J. C. *Inorg. Chem.* **2015,** *54* (19), 9256-9262.
189. *SAINT*, Version 8.18C; Bruker AXS Inc.: Madison, Wisconson, USA, 2012.
190. *SADABS*, Version 2008/1; Bruker AXS Inc.: Madison, Wisconsin, USA, 2008.
191. Farrugia, L. J. *J. Appl. Crystallogr.* **2012,** *45*, 849-854.
192. Dolomanov, O. V.; Bourhis, L. J.; Gildea, R. J.; Howard, J. A. K.; Puschmann, H. *J. Appl. Crystallogr.* **2009,** *42*, 339-341.
193. Sheldrick, G. M. *Acta Cryst. A* **2008,** *64*, 112-122.
194. Sluis, P. v. d.; Spek, A. L. *Acta Cryst. A* **1990,** *46*, 194-201.
195. Spek, A. L. *J Appl. Crystallogr.* **2003,** *36*, 7-13.
196. Anderson, H. H. *J. Am. Chem. Soc.* **1960,** *82* (6), 1323-1325.
197. Bielawski, M.; Zhu, M.; Olofsson, B. *Adv. Synth. Catal.* **2007,** *349* (17-18), 2610-2618.

198. Jordan, R. F.; Echols, S. F. *Inorg. Chem.* **1987,** *26* (3), 383-386.
199. Piglosiewicz, I. M.; Beckhaus, R.; Wittstock, G.; Saak, W.; Haase, D. *Inorg. Chem.* **2007,** *46* (18), 7610-7620.
200. Scholz, S.; Scheibitz, M.; Schödel, F.; Bolte, M.; Wagner, M.; Lerner, H.-W. *Inorg. Chim. Acta* **2007,** *360* (10), 3323-3329.
201. Cowley, R. E.; Bontchev, R. P.; Duesler, E. N.; Smith, J. M. *Inorg. Chem.* **2006,** *45* (24), 9771-9779.

Appendices

Appendix A – Selected NMR spectra

A.1 Selected NMR spectra pertaining to Chapter 2

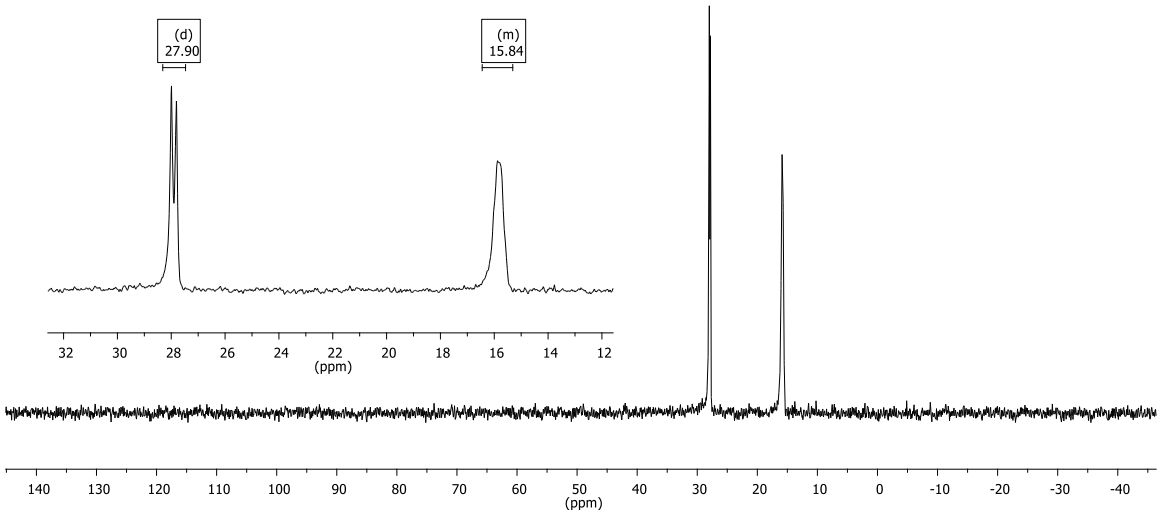

Figure A.1.1 $^{31}P\{^{1}H\}$ NMR spectrum (121.4 MHz, C_6D_6) of $(^{Cy}[NPN^{Si}]Ta)_2(\mu\text{-}\eta^2\text{:}\eta^1\text{-}N_2)(\mu\text{-}H)_2$ (**2.4**).

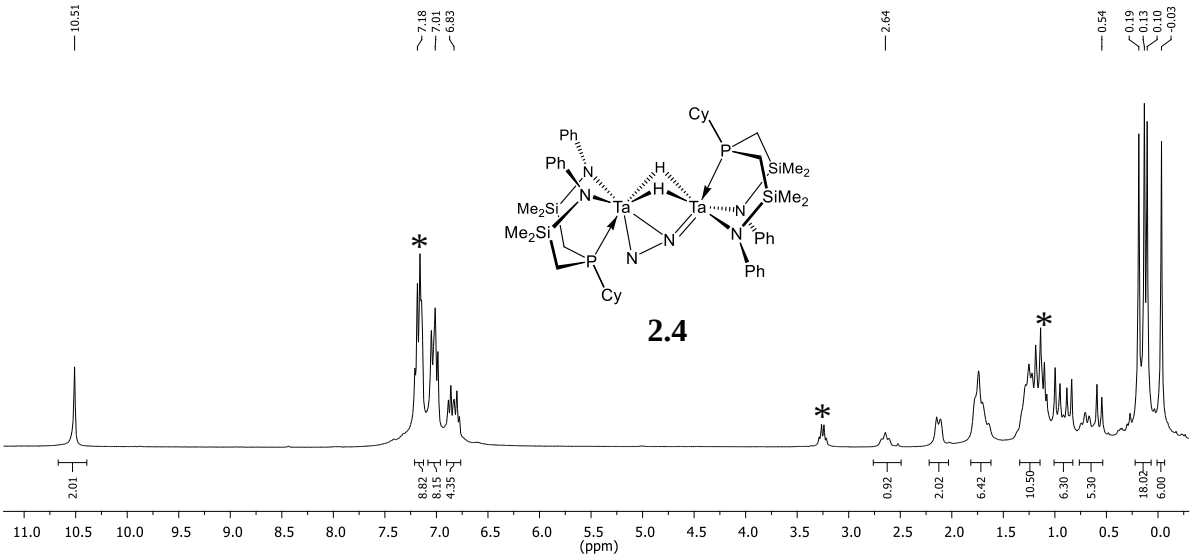

Figure A.1.2 $^{1}H\{^{31}P\}$ NMR spectrum (300 MHz, C_6D_6) of **2.4**. Resonances denoted with (*) indicate residual solvent impurities from benzene and diethyl ether, respectively.

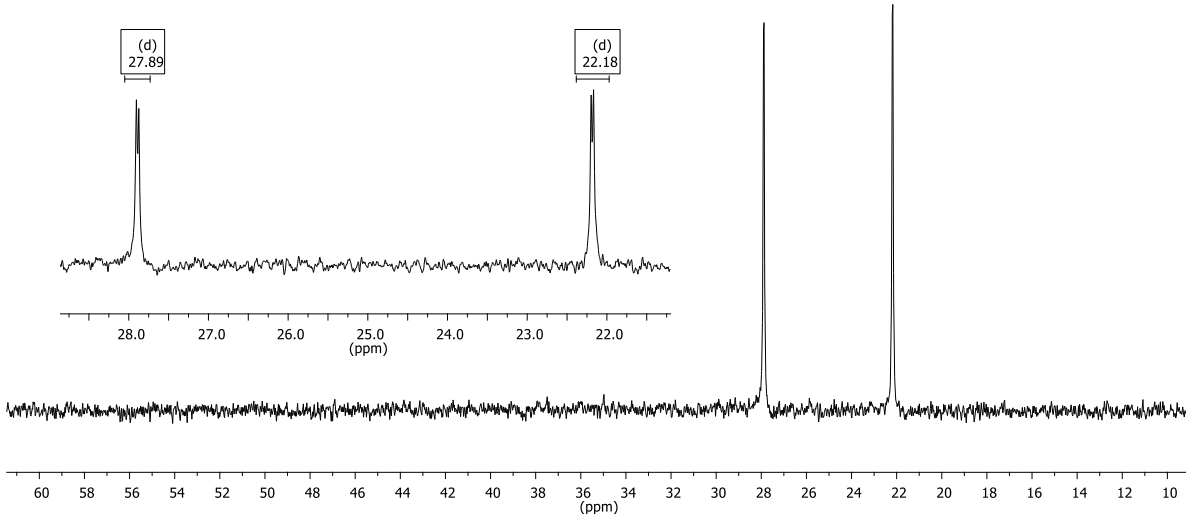

Figure A.1.3 $^{31}P\{^{1}H\}$ NMR spectrum (161.9 MHz) of $^{Cy}[NPN^{Si}]TaH(BuSiN\text{-}\mu\text{-}Si(H)Bu\text{-}\mu\text{-}N)(\mu\text{-}H)_2Ta[NPN^{Si}]^{Cy}$ (**2.7**) in C_6D_6.

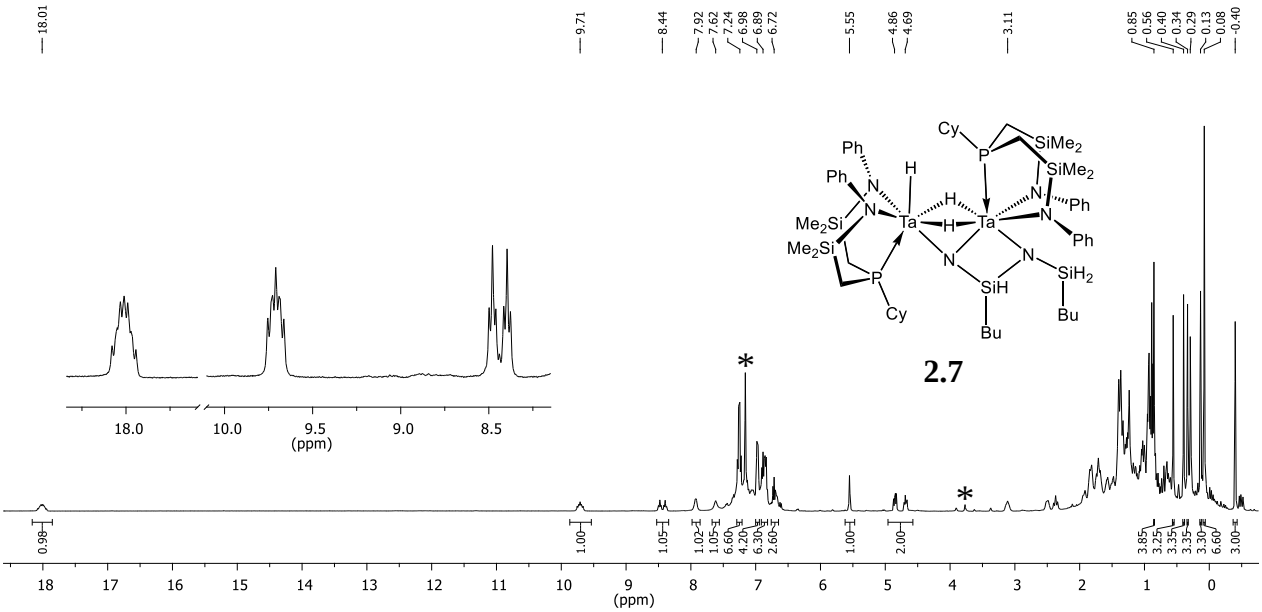

Figure A.1.4 ^{1}H NMR spectrum (400 MHz, C_6D_6) of **2.7**. Resonances denoted with (*) indicate residual benzene and $^{n}BuSiH_3$, respectively. The singlet at δ 0.29 corresponds to a silicone grease impurity.

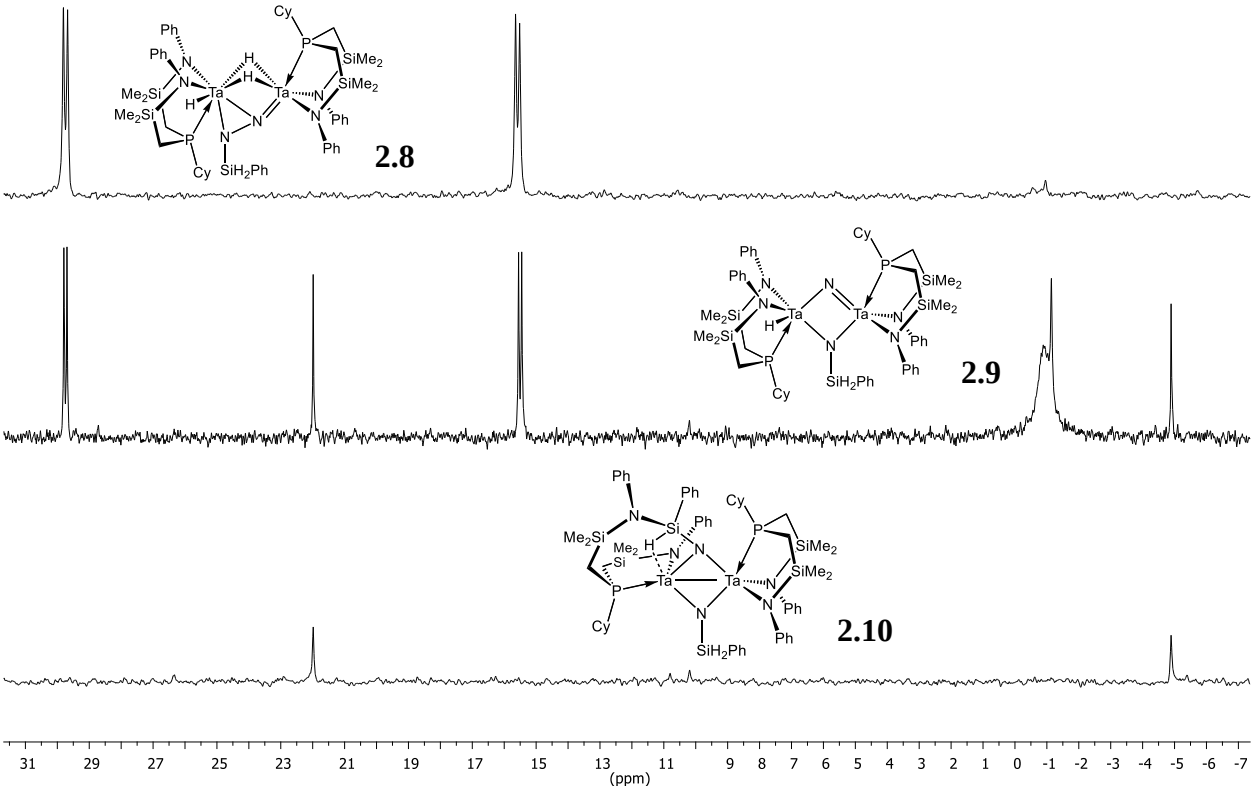

Figure A.1.5 $^{31}P\{^{1}H\}$ NMR spectra (161.9 MHz, C_6D_6) recorded after treatment of **2.4** with excess $PhSiH_3$, showing resonances corresponding to **2.8** (δ 29.7 and 15.5), **2.9** (δ -1.0), and **2.10** (δ 22.0 and -4.9).

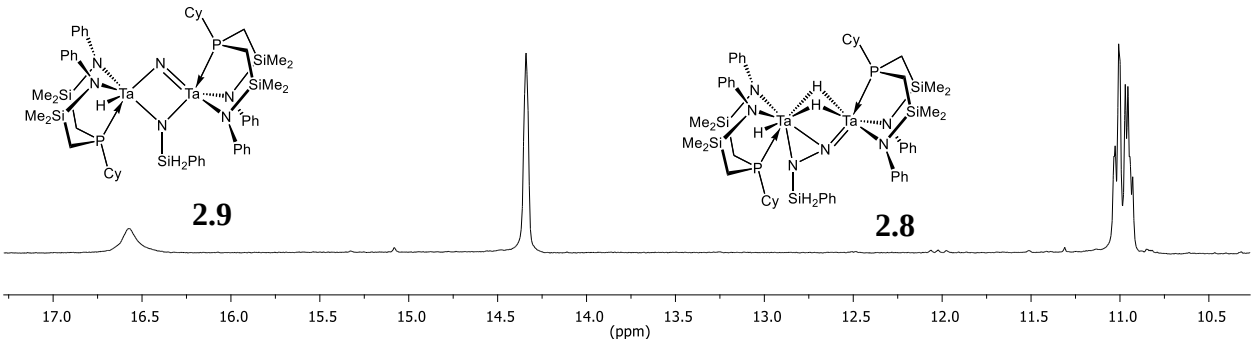

Figure A.1.6 $^{1}H\{^{31}P\}$ NMR spectrum (400 MHz, C_6D_6) recorded after treatment of **2.4** with excess $PhSiH_3$, focused on the hydride region, showing resonances corresponding to the bridging and terminal tantalum hydrides of **2.8** (δ 11.0 and 14.3, respectively) and the terminal tantalum hydride of **2.9** (δ 16.5).

A.2 Selected NMR spectra pertaining to Chapter 3

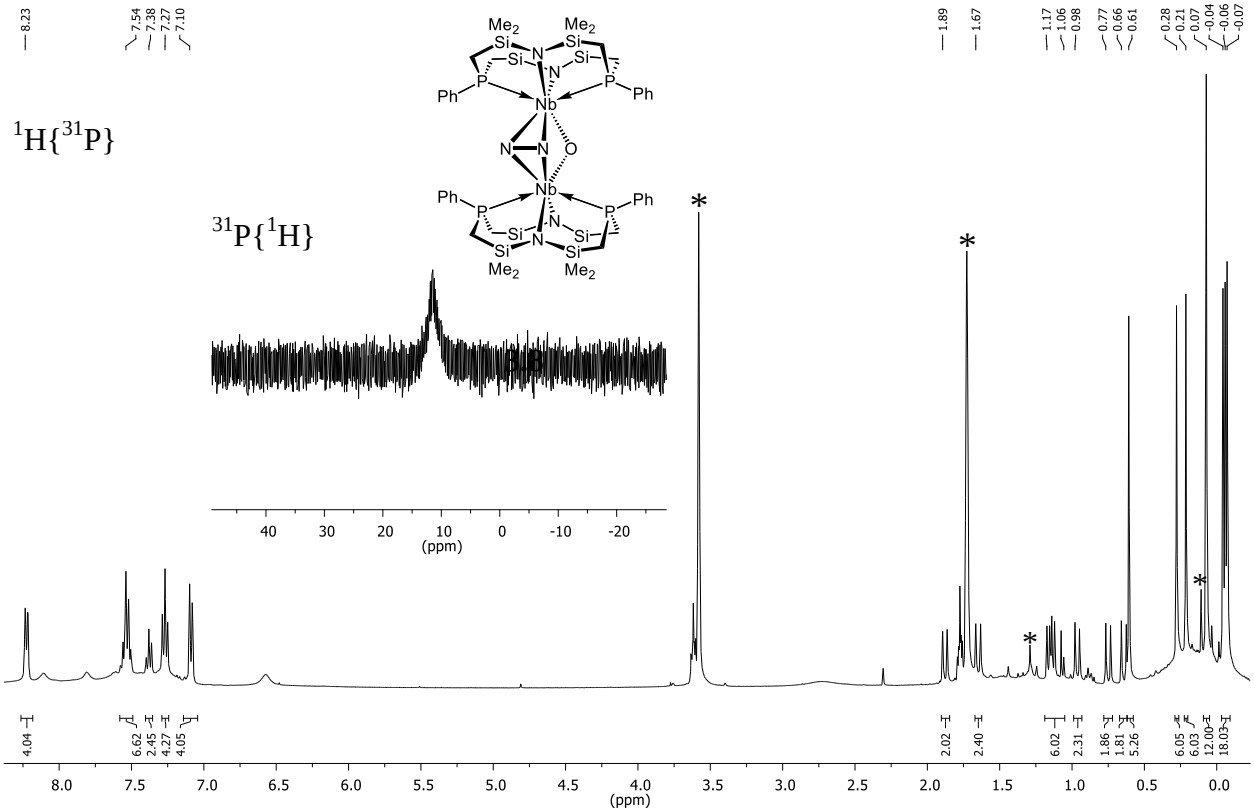

Figure A.2.1 ^{31}P{^{1}H} NMR (161.9 MHz) spectrum (inset) and ^{1}H{^{31}P} NMR spectrum (400 MHz) of ([P_2N_2]Nb)$_2$(μ-η^2:η^2-N_2)(μ-O) (**3.8**) in THF-d_8. Resonances denoted with (*) indicate residual solvent impurities from THF and hexane, respectively. Minor broad resonances correspond to an unidentified paramagnetic impurity.

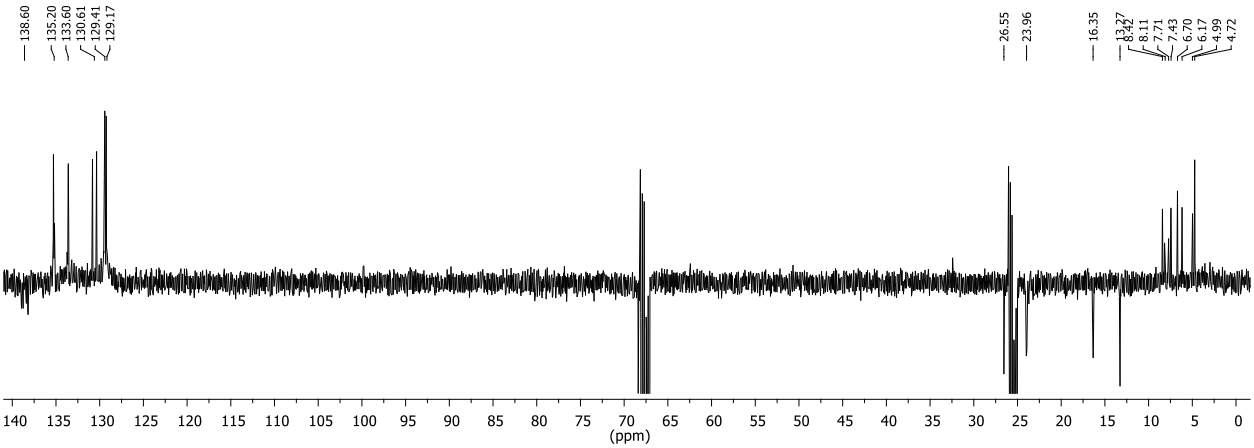

Figure A.2.2 ^{13}C APT NMR spectrum (100.6 MHz, THF-d_8) of **3.8** (with methine and methyl carbons in a positive phase and negatively phased quaternary carbons and methylene carbons).

A.3 Selected NMR spectra pertaining to Chapter 4

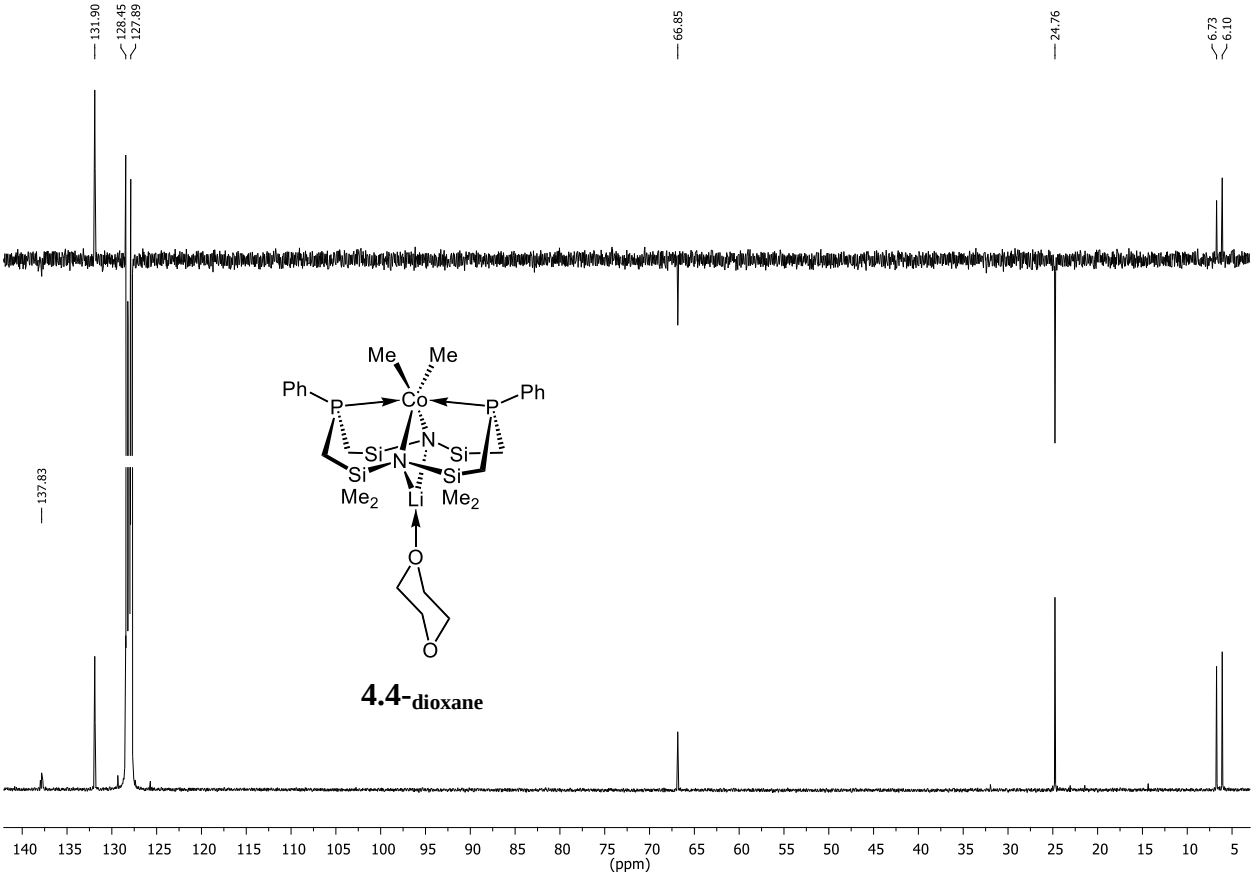

Figure A.3.1 $^{13}C\{^{1}H\}$ NMR spectrum (100.6 MHz, C_6D_6) of **4.4-$_{dioxane}$** (bottom) and ^{13}C APT NMR spectrum (top) displaying methine and methyl carbons in a positive phase, and negatively phased quaternary carbons and methylene carbons.

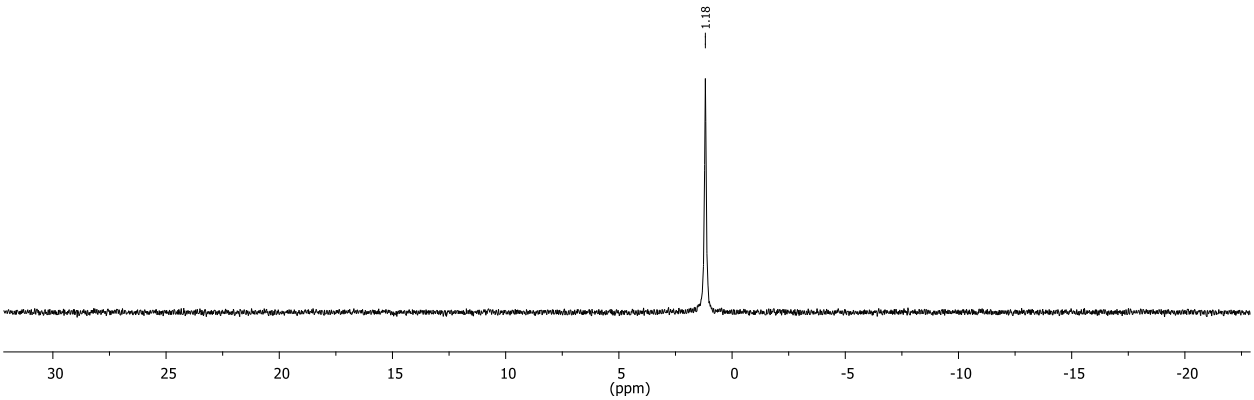

Figure A.3.2 ^{7}Li NMR (155.5 MHz, C_6D_6) spectrum of **4.4-$_{dioxane}$**.

A.4 Selected NMR spectra pertaining to Chapter 5

^{31}P NMR (161.9 MHz, C_6D_6) δ 32.82 (d, *J* = 107.8 Hz), 22.80 (d, *J* = 127.3 Hz), 20.00 (d, *J* = 143.5 Hz), 13.19 (d, *J* = 202.2 Hz).

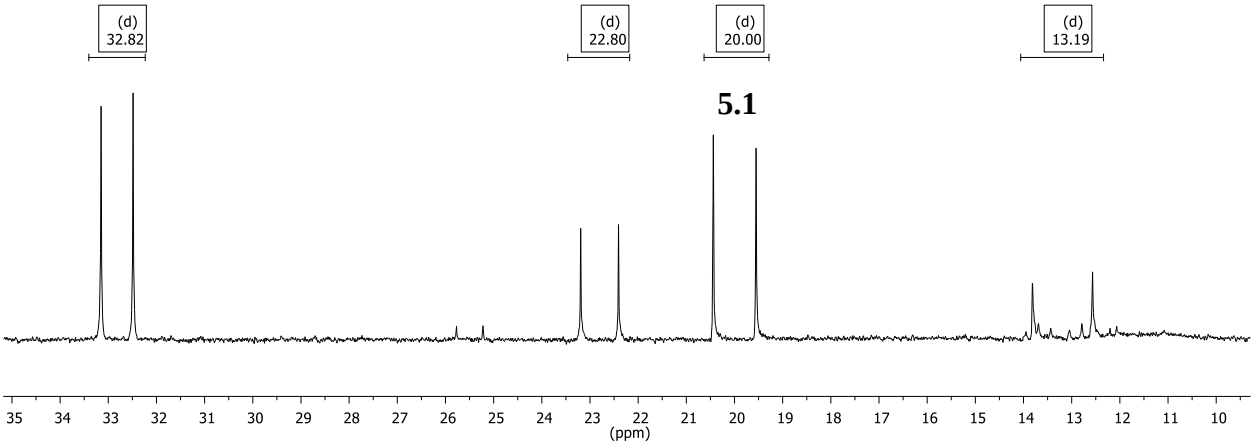

Figure A.4.1 $^{31}P\{^1H\}$ NMR spectrum (161.9 MHz, C_6D_6) of the material isolated from heating a THF solution of *syn*-$[P_2N_2]Li_2$ with half an equivalent of $[Rh(COD)Cl]_2$ at 60 °C for 12 h, showing resonances corresponding to complex **5.1**, in addition to several unidentified new rhodium species.

^{31}P NMR (161.9 MHz, C_6D_6) δ 33.65 (d, *J* = 95.9 Hz), 21.03 (d, *J* = 104.8 Hz), 20.60 (d, *J* = 114.3 Hz).

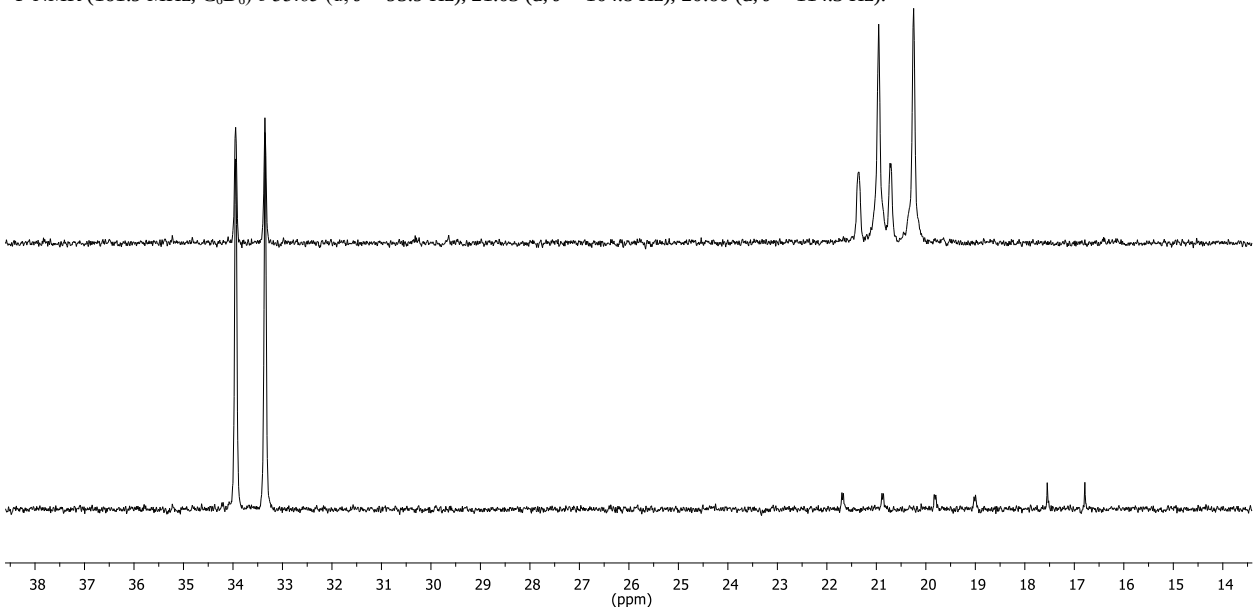

Figure A.4.2 Comparison of the $^{31}P\{^1H\}$ NMR spectra (161.9 MHz, C_6D_6) of the material isolated after the treatment of complex **5.1** with H_2 gas, before heating (top) and after heating at 80 °C for 12 h (bottom).

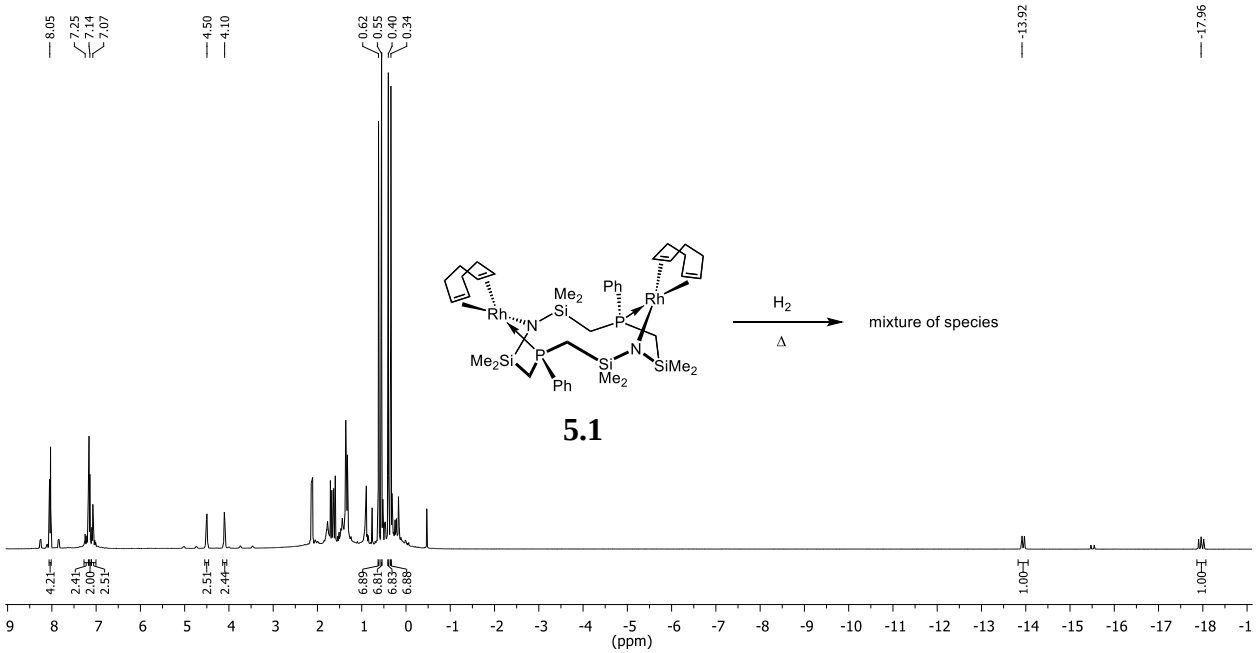

Figure A.4.3 $^1H\{^{31}P\}$ NMR spectrum (400 MHz, C_6D_6) of the material isolated after the treatment of complex **5.1** with H_2 gas, after heating at 80 °C for 12 h.

^{31}P NMR (161.9 MHz, C_6D_6) δ 27.06 (d, *J* = 101.0 Hz), 16.56 (d, *J* = 99.6 Hz).

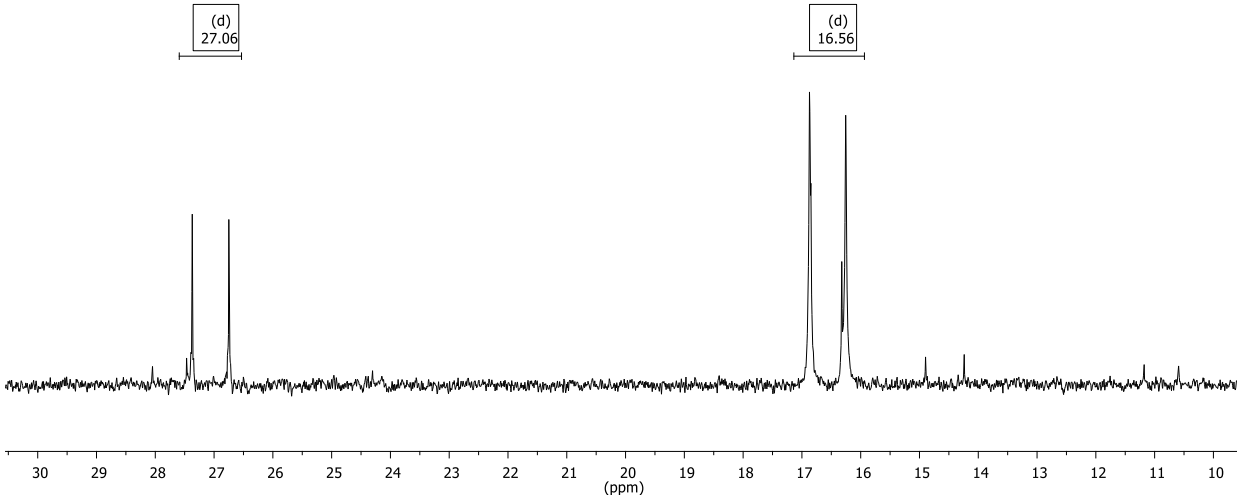

Figure A.4.4 $^{31}P\{^1H\}$ NMR spectrum (161.9 MHz, C_6D_6) of the material isolated after treatment of ([Rh(COE)][P_2N_2]Li)$_2$(dioxane) (**5.4**) with excess MeI.

^{31}P NMR (161.9 MHz, C_6D_6) δ 63.76 (d, *J* = 132.6 Hz), 16.64 (d, *J* = 84.6 Hz).

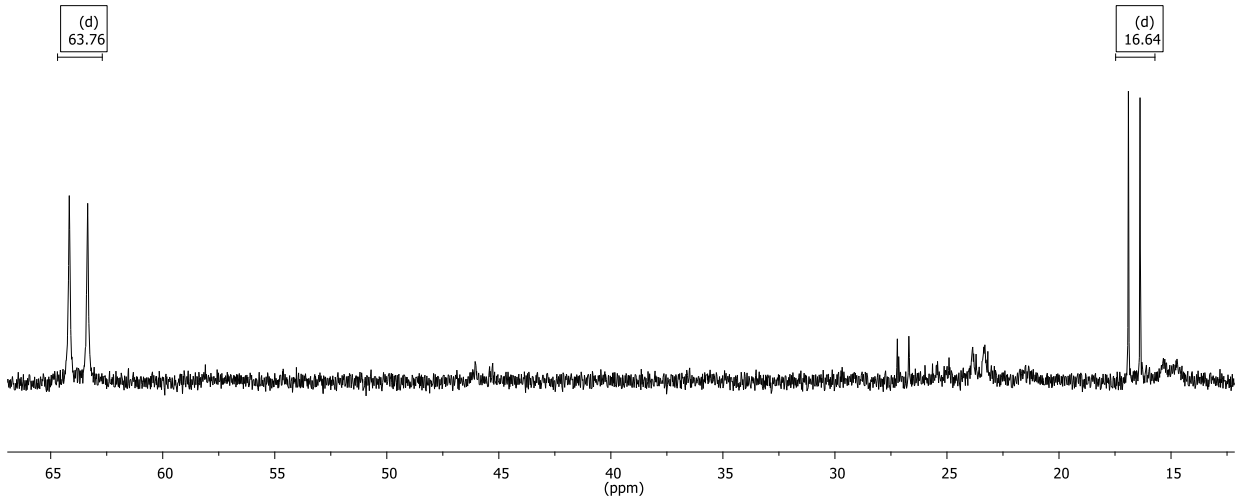

Figure A.4.5 $^{31}P\{^1H\}$ NMR spectrum (161.9 MHz, C_6D_6) of the material isolated after treatment of ([Rh(COE)][P_2N_2]Li)$_2$(dioxane) (**5.4**) with I-CH_2CH_2-I.

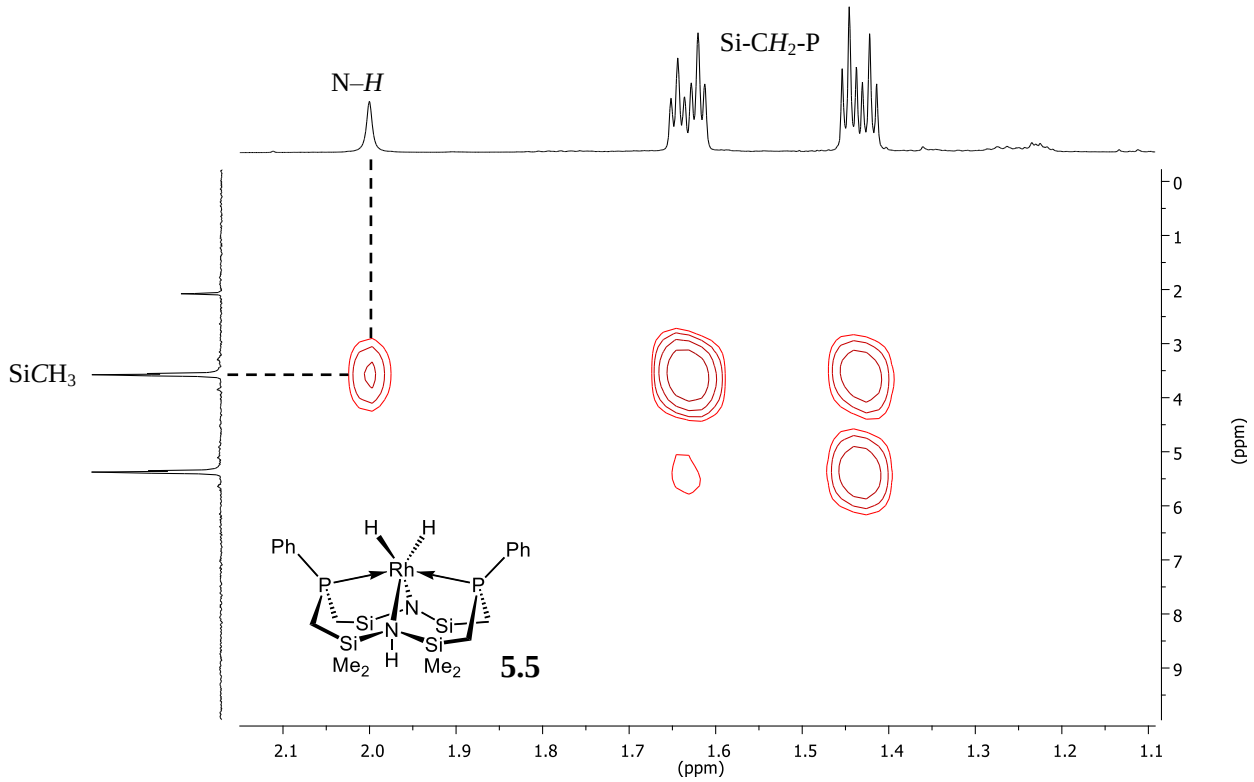

Figure A.4.6 ^{1}H–^{13}C HMBC NMR spectrum (400 MHz, ^{1}H and 100.6 MHz, ^{13}C external projections, C_6D_6) of **5.5** displaying a multiple-bond correlation between the N–H proton and silyl methyl carbons.

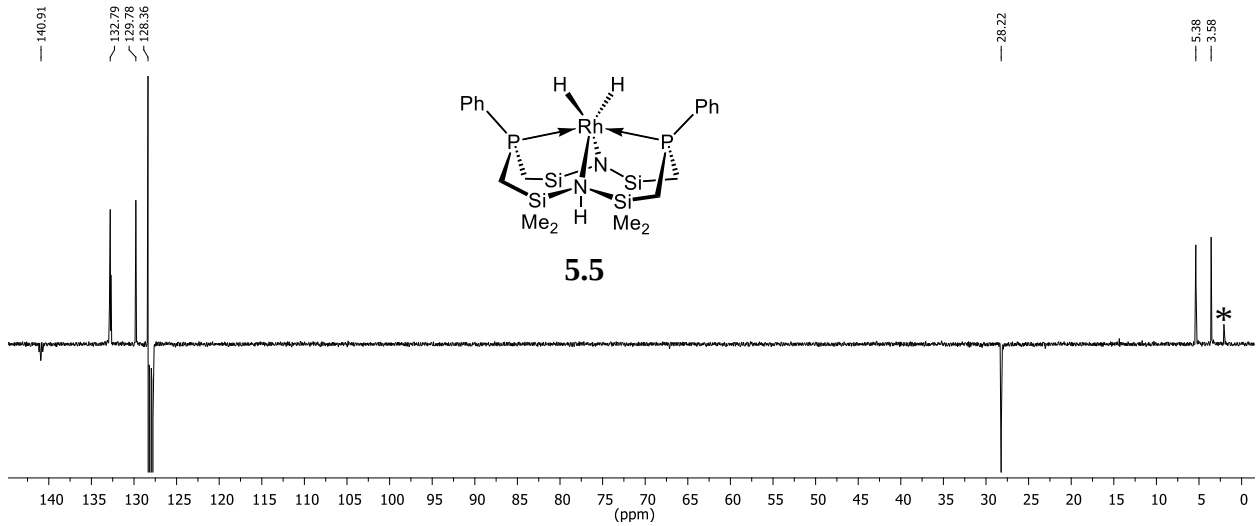

Figure A.4.7 ^{13}C APT NMR spectrum (100.6 MHz, C_6D_6) of **5.5** (with methine and methyl carbons in a positive phase and negatively phased quaternary carbons and methylene carbons). (Resonance denoted with (*) corresponds to residual HMDSO).

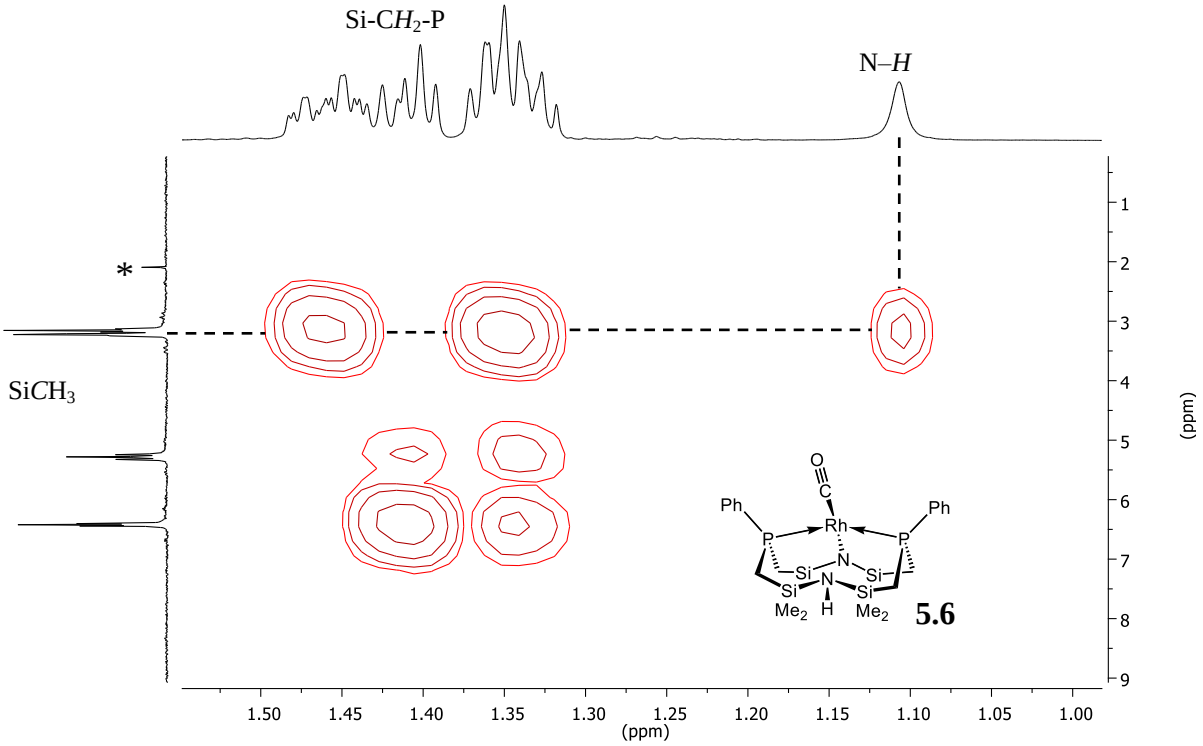

Figure A.4.8 ^{1}H–^{13}C HMBC NMR spectrum (400 MHz, ^{1}H and 100.6 MHz, ^{13}C external projections, C_6D_6) of **5.6** displaying a multiple-bond correlation between the N–H proton and silyl methyl carbons. (Resonance denoted with (*) corresponds to residual HMDSO).

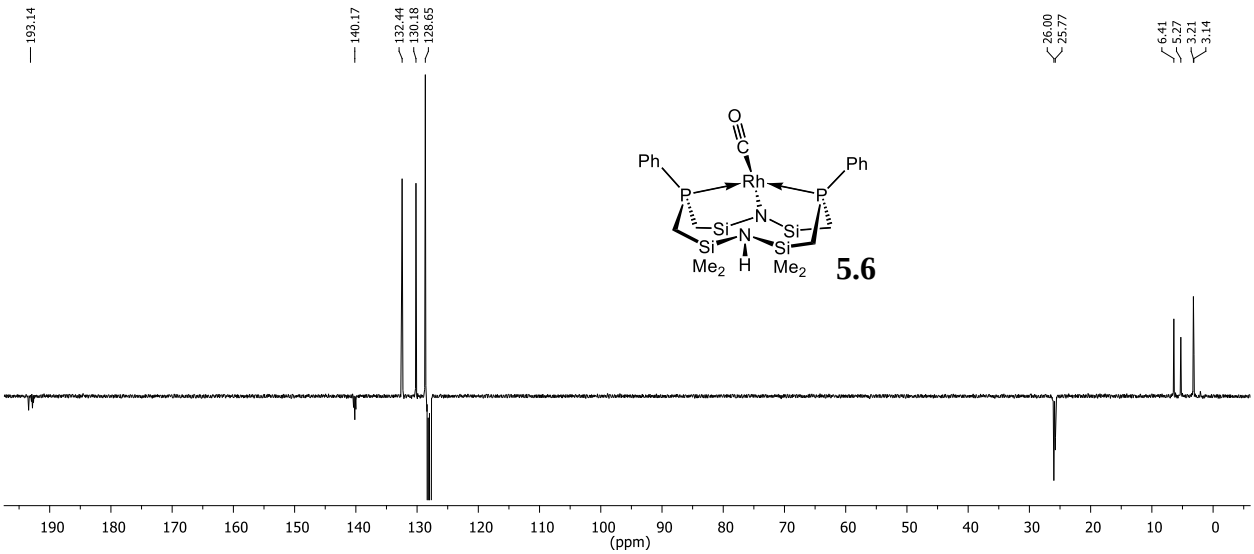

Figure A.4.9 ^{13}C APT NMR spectrum (100.6 MHz, C_6D_6) of **5.6** (with methine and methyl carbons in a positive phase and negatively phased quaternary carbons and methylene carbons).

Appendix B – IR spectra

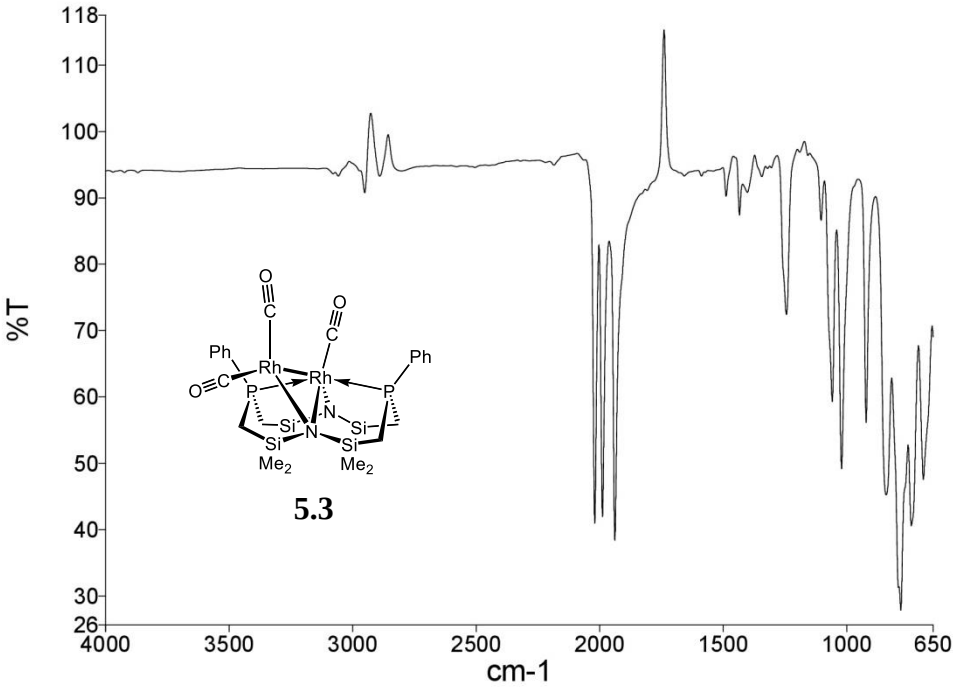

Figure B.1 IR spectrum of complex **5.3** (ν_{CO} = 1938, 1988 and 2020 cm^{-1}).

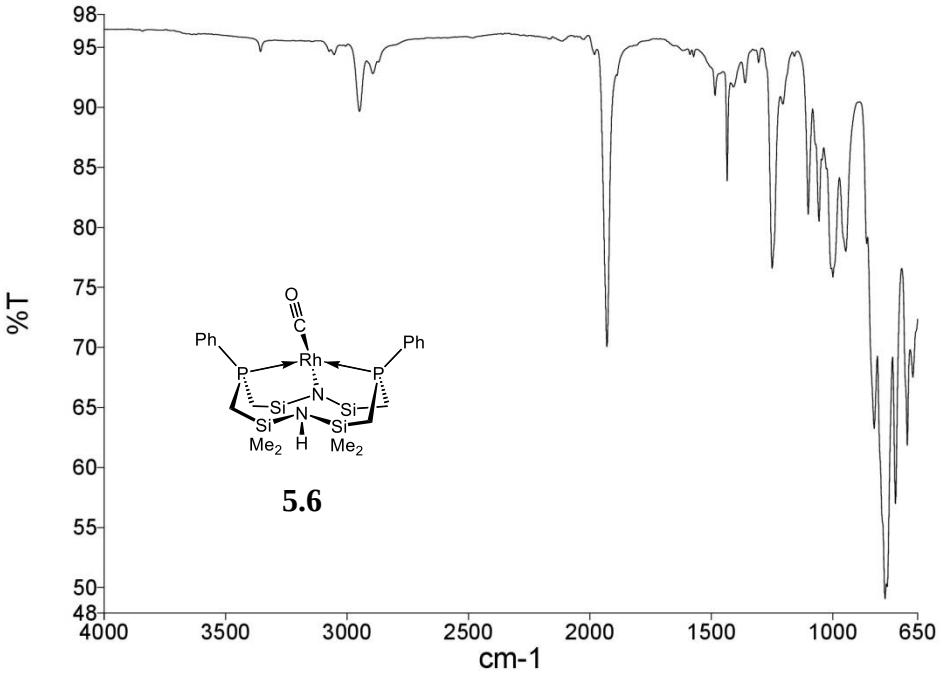

Figure B.2 IR spectrum of complex **5.6** (ν_{CO} = 1929 cm^{-1}).

Appendix C – Crystallographic data

Table C.1 Crystal structure and refinement data for **2.4** and **2.7**

	2.4	**2.7**
Chemical formula	$C_{48}H_{76}N_6P_2Si_4Ta_2$	$C_{56}H_{98}N_6P_2Si_6Ta_2$
Formula weight	1273.34	1447.78
Crystal system	Monoclinic	Triclinic
Space group	P 2_1/c	P -1
a / Å	11.3156(4)	13.6809(19)
b / Å	23.4550(9)	13.6965(16)
c / Å	20.0417(6)	20.954(3)
α / °	90	76.560(7)
β / °	95.298(2)	75.492(7)
γ / °	90	89.665(8)
Volume / $Å^3$	5296.5(3)	3691.4(8)
T / K	90(2)	90(2)
Z	4	2
μ / mm^{-1}	4.318	3.137
ρ (calcd) / g/cm^3	1.597	1.303
F(000)	2552	1472
Absorption correction	Multi–scan	Multi–scan
Crystal size / mm	0.09 x 0.05 x 0.03	0.27 x 0.25 x 0.12
Wavelength / Å	0.71073	0.71073
Reflections collected	52372	68346
Unique reflections	9657 (R_{int} = 0.1173)	21572 (R_{int} = 0.0520)
Data / restraints / parameters	9657 / 591 / 567	21572 / 753 / 748
Goodness-of-fit on F^2	0.991	0.992
R indices [I >2σ(I)] / R1, wR2	0.0461, 0.0568	0.0369, 0.0850
R indices (all data) / R1, wR2	0.1107, 0.0684	0.0581, 0.0919
Completeness to theta max.	0.992	0.997
Max. and min. transmission	0.8785, 0.7657	0.6863, 0.5643
Theta range for data collection / °	1.340 – 25.418	2.852 – 30.193

$R1 = \Sigma \, \| F_o | - | F_c \| / \Sigma | F_o |$; $wR2 = [\Sigma \{w(F_o^2 - F_c^2)^2\} / \Sigma w(F_o^2)^2]^{1/2}$

Table C.2 Crystal structure and refinement data for **3.1** and **3.2**

	3.1	**3.2**
Chemical formula	$C_{48}H_{84}N_6Nb_2P_4Si_8$	$C_{56}H_{106}Al_2N_6Nb_2OP_4Si_8$
Formula weight	1279.63	1467.84
Crystal system	Monoclinic	Monoclinic
Space group	$P2_1/c$	$P2_1/c$
a / Å	14.464(2)	17.365(2)
b / Å	13.426(2)	19.114(3)
c / Å	33.465(5)	22.852(2)
α / °	90	90
β / °	99.452(4)	91.773(3)
γ / °	90	90
Volume / $Å^3$	6410.5(17)	7581.4(15)
T / K	90(2)	90(2)
Z	4	4
μ / mm^{-1}	0.643	0.575
ρ (calcd) / g/cm^3	1.326	1.286
F(000)	2672	3088
Absorption correction	Multi–scan	Multi–scan
Crystal size / mm	0.20 x 0.15 x 0.13	0.12 x 0.03 x 0.03
Wavelength / Å	0.71073	0.71073
Reflections collected	41562	24123
Unique reflections	9536 (Rint = 0.1315)	13529 (Rint = 0.1878)
Data / restraints / parameters	9536 /0 / 613	13529 / 789 / 734
Goodness-of-fit on F^2	1.023	0.940
R indices [I >2σ(I)] / R1, wR2	0.0916, 0.1936	0.0782, 0.1149
R indices (all data) / R1, wR2	0.1564, 0.2302	0.2174, 0.1551
Completeness to theta max.	0.994	0.773
Max. and min. transmission	0.9202, 0.7908	0.9829, 0.8463
Theta range for data collection / °	2.854 – 47.208	3.602 – 55.088

$R1 = \Sigma \, \| F_o | - | F_c \| / \Sigma | F_o |$; $wR2 = [\Sigma \{w(F_o^2 - F_c^2)^2\} / \Sigma w(F_o^2)^2]^{1/2}$

Table C.3 Crystal structure and refinement data for **3.4** and **3.5**

	3.4	**3.5**
Chemical formula	$C_{64}H_{90}BF_{10}N_6Nb_2OP_4Si_8$	$C_{48}H_{84}I_2N_6Nb_2P_4Si_8$
Formula weight	1694.64	1533.44
Crystal system	Monoclinic	Monoclinic
Space group	$P2_1/c$	C2/c
a / Å	16.3620(11)	18.363(10)
b / Å	16.8523(12)	16.287(9)
c / Å	30.418(2)	26.020(16)
α / °	90	90
β / °	103.462(2)	101.285(17)
γ / °	90	90
Volume / $Å^3$	8156.9(10)	7632(8)
T / K	90(2)	100(2)
Z	4	4
μ / mm^{-1}	0.542	1.359
ρ (calcd) / g/cm^3	1.38	1.495
F(000)	3492	3496
Absorption correction	Multi–scan	Multi–scan
Crystal size / mm	0.40 x 0.34 x 0.24	0.36 x 0.28 x 0.25
Wavelength / Å	0.71073	0.71073
Reflections collected	74984	25569
Unique reflections	18727 (Rint = 0.0551)	7376 (Rint = 0.1913)
Data / restraints / parameters	18727 / 0 / 873	7376 / 12 / 378
Goodness-of-fit on F^2	1.020	0.958
R indices [I >2σ(I)] / R1, wR2	0.0471, 0.1031	0.1074, 0.2904
R indices (all data) / R1, wR2	0.0805, 0.1218	0.2028, 0.3487
Completeness to theta max.	0.996	0.932
Max. and min. transmission	0.8780, 0.7752	0.7119, 0.3180
Theta range for data collection / °	2.56 – 55.068	3.372 – 52.974

$R1 = \Sigma \, \| F_o | - | F_c \| / \Sigma | F_o |$; $wR2 = [\Sigma \{w(F_o^2 - F_c^2)^2\} / \Sigma w(F_o^2)^2]^{1/2}$

Table C.4 Crystal structure and refinement data for **3.6** and **3.7**

	3.6	**3.7**
Chemical formula	$C_{32}H_{50}F_3N_2NbO_3P_2SSi_4$	$C_{48}H_{84}BF_7N_4Nb_2P_4Si_8$
Formula weight	867.01	1395.41
Crystal system	Monoclinic	Monoclinic
Space group	C2/c	$P2_1/n$
a / Å	22.9239(19)	13.3229(9)
b / Å	21.2106(17)	30.959(3)
c / Å	19.2535(16)	17.3479(13)
α / °	90	90
β / °	123.623(2)	108.470(2)
γ / °	90	90
Volume / $Å^3$	7795.4(11)	6786.8(9)
T / K	90(2)	100(2)
Z	8	4
μ / mm^{-1}	0.617	0.631
ρ (calcd) / g/cm^3	1.477	1.436
F(000)	3600	3046
Absorption correction	Multi–scan	Multi–scan
Crystal size / mm	0.20 x 0.05 x 0.03	0.33 x 0.22 x 0.20
Wavelength / Å	0.71073	0.71073
Reflections collected	54889	62267
Unique reflections	7163 (Rint = 0.0798)	8305 (Rint = 0.0820)
Data / restraints / parameters	7163 / 656 / 501	8305 / 0 /732
Goodness-of-fit on F^2	1.049	1.049
R indices [I >2σ(I)] / R1, wR2	0.0412, 0.0997	0.0529, 0.1225
R indices (all data) / R1, wR2	0.0706, 0.1151	0.0733, 0.1353
Completeness to theta max.	0.999	0.994
Max. and min. transmission	0.9817, 0.8772	0.8814 – 0.7485
Theta range for data collection / °	2.87 – 50.754	2.63 – 44.07

$R1 = \Sigma \, \| F_o | - | F_c \| / \Sigma | F_o |$; $wR2 = [\Sigma \{w(F_o^2 - F_c^2)^2\} / \Sigma w(F_o^2)^2]^{1/2}$

Table C.5 Crystal structure and refinement data for **3.8**

	3.8
Chemical formula	$C_{48}H_{84}N_6Nb_2OP_4Si_8$
Formula weight	1295.63
Crystal system	Triclinic
Space group	P-1
a / Å	14.2608(11)
b / Å	14.4493(12)
c / Å	19.0821(15)
α / °	98.128(3)
β / °	94.599(4)
γ / °	107.412(3)
Volume / $Å^3$	3682.8(5)
T / K	100(2)
Z	2
μ / mm^{-1}	0.575
ρ (calcd) / g/cm^3	1.363
F(000)	1590
Absorption correction	Multi–scan
Crystal size / mm	0.66 x 0.43 x 0.39
Wavelength / Å	0.71073
Reflections collected	68251
Unique reflections	18014 (Rint = 0.0268)
Data / restraints / parameters	18014 / 0 /771
Goodness-of-fit on F^2	1.047
R indices [I >2σ(I)] / R1, wR2	0.0433, 0.1072
R indices (all data) / R1, wR2	0.0530, 0.1144
Completeness to theta max.	0.977
Max. and min. transmission	0.7991, 0.6986
Theta range for data collection / °	3.018 – 56.746

$R1 = \Sigma \, \| F_o | - | F_c \| / \Sigma | F_o |$; $wR2 = [\Sigma \{w(F_o^2 - F_c^2)^2\} / \Sigma w(F_o^2)^2]^{1/2}$

Table C.6 Crystal structure and refinement data for **$[P_2N_2]VCl$** and **$([P_2N_2]V)_2(\mu\text{-}N_2)$**

	$[P_2N_2]VCl$	**$([P_2N_2]V)_2(\mu\text{-}N_2)$**
Chemical formula	$C_{24}H_{42}ClN_2P_2Si_4V$	$C_{48}H_{84}N_6P_4Si_8V_2$
Formula weight	619.28	1195.69
Crystal system	Orthorhombic	Triclinic
Space group	$P2_12_12_1$	P-1
a / Å	8.7825(6)	11.5835(16)
b / Å	17.4256(12)	12.4004(17)
c / Å	21.1244(14)	25.644(4)
α / °	90	83.599(8)
β / °	90	81.122(8)
γ / °	90	65.252(7)
Volume / $Å^3$	3232.9(4)	3300.6(8)
T / K	90(2)	100(2)
Z	4	2
μ / mm^{-1}	0.653	0.560
ρ (calcd) / g/cm^3	1.272	1.203
F(000)	1304	1264
Absorption correction	Multi–scan	Multi–scan
Crystal size / mm	0.64 x 0.16 x 0.14	0.37 x 0.26 x 0.24
Wavelength / Å	0.71073	0.71073
Reflections collected	40170	43831
Unique reflections	9498 (Rint = 0.0405)	12446 (Rint = 0.0858)
Data / restraints / parameters	9498 / 0 /307	12446 / 6 / 613
Goodness-of-fit on F^2	1.02	1.161
R indices [I >2σ(I)] / R1, wR2	0.0270, 0.0589	0.1437, 0.3582
R indices (all data) / R1, wR2	0.0321, 0.0613	0.1593, 0.3655
Completeness to theta max.	0.999	0.988
Max. and min. transmission	0.9126, 0.8116	0.8742, 0.6337
Theta range for data collection / °	3.03 – 60.152	1.61 – 51.45

$R1 = \Sigma \, \| F_o | - | F_c \| / \Sigma | F_o |$; $wR2 = [\Sigma \{w(F_o^2 - F_c^2)^2\} / \Sigma w(F_o^2)^2]^{1/2}$

Table C.7 Crystal structure and refinement data for **3.9** and **3.10**

	3.9	**3.10**
Chemical formula	$C_{24}H_{42}I_1N_2P_2Si_4V_1$	$C_{56}H_{78}BN_2O_2P_2Si_4V$
Formula weight	710.75	1047.25
Crystal system	Monoclinic	Monoclinic
Space group	$P2_1/c$	$P2_1/n$
a / Å	10.937(2)	15.2407(7)
b / Å	8.8999(19)	23.7196(12)
c / Å	33.950(7)	19.4714(8)
α / °	90	90
β / °	97.010(5)	91.576(2)
γ / °	90	90
Volume / $Å^3$	3279.8(12)	7036.3(6)
T / K	90(2)	100(2)
Z	2	4
μ / mm^{-1}	1.504	0.288
ρ (calcd) / g/cm^3	1.439	0.989
F(000)	1448	2232
Absorption correction	Multi–scan	Multi–scan
Crystal size / mm	0.24 x 0.20 x 0.19	0.91 x 0.41 x 0.34
Wavelength / Å	0.71073	0.71073
Reflections collected	47981	51726
Unique reflections	6962 (Rint = 0.1072)	12789 (Rint = 0.0446)
Data / restraints / parameters	6962 / 0 / 315	12789 / 0 /621
Goodness-of-fit on F^2	1.068	1.760
R indices [I >2σ(I)] / R1, wR2	0.0695, 0.1730	0.1240, 0.3909
R indices (all data) / R1, wR2	0.0867, 0.1817	0.1473, 0.4141
Completeness to theta max.	0.990	0.998
Max. and min. transmission	0.7514, 0.6377	0.9067, 0.8050
Theta range for data collection / °	3.752 – 53.369	3.35 – 50.594

$R1 = \Sigma \, \| F_o | - | F_c \| / \Sigma | F_o |$; $wR2 = [\Sigma \{w(F_o^2 - F_c^2)^2\} / \Sigma w(F_o^2)^2]^{1/2}$

Table C.8 Crystal structure and refinement data for **3.11**

	3.11
Chemical formula	$C_{25}H_{45}N_2P_2Si_4V$
Formula weight	598.87
Crystal system	Monoclinic
Space group	$P2_1/c$
a / Å	11.0048(6)
b / Å	8.9012(5)
c / Å	33.5611(18)
α / °	90
β / °	95.564(3)
γ / °	90
Volume / $Å^3$	3272.0(3)
T / K	100(2)
Z	4
μ / mm^{-1}	0.564
ρ (calcd) / g/cm^3	1.216
F(000)	1272
Absorption correction	Multi–scan
Crystal size / mm	0.51 x 0.34 x 0.31
Wavelength / Å	0.71073
Reflections collected	26012
Unique reflections	9512 (Rint = 0.0287)
Data / restraints / parameters	9512 / 0 / 316
Goodness-of-fit on F^2	0.933
R indices [I >2σ(I)] / R1, wR2	0.0327, 0.1136
R indices (all data) / R1, wR2	0.0396, 0.1221
Completeness to theta max.	0.990
Max. and min. transmission	0.8396, 0.7766
Theta range for data collection / °	2.438 – 60.138

$R1 = \Sigma \, \| F_o | - | F_c \| / \Sigma | F_o |$; $wR2 = [\Sigma \{w(F_o^2 - F_c^2)^2\} / \Sigma w(F_o^2)^2]^{1/2}$

Table C.9 Crystal structure and refinement data for **4.1** and **4.2**

	4.1	**4.2**
Chemical formula	$C_{24}H_{42}CoN_2P_2Si_4$	$C_{24}H_{42}CoN_2O_2P_2Si_4$
Formula weight	591.82	623.82
Crystal system	Monoclinic	Triclinic
Space group	Pn	P-1
a / Å	12.1878(12)	11.5331(4)
b / Å	14.6289(13)	13.3411(6)
c / Å	17.8641(19)	21.1798(8)
α / °	90	81.417(2)
β / °	101.525(6)	84.160(2)
γ / °	90	88.851(2)
Volume / $Å^3$	3120.8(5)	3205.6(2)
T / K	100(2)	100(2)
Z	4	4
μ / mm^{-1}	0.822	0.808
ρ (calcd) / g/cm^3	1.260	1.293
F(000)	1252	1316
Absorption correction	Multi–scan	Multi–scan
Crystal size / mm	0.55 x 0.48 x 0.38	0.40 x 0.19 x 0.19
Wavelength / Å	0.71073	0.71073
Reflections collected	24965	25301
Unique reflections	17675 (Rint = 0.0274)	14276 (Rint = 0.0224)
Data / restraints / parameters	17675 / 2 / 611	14276 / 0 / 647
Goodness-of-fit on F^2	0.756	0.911
R indices [I >2σ(I)] / R1, wR2	0.0359, 0.0983	0.0416, 0.1180
R indices (all data) / R1, wR2	0.0418, 0.1056	0.0522, 0.1279
Completeness to theta max.	0.977	0.959
Max. and min. transmission	0.7317, 0.6193	0.8577, 0.7607
Theta range for data collection / °	3.628 – 60.166	3.55 – 55.218

$R1 = \Sigma \, \| F_o | - | F_c \| / \Sigma | F_o |$; $wR2 = [\Sigma \{w(F_o^2 - F_c^2)^2\} / \Sigma w(F_o^2)^2]^{1/2}$

Table C.10 Crystal structure and refinement data for **4.3** and **4.4-$_{MeCN}$**

	4.3	**4.4-$_{MeCN}$**
Chemical formula	$C_{24}H_{42}CoI_1N_2P_2Si_4$	$C_{28}H_{51}CoLiN_3P_2Si_4$
Formula weight	718.72	669.88
Crystal system	Orthorhombic	Orthorhombic
Space group	$Pca2_1$	$Pca2_1$
a / Å	16.7871(7)	19.5403(11)
b / Å	12.6048(5)	9.7909(5)
c / Å	31.2319(13)	19.1494(11)
α / °	90	90
β / °	90	90
γ / °	90	90
Volume / $Å^3$	6608.6(5)	3663.6(3)
T / K	100(2)	90(2)
Z	8	4
μ / mm^{-1}	1.712	0.708
ρ (calcd) / g/cm^3	1.445	1.215
F(000)	2928	1424
Absorption correction	Multi–scan	Multi–scan
Crystal size / mm	0.32 x 0.25 x 0.21	0.20 x 0.15 x 0.15
Wavelength / Å	0.71073	0.71073
Reflections collected	35144	20623
Unique reflections	10973 (Rint = 0.0274)	6577 (Rint = 0.0286)
Data / restraints / parameters	10973 / 1 / 629	6577 / 1 / 363
Goodness-of-fit on F^2	1.062	1.084
R indices [I >2σ(I)] / R1, wR2	0.0413, 0.1299	0.0364, 0.1258
R indices (all data) / R1, wR2	0.0432, 0.1315	0.0385, 0.1277
Completeness to theta max.	0.997	0.999
Max. and min. transmission	0.6980, 0.6088	0.8992, 0.8130
Theta range for data collection / °	3.232 – 49.996	4.16 –50.75

$R1 = \Sigma \, \| F_o | - | F_c \| / \Sigma | F_o |$; $wR2 = [\Sigma \{w(F_o^2 - F_c^2)^2\} / \Sigma w(F_o^2)^2]^{1/2}$

Table C.11 Crystal structure and refinement data for **4.4-$_{dioxane}$** and **4.5**

	4.4-$_{dioxane}$	**4.5**
Chemical formula	$C_{30}H_{56}CoLiN_2O_2P_2Si_4$	$C_{28}H_{53}CoN_2P_2Si_5$
Formula weight	716.93	679.04
Crystal system	Triclinic	Triclinic
Space group	P-1	P-1
a / Å	10.002(3)	10.4889(6)
b / Å	12.763(3)	11.1934(7)
c / Å	14.783(4)	16.9411(10)
α / °	80.040(5)	82.587(3)
β / °	84.666(5)	74.756(3)
γ / °	83.444(6)	71.917(3)
Volume / $Å^3$	1841.5(8)	1821.79(19)
T / K	90(2)	100(2)
Z	2	2
μ / mm^{-1}	0.712	0.744
ρ (calcd) / g/cm^3	1.293	1.238
F(000)	764	724
Absorption correction	Multi–scan	Multi–scan
Crystal size / mm	0.18 x 0.13 x 0.10	0.42 x 0.32 x 0.28
Wavelength / Å	0.71073	0.71073
Reflections collected	22407	32178
Unique reflections	6428 (Rint = 0.0403)	8413 (Rint = 0.0229)
Data / restraints / parameters	6428 / 0 / 389	8413 / 0 / 354
Goodness-of-fit on F^2	1.018	0.980
R indices [I >2σ(I)] / R1, wR2	0.0344, 0.0763	0.0338, 0.1134
R indices (all data) / R1, wR2	0.0511, 0.0832	0.0384, 0.1192
Completeness to theta max.	0.978	0.996
Max. and min. transmission	0.9313, 0.8144	0.8119, 0.7588
Theta range for data collection / °	3.256 – 50.236	2.494 – 55.178

$R1 = \Sigma \, \| F_o | - | F_c \| / \Sigma | F_o |$; $wR2 = [\Sigma \{w(F_o^2 - F_c^2)^2\} / \Sigma w(F_o^2)^2]^{1/2}$

Table C.12 Crystal structure and refinement data for **5.1** and **5.2**

	5.1	**5.2**
Chemical formula	$C_{40}H_{66}N_2P_2Rh_2Si_4$	$C_{32}H_{54}I_2N_2P_2Rh_2Si_4$
Formula weight	955.06	1100.71
Crystal system	Monoclinic	Orthorhombic
Space group	$P2_1/n$	$P2_12_12$
a / Å	10.3474(6)	14.399(2)
b / Å	16.4155(12)	11.0164(15)
c / Å	25.8521(18)	13.9673(19)
α / °	90	90
β / °	100.362(2)	90
γ / °	90	90
Volume / $Å^3$	4319.6(5)	2215.(5)
T / K	90(2)	90(2)
Z	4	2
μ / mm^{-1}	0.980	2.349
ρ (calcd) / g/cm^3	1.469	1.758
F(000)	1984	1164
Absorption correction	Multi–scan	Multi–scan
Crystal size / mm	0.17 x 0.09 x 0.08	0.24 x 0.22 x 0.12
Wavelength / Å	0.71073	0.71073
Reflections collected	31583	24481
Unique reflections	7645 (Rint = 0.0572)	6528 (Rint = 0.0228)
Data / restraints / parameters	7645 / 0 / 459	6528 / 243 / 249
Goodness-of-fit on F^2	0.971	1.277
R indices [I >2σ(I)] / R1, wR2	0.0333, 0.0699	0.0491, 0.1252
R indices (all data) / R1, wR2	0.0559, 0.0779	0.0497, 0.1255
Completeness to theta max.	0.998	0.999
Max. and min. transmission	0.9246, 0.8418	0.7544, 0.5738
Theta range for data collection / °	2.952 – 50.11	2.916 – 60.214

$R1 = \Sigma \, \| F_o | - | F_c \| / \Sigma | F_o |$; $wR2 = [\Sigma \{w(F_o^2 - F_c^2)^2\} / \Sigma w(F_o^2)^2]^{1/2}$

Table C.13 Crystal structure and refinement data for **5.3** and **5.4**

	5.3	**5.4**
Chemical formula	$C_{27}H_{42}N_2O_3P_2Rh_2Si_4$	$C_{68}H_{120}Li_2N_4O_2P_4Si_8Rh_2$
Formula weight	822.74	1594.00
Crystal system	Orthorhombic	Monoclinic
Space group	Pbac	$P2_1/n$
a / Å	18.6516(6)	10.7614(5)
b / Å	18.4826(7)	22.3119(13)
c / Å	20.5654(7)	17.1063(8)
α / °	90	90
β / °	90	92.872(2)
γ / °	90	90
Volume / $Å^3$	7089.5(4)	4102.2(4)
T / K	90(2)	100(2)
Z	8	2
μ / mm^{-1}	1.186	0.639
ρ (calcd) / g/cm^3	1.542	1.281
F(000)	3344	1657
Absorption correction	Multi–scan	Multi–scan
Crystal size / mm	0.21 x 0.20 x 0.18	0.27 x 0.17 x 0.17
Wavelength / Å	0.71073	0.71073
Reflections collected	67495	16275
Unique reflections	8134 (Rint = 0.0388)	7270 (Rint = 0.0405
Data / restraints / parameters	8134 / 0 / 369	7270 / 30 / 493
Goodness-of-fit on F^2	0.832	1.058
R indices [I >2σ(I)] / R1, wR2	0.0237, 0.0890	0.0513, 0.1297
R indices (all data) / R1, wR2	0.0361, 0.1093	0.0778, 0.1443
Completeness to theta max.	1.000	0.972
Max. and min. transmission	0.8078, 0.7558	0.8971, 0.6689
Theta range for data collection / °	3.68 – 55.002	3.65 – 50.628

$R1 = \Sigma \, \| F_o | - | F_c \| / \Sigma | F_o |$; $wR2 = [\Sigma \{w(F_o^2 - F_c^2)^2\} / \Sigma w(F_o^2)^2]^{1/2}$

Table C.14 Crystal structure and refinement data for **5.5** and **5.6**

	5.5	**5.6**
Chemical formula	$C_{24}H_{45}N_2P_2Si_4Rh_1$	$C_{25}H_{43}N_2O_1P_2Si_4Rh_1$
Formula weight	638.83	664.83
Crystal system	Monoclinic	Monoclinic
Space group	$P2_1/c$	$P2_1/c$
a / Å	15.1347(8)	12.5800(8)
b / Å	10.0758(5)	12.3256(9)
c / Å	20.3672(10)	21.3803(15)
α / °	90	90
β / °	95.293(2)	99.158(3)
γ / °	90	90
Volume / $Å^3$	3092.6(3)	3272.9(4)
T / K	100(2)	100(2)
Z	4	4
μ / mm^{-1}	0.827	0.787
ρ (calcd) / g/cm^3	1.372	1.349
F(000)	1336	1384
Absorption correction	Multi–scan	Multi–scan
Crystal size / mm	0.48 x 0.35 x 0.28	0.61 x 0.58 x 0.51
Wavelength / Å	0.71073	0.71073
Reflections collected	35414	26212
Unique reflections	9055 (Rint = 0.0269)	9519 (Rint = 0.0204)
Data / restraints / parameters	9055 / 0 / 318	9519 / 0 / 324
Goodness-of-fit on F^2	1.134	1.025
R indices [I >2σ(I)] / R1, wR2	0.0231, 0.0649	0.0221, 0.0537
R indices (all data) / R1, wR2	0.0268, 0.0667	0.0251, 0.0550
Completeness to theta max.	0.999	0.995
Max. and min. transmission	0.7933, 0.7095	0.6694, 0.6241
Theta range for data collection / °	2.702 – 60.09	3.826 – 60.044

$R1 = \Sigma \, \| F_o | - | F_c \| / \Sigma | F_o |$; $wR2 = [\Sigma \{w(F_o^2 - F_c^2)^2\} / \Sigma w(F_o^2)^2]^{1/2}$

Table C.15 Crystal structure and refinement data for **6.1**

	6.1
Chemical formula	$C_{26}H_{46}F_6N_3O_6P_2S_2Si_4V$
Formula weight	900.01
Crystal system	Monoclinic
Space group	$P2_1/n$
a / Å	13.5408(10)
b / Å	16.0782(12)
c / Å	20.2699(16)
α / °	90
β / °	98.145(2)
γ / °	90
Volume / $Å^3$	4368.5(6)
T / K	90(2)
Z	4
μ / mm^{-1}	0.577
ρ (calcd) / g/cm^3	1.478
F(000)	2024
Absorption correction	Multi–scan
Crystal size / mm	0.30 x 0.18 x 0.16
Wavelength / Å	0.71073
Reflections collected	30711
Unique reflections	7737 (Rint = 0.0418)
Data / restraints / parameters	7737 / 0 / 505
Goodness-of-fit on F^2	1.044
R indices [I >2σ(I)] / R1, wR2	0.0543, 0.1446
R indices (all data) / R1, wR2	0.0718, 0.1560
Completeness to theta max.	0.998
Max. and min. transmission	0.9118, 0.8186
Theta range for data collection / °	3.246 – 50.144

$R1 = \Sigma \, \| F_o | - | F_c \| / \Sigma | F_o |$; $wR2 = [\Sigma \{w(F_o^2 - F_c^2)^2\} / \Sigma w(F_o^2)^2]^{1/2}$